Government of Western Australia

Department of
Mines and Petroleum

REPORT
163

MRIWA REPORT PROJECT M426: EXPLORATION TARGETING FOR BIF-HOSTED FE DEPOSITS IN THE PILBARA CRATON, WESTERN AUSTRALIA

by P Duuring, Y Teitler, S Hagemann, and T Angerer

mriwa
Minerals Research Institute of Western Australia

EXPLORATION INCENTIVE SCHEME

THE UNIVERSITY OF WESTERN AUSTRALIA

Centre for EXPLORATION TARGETING

Geological Survey of Western Australia

Government of **Western Australia**
Department of **Mines and Petroleum**

REPORT 163

MRIWA REPORT PROJECT M426: EXPLORATION TARGETING FOR BIF-HOSTED FE DEPOSITS IN THE PILBARA CRATON, WESTERN AUSTRALIA

by
P Duuring, Y Teitler, S Hagemann, and T Angerer

Perth 2016

Geological Survey of Western Australia

MINISTER FOR MINES AND PETROLEUM
Hon. Sean K L'Estrange MLA

DIRECTOR GENERAL, DEPARTMENT OF MINES AND PETROLEUM
Richard Sellers

EXECUTIVE DIRECTOR, GEOLOGICAL SURVEY OF WESTERN AUSTRALIA
Rick Rogerson

REFERENCE
The recommended reference for this publication is:
Duuring, P, Teitler, Y, Hagemann, S and Angerer, T 2016, MRIWA Report Project M426: Exploration Targeting for BIF-hosted Fe deposits in the Pilbara Craton, Western Australia: Geological Survey of Western Australia, Report 163, 263p.

National Library of Australia Cataloguing-in-Publication entry:

Creator:	Duuring, Paul, author.
Title:	Exploration targeting for BIF-hosted Fe deposits in the Pilbara Craton, Western Australia / Paul Duuring, Yoram Teitler, Steffen Hagemann and Thomas Angerer
ISBN:	9781741687101 (ebook)
Subjects:	MRIWA M426 Project. Iron ores--Geology--Western Australia--Pilbara Craton. Heavy minerals--Prospecting--Western Australia--Pilbara Craton. Geology, Stratigraphic--Western Australia--Pilbara Craton.
Other Creators/Contributors:	Teitler, Yoram, author. Hagemann, Steffen G., author. Angerer, Thomas, author. Geological Survey of Western Australia, issuing body.
Dewey Decimal Classification:	551.715

About this publication
This Report presents the results of the Minerals Research Institute of Western Australia (MRIWA) Project M426 'Exploration Targeting for BIF-hosted Fe deposits in the Pilbara Craton, Western Australia'. The Geological Survey of Western Australia (GSWA) is releasing the Report to ensure a wider distribution for the results, which includes the detailed characterization of representative Fe deposits and tools for their exploration. Although GSWA provided support to the project, the scientific content of the Report, and the drafting of figures, has been the responsibility of The University of Western Australia. No editing has been undertaken by GSWA.

Published 2016 by Geological Survey of Western Australia
This Report is published in digital format (PDF) and is available online at <www.dmp.wa.gov.au/GSWApublications>.

Further details of geological publications and maps produced by the Geological Survey of Western Australia are available from:
Information Centre
Department of Mines and Petroleum
100 Plain Street
EAST PERTH WESTERN AUSTRALIA 6004
Telephone: +61 8 9222 3459 Facsimile: +61 8 9222 3444
www.dmp.wa.gov.au/GSWApublications

Cover photograph: Panoramic view of spinifex-covered basalt hills located to the west of the Corunna Downs iron ore prospects

mriwa
Minerals Research Institute
of Western Australia

REPORT NO. 311

Exploration Targeting for BIF-hosted Fe deposits in the Pilbara Craton, Western Australia

Results of research carried out as MRIWA Project M426

in the Centre for Exploration Targeting, University of Western Australia, Australia

by

Paul Duuring, Yoram Teitler, Steffen Hagemann and Thomas Angerer

May 2015

Distributed by: MRIWA
Mineral House
100 Plain Street
Perth WA 6000
to which all enquiries should be addressed

ISBN 1920981721

Table of Contents

List of Figures

Executive Summary

Chapter 1:

Chapter 2:

Chapter 3:

Chapter 4:

Chapter 5:

List of Tables

Acknowledgements

The M426 team, Paul Duuring, Yoram Teitler, Steffen Hagemann, Christina Hemme, Nils Kollert and Thomas Angerer would like to acknowledge the support of numerous individuals in the completion of M426. In particular we acknowledge the financial and logistical support of our sponsors, Atlas Iron Ltd, Geological Survey of Western Australia and the Minerals Research Institute of Western Australia.

The research team acknowledges the support from the Centre for Exploration Targeting through assistance provided during project development (Cam McCuaig) and advice provided associated with managing the project (Estelle Dawes, Gillian Evans, Rong-Chyi Ngoh). Stephane Roudaut is thanked for his assistance with sample photography, mineral separations and with the compilation of the GIS database. We thank members of the Centre for Microscopy, Characterisation and Analysis (CMCA) at the University of Western Australia (Janet Muhling, Malcolm Roberts) for their advice regarding the preparation of samples as well as their imagery and analysis.

David Flanagan is gratefully acknowledge as being the catalyst for the project through the presentation that he gave the CET in 2012 and his encouragement during a follow-up visit at the Atlas Iron Ltd office. The geological staff at Atlas Iron Ltd provided exceptional support and enthusiasm during the life of the project. We particularly thank Pip Darvall, Neil Hannaway, Paul Howard and Anil Chatterji for stimulating discussions that contributed to the outcomes of the project. We enjoyed discussions with the Atlas Iron exploration geologists and appreciated their interest and enthusiasm with the project.

We would like to acknowledge the consistent support from the Geological Survey of Western Australia. In particular, discussions with Arthur Hickman greatly benefited our understanding about lithostratigraphic relationships in the Pilbara and influenced our GIS compilation and prospectivity analysis of the Craton.

Tony Bagshaw and Penny Atkins from MRIWA are thanked for their support and advice associated with the management of the M426 project.

Lastly, we acknowledge discussions and technical support at various stages during the project from:

Noreen Evans and Brad McDonald (AGOS- GeoHistory Laser Ablation ICPMS Facility at Curtin University)

Martin Van Kranendonk (Pilbara geology)

Svetlana Tessalina (Re-Os isotope systematics, Curtin University)

Adrian Boyce (Oxygen isotope analysis at the University of Glasgow).

Executive Summary

Introduction

The MRIWA M426 project was a joint research initiative coordinated by the Minerals Research Institute of Western Australia (MRIWA) and involving Atlas Iron Ltd, the Centre for Exploration Targeting (CET) at the University of Western Australia, RWTH Aachen University and the Geological Survey of Western Australia. The two-year M426 project commenced at the beginning of 2013 and concluded in March 2015. Project personnel included Drs Paul Duuring and Steffen Hagemann (CET) as Chief Investigators, Dr Yoram Teitler (CET) as post-doctoral researcher, and Dr Thomas Angerer (CET adjunct) as an affiliated researcher. Ms Christina Hemme and Mr Nils Kollert (Aachen University) undertook focussed MSc research projects within the broader M426 project.

Stratigraphic relationships in the Pilbara Craton

The Pilbara Craton, exposed over an area of 530 x 230 km in the north-western part of Western Australia (Fig. 1), comprises five Terranes: the 3530–3170 Ma East Pilbara Terrane (EPT), representing the ancient nucleus of the Craton, the 3180 Ma Kurrana Terrane (KT) and the 3270–3110 Ma West Pilbara Superterrane (WPST), which is a collage of three distinct Terranes including the 3270 Ga Karratha Terrane, the 3200 Ma Regal Terrane, and the 3130–3110 Ma Sholl Terrane. These Terranes have unique lithostratigraphy, granitic supersuites, structural map patterns, geochemistry and tectonic histories (Van Kranendonk et al., 2002, 2007; Hickman, 2004, 2012). They consist of four principal elements: (i) volcano-sedimentary rocks distributed in a number of early to Mesoarchaean (3530-3050 Ma) greenstone belts, (ii) granitic rocks of similar ages, forming either large, polyphase complexes or single intrusions, (iii) late basins (3050–2930 Ma) of clastic sedimentary rocks and (iv) post-orogenic granites and ultramafic intrusions (2890–2830 Ma) (Hickman and Van

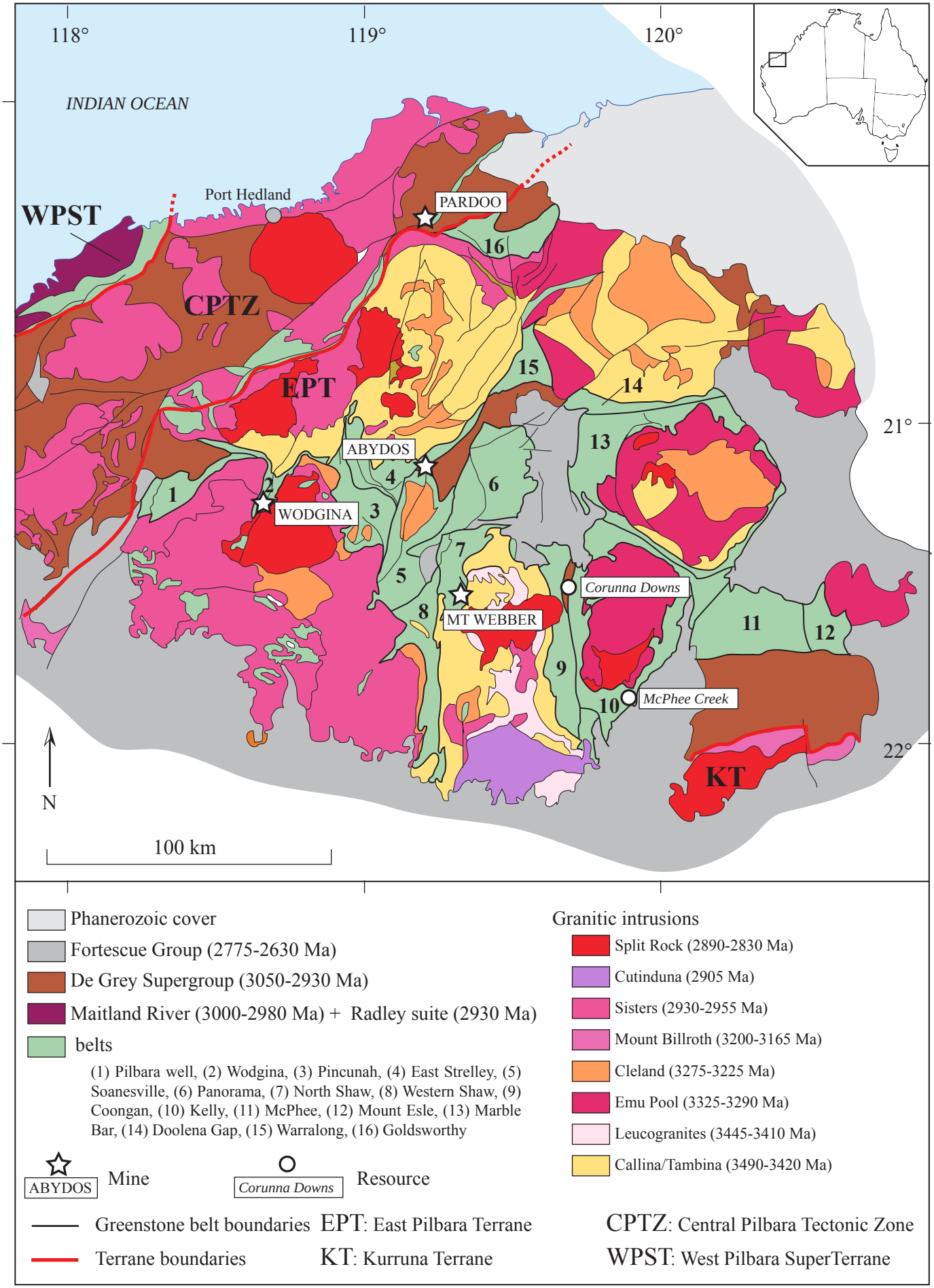

Figure 1: Simplified geology map of the North Pilbara craton including the location of the Wodgina iron camp and active iron ore mines across the North Pilbara. *Modified after Hickman, 2012.*

Kranendonk, 2012). All of these rocks are unconformably overlain by volcano-sedimentary rocks of the >2775 Ma Hamersley Basin (Arndt et al., 1991; Trendall et al., 2004), and intruded by dolerite dykes. The regional deformation history of the Pilbara Craton is summarised by Hickman and Van Kranendonk (2008) and includes up to 12 (D1 to D12) deformation events recorded between 3490 and 2890 Ma. In this scheme, the East Pilbara Terrane and the West Pilbara Superterrane display distinct deformation histories prior to the accretion of these terranes at ca. 3070 Ma. Four early deformation events (D1 to D4, ranging from 3490 to 3240 Ma) are associated with progressive doming of granitic intrusions and creation of synvolcanic structures in the East Pilbara, whereas only one deformation event, dated at ca. 3160 Ma, is recorded in the West Pilbara Superterrane. The East Pilbara Terrane collided with the West Pilbara Superterrane during the Prinsep Orogeny event (D5, ca. 3070 Ma). Subsequently, both Terranes share a common deformation history characterised by deformation events D6 to D12, taking place from 3020 to 2890 Ga and including a major transpressional event at ca. 2950-2940 Ma (North Pilbara orogeny, D9). Several deformation events of moderate intensity occurred during the deposition of the 2775-2630 Ma Fortescue Group.

Similar to the Yilgarn Craton, the North Pilbara Fe deposits are mostly hosted by Mesoarchaean BIF units within, or unconformably overlying, greenstone belt volcano-sedimentary sequences. In the North Pilbara, these BIF occurrences are hosted by discrete formations, specifically the 3.23 Ga Pincunah banded-iron Member of the Kangaroo Caves Formation, (ii) the 3.19 Paddy Market Formation and (iii) the 3.02 Ga Cleaverville Formation. The Kangaroo Caves and Paddy Market Formations were deposited prior to the accretion of the different Terranes during the Prinsep orogeny and are, therefore, restricted to the East Pilbara Terrane (Pincunah BIF: North Shaw and Pincunah greenstone belts; Paddy Market BIF: North Shaw and Soanesville greenstone belts). Deep hydrothermal settings are

inferred for the deposition of the Pincunah BIF, whereas the Paddy Market Formation was deposited under mid- to-outer-fan and basin-plain settings as part of the Soanesville sedimentary basin (Eriksson, 1981; Hickman, 2012). In contrast, the De Grey Superbasin formed after 3.02 Ga through crustal relaxation and extension after collision between the granite–greenstone Terranes and is exposed in most parts of the North Pilbara Craton. It usually includes a basal conglomerate and sandstone overlain by a ~ 1 km-thick unit of BIF, chert and black shale of the Cleaverville Formation.

Despite intensive field mapping campaigns performed by government geological surveys during the last few decades, the identification of some BIF exposures in the North Pilbara remains problematic due to uncertainties in depositional ages and correlations across the different greenstone belts. Recently, survey mapping programs led by A. Hickman (Van Kranendonk et al., 2006, 2007; Hickman, 2012) resulted in the revision of the stratigraphy and lithofacies subdivisions within the Pilbara Craton. This revision includes the volcano-sedimentary sequence at Abydos based on recent dating and correlations between greenstone belts; BIF units formerly assigned to the Paddy Market Formation (ca. 3.19 Ga) are reassigned to the 3.02 Ga Cleaverville Formation (Hickman, 2012).

Corunna Downs iron camp

The Split Rock and Runway deposits at Corunna Downs contain goethite-martite rich ore bodies hosted by jaspilitic BIF of the 3020 Ma Cleaverville Formation in the Coongan greenstone belt of the Pilbara Craton, Western Australia. One major deformation event related to the 2950-2940 Ma North Pilbara Orogeny (regional D9) affects the Cleaverville BIF. This deformation event involves N-S to NNE-SSW sinistral shearing combined with reverse, east-side-up displacement resulting in the formation of tight subvertically plunging folds. Unweathered BIF records an early stage of hypogene magnetite alteration likely related

to circulation of reduced fluids at ca 2950 Ma. Although stage 1 hypogene alteration is widespread and pervasive, it is largely concentrated along, or proximal to, high strain D9 shear zones, which represent focused pathways for hydrothermal fluids. Hypogene magnetite alteration results in an initial upgrade in iron in the BIF from ca 30 to 40-45 wt% Fe and is associated with a similar decrease in SiO_2 through leaching of chert. Restricted occurrence of crystalline platy hematite postdating magnetite suggests that the widespread reduced hypogene alteration may have been followed by local secondary hypogene alteration involving oxidizing fluids. The significance and timing of this event remains poorly constrained; it is speculated that it could be related to hydrothermal alteration at ca. 2165 Ma. A recent, supergene alteration partly replaces magnetite-(±platy hematite) rich proto-ore, forming the large volumes of goethite-martite that comprise the main portion of high-grade ore zones in both deposits. The timing of martitisation remains unclear, although recent supergene alteration most likely caused the martitisation of magnetite. It cannot be excluded, however, that early (Precambrian) martitisation occurred through the circulation of ancient oxidizing supergene fluids. The complex, supergene alteration sequence initiates with the solid state oxidation of magnetite to martite; the large amounts of W incorporated by chemisorption into martite suggest that the onset of weathering mostly involved alkaline (modified) meteoric water. Further development of the supergene system involved the formation of botryoidal hematite, anhedral and botryoidal goethite, reflecting the evolution of this long-lived weathering system. Together with textural observations, important differences in the trace element composition of goethite, including Zn, Ni, U or Pb, confidently allows the distinction of two main events of goethitisation, referred to in this contribution as stage 4 and stage 6 goethite, respectively. Importantly, Zn and Ni positive anomalies identified from mineral and whole-rock geochemistry are demonstrably related to deposit-scale anomalies identified from company assay data. Interestingly, among the four main resources recognised

at Corunna Downs, only the Split Rock and Runway deposits display these anomalies. It is proposed that these elements, enriched in the goethite ore zones, are sourced from adjacent shale. The ubiquitous spatial distribution of stage 4 goethite indicates that it represents the dominant mineralisation stage responsible for the formation of volumetrically important ore bodies at Corunna Downs. Microplaty hematite that formed between stages 4 and 6 is restricted to a few surface exposures and is tentatively interpreted to be a local dewatering product of stage 4 goethite rather than a hydrothermal alteration product after ancient (Proterozoic) supergene goethite. The present study would certainly benefit from additional field and analytic work with respect to mining development and better access to subsurface exposures along pit walls. Such interpretations may also be either supported or challenged by similar studies conducted in other iron camps of the Pilbara.

Wodgina iron camp

The Anson and Dragon deposits at Wodgina principally consist of goethite-martite rich ore bodies hosted by two to three BIF macrobands of the 3020 Ma Cleaverville Formation in the Wodgina greenstone belt of the Pilbara Craton, Western Australia. Two major deformation events (D8 and D9 events in the regional deformation scheme) affect the Cleaverville BIF. The D8 deformation event involves tight, W- to NW-shallowly-plunging D8 folds associated with several high strain zones. The D9 deformation event is expressed as upright, tight, steep NNE-plunging folds and is responsible for the regional syncline of the Wodgina greenstone belt. Unweathered BIF records an early stage of euhedral magnetite precipitation, likely related to regional low-grade metamorphism and circulation of metamorphic-driven reduced fluids at ca 2215-2165 Ma. Although stage 1 alteration is widespread and pervasive, it is largely concentrated along or proximal to high strain D8 shear zones, which represent focused pathways for hydrothermal fluids. Metamorphic magnetite locally results in an initial upgrade of iron in the BIF from ca 30 to 40-45 wt% Fe and is associated with a similar

decrease in SiO_2 through leaching of chert. Subsequent martitisation (stage 2) of stage 1 magnetite is interpreted as an early (Precambrian) process caused by descending ancient meteoric waters interacting with BIF. Stage 2 martitisation is associated with an increase in Ti, Sn, V and Ga concentrations, the two latter elements being potential pathfinders for martite-rich zones. A recent, supergene alteration partly replaces martite-rich BIF, forming the large volumes of goethite that comprise the main portion of high-grade ore zones in both deposits. The recent supergene sequence is dominantly represented by stage 5 goethite, characterized by limited contamination by deleterious elements. Further development of the supergene system involved the formation of botryoidal to anhedral hematite, and late botryoidal goethite. Together with textural observations, important differences in the trace element composition of goethite, including the strong increase in Zn within stage 7 goethite, are interpreted to reflect environmental changes in the Pilbara from tropical to semi-arid conditions since the late Cretaceous. The ubiquitous spatial distribution of stage 5 goethite indicates that it represents the dominant mineralisation stage responsible for the formation of volumetrically important ore bodies at Corunna Downs. Nevertheless, it is proposed that stage 7 goethitisation is also of significant importance in the formation of large iron ore bodies at Wodgina. This late mineralisation event may be targeted using Zn as a relevant elementary pathfinder.

Abydos iron camp

The Trigg and Mettams deposits at Abydos consist of goethite-martite rich ore bodies hosted by a 100 to 250 m-wide jaspilitic BIF macroband of the 3.02 Ga Cleaverville Formation in the East Strelley greenstone belt of the Pilbara Craton, Western Australia. One major deformation event at ca. 2950-2940 Ma (North Pilbara Orogeny, regional deformation event D9) affects the Cleaverville BIF through tilting of the BIF units and emplacement of bedding-parallel, broad fault zones. Unweathered BIF records an early stage of euhedral magnetite

precipitation concentrated along D9 fault zones, likely related either to the North Pilbara Orogeny or to regional low-grade metamorphism to metasomatism from 2215 to 2145 Ma. Although stage 1 alteration is widespread and pervasive, it is largely concentrated along, or proximal to, high strain D3 shear zones, which represent focused pathways for hydrothermal fluids. Formation of D9 fault zone-hosted, metamorphic or metasomatic magnetite locally results in an initial upgrade of iron in the BIF from ca 30 to 40-45 wt% Fe. Subsequent martitisation (stage 2) of stage 1 magnetite and formation of microplaty hematite (stage 3) is interpreted as an early (Proterozoic) process caused by heated, descending ancient meteoric waters interacting with BIF. Stage 1 magnetite and stage 2 martite are associated with relatively high amounts of Ti and V which represent potential pathfinders for alteration stages 1 and 2. A recent (Cenozoic?) supergene alteration partly replaces martite-rich BIF, forming the large volumes of goethite that comprise the main portion of high-grade ore zones in both deposits. The recent supergene sequence is dominantly represented by stage 5 goethite, mainly occurring as disseminated anhedral goethite via pervasive fluid related weathering. Further development of the supergene system involved the formation of vein-hosted, massive botryoidal goethite. The ubiquitous spatial distribution of stage 5 goethite indicates that it represents the dominant mineralisation stage responsible for the formation of volumetrically important ore bodies at Corunna Downs. Nevertheless, stage 6 goethitisation is also of significant importance in the formation of the larger iron ore body at Trigg. Stage 5 goethite may be confidently targeted using a combination of elements including Ni, As, Zn and Be. Stage 6 event may be targeted using Zn or Be as relevant, standalone elementary pathfinders.

Pardoo iron camp

The ALX deposit at Pardoo principally consists of supergene-modified hypogene goethite-martite rich ore body hosted near the base of the Ord Ridley BIF member of the 3.02 Ga Cleaverville Formation. In contrast, the nearby Bobby deposit, hosted by the Bobby BIF

member, only consists of supergene goethite ore. One major deformation event at ca. 2950-2940 Ma (North Pilbara Orogeny, regional deformation event D9) affects the Cleaverville BIF in both deposits, through tilting of the BIF units. In the Ord Ridley BIF member, this event is also associated with the emplacement of bedding-parallel, broad fault zones that record an early stage of euhedral magnetite precipitation. Stage 1 magnetite is largely concentrated along, or proximal to, high strain D9 shear zones, which represent focused pathways for hydrothermal fluids, locally resulting in an initial upgrade in iron in the BIF from ca 30 to 40-45 wt% Fe. Subsequent formation of platy hematite (stage 2) and martite (stage 3) after stage 1 magnetite is interpreted as an early (Proterozoic) process caused by heated, descending ancient meteoric waters interacting with BIF, although the occurrence of secondary martitisation during recent supergene alteration is suggested. The positive W anomaly identified from whole-rock geochemistry in hypogene ore at ALX is demonstrably related to the elevated W concentrations in martite. The recent supergene sequence is dominantly represented by stage 4 goethite, essentially occurring as disseminated anhedral goethite formed through pervasive hydrothermal alteration. Further development of the supergene hydrothermal fluid system involved the formation of vein-hosted, massive botryoidal goethite (stage 5). The ubiquitous spatial distribution of stage 4 goethite indicates that it represents the dominant mineralisation stage responsible for the formation of volumetrically important ore bodies at Pardoo. Stage 5 goethite may be targeted using a several pathfinder elements including Ni, As, Zn, Cu and P.

Geological synthesis, Mineral Systems model for BIF-hosted iron deposits in the Pilbara Craton and implications for exploration

This study documents the: (i) geological framework, (ii) deformation histories, (iii) controls on iron ore formation, (iv) multi-stage hypogene and supergene fluid alteration events affecting BIF and (v) geochemical signatures of their respective high-grade iron orebodies. A

Mineral Systems model for the genesis of BIF-hosted iron orebodies is presented for the Pilbara Craton with implications for iron ore exploration.

Following the recent revision of the lithostratigraphy of the Pilbara Craton by the GSWA, the BIF macrobands that host iron ore in the Abydos, Pardoo, Wodgina and Corunna Downs iron camps are now classified as 3020 Ma Cleaverville Formation. In comparison, BIF macrobands of the 3230 Ma Pincunah Bander Iron Member of the Kangaroo Caves Formation and the 3190 Ma Paddy Market Formation do not host comparable iron ore deposits in terms of resource size. A comparison of mapped and sampled BIF macrobands from the studied iron camps demonstrates important facies variations from west to east across the East Pilbara Terrane. Specifically, primary BIF macrobands are generally more iron-rich, thicker and have a higher proportion of BIF versus Fe-poor sedimentary rocks (such as chert and siltstone) in the eastern parts of the East Pilbara Terrane. These craton-scale observations support a depositional model for the Cleaverville Formation in the East Pilbara Terrane wherein the Gorge Creek basin progressively deepens both spatially, from west to east, and temporally, with a deepening of the basin through time. REE + Y trends for examples of least-altered BIF sampled from each camp indicate that the representative BIF macrobands from the Cleaverville Formation formed from anoxic seawater with strong hydrothermal influence, equivalent to note trends for Meso- to Late-Archean BIF occurrences reported in the Yilgarn Craton and South Africa.

Cleaverville Formation BIF in all the studied iron camps record a similar deformation history that is compatible with that documented by previous workers for the Pilbara Craton. Although early folds and shear zones are present in the Wodgina camp, the dominant deformation event recorded by each camp is equivalent to the regional D9 event for the Pilbara Craton. This event is expressed in the camps by the prevalence of fold hinges and shear zones located along fold limbs. Subsequent deformation events resulted in the

tightening of these fold hinges, the transposition of structural elements and bedding planes, and the transition to transpressional deformation and associated strike-slip shearing along steeply dipping contacts within the folded greenstone belts.

Iron ore types are remarkably similar in all iron camps in the East Pilbara Terrane. Iron ore types include, in order of formation: (i) hypogene magnetite-rich ore hosted by early shear zones, (ii) martite-rich BIF with local platy hematite, which are the product of early hypogene and/or late supergene alteration events, (iii) goethite and goethite-martite ores that result from intense supergene goethitisation of least-altered, magnetite- or martite-altered BIF, (iv) a second stage of vitreous goethite ore expressed as late veins of massive to botryoidal goethite, with colloform silica, and (v) ochreous goethite ore.

The analysis of representative bulk rock samples of these iron ore types (combined with in situ LA-ICP-MS analysis of iron oxide minerals) demonstrates useful pathfinder element indices associated with the increase in total iron content and the decrease in silica for altered BIF. In all studied camps, it is noted that high-grade goethite-rich supergene orebodies have enrichments in P and Zn that correspond to matching enrichments in stages 5 and 7 goethite. In most camps, stages 5 and 7 goethite-rich orebodies are indicated by enrichments in Ni, As, Ba, Cu or U. In contrast, localised enrichments in Ti, V, W, Sb or Ga are restricted to specific camps. The widely present pathfinder elements (P and Zn) are most useful in terms of their craton-wide application. The more localised element enrichments indicate that camp- to deposit-scale geological controls are influencing these enrichment patterns. For example, the presence of carbonaceous shale units likely controls the presence of local Ni and Zn enrichment in areas of the Corunna Downs camp.

The Mineral Systems model for the genesis of BIF-hosted iron orebodies in the Pilbara Craton identifies four critical elements: (i) BIF fertility, (ii) structural architecture governing

rock permeability and degree of fluid interaction with BIF, (iii) Si-under saturated fluids and (iv) surficial modification and preservation.

The main critical element for the formation of BIF-hosted iron ore is the occurrence of BIF macrobands that have a strong potential (fertility) for subsequent upgrade and mineralisation. The fertility of a given BIF macroband is primarily controlled by the extent, thickness and iron content of the primary BIF. Within the North Pilbara, BIF macrobands from the Cleaverville Formation display much greater thicknesses and are more laterally continuous compared to earlier BIF macrobands of the 3190 Ma Paddy Market Formation and the Pincunah Iron Member of the 3230 Ma Kangaroo Caves Formation. The Cleaverville Formation, therefore, represents the most prospective target for BIF-hosted iron ore in the North Pilbara Craton. The recognition of these fertile BIF macrobands at a Terrane scale largely relies on the availability of accurate outcrop geology maps, combined with geophysical surveys in areas of cover. An important outcome of this study is a GIS-based prospectivity database for the Pilbara Craton (see the digital appendices). This GIS database includes geological outcrop and interpretation maps sourced from GSWA. BIF macrobands are categorised based on their host formation, age and dominant lithofacies. A qualitative ranking system has been used to identify the prospectivity of these macrobands. The western extension of the Wodgina greenstone belt is highlighted as an important potential acquisition target based on the likelihood that it hosts BIF macrobands that are comparable in primary chemistry to that documented in the Wodgina iron ore deposits. Important structural elements that control hypogene and supergene orebodies, such as multiple tight folds and stage 1 magnetite altered shear zones, may be present in this area.

A second critical element for the formation of BIF-hosted iron ore in the North Pilbara is the structural thickening of primary BIF macrobands via folding or shear zone duplication, together with the generation of broad damage zones related to shear zones or fault zones,

which favour the circulation of fluids and alteration of BIF macrobands. The presence of shear zone-hosted stage 1 magnetite in all studied camps suggests the importance of early-formed structures in that they increase the total iron content of the primary BIF macrobands, but they also localise stress during subsequent deformation events and are common sites for reactivation. Consequently, early-formed structures are favourable targets within a district due to their potential to be reactivated and to be the loci for fluid alteration of BIF. These structures can be recognised during mapping based on the observation of 1 to 10 m-thick zones of increasing strain, coincident with decreasing mesoband and microband thicknesses. The confluence of reactivated early-formed shear zones and fold hinge zones are the best target for the generation of high-volume, high-quality, goethite-hematite orebodies (e.g. the Split Rock deposit, Corunna Downs iron camp). In these areas, the plunge of fold axes and intersection lineations derived from merging shear zones can be used to predict the plunge of high-grade ore zones.

A third critical element for the formation of BIF-hosted iron deposits is the availability of abundant Si-under saturated fluids. Stage 1 magnetite likely precipitated from a relatively reduced, hot, deeply circulating, silica-bearing fluid. This hypogene fluid alteration event also resulted in the localised addition of hypogene quartz to BIF, thus moderating the potential benefit of adding hydrothermal iron oxides to the primary BIF. Consequently, stand-alone examples of shear zone-hosted magnetite-rich ore zones are likely to have a significant silica content. These magnetite-enriched occurrences require subsequent supergene alteration to remove the silica to form a high-grade iron ore. In comparison with hypogene fluids, the composition of later supergene fluids is likely to be influenced by the weathering environment in which these fluids were sourced and the interaction between these surface-derived oxidised, low-temperature fluids and rocks encountered along the fluid pathway. Under warm and wet conditions (i.e. stage 5 alteration at 70 to 50 Ma), weathering involved

acidic, Si-under saturated meteoric fluids. These fluids have a strong potential to dissolve silica, thus favouring the concentration of iron in BIF macrobands and the formation of goethite ore. However, under semi-arid conditions (i.e. stage 7; <50 Ma) meteoric fluids have a neutral pH and are, therefore, less efficient for the dissolution of silicate minerals.

A fourth critical element for the formation of BIF-hosted iron deposits in the Pilbara is the length of time that these primary and hypogene magnetite-rich BIF macrobands were exposed at surface and subjected to the interaction with near-surface derived supergene fluids, as well as the necessary preservation of these supergene or supergene-modified ore bodies. Preservation is greatest in the arid interior, beyond the marginal zones of valley incision, or on land surfaces with mainly subdued relief. The development of lateritic hard caps on top of iron deposits in most camps protects underlying ore bodies from complete erosion. The location of hard cap over fold hinges and intersecting steeply dipping shear zones (detected from structural mapping and interpretation of geophysical data) is a target area for exploration on the basis of the likely preservation of deeper (hidden) ore zones. In some areas of the Pilbara, the presence of eolian or fluviatile sediments on top of BIF-hosted iron orebodies may provide favourable conditions for the preservation of the iron ore bodies. The Cleaverville Formation documented in the Isabella 1:100,000 geology map is here identified as an exploration target based on the potential to discover iron orebodies within BIF macrobands that are hidden beneath a veneer of eolian cover.

Step-wise guidelines for exploration strategy include: (i) the compilation of remotely acquired data sets to map out anomalously thickened areas of BIF macrobands, (ii) establishing the geophysical and geochemical properties of unmineralised, unaltered BIF macrobands in the area so as to define a base-level for comparison, (iii) establish the district-scale deformation history and identifying the earliest structures and (iv) ranking regional-scale targets and test by field-based mapping. An early assessment of the likely endowment

of a new exploration district or deposit-scale target can be made by applying a Power Law distribution curve to known resource sizes in a given district. Gaps within this decreasing frequency curve highlight potential undiscovered orebodies. A second measure of a new district or deposit's potential endowment may be assessed during early stages of drilling by measuring the distribution of iron grades. The high-quality iron deposits are those with a greater proportion of high-grade iron ore intersected by drilling (e.g. the Trigg deposit in the Abydos camp and the Alice deposit in the Pardoo camps). Provided that the drill density is sufficient, these types of plots are useful for comparing the quality of iron deposits. This frequency distribution for iron grades from drilling is useful for the early assessment of an exploration target.

Introduction

Project details

The MRIWA M426 project was a joint research initiative coordinated by the Minerals Research Institute of Western Australia (MRIWA) and involving Atlas Iron Ltd Pty, the Centre for Exploration Targeting (CET) at the University of Western Australia, RWTH Aachen University and the Geological Survey of Western Australia. The two-year M426 project commenced at the beginning of 2013 and concluded in 2015. Project personnel included Drs Paul Duuring and Steffen Hagemann (CET) as Chief Investigators, Dr Yoram Teitler (CET) as post-doctoral researcher and Dr Thomas Angerer (CET adjunct) as an affiliated researcher. Ms Christina Hemme and Mr Nils Kollert (Aachen University) undertook focussed MSc research projects within the broader M426 project.

Background to the study

Exploration strategies for detecting high-grade (>55 wt. %) iron ore in the Pilbara Craton have historically relied upon the identification of exposed supergene hematite-goethite-rich orebodies. For example, the Mt. Webber and McPhee Creek hematite-goethite deposits are two such iron ore occurrences that were readily identified using conventional techniques, including aerial photography, satellite imagery and field mapping. However, exploration in the Pilbara is reaching a mature state in that discovery success is slowing using the current exploration model. The opportunity now exists to develop a more predictive exploration strategy for the Pilbara Craton using innovative techniques; a strategy that targets (i) near-surface supergene hematite-goethite ore, (ii) deeper extensions of hypogene magnetite-rich ore and genetically related alteration zones, and (iii) the detection of "blind" supergene and/or hypogene orebodies beneath surface transported cover and unmineralised BIF.

The key to this predictive approach to exploration lies in establishing the geological criteria that control the location of high-grade iron orebodies within several iron ore camps before extrapolating these findings to the remainder of the Pilbara Craton in the form of a Mineral Systems model. For this reason, the Corunna Downs, Wodgina, Abydos and Pardoo iron camps were selected as important localities for understanding the combined effects of supergene and hypogene processes on the formation of high-grade iron ore. Within this group, the Wodgina iron camp was targeted as an important field area for testing the hypothesis that fluids derived from felsic magmas may contribute to iron mineralisation in nearby BIF on the basis of the close proximity between pegmatite-hosted Ta ore deposits and BIF-hosted iron ore at Wodgina.

Project objectives

The main aims of the M426 project were to:

(i) Document the key geological relationships for a diverse range of iron ore camps in the Pilbara Craton (Corunna Downs, Wodgina, Abydos, and Pardoo);

(ii) Identify fundamental controls on high-grade iron ore for each iron camp;

(iii) Extrapolate these findings to the craton scale and develop a Mineral Systems model for BIF-hosted iron ore in the Pilbara Craton; and

(iv) Translate the Mineral Systems model into a predictive approach to iron exploration in the Pilbara Craton.

Research methodology

(i) A scoping study was performed at the beginning of the M426 project with the aim of selecting the most important iron camps for detailed study.

(ii) Detailed geological fieldwork was conducted through a series of fieldtrips at Corunna Downs, Wodgina, Abydos and Pardoo by Drs Yoram Teitler, Paul Duuring and Steffen Hagemann. In addition, MSc students Christina Hemme and Nils Kollert performed several phases of fieldwork in the Pardoo camp. Their MSc theses were finalised and delivered to M426 sponsors in August 2014.

(iii) A GIS compilation and BIF prospectivity map was produced and delivered to project sponsors in July 2014.

(iv) Laboratory-based studies were the focus of research conducted in the second half of the project and included petrological examinations (conventional microscopy and SEM), bulk rock and mineral geochemical studies (LA-ICPMS and WDS), as well as isotope analysis (O isotope and Re-Os).

Project reporting of key research findings

Research progress and findings were delivered to M426 project sponsors on a regular basis through a combination of methods that included:

(i) End of Month reports;

(ii) End of Fieldtrip reports with informal presentations to Atlas Iron Ltd;

(iii) Progress reports that summarised key findings;

(iv) Weekly to fortnightly visits by Drs Yoram Teitler and Paul Duuring to the Atlas Iron company office in Perth for the purpose of discussions;

(v) Quarterly MRIWA Reports;

(vi) Three MRIWA Progress Meetings with presentations and posters; and

(vii) A Final MRIWA Meeting with Final Project Report.

Layout of the final report

The final report is organised as a series of chapters with appendices. The first four chapters document key geological relationships and controls on high-grade iron ore bodies in the Corunna Downs, Wodgina, Abydos and Pardoo iron camps. The final chapter provides a synthesis of the data and interpretations from the individual camps in the form of a Mineral Systems model for the Pilbara Craton. Major implications for iron ore exploration are identified in each camp-scale study, as well as in the final synthesis chapter. The appendices include relevant digital data associated with the M426 project. Key hand specimens and thin sections that are the source for data in the M426 project are housed by the UWA Geology museum.

Chapter 1: Multistage hypogene-supergene Fe mineralisation in BIF-hosted iron ore at Corunna Downs, North Pilbara Craton

I. Introduction

Exploration for banded iron formation (BIF)-hosted Fe ore in Western Australia has historically targeted Palaeoproterozoic, Superior-type BIFs of the Hamersley Province where a number of world-class, martite – microplaty hematite ± magnetite deposits have been discovered and mined for more than 50 years (e.g. Mount Whaleback, Mount Tom Price, Barley et al., 1999; Li et al., 1993; Morris, 1985; Muller et al., 2005; Powell et al., 1999; Thorne et al., 2004, 2009; Webb et al., 2003). However, due to the advanced maturity of exploration and the increasing difficulty in discovering new deposits in the Hamersley Basin, the past decade has seen the emergence of Archaean granite-greenstone terranes, such as those exposed in the Yilgarn and North Pilbara Cratons, as new fields of exploration for BIF-hosted iron ore. The dominant controls on the formation of iron ore in the Yilgarn Craton have been documented through a number of recent studies, highlighting the importance of hypogene magnetite–(martite–microplaty hematite) mineralisation through sodic

metasomatism (Angerer and Hagemann, 2010; Angerer et al., 2012; Duuring and Hagemann, 2010, 2012a, 2012b). In contrast, Fe deposits in the North Pilbara have received minor scientific attention (Kerr et al., 1994) despite the occurrence of historical mines (e.g. Yarrie mine). Currently, several deposits in the North Pilbara are mined by Atlas Iron Ltd. (e.g. Wodgina, Pardoo, Mt Webber and Abydos mines), with an additional number of recently defined resources (e.g. McPhee Creek, Corunna Downs).

The Corunna Downs iron camp located in the Coongan greenstone belt hosts several known surface expressions of high-grade (> 57 wt% Fe) ore bodies that extend for about 600-800 m in strike length and 200-300 m width, and from surface to over 200 m depth. The Fe camp has a total resource of more than 51 Mt Fe (grade and cut-off values of 57.5 and 50.0 wt% Fe, respectively; ASX release May 2014) with particularly low contamination by accessory elements (P= 0.09 wt%, Al_2O_3 = 1.6 wt%). The Corunna Downs iron camp therefore represents one of the most economically attractive iron camps in the North Pilbara and its recent recognition supports the potential for other significant (>50 Mt) resource discoveries in the region. Consequently, Corunna Downs is an important case study site for examining geological processes involved in the formation of large volumes (>50 Mt) of high-quality ore.

Since exploration in the Coongan greenstone belt and elsewhere in the North Pilbara has now reached a significantly mature state, the opportunity exists to develop a more tailored strategy that targets near-surface ore bodies through the elaboration of practical tools and vectors to mineralisation. Such exercise requires an accurate understanding of the primary controls and processes involved in ore formation, and the Corunna Downs iron camp constitutes in this sense an excellent natural laboratory for characterizing ore-forming processes.

In this Chapter, we briefly review BIF occurrences and their potential for mineralisation in the North Pilbara Craton. Subsequently, a detailed geological description is provided for the

Corunna Downs iron camp, with specific reference to two areas of geologic and economic importance, the Split Rock and Runway deposits. A multidisciplinary approach was applied, which included geological mapping and core logging, combined with microscopy, bulk geochemical analysis and mineral microanalysis.

II. Regional Geology

The Pilbara Craton, exposed over an area of 530 x 230 km in the north-western part of Western Australia (Fig. 1), is composed of five terranes: the 3.53–3.17 Ga East Pilbara Terrane (EPT), representing the ancient nucleus of the craton; the 3.18 Ga Kurrana Terrane (KT) and the 3.27–3.11 Ga West Pilbara Superterrane (WPST), which is a collage of three distinct terranes including the 3.27 Ga Karratha Terrane, the 3.20 Ga Regal Terrane, and the 3.13–3.11 Ga Sholl Terrane. These terranes have unique lithostratigraphy, granitic supersuites, structural map patterns, geochemistry and tectonic histories (Van Kranendonk et al., 2002, 2007; Hickman, 2004). They consist of four principal elements: (i) volcano-sedimentary rocks distributed in a number of early to Mesoarchaean (3.53-3.05 Ga) greenstone belts, (ii) granitic rocks of similar ages, forming either large, polyphase complexes or single intrusions, (iii) late basins (3.05–2.93 Ga) of clastic sedimentary rocks and (iv) post-orogenic granites and ultramafic intrusions (2.89–2.83 Ga) (Hickman and Van Kranendonk, 2012). All of these rocks are unconformably overlain by volcano-sedimentary rocks of the. 2.78–2.45 Ga Hamersley Basin (Arndt et al., 1991; Trendall et al., 2004), and intruded by dolerite dykes.

The regional deformation history of the Pilbara Craton is summarised by Hickman and Van Kranendonk (2008a) and includes up to 12 (D1 to D12) deformation events recorded between 3490 and 2890 Ma. In this scheme, the East Pilbara Terrane and the West Pilbara

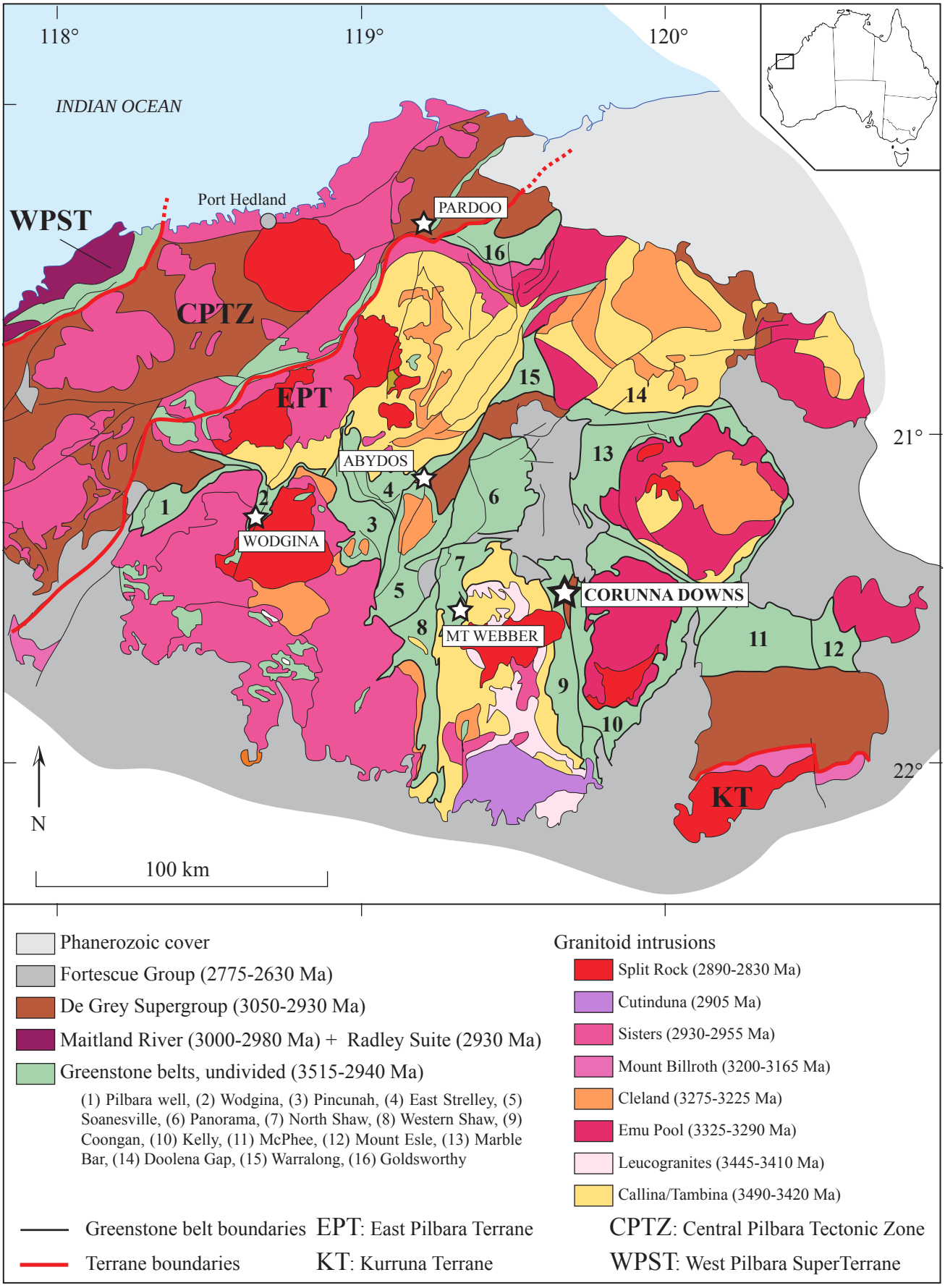

Figure 1: Simplified geology map of the North Pilbara craton including the location of the Corunna Downs iron camp and active iron ore mines across the North Pilbara. *Modified after Hickman, 2012.*

Superterrane display distinct deformation histories prior to the accretion of these terranes at ca. 3070 Ma. Four early deformation events (D1 to D4, ranging from 3490 to 3240 Ma) are associated with progressive doming of granitic intrusions and creation of synvolcanic structures in the East Pilbara, whereas only one deformation event, dated at ca. 3160 Ma, is recorded in the West Pilbara Superterrane. The East Pilbara Terrane collided with the West Pilbara Superterrane during the Prinsep Orogeny event (D5, ca. 3070 Ma). Subsequently, both terranes share a common deformation history characterised by deformation events D6 to D12, taking place from 3020 to 2890 Ga and including a major transpressional event at ca. 2950-2940 Ma (North Pilbara orogeny, D9). Several deformation events of moderate intensity occurred during the deposition of the 2775-2630 Ma Fortescue Group.

Similar to the Yilgarn Craton, the North Pilbara Fe deposits are mostly hosted by Mesoarchaean BIF units within, or unconformably overlying, greenstone belt volcano-sedimentary sequences. In the North Pilbara, these BIF occurrences are hosted by discrete formations, specifically the 3.23 Ga Pincunah banded-iron member of the Kangaroo Caves Formation, (ii) the 3.19 Paddy Market Formation and (iii) the 3.02 Ga Cleaverville Formation. The Kangaroo Caves and Paddy Market Formations were deposited prior to the accretion of the different terranes at ca. 3.07 Ga (Prinsep orogeny; Hickman, 2012) and are therefore restricted to the East Pilbara Terrane (Pincunah BIF: North Shaw and Pincunah greenstone belts; Paddy Market BIF: North Shaw and Soanesville greenstone belts). Deep hydrothermal settings are inferred for the deposition of the Pincunah BIF, whereas the Paddy Market Formation was deposited under mid- to-outer-fan and basin-plain settings as part of the Soanesville sedimentary basin (Hickman, 2012). In contrast, the De Grey Superbasin formed through crustal relaxation and extension after collision at ca. 3.07 Ga of the granite–greenstone terranes and is exposed in most parts of the North Pilbara Craton. It usually consists of basal conglomerate and sandstone overlain by a ~ 1 km-thick unit of BIF, chert

and black shale of the Cleaverville Formation. Importantly, the Cleaverville BIF usually yields a higher Fe content (ca. 35 wt%) compared to the Paddy Market or Pincunah BIFs (25-30 wt%) (Hickman, A.H.; personal comment). Nevertheless, significant lateral facies variations are observed, including a decrease in the proportion of clastic sediments at the benefit of BIF from west (e.g. Wodgina) to east (e.g. Corunna Downs) interpreted to reflect increasing depths of deposition.

Despite intensive field mapping campaigns performed by government geological surveys during the last few decades, the identification of some BIF exposures in the North Pilbara remains problematic due to uncertainties in depositional ages and correlations across the different greenstone belts. Recently, survey mapping programs led by A. Hickman led to the revision of the stratigraphy and lithofacies subdivisions of Van Kranendonk et al. (2007). This revision included the reassignment of several exposures of the Paddy Market Formation to the Cleaverville Formation. It is also important to note that the appellation "Nimingarra Iron formation", which corresponds to the BIF-rich successions of the Goldsworthy greenstone belt and their equivalents in the Pardoo area, no longer exists and has been integrated into the Cleaverville Formation. Minor additional BIF occurrences have been documented throughout the 3.52-3.45 Ga volcanic-dominated sequence of the Warrawoona group.

III. Methodology

Mapping and sampling strategy

Surface lithologic and structural mapping were conducted at a 1:2,000 scale within and in the surrounding areas of the Split Rock and Runway prospects (Fig. 5, 6). Field observations

were digitised using the ArcGIS program. In addition, seven diamond drill holes were logged in detail to examine variations in rock types, alteration styles and alteration intensity. Drill holes were chosen based on their spatial distribution (intersecting distal, intermediate and proximal positions relative to high-grade Fe mineralisation) and on their depth of penetration beneath the near-surface weathering profile. The maximum vertical extent of these logged holes is 240 m, whereas the base of intense weathering at Corunna Downs is about 60–100 m, but locally extends to considerably greater depths (i.e. ~200 m) along lithological contacts or steeply dipping fault zones. Structural orientations are given as dip angle/strike or plunge/trend orientations, with reference to magnetic north. Location coordinates are given using the Geocentric Datum of Australia 1994 (GDA94), MCA Zone 50, geographic coordinate system. Geochemical data extracted from the Atlas Iron Ltd. drill hole database were interpolated using the Leapfrog Geo and ArcGIS programs to further constrain the geometry of lithologic units and mineralisation envelopes at depth. Deposit cross-sections were generated using a combination of surface and diamond drill core observations, plus company geochemical data.

The distinction between the main least-altered rock types (BIF, cherty BIF, chert, and terrigeneous units) in field geological maps, cross sections and 3D geological models is based on direct observation of these rocks, supported by their geochemistry. Banded iron formation contains more than 35 vol% iron-oxide rich bands (i.e. >25 wt % Fe equivalent in drill holes). Chert comprises less than 15 vol% iron-oxide rich bands (i.e. <10 wt % Fe), whereas cherty BIF displays an intermediate composition between chert and BIF (i.e. 15 to 35 vol% iron-oxide rich bands and 10 to 25 wt% Fe). Mapped terrigeneous sedimentary rocks (e.g. shale, siltstone) display a high Al content (up to 20 wt % Al_2O_3). Carbonaceous-rich shale contains >0.1 wt % S. Goethitic vs. hematitic (martite-rich) ore zones are distinguished using the Fe and LOI content applied to high-grade (>50 wt % Fe) zones. Considering that (i) high-grade

zones are essentially (>90%) composed of iron oxides and (ii) goethite is the only hydrated phase participating in the LOI content, the ratio *R* defined such as *R = 620*LOI/Fe* provides a first-order estimate of the goethite vs. hematite (martite) content in areas with high-grade iron ore.

Analytical strategy

Seventy-six hand specimens were collected from surface exposures and diamond drill core. Sampling was conducted from distal to proximal areas relative to the known deposits for the purpose of identifying changes in mineralisation styles and intensity. Forty-five polished thin sections were prepared from collected samples and examined using reflected/transmitted light and scanning electron microscopy. Twenty-seven hand specimens were crushed using a mild steel vibrating disc pulveriser (with potential contamination of Fe up to 0.2 %) at Actlabs, Canada, and pulps were analysed for whole-rock major and trace element geochemistry. Major element oxides were analysed using XRF with Li borate fusion. Trace elements were analysed by ICP-MS with Li borate fusion followed by nitric acid digestion. The loss on ignition (LOI) component was determined by drying sample powders overnight at 110 °C, ignition at 1,100 °C for 25 min and subsequent measurement of the weight loss. The FeO, C-S contents of the powdered samples were determined using titration and infrared methods, respectively. Analytical accuracy was tested with the international geochemical BIF standard FeR-3 from Temagami, Canada (Bau and Alexander, 2009). Accuracy was tested with blind duplicates and is less than 0.2% for major oxides and less than 1% for trace elements.

In situ trace element chemistry analysis was conducted on 15 thin sections by LA-ICP-MS at Curtin University using the GSD international standard for calibration. Ablation time and spot sizes were 45 seconds and 75 to 90 microns, respectively. Data processing was conducted using the Sills program.

IV. Geology of the Split Rock and Runway deposits, Corunna Downs iron camp

Coongan greenstone belt geology

The Corunna Downs project is located about 40 km south-east of Marble Bar and lies within the Coongan greenstone belt, adjacent to the Kelly greenstone belt. Both greenstone belts are interpreted to define a regional syncline that stretches along a N-S trend and is bound by the Shaw and the Corunna Downs granitoid complexes to the west and to the east, respectively (Fig. 2). The Euro Basalt (ca. 3350 Ma) is the dominant stratigraphic unit in both greenstone belts. The basalt conformably overlies the Strelley Pool Chert and is either conformably overlain by the 3325–3319 Ma Wyman Formation, or is in faulted contact with ultramafic intrusive rocks of the 3180 Ma Dalton Suite along the eastern margin of the Coongan greenstone belt (Fig. 2). These units are unconformably overlain by the 3020 Ma Cleaverville Formation, which is at least 750 m thick in the northern section of the Coongan greenstone belt (Bagas et al., 2004). The Cleaverville Formation is in turn unconformably overlain by the ca. 2770 Ma Mount Roe Basalt and younger volcano-sedimentary units of the 2770-2690 Ma Fortescue Group.

A brief description of the regional geologic history for the Coongan greenstone belt is given by Bagas et al. (2004). Hereafter we use the subscript B to refer to the nomenclature of Bagas et al. (2004). This deformation scheme include (i) emplacement of early components of the Shaw and Corunna Downs Granitoid Complexes ($D1_B$ event, ca. 3490-3400 Ma;), (ii) a major doming event ($D2_B$, ca. 3315 Ma) during emplacement of the Corunna Downs and Shaw Granitoid Complexes, accompanied by tilting and large-scale open to tight folding of the Warrawoona Group, coincident with the development of a penetrative foliation and lineation in these rocks throughout the Coongan Syncline, and layer-parallel normal and reverse faults within the greenstone belts (Bagas et al., 2004), (iii) the emplacement, after the deposition of

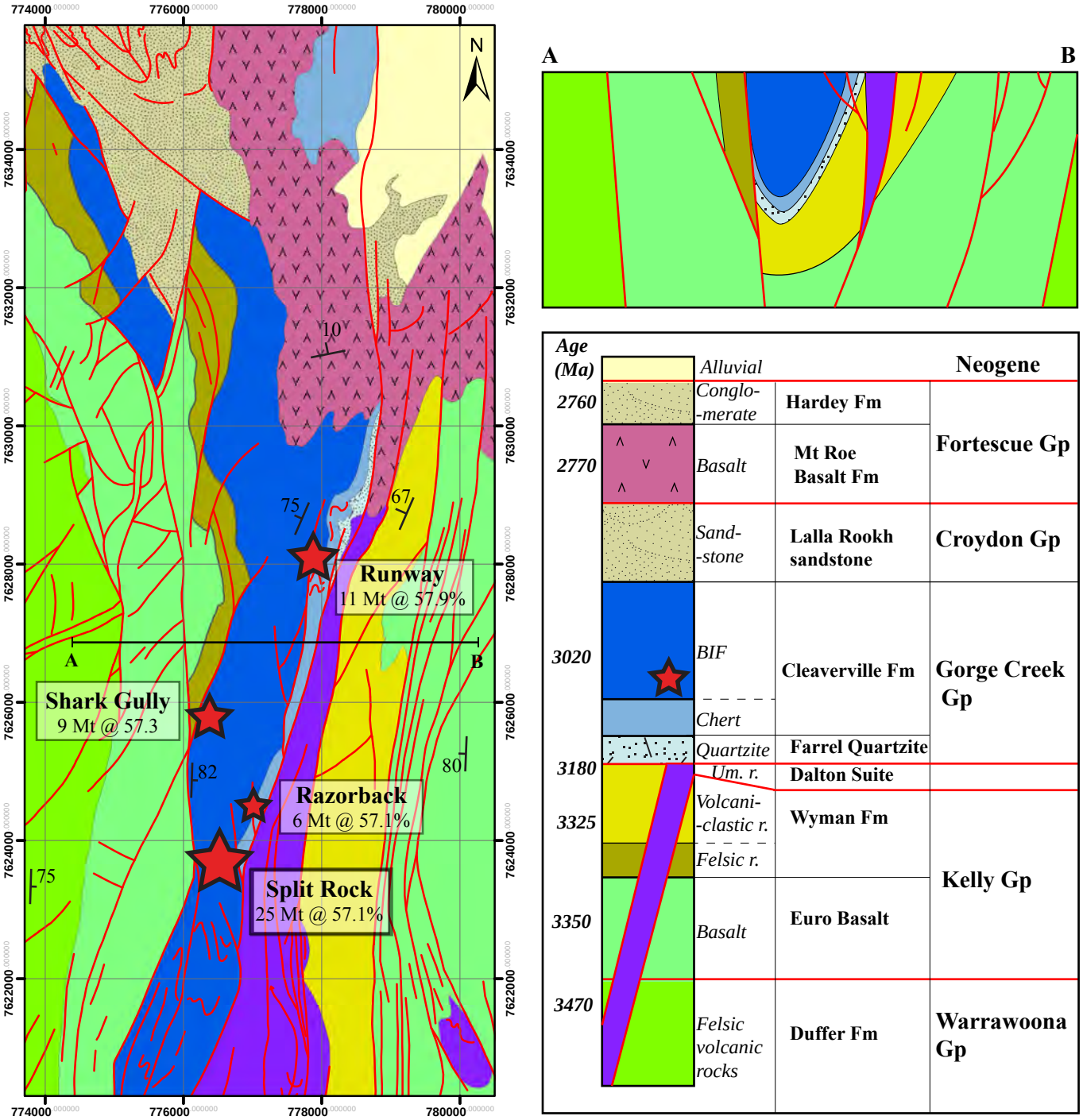

Figure 2: Simplified geology map, cross-section and lithostratigraphic sequence of the Corunna Downs iron camp. The location of the Split Rock, Runway, Shark Gully and Razorback deposits are included. *Modified after Hickman and Van Kranendonk, 2008b.* r.:rocks, Um.:ultramafic

the Cleaverville Formation but prior to the deposition of the Fortescue Group, of splayed north-northeasterly striking faults ($D3_B$), which locally repeat the stratigraphy of the Kelly and Gorge Creek Groups as a result of steep reverse, east-side-up displacement, and (iv) the development of several brittle faults ($D4_B$) interpreted to be synchronous with or younger than the Mount Roe Basalt (Van Kranendonk et al., 2002) and striking towards the northeast with northwest-side-down displacement.

Lithological and structural relationships in the Cleaverville Formation, Corunna Downs

Least-altered rock types of the Cleaverville Formation exposed in the Corunna Downs camp include BIF, cherty BIF, chert, siltstone and carbonaceous shale (Fig 3). BIF occurrences mainly display a typical jaspilitic facies (Fig. 3A), although non-jaspilitic BIF exposures is present locally. Cherty BIF (Fig 3B) and chert (Fig. 3D) generally do not display the fine dusting of hematite in jaspilite, with the exception of well-exposed jaspilitic chert unit in the Split Rock deposit area (Fig. 3C). A number of siltstone (Fig. 3E) and carbonaceous shale units (Fig. 3F) are interbedded at different scales with BIF horizons, highlighting the alternation of clastic to chemical sedimentation processes during the deposition of the Cleaverville Formation. The Split Rock and the Runway deposits are hosted by a ca. 300 m-wide, jaspilitic BIF macroband with minor interbedded chert and cherty BIF bands. In both deposits, the jaspilitic BIF macroband that hosts iron ore directly overlies a carbonaceous shale macroband, suggesting that these deposits developed in the same BIF macroband.

Deformation history at Corunna Downs

In this section, local deformation sequence at Corunna Downs is referred to using the subscript CD. Structures that are representative of the $D3_B$ and $D4_B$ events documented by Bagas et al. (2004) in the Coongan greenstone belt are well expressed in the Split Rock and Runway deposit areas (that is, local $D1_{CD}$ and $D2_{CD,}$ respectively). In both deposits, the

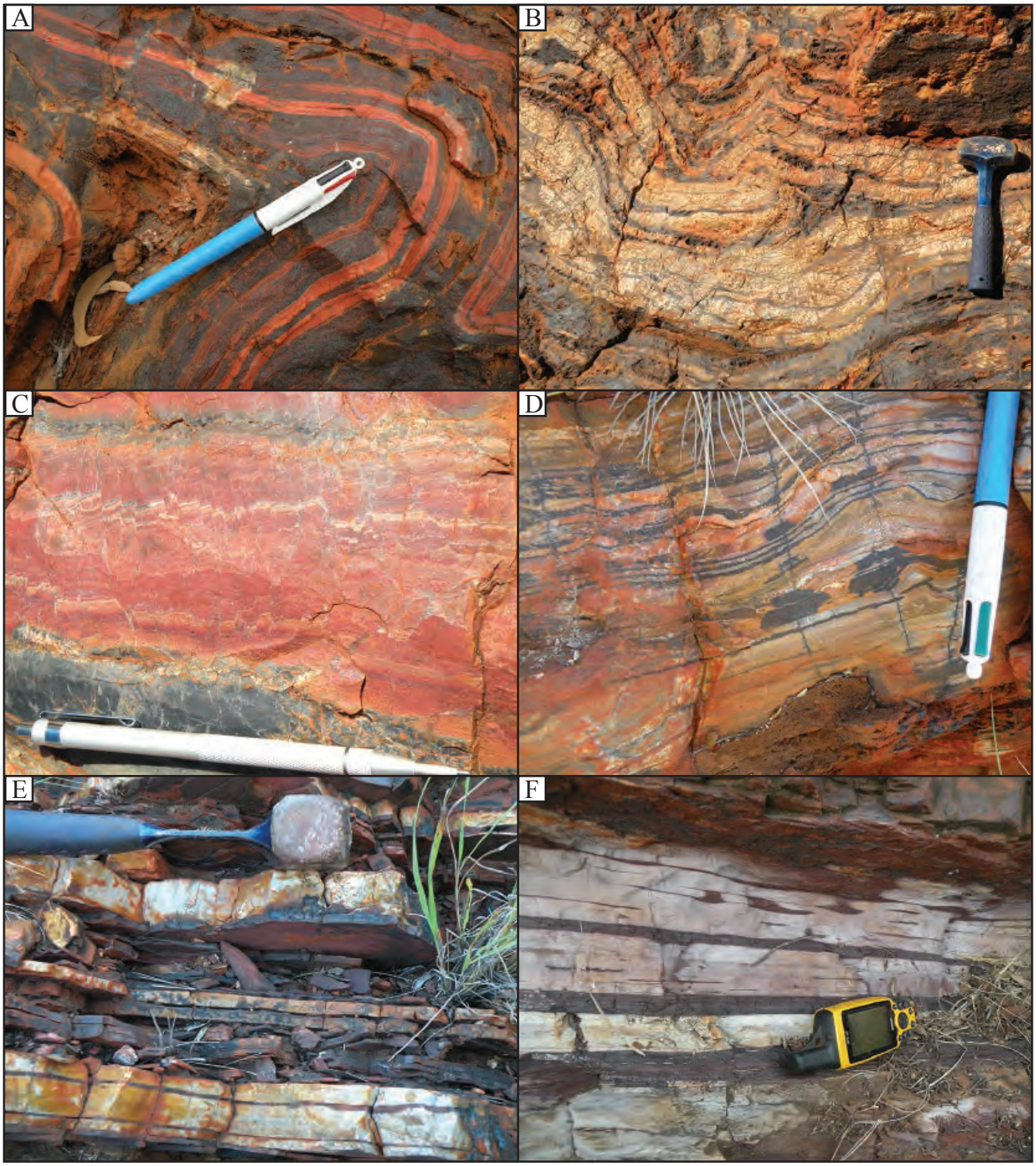

Figure 3: Dominant rock types exposed in the Corunna Downs iron camp. (A) jaspilitc BIF, (B) cherty BIF, (C) jaspilitic chert, (D) chert, (E) siltstone and chert and (F) shale.

Cleaverville Formation displays a N-S to NNE-SSW trend and a subvertical to steep westward dip (Fig. 4I). The earliest structures observed are tight, N- to NNE-steeply plunging $F1_{CD}$ folds (Fig. 4A, B, I). Late-$D1_{CD}$, sinistral brittle-ductile shear zones are commonly located along fold limbs (Fig. 4D) and lithological contacts, where they are aligned parallel to contacts, or cutting units at low angles (Fig. 4C).

At the Split Rock deposit, BIF macrobands are mainly subvertical or steeply dipping towards the west. The macrobands define a deposit-scale $D1_{CD}$ antiform with a subvertical to north-plunging fold axis, which is interpreted as an overturned syncline based on the observation that the carbonaceous shale macroband to the east of the Split Rock deposit underlies the main BIF macroband in the stratigraphic sequence. The Split Rock antiform is partly truncated along its western limb by a late $D1_{CD}$, steeply E-dipping, NNE trending, sinistral shear zone that displays reverse, east-side-up displacement (Fig. 5). The eastern limb of the Split Rock antiform displays multiple S-shaped parasitic folds at centimetre to metre scales.

At the Runway deposit, BIF macrobands dip towards the west without evidence for a large deposit-scale fold (Fig. 6). Rather, the widespread occurrence of Z-shaped folds in BIF at the Runway deposit is likely related to the accommodation of the sinistral displacement along several documented $D1_{CD}$ faults in the area. Alternatively, the deposit could correspond to the preservation of the western, truncated portion of a deposit-scale $D1_{CD}$ fold. Both deposits display zones of intense hydraulic brecciation along a NNE-SSW trend (Fig. 4E, F).

Minor $D2_{CD}$ faults cut $D1_{CD}$ folds in the Split Rock area (Fig. 4G). Localised, steeply eastward plunging open folds were presumably assigned to the $D2_{CD}$ deformation event (Fig 4H).

For clarification purposes, we hereafter use the regional deformation nomenclature (D_1 to D_{12}) proposed by Hickman and Van Kranendonk (2008a) rather than the local scheme used

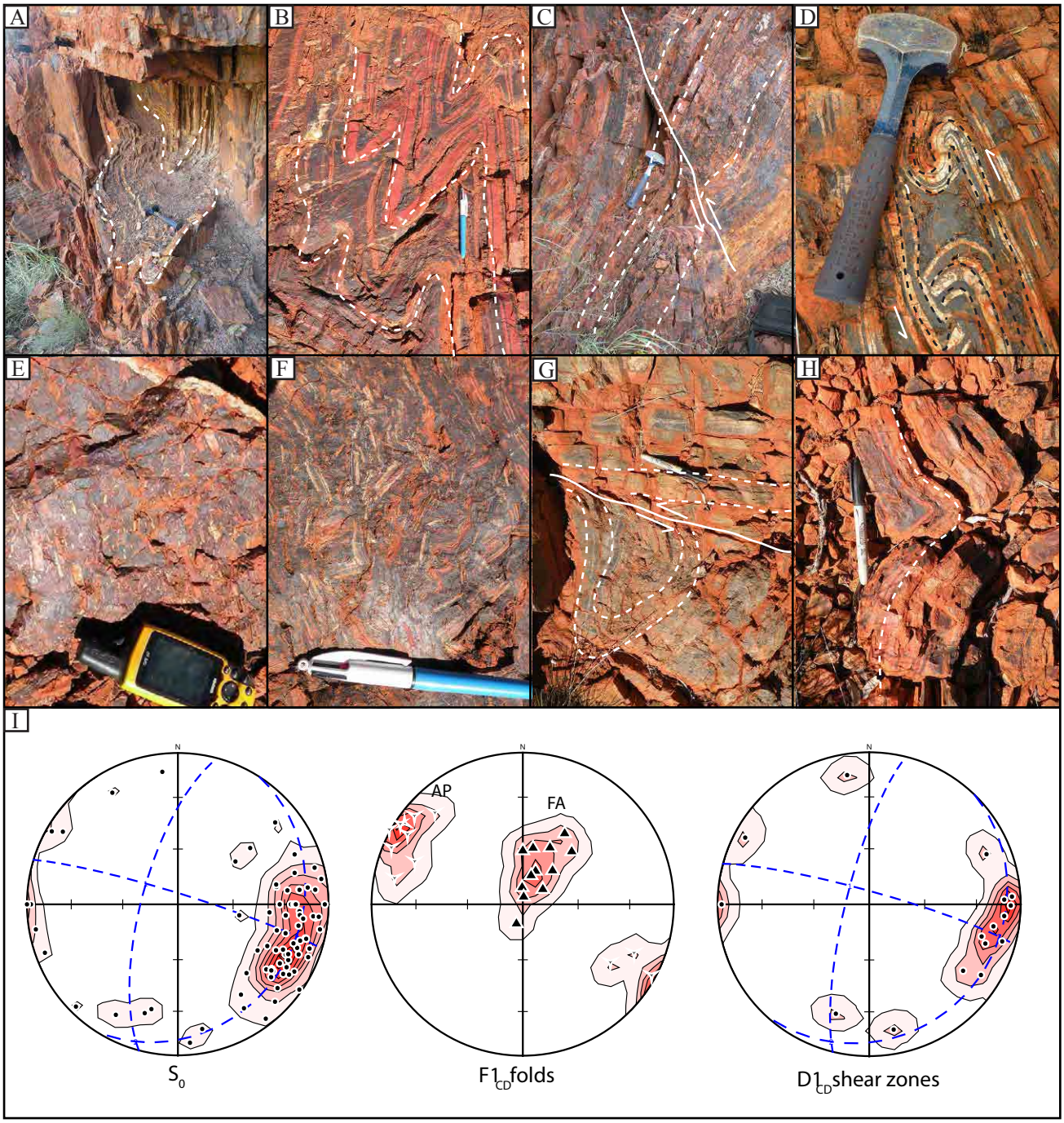

Figure 4: (A-H) Photographs of deformation styles at Corunna Downs and (I) structural data for bedding, $D1_{CD}$ (regional D9) folds and shear zones. (A,B) $F1_{CD}$ tight folds, (C-D) $D1_{CD}$ sinistral shear zone, (E-F) $D1_{CD}$ magnetite-rich hydrothermal breccia, (G) $D2_{CD}$ brittle fault and (H) late open fold. All photographs are facing North.

by Bagas et al. (2004). Local deformation event $D1_{CD}$ is interpreted to correspond to the regional deformation events D9. Which one of the regional deformation events corresponds to local $D2_{CD}$ is unclear. It is speculated that $D2_{CD}$ corresponds to a late stage of deformation associated with the regional D9 event.

Iron mineralisation and ore styles

Surface exposures and drill cores from the Split Rock and Runway deposits record several successive mineralisation events, resulting in a variety of ore styles:

(i) Hypogene coarse-grained (up to 1 mm) euhedral magnetite (Fe_3O_4)-rich ore zones are located within $D1_{CD}$ shear zones that cut jaspilitic BIF macrobands. Magnetite-rich veins (Fig. 7A) are also present in distal areas to D3 shear zones where they are associated with pervasive crystallisation in the least-altered BIF. Hypogene magnetite alteration results in the sub-economic upgrade of iron in BIF from ca. 55 to 70 wt. % Fe_2O_3 (see section V, Fig. 8).

(ii) Friable, cherry-red martite ore (Fig. 7B) results from the pseudomorphic replacement of primary and hypogene magnetite in BIF by hematite (Fe_2O_3). The leaching of silica-rich bands results in the low hardness and friable physical properties of martite ore. This ore type is not exposed as outcrop, but is common at depth. Martite ore displays the highest iron grades with Fe_2O_3 content up to 93 wt % (Fig. 8).

(iii) Bedded- to massive-textured, anhedral goethite (FeOOH) and goethite-martite ores (Fig. 7G) result from intense supergene goethitisation of least-altered and hypogene magnetite-altered BIF, respectively. Goethitisation occur preferentially along existing geological structures (mainly D3 shear zones) that transport

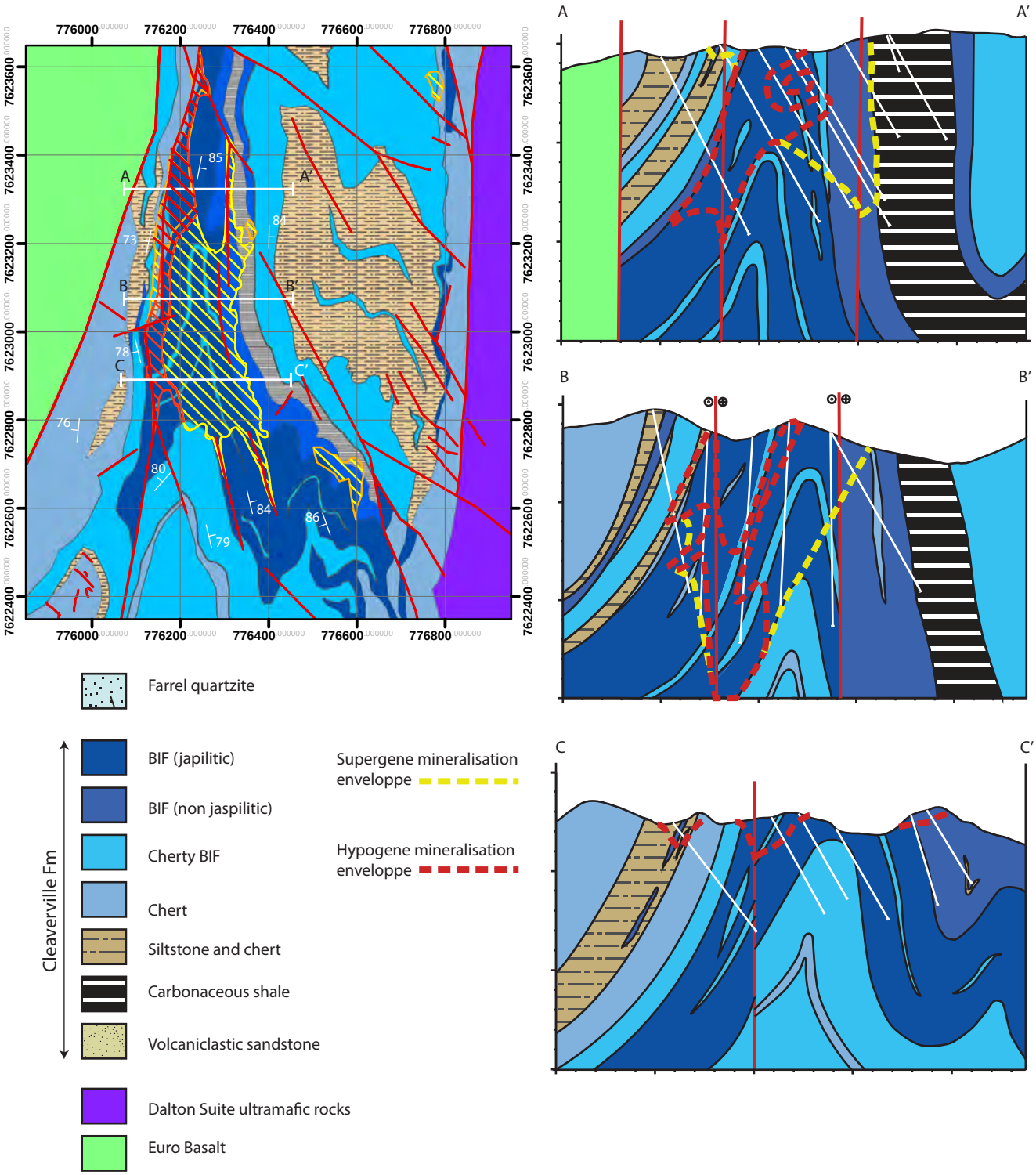

Figure 5: Geology map and cross-sections of the Split Rock deposit

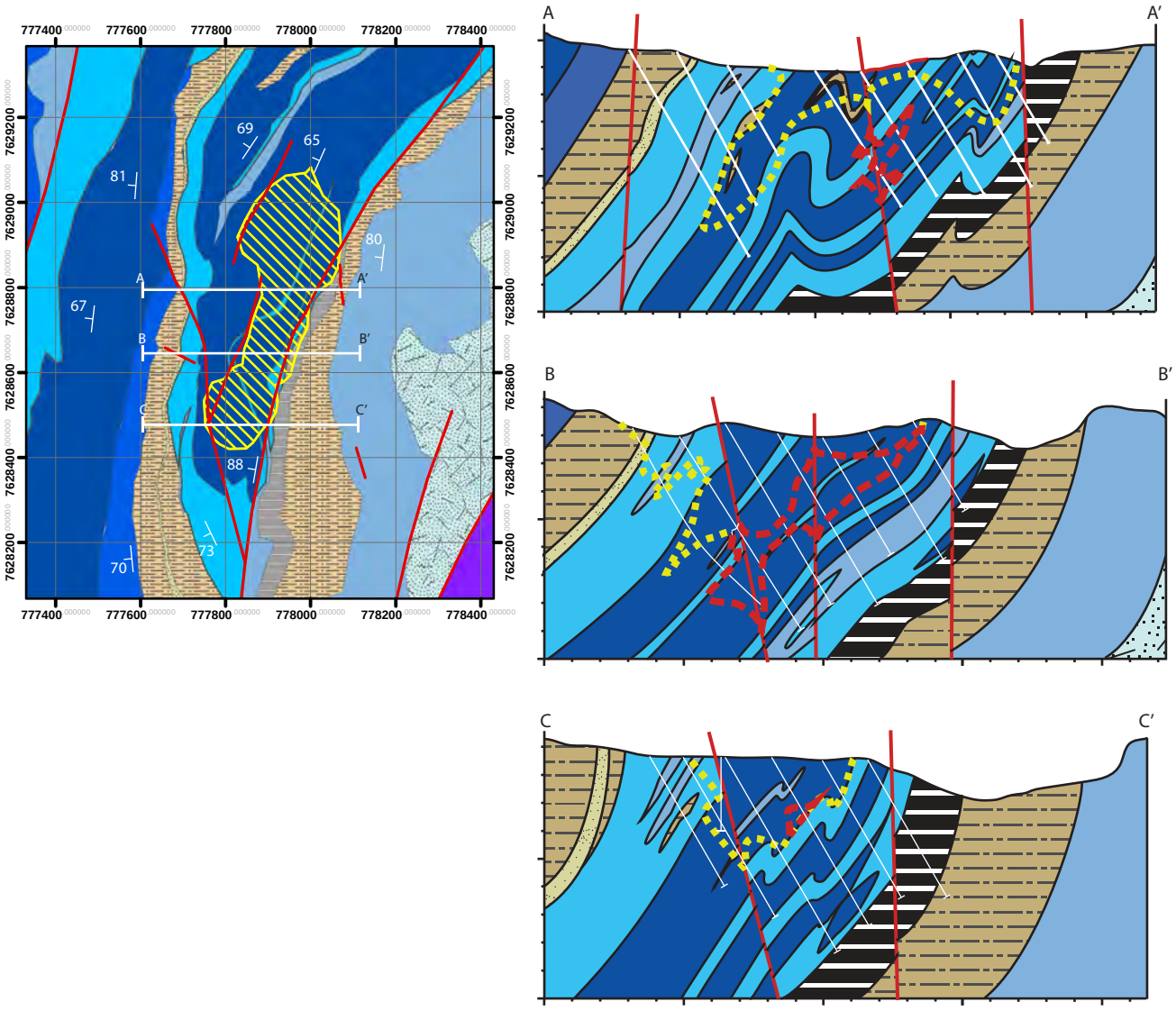

Figure 6: Geology map and cross-sections of the Runway deposit

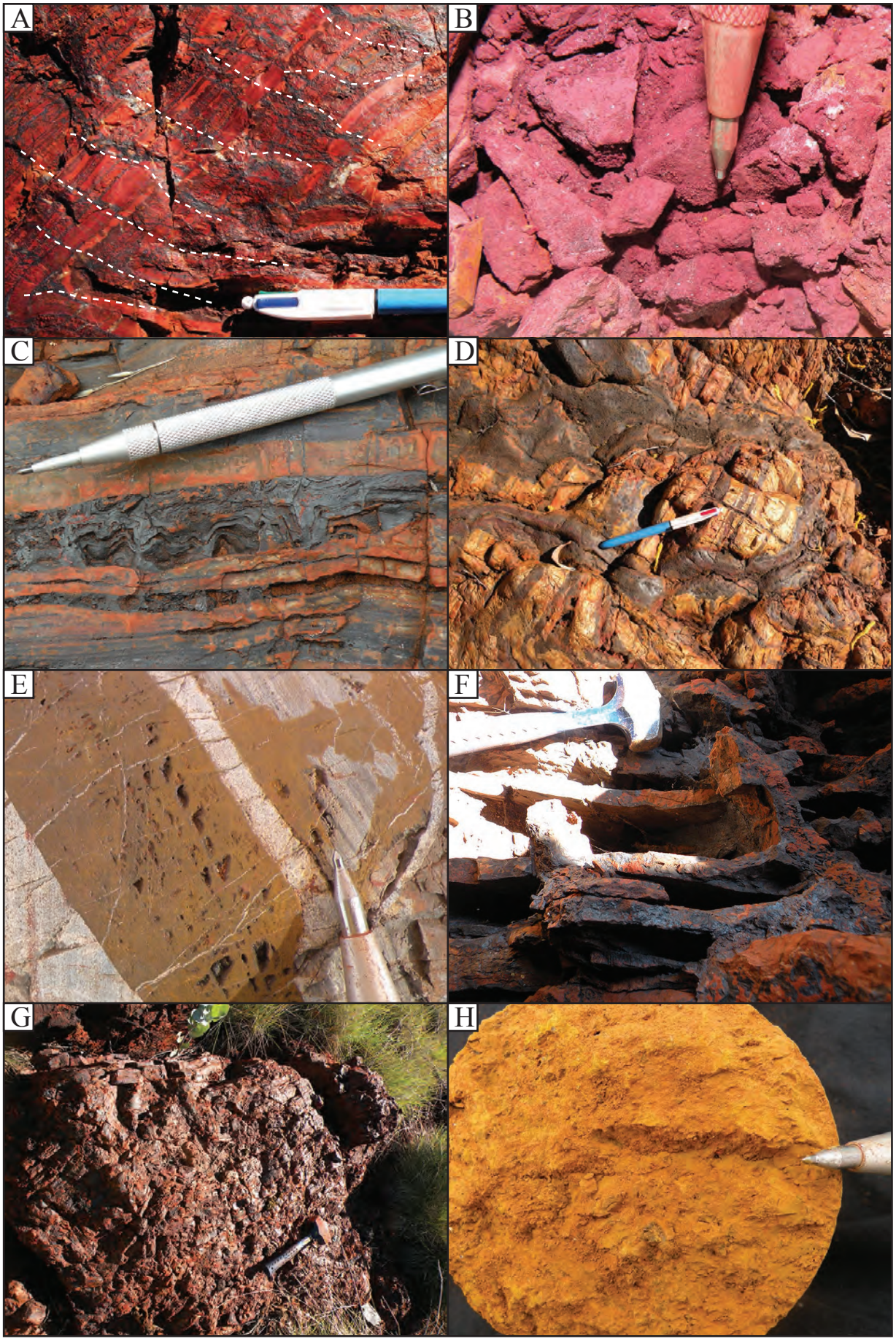

Figure 7: Photographs of the different mineralisation styles at Corunna Downs. (A) Hypogene magnetite-rich veins cutting jaspilitic BIF, (B) martite-rich ore, (C) botryoidal hematite replacing primary iron oxide-rich bands, (D) massive goethite vein cutting BIF, (E) pervasive goethitisation of chert, (F) box-work-textured goethite-rich ore resulting from leaching of silica-rich bands, (G) bedded to massive goethite-rich ore and (H) ochreous goethite ore.

supergene fluids, overprinting the early stages of magnetite and martite formation, but also forming < 30 cm-thick goethite veins (Fig. 7D, 7F) and as pervasive replacement of chert and other iron oxides (Fig. 7E). Goethite often forms typical botryoidal structures in veins filling open space vugs (Fig. 7C). Monomineralic goethite ore has a maximum Fe_2O_3 content of ca 85 wt. % (Fig. 8).

(iv) Ochreous goethite ore (limonite) replaces bedded- to massive-textured goethite and fills vugs in BIF and other ore types. The presence of ochreous goethite is characterised by a slight decrease (ca. 5 to 10 wt.% Fe_2O_3) in the iron grade of the goethite ore (Fig. 8). Similar to the friable martite ore, ochreous goethite ore (limonite) is mainly observed in drill cores (Fig. 7H).

(v) Weakly-expressed manganese oxide mineralisation occurs as veins that cut vitreous and ochreous goethite mineralisation zones, within and slightly below the water table.

V. Geochemical changes associated with iron mineralisation

Results of whole-rock major, trace and rare earth element chemistry for the different samples collected from the Split Rock and Runway deposits are presented in this section (see Tables 1 to 3). All samples exhibit systematic changes in major and trace element compositions compared to the parent BIF.

Least altered BIF

Three samples of least altered BIF yield Fe_2O_3 and SiO_2 average contents of ca 57 and 41 wt. %, respectively, with low LOI (3 wt. %) contents (Fig. 8). These values are consistent with the typical composition of the Cleaverville BIF in the East Pilbara Terrane (Van Kranendonk

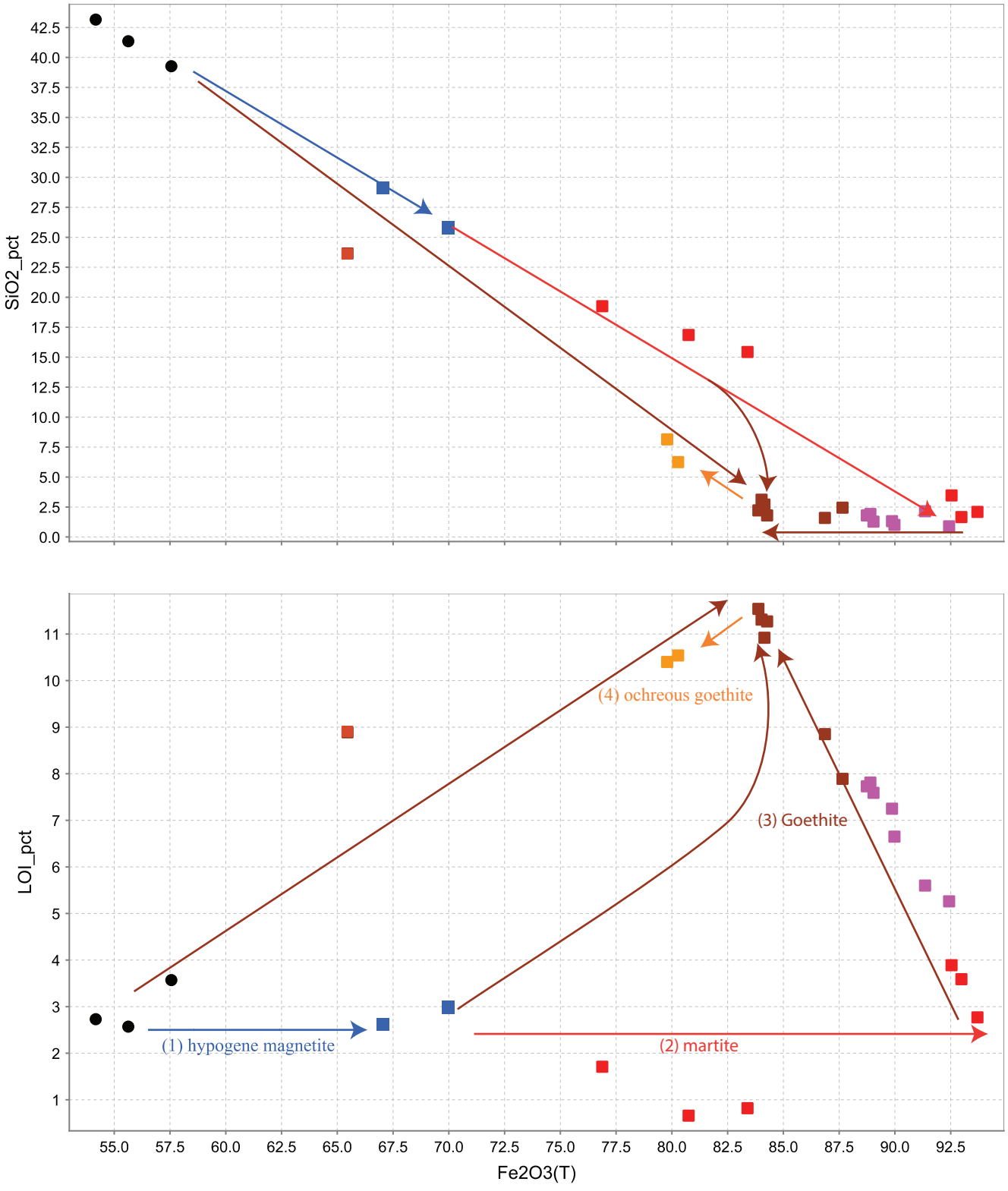

Figure 8: Whole-rock geochemistry plots of SiO_2 (wt. %) and LOI (wt. %) as a function of Fe_2O_3(T) (wt. %). Major changes in the whole-rock chemistry from least-altered BIF to ochreous goethite ore are highlighted by stage 1 to 4 arrows.

et al., 2002). Other major oxides, including FeO, MgO, CaO and Al_2O_3, display concentrations below 1 wt. % (Fig. 9). Except for Zn (25-60 ppm), transition metals are below 25 ppm (Ni, W > Cu, Sb > Co). REE+Y concentrations normalised to PAAS (McLennan, 1989) and to C1 chondrite (Sun and McDonough, 1991) are shown in Fig. 10. The least altered BIF is depleted in REE+Y compared to the C1 chondrite; the REE+Y profile displays strongest depletion of LREE with significant positive anomalies of La, Eu and Y. Conversely, REE+Y are enriched compared to C1 chondrite, with a slight enrichment of HREE (x2 to x5) and stronger enrichment of LREE (x4 to x20).

Hypogene magnetite-enriched BIF

The two analysed samples of hypogene altered BIF display an increase in Fe_2O_3 of ca. 10 to 15 wt. % and a corresponding decrease in SiO_2 compared to the least altered BIF (Fig. 8). Only a slight increase in the FeO content is observed, at odds with the apparent proportion of hypogene magnetite (15 to 30%) in hand specimens. This discrepancy likely arises from the fact that a significant portion of hypogene magnetite is pseudomorphed by martite in these samples. None of the other major oxides, transitional metals or REE exhibit any statistically significant differences in concentration compared to the parent BIF, with the exception that Eu displays a positive anomaly.

Martite ore

Martite ore samples display the highest grade documented in this study with a maximum Fe_2O_3 concentration of ca. 93 wt. %, with minor (ca. 2 wt. %) amounts of SiO_2 and LOI (Fig. 8). The formation of martite ore from its magnetite-rich BIF precursor is characterised by several changes in other major oxide chemistry, including (i) a ca. 250 % increase in Al_2O_3 and (ii) a decrease of FeO to values similar to that of the least altered BIF (ca 0.5 wt. %), highlighting the complete oxidation of magnetite to martite (Fig. 9). Within the transitional

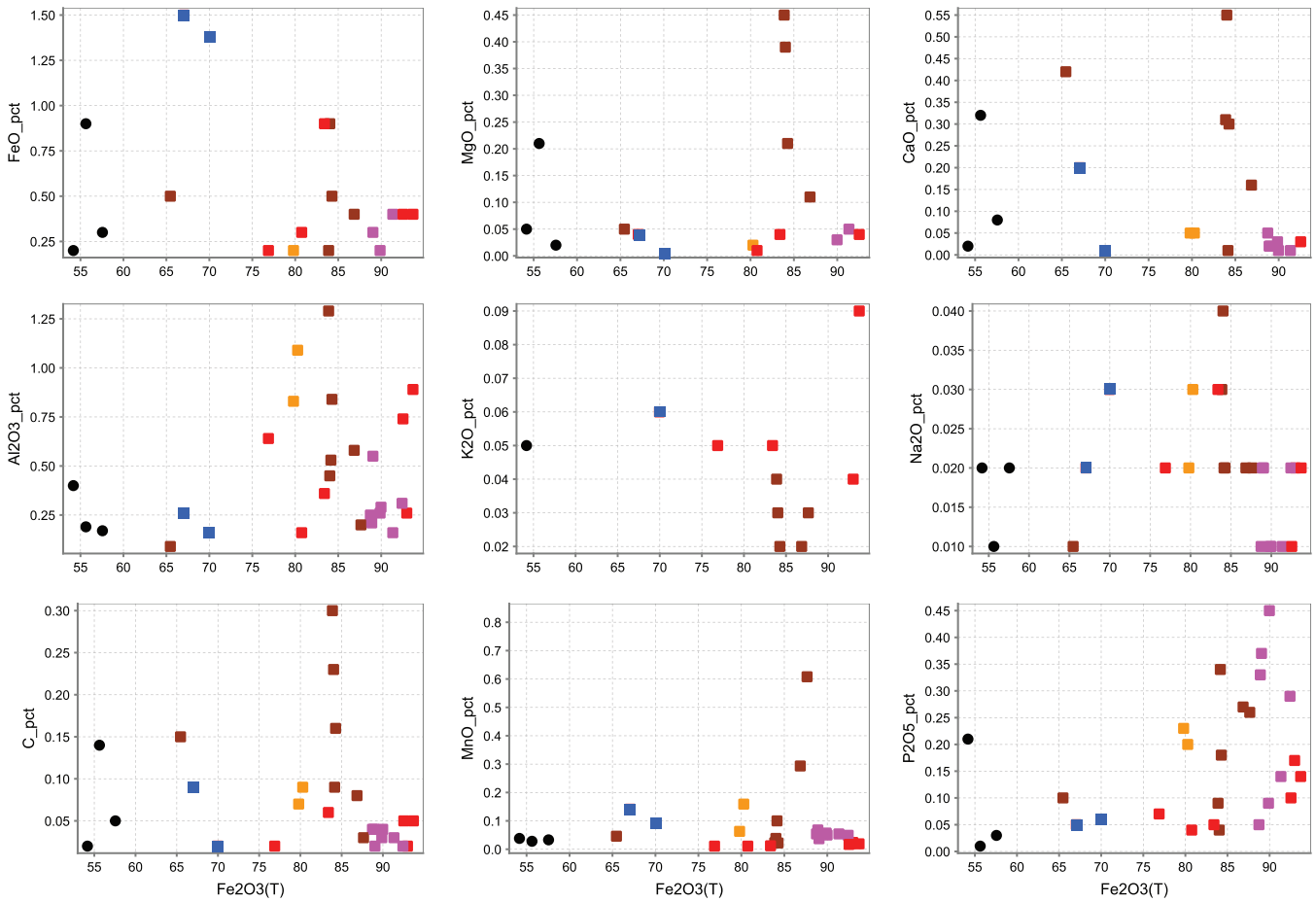

Figure 9: Whole-rock geochemistry plots of second-order oxides as a function of Fe_2O_3(T) (wt. %). See Figure 8 caption for colour coding.

metal group, W and Sb concentrations show an increase of ca. 500 and 300 %, respectively (Fig. 10). The REE pattern of the martite ore samples exhibits an increase in both LREE and HREE compared to the hypogene altered BIF, together with the appearance of a slight positive Ce anomaly (Fig. 11).

Goethite and goethite-martite ores

Goethitic ore is characterised by an increase in the LOI content of ca. 8 wt. % and a similar decrease in the Fe_2O_3 content compared to the martitic ore (Fig. 8). Major oxides and other base cations are largely enriched in the goethite ore zone, including Al_2O_3, MgO, CaO, MnO and P_2O_5. Similar enrichments are observed for transitional metals such as Ni, Co, Cu and Zn (Fig. 10). The REE patterns of goethite ore samples display high variability and potential changes in the REE concentration associated with the goethitisation process remain unclear. Goethite-martite ore geochemistry reflects the mixed contribution of martite (positive W, Sb anomalies) and goethite (positive P_2O_5, Ni, Co and Zn anomalies) (Figs 8-11).

Limonite (ochreous goethite)

The ochreous goethite samples are characterised by a slight (5 wt. %) increase in SiO_2 at the expense of Fe_2O_3 compared to the goethite ore samples (Fig. 8). Positive Al_2O_3 and P_2O_5 anomalies documented in the goethite ore persist in the ochreous goethite, but other major oxides do not exhibit any significant changes compared to the least altered BIF (Fig. 9). Transitional metal and REE concentrations in the ochreous goethite are similar to those of the goethite ore.

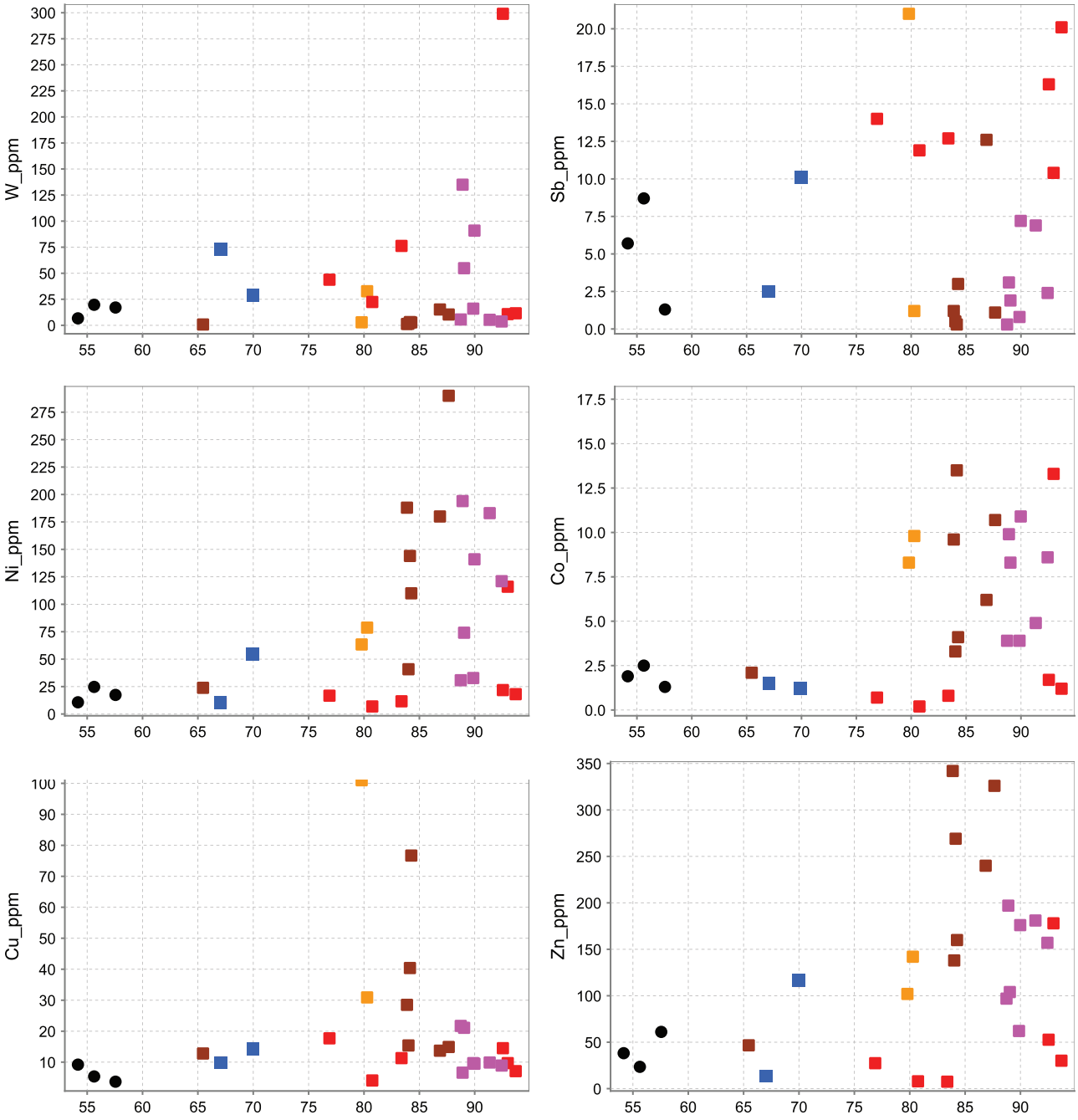

Figure 10: Whole-rock geochemistry plots of Sb, W, Sb, Ni, Co, Cu and Zn as a function of $Fe_2O_3(T)$ (wt. %). See Figure 8 caption for colour coding.

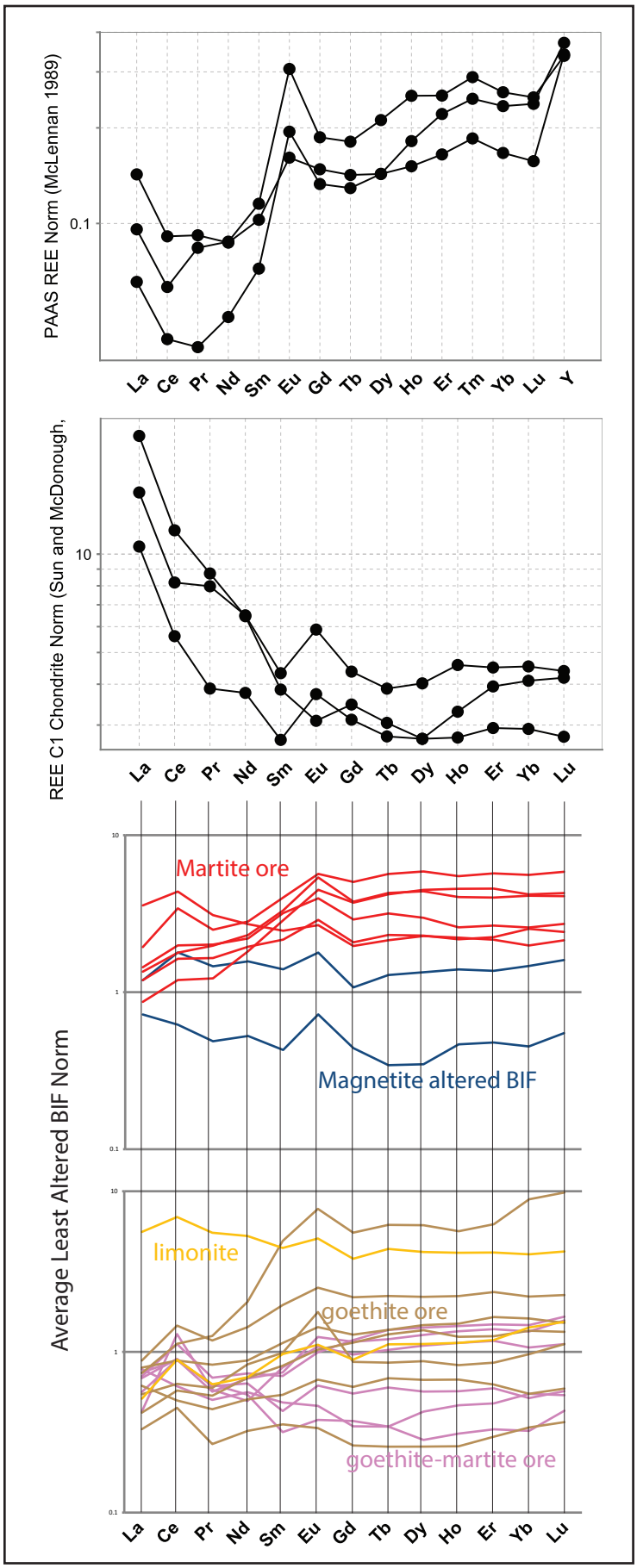

Figure 11: REE patterns of least-altered BIF normalised to PAAS and C1 chondrite (top) and REE patterns of the different alteration styles normalised to least-alterd BIF (bottom).

Sample	Rock type	Alteration intensity	Alteration style	Site	Al2O3	CaO	Fe2O3	Fe2O3(T)	FeO	K2O	LOI	MgO	MnO	Na2O	P205	SiO2	TiO2	S	C	Total
CD1-M05	jaspilitic BIF	moderate	magnetite martite	Split Rock	0.26	0.2	65.38	67.05	1.5	< 0.01	2.62	0.04	0.141	0.02	0.05	29.1	0.009	0.08	0.09	99.5
CD6-M08	jaspilitic BIF	least altered	least altered	Split Rock	0.19	0.32	54.62	55.63	0.9	< 0.01	2.57	0.21	0.028	0.01	0.01	41.35	0.006	0.02	0.14	100.3
CDDH1-09	BIF	moderate	goethite	Split Rock	0.09	0.42	64.91	65.46	0.5	< 0.01	8.89	0.05	0.046	0.01	0.1	23.65	0.002	0.02	0.15	98.72
CDDH1-11	jaspilitic BIF	high	ochreous goethite	Split Rock	0.83	0.05	79.57	79.79	0.2	< 0.01	10.4	< 0.01	0.063	0.02	0.23	8.14	0.026	0.02	0.07	99.54
CDDH1-16	jaspilitic BIF	high	martite - goethite	Split Rock	0.25	0.05	88.63	88.74	< 0.1	< 0.01	7.73	< 0.01	0.054	0.01	0.05	1.8	0.003	0.01	0.04	98.69
CDDH1-17	jaspilitic BIF	high	goethite	Split Rock	0.26	0.03	89.64	89.87	0.2	< 0.01	7.25	< 0.01	0.057	0.01	0.09	1.32	0.004	0.01	0.03	98.86
CDDH1-18	jaspilitic BIF	high	martite - goethite	Split Rock	0.55	0.02	88.71	89.04	0.3	< 0.01	7.59	< 0.01	0.037	0.02	0.37	1.28	0.01	0.01	0.02	98.88
CDDH2-03	jaspilitic BIF	least altered	least altered	Split Rock	0.17	0.08	57.22	57.56	0.3	< 0.01	3.57	0.02	0.033	0.02	0.03	39.27	0.005	< 0.01	0.05	100.8
CDDH2-07	jaspilitic BIF	high	goethite	Split Rock	0.2	< 0.01	87.54	87.65	< 0.1	0.03	7.89	< 0.01	0.375	0.02	0.26	2.45	0.003	< 0.01	0.03	98.85
CDDH2-08	jaspilitic BIF	high	martite	Split Rock	0.26	< 0.01	92.87	92.98	< 0.1	0.04	3.59	< 0.01	0.637	0.02	0.17	1.66	0.009	< 0.01	0.02	99.31
CDDH2-09	jaspilitic BIF	high	martite	Split Rock	0.16	0.01	90.91	91.35	0.4	< 0.01	5.6	0.05	0.054	0.01	0.14	2.15	0.001	0.02	0.03	99.54
CDDH2-10	jaspilitic BIF	high	martite	Split Rock	0.16	0.01	69.85	69.97	< 0.1	0.06	2.98	< 0.01	0.841	0.03	0.06	25.8	0.002	0.02	0.02	99.89
CDDH2-14	jaspilitic BIF	high	martite	Split Rock	0.31	< 0.01	92.32	92.43	< 0.1	< 0.01	5.26	< 0.01	0.049	0.02	0.29	0.89	0.005	0.01	0.02	99.2
CDDH3-01	jaspilitic BIF	high	martite - goethite	Split Rock	0.21	0.02	88.79	88.9	< 0.1	< 0.01	7.81	< 0.01	0.068	0.02	0.33	1.92	0.008	0.01	0.04	99.27
CDDH3-02	jaspilitic BIF	high	goethite	Split Rock	0.53	0.01	84.04	84.15	< 0.1	< 0.01	10.92	< 0.01	0.1	0.02	0.34	2.71	0.005	0.01	0.09	98.77
CDDH3-04	jaspilitic BIF	least altered	least altered	Split Rock	0.4	0.02	53.94	54.17	0.2	0.05	2.73	0.05	0.038	0.02	0.21	43.16	0.014	0.02	0.02	100.9
CDDH3-09	jaspilitic BIF	high	ochreous goethite	Split Rock	1.09	0.05	80.17	80.28	< 0.1	< 0.01	10.54	0.02	0.159	0.03	0.2	6.25	0.069	0.03	0.09	98.69
CDDH3-19.4	jaspilitic BIF	high	martite - goethite	Split Rock	0.29	0.01	89.87	89.98	< 0.1	< 0.01	6.65	0.03	0.05	0.01	0.45	1.01	0.005	0.01	0.04	98.49
CDDH5- 2	jaspilitic BIF	high	martite - goethite	Split Rock	0.89	1.76	82.23	82.34	0.1	0.08	11.08	1.41	0.095	0.06	0.57	2.14	0.011	< 0.01	0.87	100.4
CDDH9- 2	jaspilitic BIF	moderate	ochreous goethite	Runway	4.81	0.43	63.8	63.91	< 0.1	0.05	12.99	0.46	0.02	0.08	0.13	15.12	0.451	0.01	0.47	98.44
CDDH9- 8	jaspilitic BIF	high	goethite	Runway	1.29	0.31	83.66	83.88	0.2	0.04	11.54	0.45	0.023	0.03	0.09	2.22	0.029	< 0.01	0.3	99.91
CDDH9- 10	jaspilitic BIF	high	goethite	Runway	0.45	0.55	83.02	84.02	0.9	0.03	11.31	0.39	0.038	0.04	0.04	3.11	0.017	< 0.01	0.23	100
CDDH9- 12	jaspilitic BIF	high	goethite	Runway	0.84	0.3	83.71	84.27	0.5	0.02	11.27	0.21	0.022	0.02	0.18	1.8	0.018	< 0.01	0.16	98.95
CDDH9- 14	jaspilitic BIF	high	martite - goethite	Runway	0.58	0.16	86.41	86.86	0.4	0.02	8.85	0.11	0.039	0.02	0.27	1.59	0.012	< 0.01	0.08	98.5
CDDH9- 15	jaspilitic BIF	high	martite	Runway	0.89	< 0.01	93.25	93.7	0.4	0.09	2.77	< 0.01	0.019	0.02	0.14	2.09	0.016	< 0.01	0.05	99.38
CDDH9- 16	jaspilitic BIF	high	martite	Runway	0.74	0.03	92.09	92.54	0.4	< 0.01	3.89	0.04	0.017	0.01	0.1	3.47	0.014	< 0.01	0.05	100.8
CDDH9- 17	jaspilitic BIF	high	martite	Runway	0.64	< 0.01	76.65	76.88	0.2	0.05	1.71	< 0.01	0.011	0.02	0.07	19.25	0.018	< 0.01	0.02	98.65
CDDH9- 18	jaspilitic BIF	high	martite	Runway	0.16	< 0.01	80.42	80.75	0.3	< 0.01	0.66	0.01	0.011	< 0.01	0.04	16.85	0.007	< 0.01	< 0.01	98.51
CDDH9- 19	jaspilitic BIF	high	martite	Runway	0.36	< 0.01	82.39	83.39	0.9	0.05	0.82	0.04	0.012	0.03	0.05	15.43	0.018	< 0.01	0.06	100.1

Table 1: Whole-rock geochemistry data for major oxides at Corunna Downs

Sample	As	Ba	Be	Bi	Co	Cr	Cs	Cu	Ga	Ge	Li	Mn	Nb	Nd	Ni	Mo	Pb	Rb	Re	Sb	Sc	Se	Sn	Sr	V	W	Zn	Zr
CD1-M05	19.7	42	1.3	0.08	1.5	36.6	0.06	9.9	0.9	5.4	0.9	1080	0.6	4	10.3	2	1.4	0.5	0.002	2.5	1	1.6	3	3.3	7	73.1	13.5	6
CD6-M08	18.9	17	1.7	0.13	2.5	58.5	0.08	5.4	0.5	3.1	0.8	198	0.6	2.97	24.7	2.52	2.9	0.4	0.002	8.7	1	1.8	17	3.7	3	19.7	23.5	4
CDDH1-09	7.1	2	0.8	0.03	2.1	16	< 0.05	12.8	0.2	< 0.5	0.6	335	< 0.1	2.13	23.9	1.17	0.7	< 0.2	0.002	< 0.2	< 1	1.3	< 1	5.7	2	0.8	46.7	1
CDDH1-11	32.8	3	2.1	0.08	8.3	67.9	< 0.05	101	5.6	0.9	0.7	470	0.4	1.77	63.4	5.8	6.2	< 0.2	0.006	21	7	3.6	4	1.1	14	2.9	102	11
CDDH1-16	15.8	5	0.5	0.02	3.9	12.4	< 0.05	21.7	0.7	2.5	< 0.5	388	0.3	1.26	30.8	0.88	2.2	< 0.2	0.002	0.3	3	1.4	< 1	1.6	3	5.6	96.9	3
CDDH1-17	9.7	18	1	0.04	3.9	16.3	< 0.05	9.7	0.3	1.9	< 0.5	417	0.1	1.87	32.8	0.95	4.4	< 0.2	0.004	0.8	3	1.3	2	1.5	2	16	62.1	2
CDDH1-18	22.6	31	1.6	0.04	8.3	28.4	< 0.05	21.1	0.7	2.5	< 0.5	233	0.2	1.74	74.1	0.69	10.5	< 0.2	0.004	1.9	8	1.8	< 1	2.6	6	54.8	104	4
CDDH2-03	6.2	7	1.3	0.04	1.3	60.1	0.1	3.7	0.4	2.2	1.9	210	1	1.72	17.4	4.25	0.9	0.4	0.003	1.3	2	1.6	3	0.9	3	17.1	61.1	4
CDDH2-07	14.4	20	1.7	0.07	10.7	13.6	< 0.05	14.9	0.3	1.7	< 0.5	2790	0.1	0.82	290	1.8	1.3	0.4	0.005	1.1	3	1.1	< 1	5.5	4	10.4	326	2
CDDH2-08	19.4	84	2.2	0.05	13.3	11.9	0.06	9.7	0.9	3.9	< 0.5	5000	0.4	6.9	116	1.22	3.7	0.5	0.004	10.4	2	1	1	15.9	6	10.8	178	3
CDDH2-09	15.2	9	1.9	< 0.02	4.9	12.9	< 0.05	9.9	0.2	3.1	< 0.5	389	0.3	1.62	183	1.88	1.5	< 0.2	0.005	6.9	2	1.3	< 1	1.9	2	5.3	181	3
CDDH2-10	14.8	53	1.5	0.03	17.7	22.8	0.07	14.2	0.2	2.5	2.8	6490	0.1	1.34	54.8	1.96	2.1	0.7	0.004	10.1	2	1.7	1	26.5	3	29.1	116	2
CDDH2-14	21	23	1.8	0.04	8.6	10	0.07	8.9	0.3	2.4	< 0.5	342	0.2	17.3	121	0.63	11.1	0.2	0.002	2.4	5	1.5	< 1	30.6	3	3.7	157	3
CDDH3-01	23.9	19	0.9	0.04	9.9	21.2	< 0.05	6.6	0.2	1.9	< 0.5	474	0.3	1.43	194	1.55	2	< 0.2	0.01	3.1	4	0.9	< 1	5.7	7	135	197	3
CDDH3-02	32.7	30	0.7	< 0.02	13.5	28.2	< 0.05	40.4	< 0.1	1.6	< 0.5	762	0.2	1.29	144	1.54	1.4	< 0.2	0.004	0.3	7	1	1	4.8	4	3.1	269	2
CDDH3-04	7.9	70	1.4	0.04	1.9	51.4	0.24	9.2	< 0.1	1.8	2.1	281	0.5	2.95	10.7	2.85	1.2	3.4	0.004	5.7	1	1.1	2	3.7	4	6.7	38.2	6
CDDH3-09	5.3	9	2.6	0.09	9.8	67.6	0.06	30.9	3	0.7	2.7	1270	0.7	13.4	78.7	1.36	22.6	0.4	0.005	1.2	11	1.9	< 1	15.2	33	32.7	142	10
CDDH3-19.4	25.4	18	0.7	0.03	10.9	18.7	< 0.05	9.5	0.3	2.5	< 0.5	373	0.2	1.38	141	1.38	2.8	< 0.2	0.004	7.2	7	0.7	< 1	4.2	5	90.9	176	3
CDDH5- 2	30.2	11	1.5	< 0.02	21.4	17.9	0.08	72.1	0.6	0.3	0.7	700	0.1	1.35	315	1.77	7.4	2	0.007	3.9	14	2.4	< 1	9.9	6	36.2	694	5
CDDH9- 2	10.5	6	1.7	0.13	2.1	176	< 0.05	24.9	9.7	0.5	< 0.5	99	2.5	7.77	49.9	0.82	1	0.9	0.008	2.8	10	3	2	7.3	76	3.3	48.7	60
CDDH9- 8	14.4	9	0.4	0.03	9.6	28.6	0.08	28.5	1.4	0.3	< 0.5	118	0.3	1.76	188	0.36	1.9	2.1	0.007	1.2	4	3	< 1	5.4	11	1.3	342	7
CDDH9- 10	9	10	0.9	0.05	3.3	25.9	0.06	15.4	1	0.3	< 0.5	231	0.5	2.25	40.8	1.65	1.8	2	0.013	0.5	< 1	2.3	< 1	6.4	8	1.5	138	2
CDDH9- 12	10	9	1.7	0.06	4.1	32.6	< 0.05	76.7	2.1	0.4	< 0.5	124	0.2	3.63	110	1.64	2.4	1.3	0.012	3	3	3.3	< 1	4.9	23	2.8	160	3
CDDH9- 14	15.9	6	2.9	0.04	6.2	25	< 0.05	13.7	1.6	0.6	< 0.5	216	0.2	5.22	180	2.65	4.8	0.8	0.014	12.6	< 1	3.2	< 1	3.5	9	15.2	240	5
CDDH9- 15	14.6	6	1.5	0.05	1.2	16.5	0.06	7.1	2.1	0.6	0.8	57	0.2	4.64	18.1	1.78	10.6	0.3	0.015	20.1	2	2.4	< 1	2.8	12	11.6	30.1	24
CDDH9- 16	12.1	7	1.5	0.07	1.7	18.6	< 0.05	104	2.2	0.4	1.3	96	0.3	7.18	21.8	1.95	6	0.2	0.013	16.3	1	3.3	< 1	3.7	13	299	52.7	2
CDDH9- 17	13.3	13	1.8	0.03	0.7	27.1	0.08	17.7	1.4	1.9	4.7	44	0.3	5.89	16.7	0.88	3.5	0.3	0.01	14	< 1	2.1	< 1	5.5	11	43.8	27.4	5
CDDH9- 18	10.2	7	1.8	0.04	0.2	11.5	< 0.05	4.1	0.8	0.3	1.2	20	0.3	4.96	6.9	1.19	3	0.2	0.012	11.9	< 1	2	< 1	3.6	8	22.4	7.9	3
CDDH9- 19	10.7	10	1	0.05	0.8	89.9	< 0.05	11.3	1.6	0.5	2.8	63	0.4	5.6	11.6	1.81	7.1	0.6	0.011	12.7	2	2.8	< 1	4	23	76.2	7.5	22

Table 2: Whole-rock geochemistry data for transitional metals at Corunna Downs

Sample	La	Ce	Pr	Nd	Sm	Eu	Gd	Tb	Dy	Ho	Er	Tm	Yb	Lu	Y	U	Th
CD1-M05	4.61	9.38	0.93	4	0.75	0.426	0.78	0.15	1.04	0.27	0.83	0.131	0.91	0.149	9.3	0.1	0.49
CD6-M08	3.66	5.02	0.74	2.97	0.64	0.331	0.87	0.14	0.99	0.25	0.72	0.117	0.73	0.108	9.1	0.05	< 0.05
CDDH1-09	2.11	3.31	0.38	2.13	0.53	0.422	0.63	0.1	0.68	0.16	0.52	0.086	0.6	0.104	7.7	0.09	0.05
CDDH1-11	1.98	4.68	0.4	1.77	0.52	0.264	0.65	0.13	0.87	0.22	0.72	0.113	0.88	0.143	7.8	0.99	0.43
CDDH1-16	1.65	6.76	0.37	1.26	0.43	0.257	0.7	0.12	0.85	0.22	0.71	0.105	0.66	0.104	9.5	0.15	0.08
CDDH1-17	2.73	5.86	0.44	1.87	0.38	0.237	0.86	0.16	1.1	0.28	0.9	0.135	0.91	0.154	14.2	0.15	0.08
CDDH1-18	2.18	4.69	0.36	1.74	0.4	0.295	0.84	0.14	0.99	0.26	0.84	0.125	0.83	0.146	11.7	0.29	0.22
CDDH2-03	2.5	3.44	0.36	1.72	0.4	0.21	0.62	0.1	0.67	0.18	0.63	0.1	0.66	0.103	10	0.08	0.13
CDDH2-07	1.28	2.35	0.17	0.82	0.19	0.08	0.19	0.03	0.2	0.05	0.18	0.032	0.21	0.034	3.2	0.22	0.06
CDDH2-08	13.8	22.9	1.97	6.9	1.32	0.637	1.43	0.25	1.77	0.43	1.31	0.198	1.23	0.199	18.4	0.22	0.24
CDDH2-09	2.66	4.74	0.39	1.62	0.23	0.147	0.4	0.07	0.44	0.11	0.36	0.051	0.32	0.053	7.2	0.16	< 0.05
CDDH2-10	2.79	3.25	0.31	1.34	0.23	0.172	0.32	0.04	0.27	0.09	0.29	0.041	0.28	0.051	5.1	0.15	0.09
CDDH2-14	17.7	34	4.11	17.3	2.81	0.995	1.75	0.24	1.35	0.29	0.89	0.137	0.87	0.142	9.4	0.11	0.1
CDDH3-01	3.02	3.2	0.32	1.43	0.26	0.11	0.25	0.04	0.33	0.09	0.29	0.048	0.34	0.05	5.5	0.1	0.13
CDDH3-02	2.38	2.61	0.28	1.29	0.29	0.16	0.44	0.08	0.52	0.13	0.38	0.057	0.34	0.055	7.6	0.19	0.08
CDDH3-04	5.45	7.25	0.81	2.95	0.57	0.174	0.69	0.11	0.67	0.15	0.47	0.075	0.47	0.068	9.2	0.16	0.55
CDDH3-09	21.6	36.2	3.51	13.4	2.38	1.21	2.76	0.51	3.25	0.8	2.52	0.348	2.51	0.392	31.8	0.63	0.46
CDDH3-19.4	2.88	4.64	0.4	1.38	0.17	0.09	0.27	0.04	0.22	0.06	0.2	0.027	0.2	0.04	3.8	0.14	0.11
CDDH5- 2	1.78	12.1	0.31	1.35	0.27	0.085	0.44	0.08	0.55	0.15	0.48	0.068	0.4	0.062	6.3	0.83	0.26
CDDH9- 2	8.21	9.52	2.16	7.77	1.5	0.535	1.85	0.32	2.1	0.45	1.42	0.226	1.39	0.203	8.6	0.83	1.83
CDDH9- 8	1.62	3.01	0.34	1.76	0.44	0.246	0.83	0.15	1.06	0.24	0.76	0.128	0.84	0.124	7.2	0.3	0.45
CDDH9- 10	3.09	4.63	0.53	2.25	0.61	0.34	0.93	0.16	1.14	0.29	1	0.156	1	0.141	9.9	0.16	0.23
CDDH9- 12	3.42	7.63	0.75	3.63	1.05	0.598	1.59	0.26	1.71	0.43	1.43	0.222	1.37	0.21	12.3	0.18	0.32
CDDH9- 14	2.86	5.88	0.8	5.22	2.63	1.85	4.01	0.72	4.77	1.09	3.78	0.721	5.52	0.912	29.2	0.24	0.22
CDDH9- 15	3.36	6.26	0.78	4.64	1.54	1.07	2.7	0.49	3.48	0.88	2.77	0.422	2.6	0.398	25.3	0.16	0.33
CDDH9- 16	7.5	17.9	1.59	7.18	2.15	1.35	3.66	0.66	4.56	1.06	3.46	0.532	3.46	0.543	22.4	0.24	0.31
CDDH9- 17	5.23	9.35	1.26	5.89	1.78	1.28	2.74	0.5	3.41	0.78	2.43	0.377	2.55	0.38	17.8	0.48	0.33
CDDH9- 18	4.62	8.55	1.05	4.96	1.16	0.688	1.51	0.27	1.78	0.42	1.36	0.232	1.57	0.225	11.5	0.08	0.15
CDDH9- 19	5.58	10.4	1.28	5.6	1.71	0.944	2.11	0.37	2.31	0.5	1.61	0.249	1.6	0.253	15.6	0.62	3.43

Table 3: Whole-rock geochemistry data for REE+Y, U and Th at Corunna Downs

VI. Paragenesis of iron-bearing phases

The Split Rock and Runway deposits exhibit a similar paragenetic mineral sequence, including one or two distinct hypogene alteration stages and five supergene alteration stages. A paragenetic sequence is proposed in Fig. 14.

Stage 0: Anhedral hematite, anhedral magnetite and chert

This assemblage defines the least altered jaspilitic BIF in the Split Rock and Runway deposits. Jaspilite bands are characterised by minor, clay-size anhedral hematite impregnating amorphous to cryptocrystalline silica. Iron oxide-rich bands are essentially composed of fine-grained (<5 μm) hematite aggregated with minor amounts of anhedral magnetite and chert.

Stage 1: Euhedral magnetite (+quartz)

Large euhedral magnetite crystals up to 500 μm in width occur as disseminated crystals in iron oxide-rich bands, and to a lesser extent in chert-rich bands (Fig. 12B). Locally, euhedral magnetite is concentrated along mm- to 10 cm-thick veins cutting across BIF bands in association with crystalline quartz (Fig. 12A). Euhedral magnetite is interpreted to have formed through the circulation of diagenetic to low-grade metamorphic fluids, concentrated along D3 shear zones, shortly after the deposition and burial of the BIF sequence.

Stage 2 platy hematite and stage 3 martite

Euhedral, stage 2 platy hematite crystals up to 100 μm in length occur in a restricted number of goethite-martite proto-ore samples collected in intermediate areas to the high-grade iron ore body at Split Rock. (Fig. 12G, H). Solid-state oxidation of stage 1 magnetite to stage 3 martite is preserved along crystallographic planes (Fig. 12C, D) or external faces (Fig 12E). The relative timing between martitisation of magnetite and formation of platy hematite remains unclear.

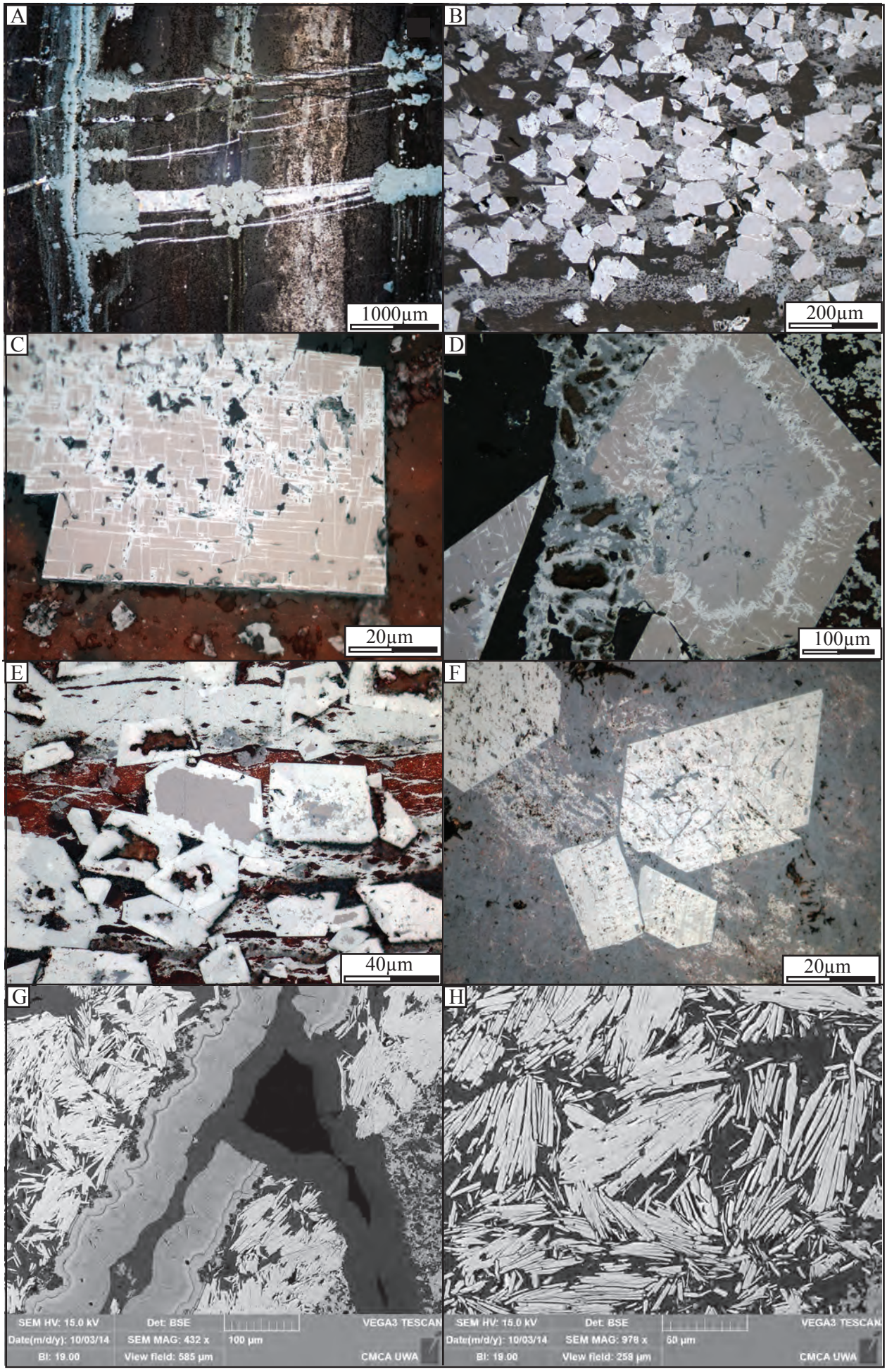

Figure 12: Optic microphotographs and BSE imaging of (A-C) stage 1 magnetite, (D-F) martitisation of stage 1 magnetite, (G) stage 2 platy hematite, stage 4 botryoidal goethite and hematite and (H) stage 2 platy hematite

Stage 4: Botryoidal goethite and hematite

This stage corresponds to the major goethitisation event responsible for the large volumes of goethitic ore at the Split Rock and Runway deposits. Goethite forms mainly through (i) direct in situ replacement of existing minerals (Fig 13E) and (ii) as vug infill after prior dissolution and leaching of other mineral phases. In larger vugs and veins, goethite that grows into space develops a botryoidal texture that locally overprints stage 3 botryoidal hematite (Fig. 13B). Stage 4 botryoidal goethite displays a homogeneous composition and lacks any zonation pattern, contrasting with the late stage 6 botryoidal goethite (see below). Locally, stage 4 is characterised by the formation of early botryoidal hematite prior to goethite formation. (Fig. 12G, 13A). Botryoidal hematite-rich veins locally cut martite and platy hematite, demonstrating that botryoidal hematite postdates martite and platy hematite (Fig. 13A).

Stage 5: Microplaty hematite

Microplaty hematite (ca. 5-10 μm in length) is present on surface exposures of outcrop in intermediate to proximal goethitic ore zones. Textural relationships indicate that microplaty hematite overgrows stage 4 anhedral goethite, or precipitates in vugs unaffected by stage 4 goethitisation (Fig. 13F), and is in turn overgrown by a second stage of botryoidal goethite (Fig. 13G).

Stage 6: Late botryoidal goethite

Stage 6 represents a late, minor event of botryoidal goethite formation. This alteration stage postdates the formation of microplaty hematite and is therefore distinguished from stage 4 botryoidal goethite (Fig. 13G). Botryoidal goethite that formed during stages 4 and 6 can be further recognised based on the occurrence of a fine zoning pattern in the latter stage (Fig.

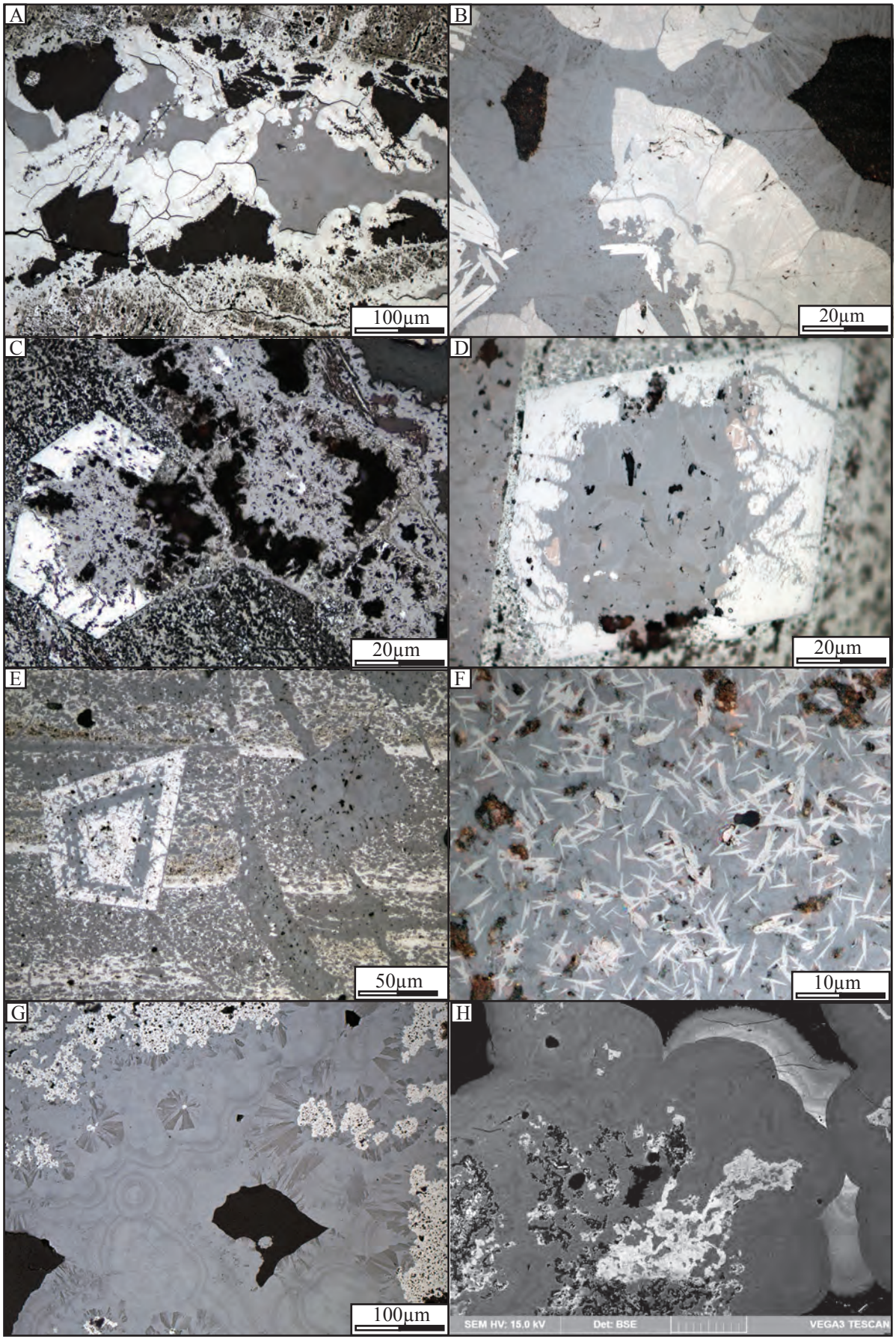

Figure 13: Optic microphotographs and BSE imaging of (A-B) stage 4 botryoidal goethite and hematite, (C-E) stage 4 pervasive goethitisation of stage 3 martite, (F) stage 5 microplaty hematite after stage 4 goethite, (G) stage 6 botryoidal hematite after stage 5 microplaty hematite and (H) stage 7 psilomelane after botryoidal goethite

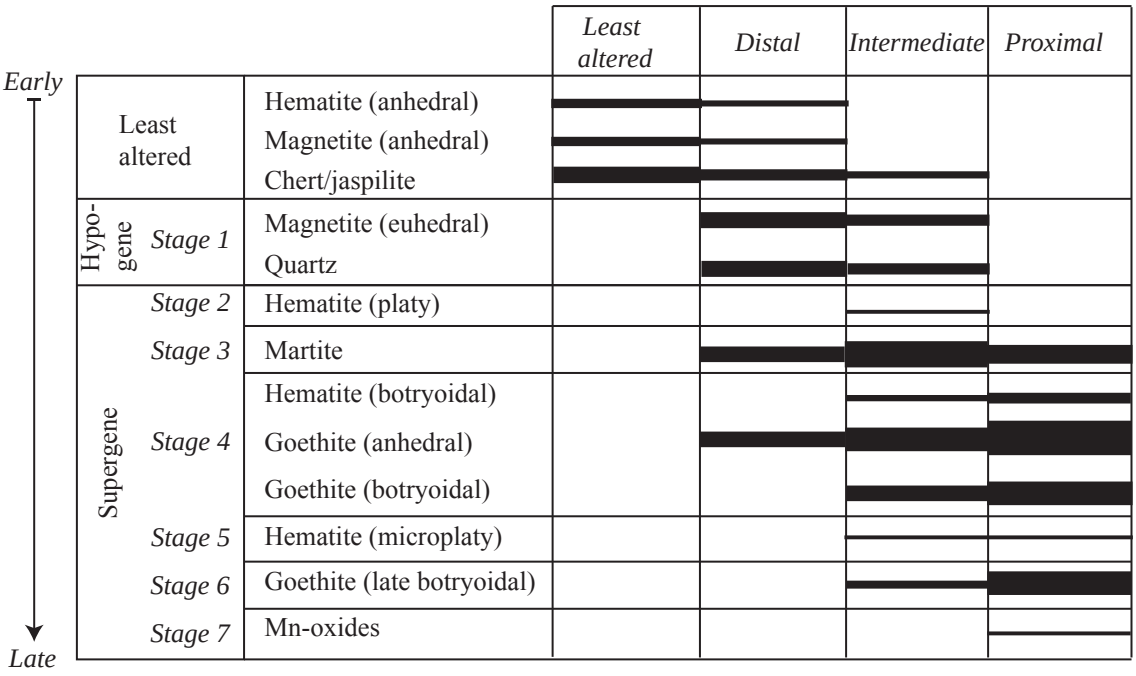

Figure 14: Paragenetic sequence for iron oxides and associated minerals at Corunna Downs

13G, H). This pattern is due to micrometre-scale changes in Al and Si content, supported by SEM observations (ranging from ca. 0 to 2 wt %), across the successive growth layers.

Stage 7: Mn-oxides

A minor stage of manganese oxide (psilomelane±pyrolusite) precipitation occurs as veins cutting through vitreous and ochreous goethite mineralisation, and as overgrowths on stage 6 botryoidal goethite (Fig. 13H). Manganese oxides are associated with the latest stage of alteration recognised in this study and do not appear to be controlled by the main structures.

VII. Mineral trace element geochemistry

This section documents the chemical composition of several iron oxide phases formed through stages 1 to 6: stage 1 euhedral magnetite, stage 2 platy hematite, stage 3 martite, stage 4 goethite and hematite, stage 5 microplaty hematite and stage 6 late botryoidal goethite. Cryptocrystalline hematite and magnetite from the least altered BIF were not analyzed due to spatial resolution limitations associated with the analytical technique.

Stage 1 magnetite

The mineral chemistry data for stage 1 hypogene magnetite indicates a Si content ranging from 3,000 to 30,000 ppm. Detected trace elements include V, Ge, Al, P, Na (10 to 100 ppm), Ni, K (10 ppm), Zn, Cr, Mg, W (1 to 10 ppm) and Ba, As, Co, Cu (0 to 1 ppm). Stage 1 magnetite is depleted in all REE compared to PAAS. Stage 1 magnetite REE patterns display a slight increase from LREE to HREE, including positive Ce and Eu anomalies (Fig. 15).

Stage 2 platy hematite –stage 3 martite

Stage 2 platy hematite is characterised by the systematic increase of most trace elements including Al, P, Mg, Ni, Co, Zn and As compared to stage 1 magnetite, together with a decrease of most REE and the disappearance of the positive Ce anomaly. Trace element chemistry of stage 3 martite is similar to that of stage 2 platy hematite, apart from higher P (up to 200 ppm) concentrations. In addition, W, and to a lesser extent Ge, V and Cr concentrations in martite define two different populations, indistinguishable from their mineral textures (Fig. 15). The first chemical population for martite is most representative of the martite sampled within the Split Rock and Runway deposits. As shown in Fig. 16, stage 2 martite exhibits a large range of W concentrations up to 150 ppm, much higher than in any other analysed iron oxide phase.

Stages 4 (anhedral and botryoidal goethite), 5 (microplaty hematite) and 6 (late botryoidal goethite)

Stages 4 to 6 represent late events of supergene alteration. Stage 4 goethite does not exhibit significant compositional differences compared to earlier iron oxide phases except an increase in Ba, Zn and REE concentrations. Particularly, stage 4 goethite yields Zn concentration of up to 1,200 ppm, whereas Zn concentrations in other iron oxides do not exceed 250 ppm (Fig. 16). Stage 4 botryoidal hematite displays a large increase in Al concentration (up to 5,000 ppm) compared to stage 1 magnetite, stage 2 platy hematite and stage 3 martite. Stage 5 microplaty hematite trace element chemistry differs from stage 4 goethite and shows a decrease in P, Ni, Co, Zn, Cu, an increase in REE concentrations, a change in the Ce anomaly from positive to negative and the appearance of a negative Y anomaly. Similarly, stage 6 late botryoidal goethite displays significant differences with stage 4 goethite including an increase in Si, Al, Mg, As, U and a decrease in P, Ca and Cr (Fig. 15,

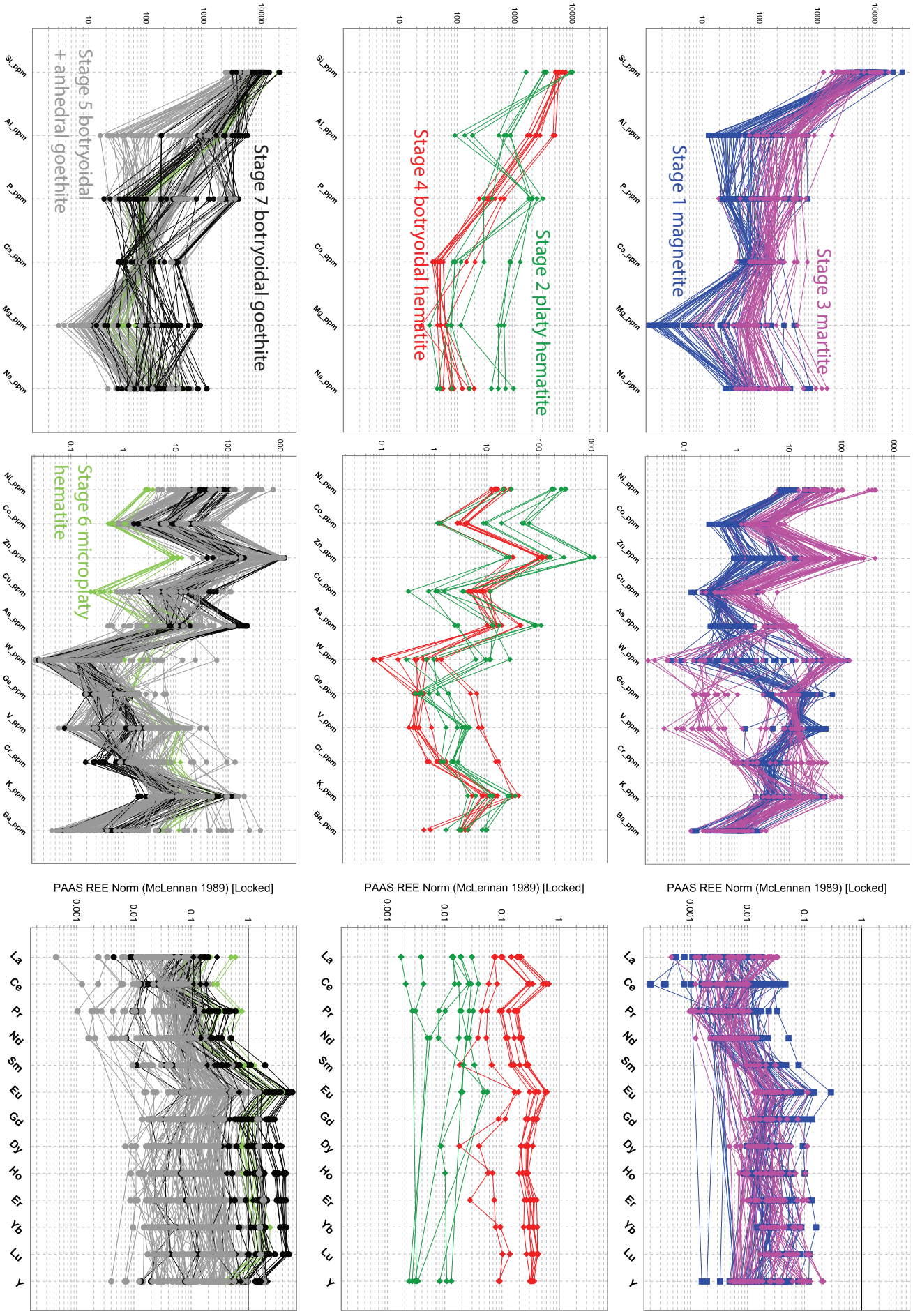

Figure 15: Trace element mineral chemistry data for stages 1 to 7 iron oxides at Corunna Downs

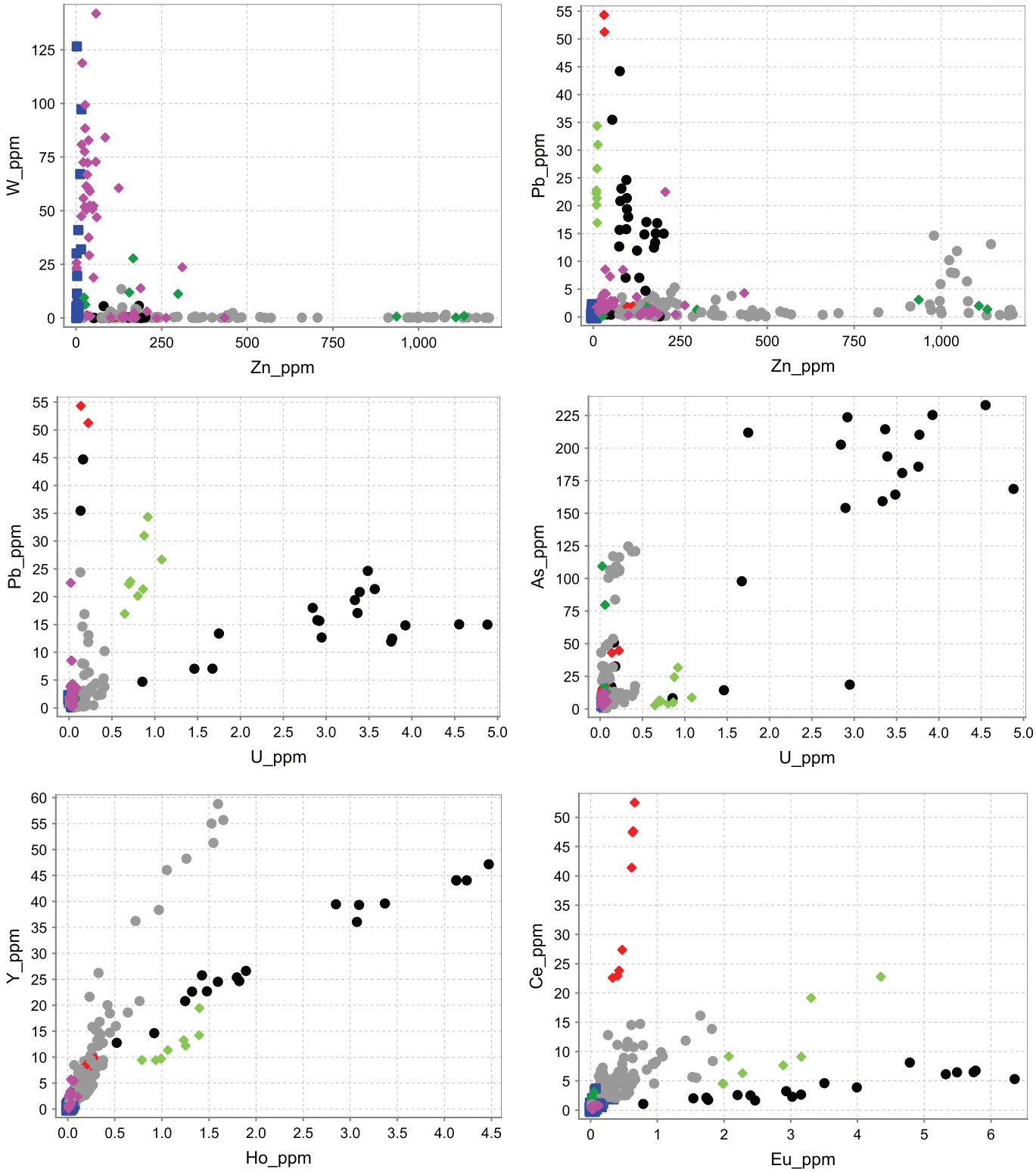

Figure 16: Trace element mineral chemistry data for stages 1 to 7 iron oxides at Corunna Downs. See Figure 15 for colour coding

16). The REE pattern of stage 6 botryoidal goethite is similar to that of stage 5 microplaty hematite. Interestingly, each style of supergene iron oxide alteration may be defined by specific trace element ratios, including Y/Ho (ca. 45 and 20 for stage 4 and stages 5-6 phases, respectively) or Ce/Eu (Fig. 16).

VIII. Descriptive genetic model for the Corunna Downs iron ore deposits

The different mineral assemblages documented in the Split Rock and Runway deposits reveal a complex mineralisation history resulting from multistage early hypogene alteration and late supergene weathering. Timing and conditions of formation of these mineral assemblages are discussed in the following section based on field and analytical investigations and integrating the geologic evolution of the Pilbara Craton. Special attention is devoted to several geochemical signatures that may be used as prediction tools for exploration.

Reduced hypogene alteration

The formation of euhedral magnetite within jaspilitic BIF represents the earliest mineralisation event recorded at the Split Rock and Runway deposits. The spatial relationship between the intensity of magnetite overprint within the BIF and the proximity with D3 shear zones supports a genetic link wherein the circulation of fluids concentrated along these high strain zones resulted in the precipitation of coarse, euhedral magnetite. Stage 1 euhedral magnetite that forms disseminated crystals along bedding is interpreted to be the product of in situ recrystallization processes. Nevertheless, the widespread occurrence of cogenetic veins of magnetite (+quartz) demonstrates that, to some extent, stage 1 mineralisation event also involved transport and reprecipitation of Fe through the circulation of alteration fluids.

Unweathered Archean BIF typically contains recrystallised, diagenetic or metamorphic magnetite and hematite, characterised by the predominance of magnetite over hematite with

increasing metamorphic grade and decreasing oxygen fugacity in the rock (Klein, 2005; Angerer and Hagemann, 2012; Nadoll et al., 2014). In situ element geochemistry of stage 1 magnetite indicates that Fe-substituting cations only occur in trace amounts (V, Ge, Al, P, Na < 100 ppm; Ni, K, Zn, Cr, Mg, W <10 ppm and Ba, As, Co, Cu < 1 ppm). In addition, the ratio Co/Ni does not exceed 0.1. Such characteristics are typical of metamorphic magnetite in BIF (Nadoll et al., 2014) and argue for a metamorphic origin for stage 1 magnetite. In contrast, hydrothermally altered magnetite in low grade metamorphic hematite–chert BIF from the Carajas Serra Norte deposits, Brazil, is characterized by average Co and Ni concentrations that exceed 500 and 350 ppm, respectively, and Co/Ni ratios greater than 1 (Figueiredo e Silva et al., 2009). The evolution of the Pilbara Craton since the deposition of the Cleaverville Formation is marked by several events that could have contributed to the formation of stage 1 euhedral magnetite:

(i) 2950-2940 Ma: The major North Pilbara orogenic event, referred to as the D9 regional deformation event (Hickman and Van Kranendonk, 2008a). D9 orogeny involved greenschist to amphibolite facies metamorphism, as indicated by metabasalts in the Croydon Group of the Mallina Basin (Van Kranendonk et al., 2002).

(ii) 2930-2900 Ma: The emplacement of late granites of the Sisters Suite and layered mafic-ultramafic intrusions of the Radley Suite, essentially confined to the western half of the Northern Pilbara Craton.

(iii) 2930-2900 Ma: The Mosquito Creek orogeny, restricted to the SE section of the northern Pilbara (regional D12).

(iv) 2900–2803 Ma: Granitic intrusion of the Cutinduna and Split Rock Supersuites and associated with pegmatite-hosted, tin-tantalum mineralisation (Huston et al., 2002).

(v) 2770-2760 Ma: The Fortescue Rifting Event, with likely thermal effects of thick plateau basalt deposition. Many older faults, such as those formed during D9, were reactivated by the regional crustal extension of this event (Thorne and Trendall, 2001).

(vi) 2215-2145 Ma: Regional prehnite-pumpellyite metamorphism with associated temperatures not exceeding 350°C (Smith et al., 1982; Rasmussen et al., 2005, White et al., 2014), followed by widespread metasomatism of the Fortescue basalts (White et al., 2014). Rasmussen et al. (2005) propose that this event was probably driven by the northward-advancing Ophthalmian fold-and-thrust belt that developed during protracted collision with the Pilbara Craton, and argue that the widespread geographic and stratigraphic distribution of ca. 2.2 Ga phosphates suggests that fluid flow was intense and pervasive.

The formation of stage 1 magnetite is most likely related either to the 2950-2940 Ma North Pilbara Orogeny or the 2215-2145 Ma regional metamorphic to metasomatic event, as other documented events are spatially confined to areas distal to the Abydos iron camp. Because the circulation of mineralising fluids along fault zones is most efficient when these structures are active, precipitation of euhedral magnetite may have taken place during the North Pilbara Orogeny, along developing D9 fault zones. Alternatively, formation of stage 1 magnetite may be related to the 2215-2145 Ma regional metamorphic to metasomatic event, with associated temperatures not exceeding 350C (Smith et al., 1982; Rasmussen et al., 2005, White et al., 2014), via the circulation of reduced fluids through reactivated D9 fault zones. Rasmussen et al. (2005) suggest that this event was probably driven by the northward-advancing Ophthalmian fold-and-thrust belt that developed during protracted collision with the Pilbara Craton, and argue that the widespread geographic and stratigraphic distribution of ca. 2.2 Ga

phosphates suggests that fluid flow was intense and pervasive. In the absence of absolute age constraints for stage 1 alteration event, both the 2950-2940 Ma and 2215-2145 Ma events could be responsible for the formation of stage 1 euhedral magnetite. Textural features indicate that the precipitation of magnetite occurred both as in situ recrystallisation of pre-existing iron oxides and from the remobilisation of Fe. The importance of Fe remobilisation in the formation of the magnetite-rich proto ore remains therefore poorly constrained, although several evidence (veins, silica leaching) point toward a relatively open system environment.

Multistage supergene alteration

Alteration stage 1 is followed by the formation of martite after magnetite and local platy hematite. The martitisation process is characterised by the systematic increase of most trace elements including Al, P, Mg, Ni, Co, Zn, W and As. The greatest enrichment compared to the magnetite precursor is observed for W whose in situ concentration increases from less than 1 ppm in stage 1 magnetite to up to 100 ppm in martite. Large volumes of martite are known to occur in various iron ore deposits in association with microplaty hematite or goethite (Angerer and Hagemann, 2010; Angerer et al., 2012; Duuring and Hagemann, 2010, 2012), and are often interpreted to be the result of oxidative fluid alteration caused by descending meteoric waters interacting with BIF. A similar interpretation is well suited for the formation of martite at Corunna Downs and would involve recent (Cretaceous to Cenozoic) supergene fluids although the existence of an ancient (Proterozoic) supergene system cannot be excluded (Angerer et al., 2015). Increase in trace element concentration associated with the martitisation process most likely relates to the higher sorption affinity of most trace elements for hematite compared to magnetite (Gimenez et al., 2007). The major W positive anomaly observed in martite crystals argues that the martitisation process involved interaction of alkaline fluids with the BIF, as the sorption of W onto clay and oxides

generally occurs at relatively high pH and appears to be a nonreversible process (Dermatas et al., 2004). In contrast, the occurrence of large, euhedral crystals of platy hematite rather support an alteration process through hot fluid circulation. The relative timing of martitisation and formation of platy hematite remains unconstrained, and it is therefore unclear whether these are simultaneous events. Considering the restricted occurrence of platy hematite, we propose that the formation of platy hematite may be inherited either from local (i) oxidative hypogene alteration following the formation of stage 1 magnetite or (ii) precipitation from heated, recent supergene-driven fluids.

Subsequent to the martitisation process, the formation of botryoidal hematite took place as early infilling of cracks and vugs that formed through progressive supergene alteration.

The major stage of supergene goethitisation (stage 4) is expressed as various textures, including local early botryoidal hematite, intense pervasive goethitisation and growth of cogenetic botryoidal goethite in open space structures. Early stage 4 botryoidal hematite displays elevated Al (up to 5,000 ppm) and REE compared to stages 1 to 3 mineral phases. Several documented occurrences of Al-rich hematite are interpreted to be inherited from the thermal dewatering of aluminous goethite (Goss, 1987; Wells et al., 1989). Such a process cannot account for the formation of stage 3 botryoidal hematite as it is clearly predating and partly replaced by goethite (see section VI). Alternatively, the formation of supergene botryoidal Al-bearing hematite is best explained by the action of early alkaline weathering fluids with moderate water activity (<0.7) associated with the downward progression of the weathering front (Trolard and Tardy, 1989), therefore shortly predating the formation of stage 4 goethite. Stage 4 goethite is characterised by an increase in Ba, Zn and REE concentrations. The Zn enrichment in stage 4 goethite is particularly significant as in situ Zn concentrations exceed 1,000 ppm (contrasting with the maximum 250 ppm observed in other iron oxide generations). Such anomalously high Zn concentrations in goethite most likely reflect high

Zn sorption affinity for goethite. It is well established that the presence of dissolved sulfate in goethite-precipitating fluids drastically increases the capability of goethite to incorporate zinc into its lattice during crystal growth (Rose and Bianchi-Mosquera, 1993; Grafe and Sparks, 2005). Interestingly, stage 4 goethite is also characterised by an increase in Ba. It is therefore suggested that local dissolution of barite (possibly from neoformed silcrete or evaporites) led to an increase in both dissolved barium and sulfate concentrations in the weathering fluids, from which the Zn- and Ba-rich goethite precipitates.

Stage 4 goethite is locally overprinted by microplaty hematite on surface exposures. Known occurrences of microplaty hematite have been documented in most iron ore deposits and may be formed under various geologic settings (see Morris, 2012). Two main models can be considered for the formation of microplaty hematite in iron ore, involving either early hypogene (hydrothermal alteration, metamorphism of ancient goethitic supergene systems) or a recent supergene, low temperature dewatering process. The latter model explains the formation of microplaty hematite after goethite dehydration with temperature not exceeding 80C (Morris, 2012). Such temperatures can be regularly reached by direct solar heating in hot and arid regions such as the Pilbara Craton (Sabins, 1987). In addition, recurrent wildfires may be responsible for local but significant heating of rocks exposed at surface. Importantly, microplaty hematite only occurs on spatially restricted surface exposures throughout the Corunna Downs camp and is absent in all studied diamond drill cores. This observation, together with the relative timing of microplaty hematite after stage 4 goethite, supports such interpretations.

The late-stage botryoidal goethite (stage 6) formed in remaining open spaces has been distinguished from stage 4 goethite based on textural (fine chemical zoning pattern) and paragenetic (postdates stage 5 microplaty hematite) observations. It occurs in proximal areas where porosity (after silica leaching) is the highest. The high levels of contaminants (Si, Al,

Mg, As, U) and the Y/Ho ratio of stage 6 goethite clearly contrast with the composition of stage 4 goethite, supporting the textural distinction previously proposed between these two stages. Further investigations, including U-Th/He dating of goethite (Shuster et al., 2005; Heim et al., 2006), would be necessary to test whether stage 4 and 6 goethite were formed within two distinct supergene alteration events or within a single, evolving weathering system. The shift in the Y/Ho ratio (from ca. 40 to ca. 18) observed in goethite stage 4 to 6 may support the latter hypothesis as progressive pedogenesis commonly involves a decrease of Y/Ho ratio due to preferential uptake of Y over Ho onto ferric oxy-hydroxides (Thompson et al., 2013).

IX. Conclusions

The Split Rock and Runway deposits at Corunna Downs principally consist of goethite-martite rich ore bodies hosted by jaspilitic BIF of the 3020 Ga Cleaverville Formation in the Coongan greenstone belt of the Pilbara Craton, Western Australia. One major deformation event (D9 regional event, corresponding to local $D1_{CD}$) affects the Cleaverville BIF. This deformation event involves N-S to NNE-SSW sinistral shearing combined with reverse, east-side-up displacement resulting in the formation of tight subvertically plunging folds. Unweathered BIF records an early stage of hypogene magnetite alteration likely related to regional low-grade metamorphism and circulation of metamorphic-driven reduced fluids at ca 2950 Ma (D9), or alternatively as late as 2140 Ma. Although stage 1 hypogene alteration is widespread and pervasive, it is largely concentrated along or proximal to high strain D9 shear zones, which represent focused pathways for alteration fluids. Hypogene magnetite alteration results in an initial upgrade in iron in the BIF from ca 30 to 40-45 wt% Fe and is associated with a similar decrease in SiO_2 through leaching of chert. Restricted occurrence of crystalline

platy hematite postdating magnetite suggests that the widespread reduced hypogene alteration may have been followed by local secondary hypogene alteration involving oxidizing fluids, but the significance and timing of this event remains poorly constrained. A recent, supergene alteration partly replaces magnetite-(±platy hematite) rich proto-ore, forming the large volumes of goethite-martite that comprise the main portion of high-grade ore zones in both deposits. The complex, supergene alteration sequence initiates with the solid state oxidation of magnetite to martite; the large amounts of W incorporated by chemisorption into martite suggests that the onset of weathering mostly involved alkaline meteoric fluids. Further development of the supergene system involved the formation of botryoidal hematite, anhedral and botryoidal goethite, reflecting the evolution of this long-lived weathering system. Together with textural observations, important differences in the trace element composition of goethite, including Zn, U or Pb, confidently allows the distinction of two main events of goethitisation, referred to in this contribution as stage 4 and stage 6 goethite, respectively. The ubiquitous spatial distribution of stage 4 goethite indicates that it represents the dominant mineralisation stage responsible for the formation of volumetrically important ore bodies at Corunna Downs. Microplaty hematite that formed between stages 4 and 6 is restricted to a few surface exposures and is tentatively interpreted to be a local dewatering product of stage 4 goethite rather than a metamorphic alteration product after ancient (Proterozoic) supergene goethite. The present study would certainly benefit from additional field and analytical work in the perspective of mining development and better access to subsurface exposures along pit walls. Such interpretations may also be either supported or challenged by similar studies conducted in other iron camps of the Pilbara.

Chapter 2: Examining the role of felsic magmatism in the formation of high-grade Fe mineralisation in Mesoarchean BIF at the Wodgina mine, Western Australia

I. Introduction

The Wodgina district, East Pilbara Terrane, Western Australia, hosts one of the world's major tantalum resources and has been mined since the early 1900s. Renewed interest during the 1980s and 1990s resulted in open-pit mining of substantial tin and tantalum resources at the Wodgina and Mount Cassiterite pegmatite (Sweetapple and Collins, 2002). More recently, several higher-grade (>50 wt.% Fe) iron ore deposits were recognised and mined within adjacent Banded Iron Formation of the 3020 Ma Cleaverville Formation, extending the life of mining activities in the Wodgina district. The onset of Direct Shipping Ore (DSO) Fe production at Wodgina takes place in a context of significant shift in iron ore exploration and mining strategies, from historically targeted Paleoproterozoic BIFs towards Archean, greenstone-hosted BIFs such as those exposed in the North Pilbara and Yilgarn Cratons. The dominant controls on the formation of iron ore in the Yilgarn Craton have been documented

through a number of recent studies, highlighting the importance of hypogene magnetite–(martite–microplaty hematite) mineralisation through sodic metasomatism (Angerer and Hagemann, 2010; Angerer et al., 2012; Duuring and Hagemann, 2010, 2012a, 2012b). In contrast, Fe deposits in the North Pilbara have received minor scientific attention (Kerr et al., 1994) despite the occurrence of historical iron ore mines (e.g. Yarrie mine). Currently, several deposits in the North Pilbara are mined by Atlas Iron Ltd. (e.g. Wodgina, Pardoo, Mt Webber and Abydos mines), with an additional number of recently defined resources (e.g. McPhee Creek, Corunna Downs).

The Wodgina iron camp located in the Wodgina greenstone belt hosts several high-grade (> 50 wt.% Fe) ore bodies that extend for about 700-1,000 m in strike length and 200-300 m width, and from surface to over 80 m depth. The Fe camp has a total resource of more than 40 Mt Fe (grade and cut-off values of 55.3 and 50.0 wt% Fe, respectively; Atlas Iron Ltd. ASX release August 2014) with moderate contamination by accessory elements (average SiO_2 = 8.9 wt%, P= 0.07 wt%, Al_2O_3 = 2.6 wt%). The Wodgina iron camp, therefore, represents an economically attractive iron district and its proximity to the world-class pegmatite-hosted, tantalum Wodgina deposit raises questions about the potential role of felsic magma-derived fluids in early alteration and upgrade of nearby BIF units. Consequently, Wodgina is an important case study site for examining geological processes involved in the formation of high-quality iron ore in the Pilbara Craton.

In this Chapter, we present the main outcomes of field and analytical investigations on iron ore-forming processes at Wodgina. A multidisciplinary approach was applied, which included geological mapping and core logging, combined with microscopy, bulk geochemical and mineral microanalysis. Documented observations and data were integrated to build a genetic model for mineralisation and develop specific tools for exploration at camp scale and elsewhere in the Pilbara Craton.

II. Regional Geology

The Pilbara Craton, exposed over an area of 530 x 230 km in the north-western part of Western Australia (Fig. 1), comprises five terranes: the 3.53–3.17 Ga East Pilbara Terrane (EPT), representing the ancient nucleus of the craton; the 3.18 Ga Kurrana Terrane (KT) and the 3.27–3.11 Ga West Pilbara Superterrane (WPST), which is a collage of three distinct terranes including the 3.27 Ga Karratha Terrane, the 3.20 Ga Regal Terrane, and the 3.13–3.11 Ga Sholl Terrane. These terranes have unique lithostratigraphy, granitic supersuites, structural map patterns, geochemistry and tectonic histories (Van Kranendonk et al., 2002, 2007; Hickman, 2004). They consist of four principal elements: (i) volcano-sedimentary rocks distributed in a number of early to Mesoarchaean (3.53-3.05 Ga) greenstone belts, (ii) granitic rocks of similar ages, forming either large, polyphase complexes or single intrusions, (iii) late basins (3.05–2.93 Ga) of clastic sedimentary rocks and (iv) post-orogenic granites and ultramafic intrusions (2.89–2.83 Ga) (Hickman and Van Kranendonk, 2012). All of these rocks are unconformably overlain by volcano-sedimentary rocks of the. 2.78–2.45 Ga Hamersley Basin (Arndt et al., 1991; Trendall et al., 2004), and intruded by dolerite dykes.

The regional deformation history of the Pilbara Craton is summarised by Hickman and Van Kranendonk (2008a) and includes up to 12 (D1 to D12) deformation events recorded between 3490 and 2890 Ma. In this scheme, the East Pilbara Terrane and the West Pilbara Superterrane display distinct deformation histories prior to the accretion of these terranes at ca. 3070 Ma. Four early deformation events (D1 to D4, ranging from 3490 to 3240 Ma) are associated with progressive doming of granitic intrusions and creation of synvolcanic structures in the East Pilbara, whereas only one deformation event, dated at ca. 3160 Ma, is recorded in the West Pilbara Superterrane. The East Pilbara Terrane collided with the West Pilbara Superterrane during the Prinsep Orogeny event (D5, ca. 3070 Ma). Subsequently, both terranes share a common deformation history characterised by deformation events D6 to

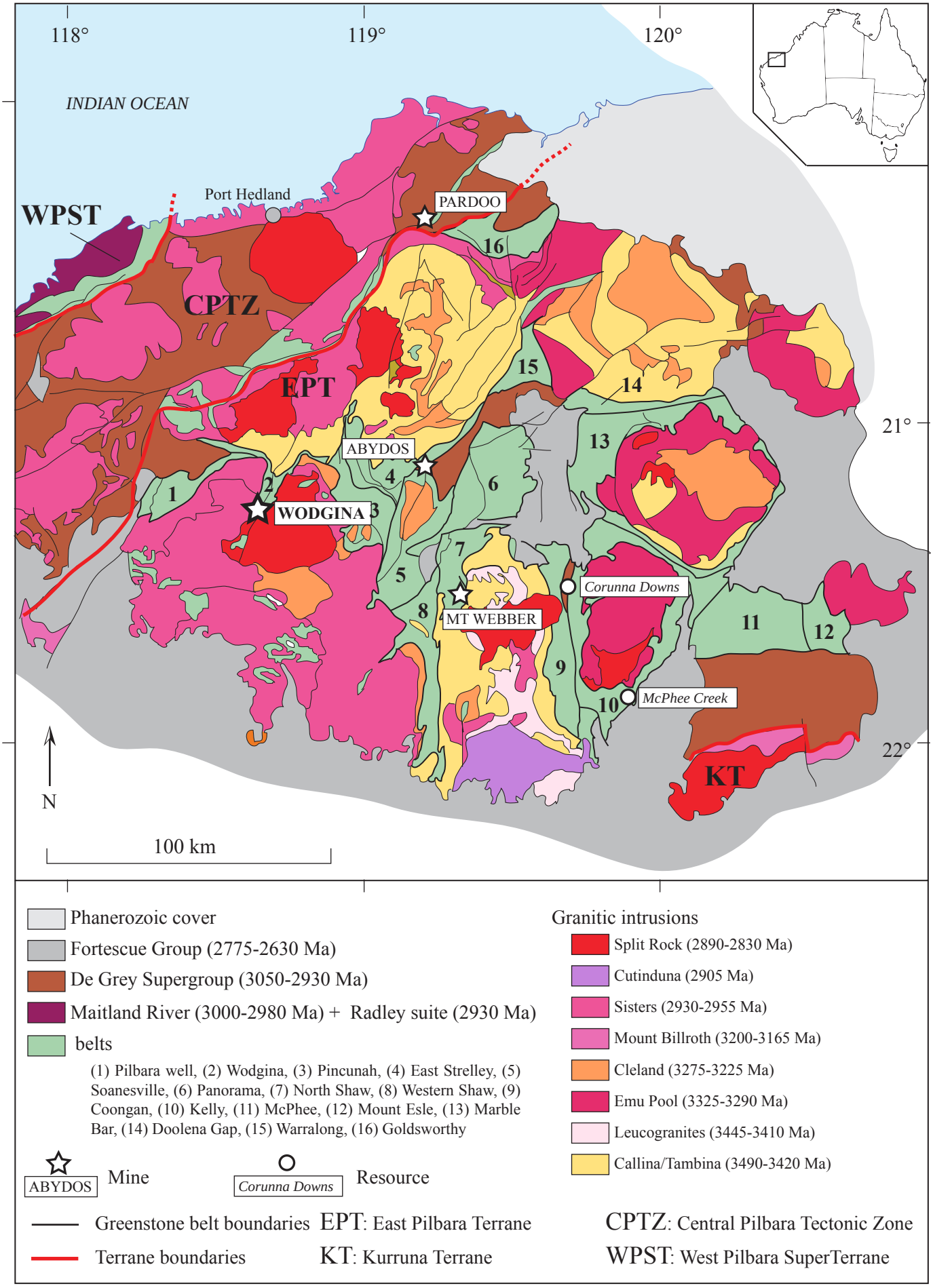

Figure 1: Simplified geology map of the North Pilbara craton including the location of the Wodgina iron camp and active iron ore mines across the North Pilbara. *Modified after Hickman, 2012.*

D12, taking place from 3020 to 2890 Ga and including a major transpressional event at ca. 2950-2940 Ma (North Pilbara orogeny, D9). Several deformation events of moderate intensity occurred during the deposition of the 2775-2630 Ma Fortescue Group.

Similarly to the Yilgarn Craton, the North Pilbara Fe deposits are mostly hosted by Mesoarchaean BIF units within, or unconformably overlying, greenstone belt volcano-sedimentary sequences. In the North Pilbara, these BIF occurrences are hosted by discrete formations, specifically the (i) 3.23 Ga Pincunah banded-iron member of the Kangaroo Caves Formation, (ii) the 3.19 Paddy Market Formation and (iii) the 3.02 Ga Cleaverville Formation. The Kangaroo Caves and Paddy Market Formations were deposited prior to the accretion of the different terranes at ca. 3.07 Ga (Prinsep orogeny; Hickman, 2012) and are, therefore, restricted to the East Pilbara Terrane (Pincunah BIF: North Shaw and Pincunah greenstone belts; Paddy Market BIF: North Shaw and Soanesville greenstone belts). Deep hydrothermal settings are inferred for the deposition of the Pincunah BIF, whereas the Paddy Market Formation was deposited under mid- to-outer-fan and basin-plain settings as part of the Soanesville sedimentary basin (Eriksson, 1981; Hickman, 2012). In contrast, the De Grey Superbasin formed at ca. 3.07 Ga through crustal relaxation and extension after collision between the granite–greenstone terranes and is exposed in most parts of the North Pilbara Craton. It mostly consists of basal conglomerate and sandstone overlain by a ~ 1 km-thick unit of BIF, chert, and black shale of the Cleaverville Formation.

Despite intensive field mapping campaigns performed by government geological surveys during the last few decades, the identification of some BIF exposures in the North Pilbara remains problematic due to uncertainties in depositional ages and correlations across the different greenstone belts. Recently, survey mapping programs led by A. Hickman (Van Kranendonk et al., 2006, 2007; Hickman, 2012) resulted in the revision of the stratigraphy and lithofacies subdivisions within the Pilbara Craton. This revision includes the volcano-

sedimentary sequence at Wodgina based on recent dating and correlations between greenstone belts; basalts and overlying BIF units formerly assigned to the Euro Basalt (3340 Ma), and Corboy (3190 Ma) formations, were reassigned to the Honeyeater basalt (3180 Ma) and Cleaverville Formation, respectively (Blewett and Champion, 2005).

III. Methodology

Mapping and sampling strategy

Surface lithologic and structural mapping were conducted at a 1:5,000 scale within and in the surrounding areas of the Anson, Avro, Dragon and Constellation deposits (Fig. 5). Field observations were digitised using the ArcGIS program. In addition, three diamond drill holes intersecting the Anson and Dragon deposits were logged in detail to examine variations in rock types, alteration styles and alteration intensity. Drill holes were chosen based on their spatial distribution (intersecting distal, intermediate and proximal positions relative to high-grade Fe mineralisation) and on their depth of penetration beneath the near-surface weathering profile. The maximum vertical extent of these logged holes is 80 m, whereas the base of intense weathering at Wodgina is about 50-60 m, but locally extends to considerably greater depths (i.e. ~over 100 m) along lithological contacts or steeply dipping fault zones. Structural orientations are given as dip angle/strike or plunge/trend orientations, with reference to magnetic north. Location coordinates are given using the Geocentric Datum of Australia 1994 (GDA94), MCA Zone 50, geographic coordinate system. Geochemical data extracted from the Atlas Iron Ltd. drill hole database were interpolated using the Leapfrog Geo and ArcGIS programs to further constrain the geometry of lithologic units and mineralisation envelopes at depth. Deposit cross-sections were generated using a combination of surface and diamond drill core observations, plus company geochemical data.

The distinction between the main least-altered rock types (BIF, cherty BIF, chert, and terrigeneous units) in field geological maps, cross sections and 3D geological models is based on direct observation of these rocks, supported by their geochemistry. Banded iron formation contains more than 35 vol% iron-oxide rich bands (i.e. >25 wt % Fe equivalent in drill holes). Chert comprises less than 15 vol% iron-oxide rich bands (i.e. <10 wt % Fe), whereas cherty BIF displays an intermediate composition between chert and BIF (i.e. 15 to 35 vol% iron-oxide rich bands and 10 to 25 wt % Fe). Mapped terrigeneous sedimentary rocks (e.g. shale, siltstone) display a high Al content (up to 20 wt % Al_2O_3).

Analytical strategy

Among the four deposits studied during field investigations (Anson, Dragon, Avro, Constellation; Fig. 4), special attention has been devoted to the Anson and Dragon (northern portion) deposits where forty-seven hand specimens have been collected from surface exposures and diamond drill core. Sampling was conducted from distal to proximal areas relative to the known deposits for the purpose of identifying changes in mineralisation styles and intensity. Thirty-six polished thin sections were prepared from collected samples and examined using reflected/transmitted light and scanning electron microscopy. Twenty-five hand specimens were crushed using a mild steel vibrating disc pulveriser (with potential contamination of Fe up to 0.2 %) at Actlabs, Canada, and pulps were analysed for whole-rock major and trace element geochemistry. Major element oxides were analysed using XRF with Li borate fusion. Trace elements were analysed by ICP-MS with Li borate fusion followed by nitric acid digestion. The loss on ignition (LOI) component was determined by drying sample powders overnight at 110 °C, ignition at 1,100 °C for 25 min and subsequent measurement of the weight loss. The FeO, C-S contents of the powdered samples were determined using titration and infrared methods, respectively. Analytical accuracy was tested with the

international geochemical BIF standard FeR-3 from Temagami, Canada (Bau and Alexander, 2009).

In situ trace element chemical analysis was conducted on four thin sections by LA-ICP-MS at Curtin University using the GSD international standard for calibration (Potts et al., 1992). Ablation time and spot sizes were 45 seconds and 75 to 90 microns, respectively. Data processing was conducted using the Sills program (Murray, 2008).

IV. Geology of the Anson and Dragon deposits, Wodgina iron camp

Wodgina greenstone belt geology

The Wodgina iron camp is located about 120 km south-west of Port Hedland and lies within the Wodgina greenstone belt. The greenstone belt forms a regional keel syncline wedged between the Yule Granitoid Complex to the south and the Carlindi Granitoid Complex to the north (Fig. 2). The belt is dominated by mafic volcano-sedimentary rocks of the Honeyeater basalts (ca. 3180 Ma). These rocks are unconformably overlain by less abundant epiclastic sediments, cherts and BIFs of the ca 3020 Ma Cleaverville Formation, which is at least 600 m thick in the central section of the Wodgina greenstone belt (Champion and Blewett, 2005).

The structural history of the Wodgina greenstone belt includes a complex series of deformation events that has been described by Blewett and Champion (2005) and Blewett (2002). Their interpretations are based on observations from the Pilgangoora area located to the north-east of the Wodgina iron camp. The deformation series (referred to as subscript BC) includes (i) $D1_{BC}$, corresponding to early schistosity only observed in the ca. 3515 Ma Coonterunah Group, (ii) $D2_{BC}$, the first fabric observed in the Kelly Group , (iii) $D3_{BC}$ is the first deformation event observed in the Wodgina iron camp and was associated with the

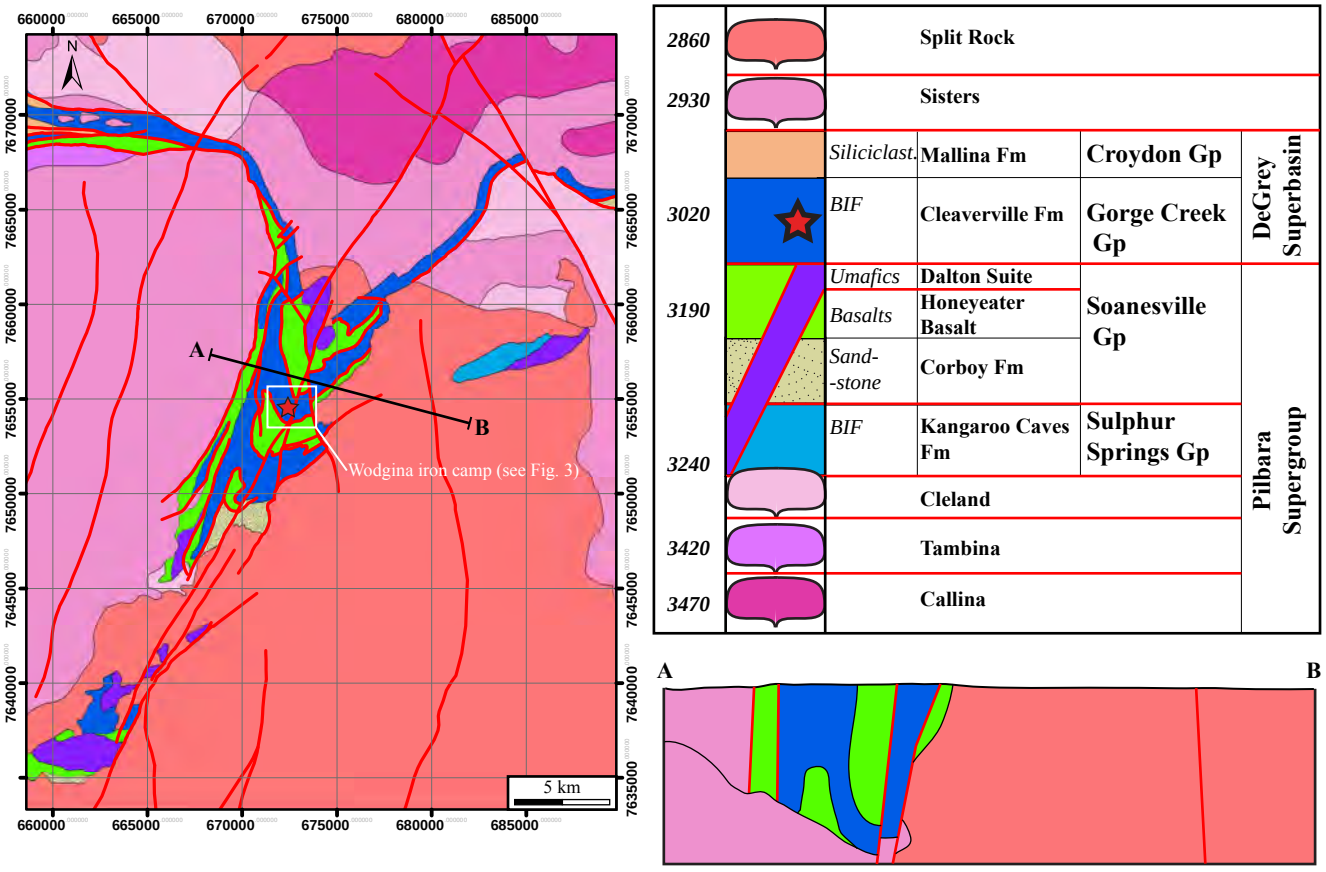

Figure 2: Simplified geology map and cross-section of the Wodgina greenstone belt. Umafics.: ultramafic rocks

progressive doming and syn-kinematic emplacement of granitoid rocks (Callina and Cleland Supersuites), resulting in upright to reclined isoclinal folds and bedding-parallel faults, (iv) $D4_{BC}$ and (v) $D5_{BC}$ locally resulted in refolding and faulting of $D3_{BC}$ folds, and (vi) $D6_{BC}$ involved regional SE-NW directed shortening at ca. 2940 Ma that resulted in high-angle reverse faults and north-easterly trending folds with axial plane parallel faults. The major north-easterly trending folds within the Wodgina greenstone belt are bounded in the west by north-northeast trending strike-slip faults that were active during the regional transpressional event. Axial plane parallel faults were formed towards the end of this compressional event. (vii) $D7_{BC}$ took place at ca. 2890 Ma (Neumayr et al., 1998) and resulted in brittle deformation of the $D6_{BC}$ folds and formation of several NNE to NNW trending sinistral faults with maximum displacements of about 500 m (Blewett and Champion, 2005; Archer, 2009). Postdating this deformation sequence, pegmatites derived from the Numbana Monzogranite intruded the Wodgina greenstone belt at 2870±90 Ma in swarms of shallow-dipping sheeted dikes and generated the Wodgina tantalum-tin deposits (Sweetapple et al., 2002). For clarification purposes, we hereafter use the regional deformation nomenclature (D1 to D12) proposed by Hickman and Van Kranendonk (2008a) rather than the local scheme used by Blewett and Champion (2005). Local deformation events $D3_{BC}$ and $D6_{BC}$ likely correspond to the regional deformation events D8 and D9, respectively.

Lithological and structural relationships in the Cleaverville Formation, Wodgina

Least-altered rock types of the Cleaverville Formation exposed in the Wodgina camp include quartzite, BIFs and shale- to siltstone-dominant turbidites (Fig 3). Contrasting with other regional occurrences of the Cleaverville Formation (Teitler et al., in prep), BIF exposures at Wodgina do not display typical jaspilitic facies (Fig. 3A) A number of 1 to 50 m-thick siltstone-chert (Fig. 3B) and shale units (Fig. 3C) are interbedded at different scales with BIF macrobands, highlighting the alternation of clastic to chemical sedimentation processes

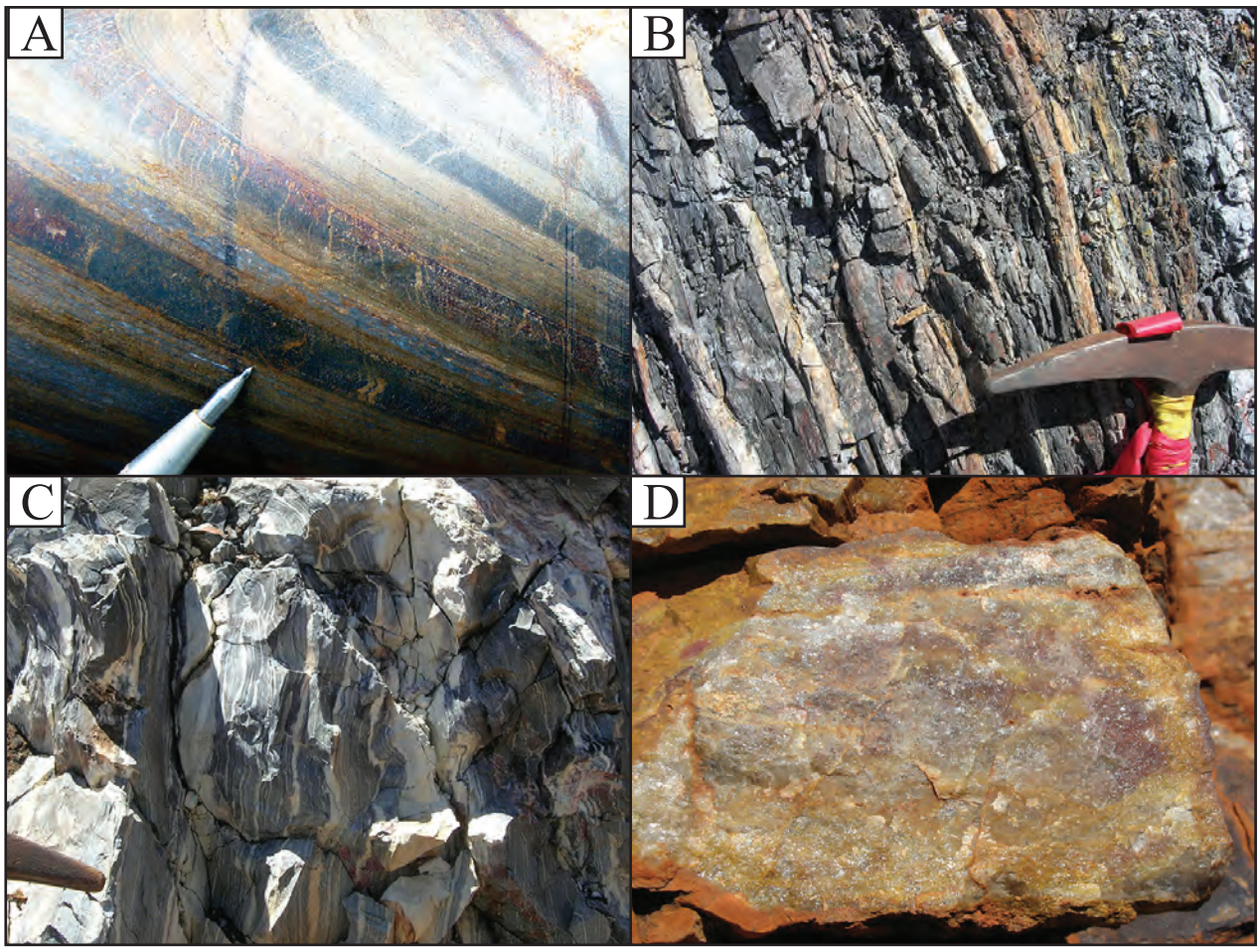

Figure 3: Dominant rock types exposed in the Wodgina iron camp. (A) BIF, (B) siltstone and chert, (C) shale and (D) quartzite

during the deposition of the Cleaverville Formation. A prominent quartzite unit occurs near the base of the Cleaverville sequence and therefore constitutes an important stratigraphic marker (Fig. 4). The Anson deposit is centred on two < 100 m-wide, genetically distinct, BIF macrobands (Fig. 4) referred to hereafter as the Anson North and Anson South BIFs, respectively. The Dragon deposit is hosted by a single BIF macroband interpreted from field investigations as corresponding to multiple fold-repetitions of the Anson North BIF. In both deposits, BIF macrobands that hosts iron ore are interbedded with minor, 1 to 20 m-thick, shale- and chert-rich bands.

Bedding in the Wodgina camp is mostly steep dipping, but varies in strike from mostly NW-trending in the western portion of the camp, to E-W trending in the central portion, to NE-trending in eastern areas (Figs. 4 and 5A).

Four generations of folds are identified in the Wodgina iron camp, referred to as WD subscript.

Early E-W trending, upright, tight folds ($F1_{WD}$) are commonly represented throughout the Wodgina iron camp and exist at a variety of scales, from metre-scale wavelengths in most deposits, to tens of metres wavelengths in the Dragon, Constellation and Avro deposits (Fig. 5B, C). These folds are best observed in the west wall of the Dragon pit, where the folded BIF and shale-siltstone intervals and a subparallel mafic dyke are folded to define tight, cylindrical, anticlinal and synclinal fold hinges that plunge about 30º to the W. This fold generation most likely corresponds to regional-scale D8 deformation event (i.e. $F3_{BC}$ following the nomenclature of Blewett and Champion, 2005). An axial planar $D1_{WD}$ foliation is locally present within the fold hinges of folds. Several 1 to 3 m-wide, high-strain zones containing crystalline magnetite-martite are located along $F1_{WD}$ fold limbs and are oriented subparallel to macro-scale bands in folded BIF. For example, a series of subparallel E-W

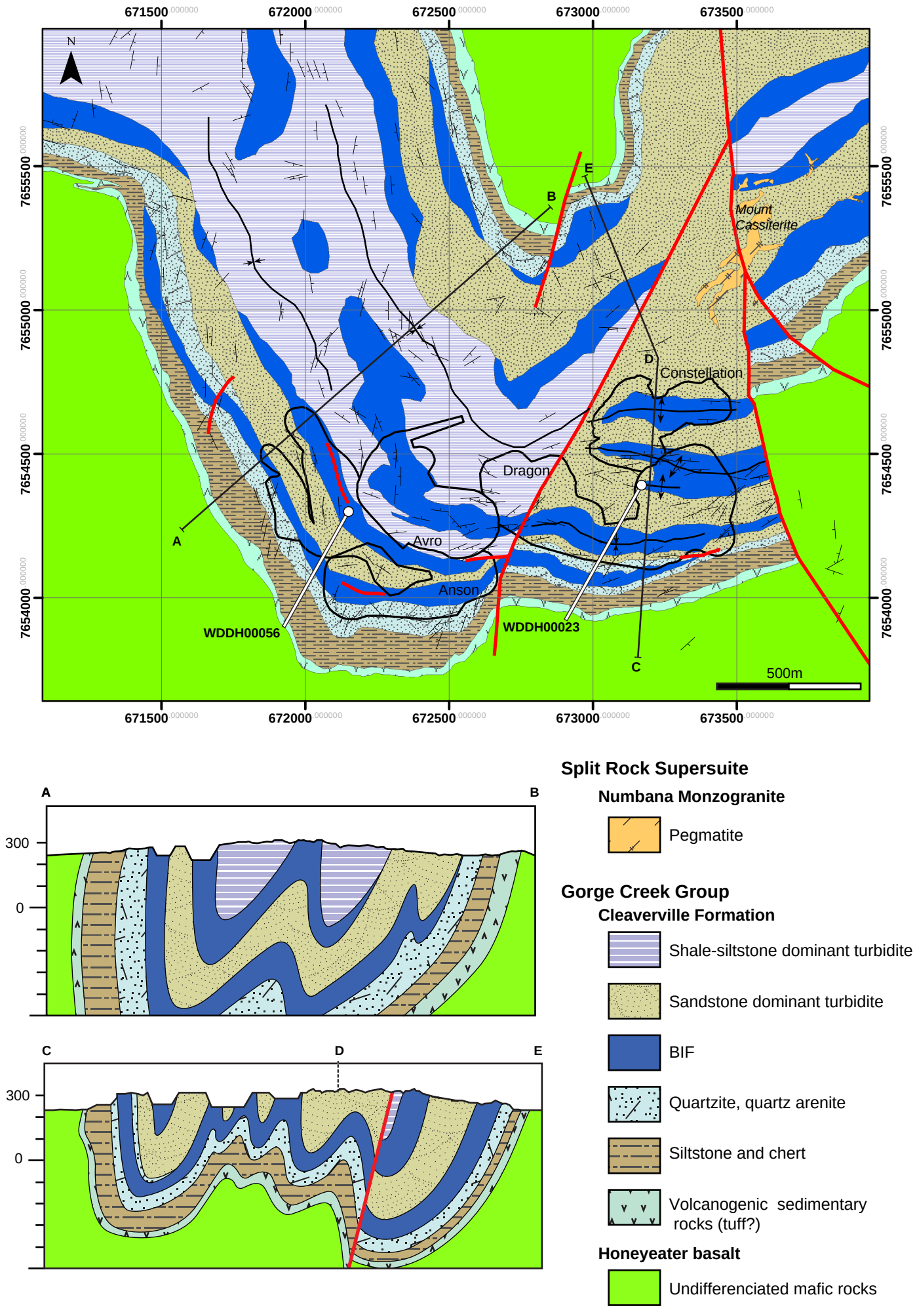

Figure 4: Simplified geology map, cross-section and lithostratigraphic sequence of the Wodgina iron camp. The locations of the Anson, Avro, Dragon and Constellation deposits are included.

trending shear zones that dip ~50º to the N and hosts crystalline magnetite are located subparallel to $F1_{WD}$-folded BIF in the southwestern and southern Anson pits. Similar crystalline magnetite-bearing shear zones are located in the NW-trending main Anson pit where they display a NNW-trend that is subparallel to stratigraphy. These magnetite-bearing (and subsequently weathered) shear zones appear to be the main structural control on higher-grade iron ore zones in the main Anson pit. These high-strain zones are interpreted to represent syn- to late-$D1_{WD}$ structures that formed along the limbs of F_3 folds in response to flexural slip during $D1_{WD}$ folding (Fig. 5D). The southern, basal banded quartzite displays an angular relationship to the contact with the BIF and to bedding within the BIF, suggesting the contact is either unconformable or is truncated at a low angle by $D1_{WD}$ faults (Archer, 2009). In the Constellation deposit, $F1_{WD}$ folded limbs in BIF are cut by several 1- to 3 m-wide, shallowly N-dipping quartz veins.

The limbs of $F1_{WD}$ folds are commonly deformed by steeply N- to NNE-plunging, upright and tight $F2_{WD}$ folds that correspond to the regional D9 event described above (event terminology after Hickman and Van Kranendonk, 2008a). These $F2_{WD}$ fold hinges are commonly present on a metre to kilometre scale throughout the Wodgina camp. The major $F2_{WD}$ synformal fold hinge is the dominant structural feature in the district, controlling the strike trend of the BIF-shale-siltstone tectono-stratigraphy (Fig. 4). Consequently, the axial plane and fold axes for $F1_{WD}$ folds changes from an E-W trending axial trace in the areas of the Dragon deposit to a more WNW trend in the Avro deposit and a NW trend in the main Anson deposit (Fig. 4). Meso-scale parasitic $F2_{WD}$ folds display M-shaped symmetric geometries in the hinge of the regional $F2_{WD}$ synform, corresponding to the position of the Dragon and Avro deposits (Fig. 5E). A N- to NNE-trending, subvertical foliation is developed in BIF and shale-siltstone in the hinges of $F2_{WD}$ folds. In these areas, fold interference patterns result from the deformation of $F1_{WD}$ folds by $F2_{WD}$ folds (Fig. 5F, G).

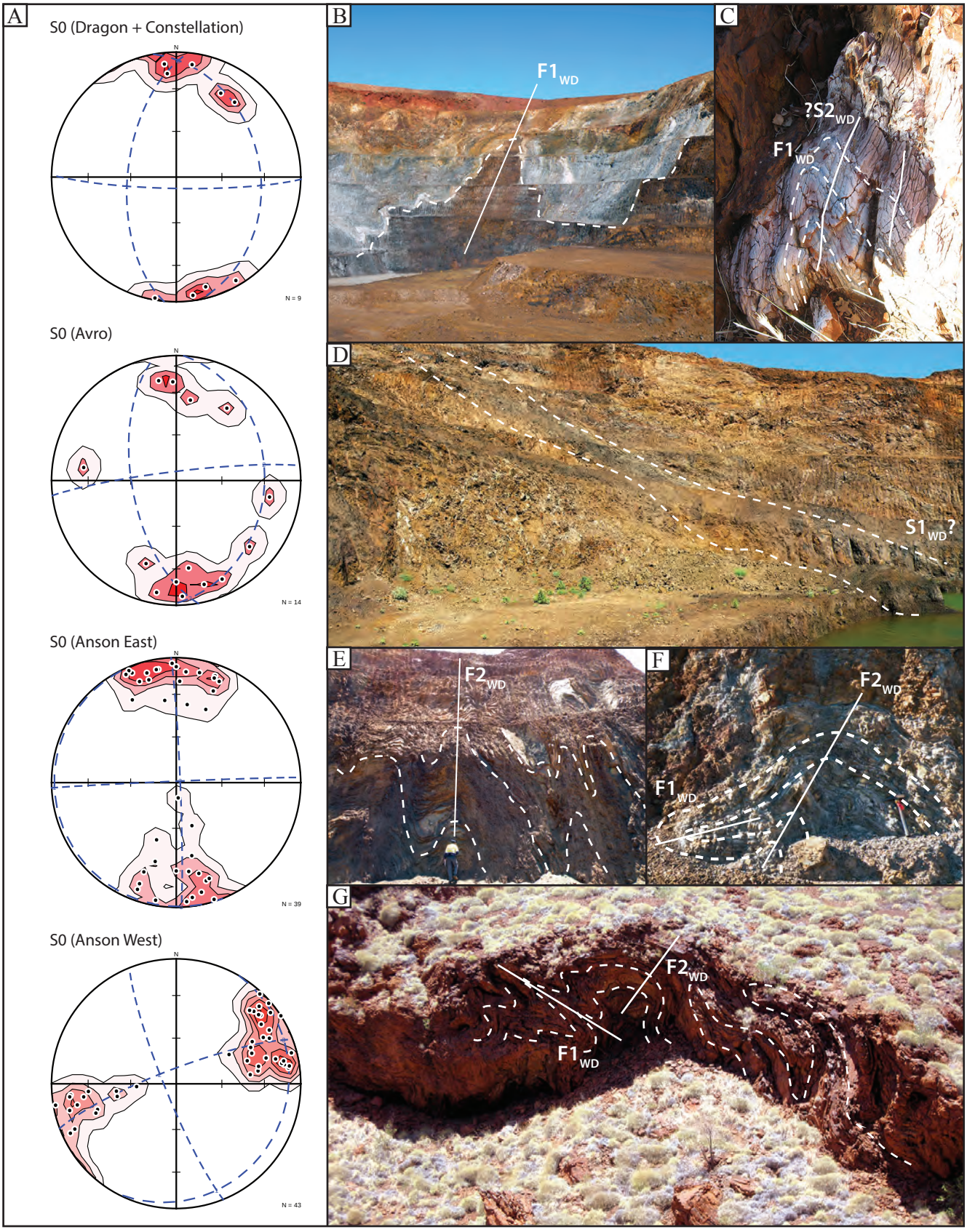

Figure 5: (A) Structural data for bedding and (B-G) Photographs of deformation styles at Wodgina.

A third generation of folds is defined by open and recumbent folds that deform the otherwise subvertical tectono-stratigraphy in the northwestern wall of the Avro pit. This locally recognised deformation event has not been assigned to a regional deformation event.

The hinge and eastern limb of the regional $F2_{WD}$ synform are cut by several N-S, NE-SW, and NW-SE trending faults (Fig. 4). The N-S trending fault that bounds the eastern margin of the Dragon and Constellation deposits is marked by a sinistral displacement ($D3_{WD}$) in excess of 500 m (Fig. 4). The fault that cuts the eastern margins of the Anson and Avro deposits is subvertical and displays east-side-up displacement of uncertain magnitude. Emplacement of pegmatites ($D4_{WD}$) at ca. 2870±90 Ma postdates all of these deformation events.

Iron mineralisation and ore styles

Most iron ore bodies in the Wodgina camp are hosted by BIF located near the base of the Cleaverville Formation. In the Anson and Dragon deposits, the BIF-hosted iron ore zones coincide with the thickened hinges of major upright and tight F_3 folds. Surface exposures and drill cores from the Anson and Dragon deposits record several successive mineralisation events, resulting in a variety of ore styles:

(i) In the Anson deposit, coarse-grained (up to 1 mm) euhedral magnetite (Fe_3O_4)-rich BIF is located within D_3 shear zones that cut BIF macrobands at low angles (Fig. 6A). In distal areas to D_3 shear zones, the BIF (Fig. 6B) may also host disseminated euhedral magnetite crystals. Coarse magnetite alteration in otherwise fresh BIF results in the sub-economic upgrade of iron concentration in BIF from ca. 45 to 65 wt.% Fe_2O_3 (see section V, Fig. 8).

(ii) Martite-rich BIF (Fig. 7B) occurs mostly in the Anson deposit and to a lesser extent in the Dragon deposit. It results from the pseudomorphic replacement of

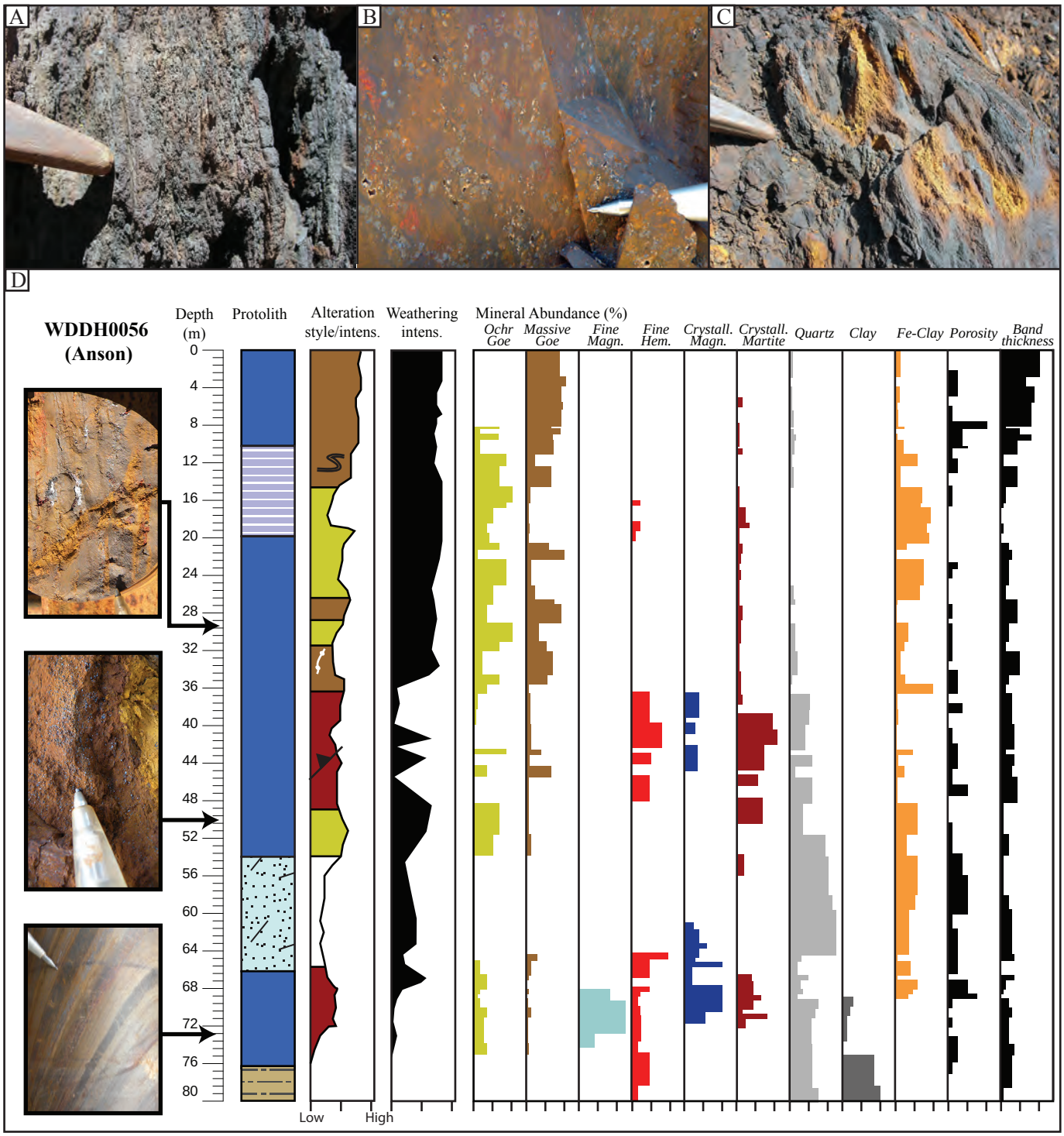

Figure 6: (A-C) Photographs of mineralisation styles at Anson and (D) Stratigraphic log of hole WDDH0056 (Anson North BIF). (A) shear-zone hosted hypogene martite ore, (B) disseminated hypogene magnetite in chert and (C) late ochreous goethite forming after hematite and goethite

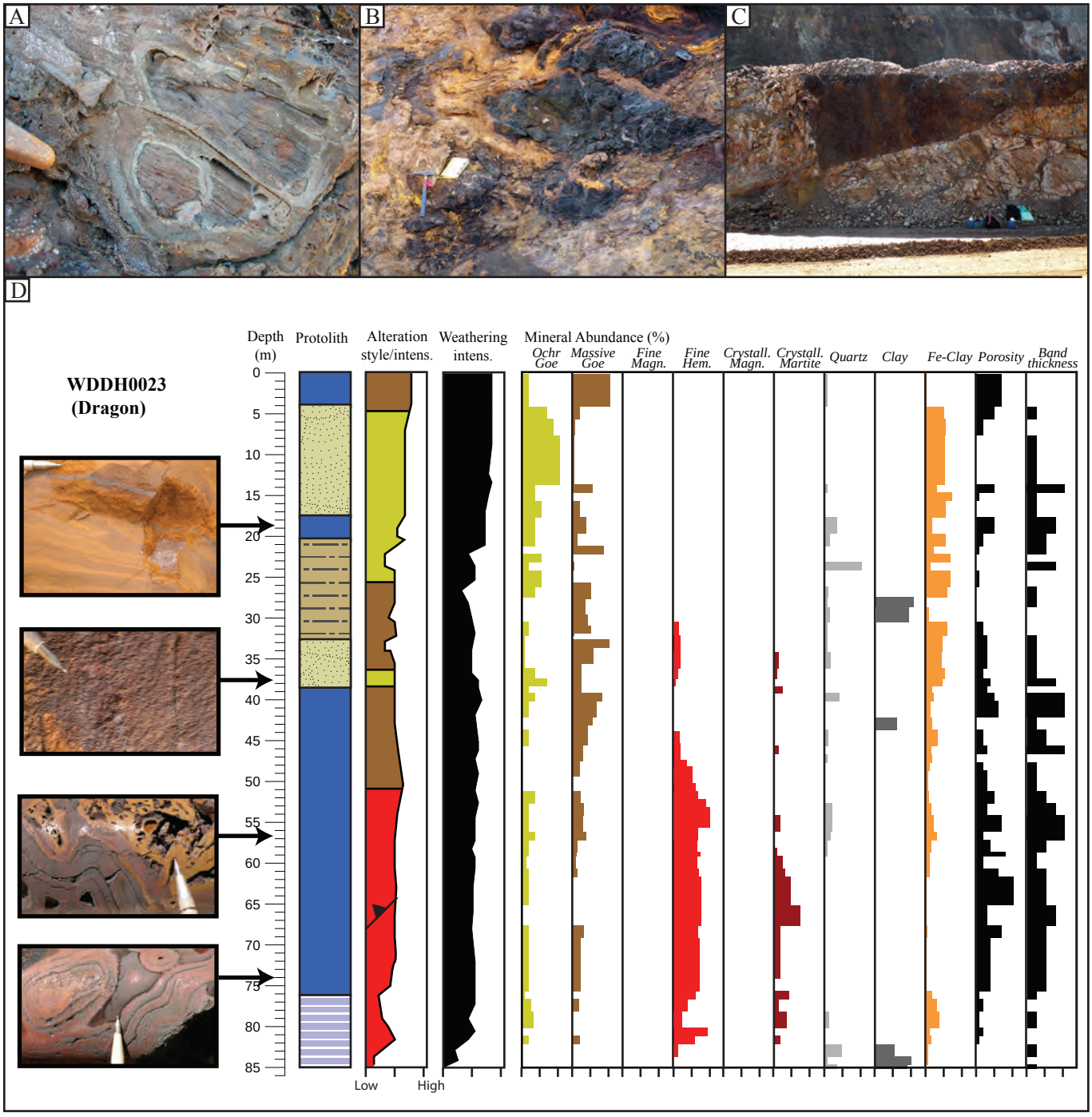

Figure 7: (A-C) Photographs of mineralisation styles at Dragon and (D) Stratigraphic log of hole WD-DH0023 (Dragon BIF). (A) slate goethite veins cutting bedded to massive goethite, (B) ochreous goethite replacing bedded goethite and (C) subhorizontal quartz-rich vein cutting BIF.

A third generation of folds is defined by open and recumbent folds that deform the otherwise subvertical tectono-stratigraphy in the northwestern wall of the Avro pit. This locally recognised deformation event has not been assigned to a regional deformation event.

The hinge and eastern limb of the regional $F2_{WD}$ synform are cut by several N-S, NE-SW, and NW-SE trending faults (Fig. 4). The N-S trending fault that bounds the eastern margin of the Dragon and Constellation deposits is marked by a sinistral displacement ($D3_{WD}$) in excess of 500 m (Fig. 4). The fault that cuts the eastern margins of the Anson and Avro deposits is subvertical and displays east-side-up displacement of uncertain magnitude. Emplacement of pegmatites ($D4_{WD}$) at ca. 2870±90 Ma postdates all of these deformation events.

Iron mineralisation and ore styles

Most iron ore bodies in the Wodgina camp are hosted by BIF located near the base of the Cleaverville Formation. In the Anson and Dragon deposits, the BIF-hosted iron ore zones coincide with the thickened hinges of major upright and tight F_3 folds. Surface exposures and drill cores from the Anson and Dragon deposits record several successive mineralisation events, resulting in a variety of ore styles:

(i) In the Anson deposit, coarse-grained (up to 1 mm) euhedral magnetite (Fe_3O_4)-rich BIF is located within D_3 shear zones that cut BIF macrobands at low angles (Fig. 6A). In distal areas to D_3 shear zones, the BIF (Fig. 6B) may also host disseminated euhedral magnetite crystals. Coarse magnetite alteration in otherwise fresh BIF results in the sub-economic upgrade of iron concentration in BIF from ca. 45 to 65 wt.% Fe_2O_3 (see section V, Fig. 8).

(ii) Martite-rich BIF (Fig. 7B) occurs mostly in the Anson deposit and to a lesser extent in the Dragon deposit. It results from the pseudomorphic replacement of

magnetite by hematite (Fe_2O_3) in BIF. The martite-rich BIF is best exposed in drill cores at depths below about 60 m where the goethite overprint is less intense (Fig 6D, 7D), although relics of martite are also commonly observed in strongly goethitised surface exposures (Fig. 7A). In the following sections, samples defined as martite-rich ore correspond to goethite-rich or anhedral hematite-rich ore samples that contain significant amounts (20% or higher) of crystalline, euhedral martite.

(iii) Bedded- to massive-textured, anhedral goethite (FeOOH) and goethite-martite ores (Fig. 7A) result from intense supergene goethitisation of least-altered and magnetite to martite-altered BIF from surface to a depth of about 60 m. The distribution of goethite-rich ores is concentrated in fold-thickened BIF located between the present surface and about 60 m deep, although goethite-rich mineralisation extends to greater depths in areas that coincide with the sheared limbs of F2 and F3 folds. Goethite-rich ore zones display a sharp basal contact with shale-siltstone units, which may have acted as an impermeable barrier to the downward circulation of near surface derived fluids. At the Dragon deposit, goethite often occurs in association with fine-grained anhedral hematite, both minerals occurring as in situ replacement of BIF but also forming a network of mineralised veins (Fig. 7A). Vitreous goethite-dominated, mixed martite-goethite and hematite-dominated ore types have maxima Fe_2O_3 contents of ca. 88, 92 and 94 wt. %, respectively (Fig. 8).

(iv) Ochreous goethite ore forms at the expense of all types of enriched BIF and is commonly present from surface to a depth of about 40 m (Fig. 6C, 6D, 7B, 7D).

(v) Weakly-expressed manganese oxide mineralisation locally occurs in the Anson deposit as veins that cut martite-goethite rich ore.

V. Bulk rock geochemical changes associated with iron mineralisation

Least-altered BIF

Five samples of least-altered BIF were analysed, including two samples from the Dragon deposit and three samples from the Anson deposit (Tables 1 to 3). Least-altered BIF from Anson yields Fe_2O_3 and SiO_2 average contents of ca. 50 and 45 wt. %, respectively, whereas the least-altered BIF from Dragon yields Fe_2O_3 and SiO_2 average contents of ca. 37 and 58 wt. %, respectively. All samples display low to moderate LOI (2.5 to 6 wt. %) contents (Fig. 8A, B). These values are consistent with the typical composition of the Cleaverville BIF in the East Pilbara Terrane (Van Kranendonk et al., 2002). The FeO concentrations do not exceed 2.5 wt% (Fig, 8D), apart from one atypical ankerite-rich sample from the Anson deposit (FeO = 17 wt %). Other major oxides, including MgO, CaO, Al_2O_3, P_2O_5 and TiO_2, display concentrations below 1 wt. % (Fig. 8). Except for Zn (50-300 ppm), transition metals are below 25 ppm. REE+Y concentrations normalised to PAAS (McLennan, 1989) and to C1 chondrite (Sun and McDonough, 1991) are shown in Fig. 9. Least-altered BIF samples are enriched in REE+Y compared to the C1 chondrite; REE+Y profiles display slight enrichment of LREE and a flat pattern for HREE. Conversely, the least-altered BIF is depleted in REE+Y compared to PAAS, with a significant enrichment of HREE compared to LREE (x10). In both the Anson and Dragon deposits, Eu displays a strong positive anomaly.

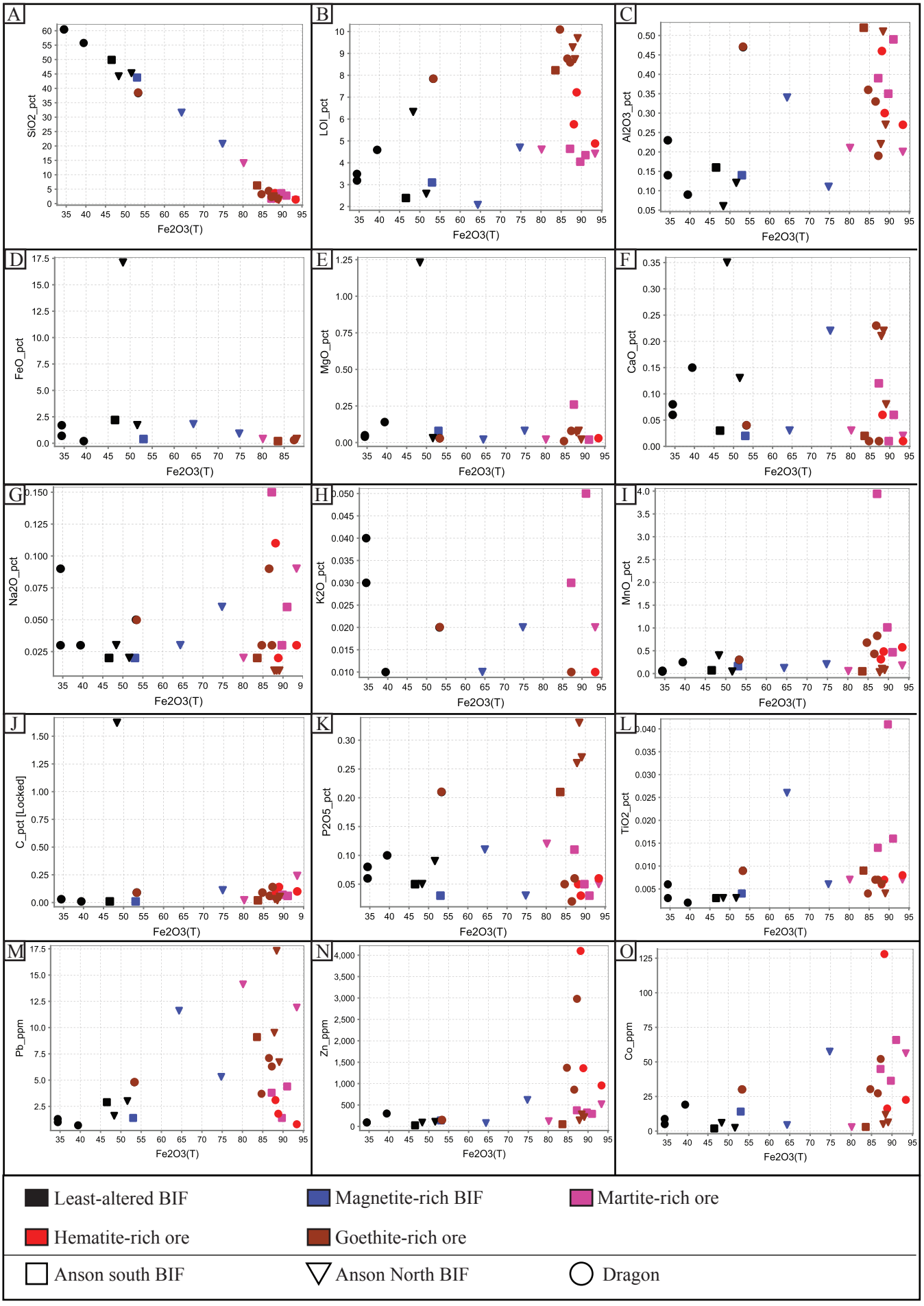

Figure 8: Whole-rock major and trace element geochemistry data for least-altered BIF and iron ore types at Wodgina.

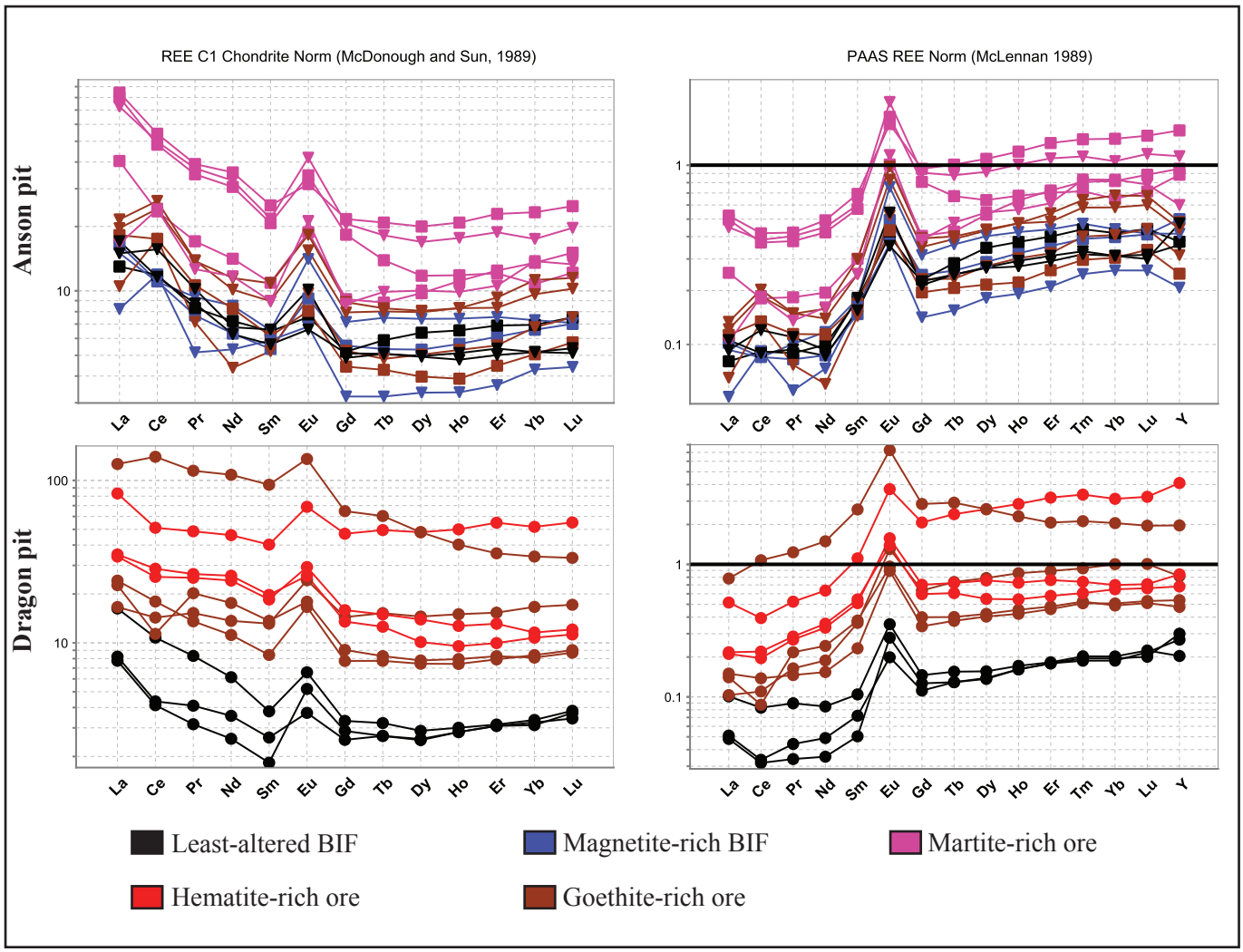

Figure 9: Whole-rock REE data for least-altered BIF and iron ore types at Wodgina.

Sample	alteration intensity	alteration style	Site	Rock type	Site	Al2O3	CaO	Fe2O3	Fe2O3(T)	FeO	K2O	LOI	MgO	MnO	Na2O	P205	SiO2	TiO2	C	S	Total
WDA6-01	high	martite + supergene hematite	Anson stage 6	BIF	Anson stage 6	0.39	0.12	87.09	87.2	< 0.1	0.03	4.64	0.26	3.941	0.15	0.11	1.71	0.014	0.06	0.1	98.56
WDA6-02	least altered	least altered	Anson stage 6	BIF	Anson stage 6	0.14	0.02	52.57	53.02	0.4	< 0.01	3.1	0.08	0.164	0.02	0.03	43.74	0.004	0.01	0.02	100.3
WDA6-03	high	martite + supergene hematite	Anson stage 6	BIF	Anson stage 6	0.49	0.06	90.91	91.02	< 0.1	0.05	4.35	0.02	0.467	0.06	0.03	2.77	0.016	0.06	0.23	99.34
WDA6-04	weak	martite	Anson stage 6	BIF	Anson stage 6	0.16	0.03	44.1	46.55	2.2	< 0.01	2.39	< 0.01	0.072	0.02	0.05	49.89	0.003	0.01	0.01	99.17
WDAM-01	moderate to stron	martite	Anson Main	BIF	Anson Main	0.11	0.22	73.78	74.78	0.9	0.02	4.69	0.08	0.202	0.06	0.03	20.71	0.006	0.11	0.06	100.9
WDAM-05	high	martite	Anson Main	BIF	Anson Main	0.2	0.02	93.28	93.39	< 0.1	0.02	4.41	< 0.01	0.175	0.09	0.05	1.23	0.007	0.24	0.47	99.57
WDDN-02	least altered	least altered	Dragon North	BIF	Dragon North	0.14	0.08	32.55	34.44	1.7	0.03	3.19	0.05	0.061	0.09	0.06	60.49	0.003	< 0.01	0.02	98.63
WDDN-05	weak	martite - goethite	Dragon North	sandstone	Dragon North	0.23	0.06	33.65	34.43	0.7	0.04	3.49	0.04	0.044	0.03	0.08	60.41	0.006	0.03	0.02	98.85
WDDN-08	high	goethite	Dragon North	BIF	Dragon North	0.33	0.23	86.43	86.54	< 0.1	< 0.01	8.76	0.08	0.431	0.09	0.02	4.42	0.007	0.06	0.05	100.9
WDDN-10	least altered	least altered	Dragon North	shale	Dragon North	22.1	0.19	18.66	18.77	0.1	0.05	10.88	0.19	0.038	0.11	0.02	47.75	0.014	0.03	0.03	100.1
WDDN-12	least altered	least altered	Dragon North	black shale	Dragon North	14.92	0.42	6.59	10.48	3.5	0.84	9.15	1.4	0.079	0.59	< 0.01	59.89	0.489	5.56	0.1	98.27
WDDN-13	high	supergene hematite	Dragon North	BIF	Dragon North	0.46	0.06	88.03	88.14	< 0.1	< 0.01	5.76	< 0.01	0.314	0.11	0.05	3.68	0.006	0.09	0.26	98.6
WDDN-16	weak	martite - goethite	Dragon North	sandstone	Dragon North	0.36	0.05	48.02	48.35	0.3	0.02	5.55	0.03	0.02	0.03	0.11	46.07	0.006	0.15	< 0.01	100.6
WDDH18-01	moderate to stron	martite - goethite	Anson stage 6	BIF	Anson stage 6	0.52	0.02	83.36	83.58	0.2	< 0.01	8.23	< 0.01	0.05	0.02	0.21	6.31	0.009	0.02	< 0.01	98.95
WDDH18-05	high	magnetite - martite	Anson stage 6	BIF	Anson stage 6	0.35	0.01	89.62	89.73	< 0.1	< 0.01	4.05	< 0.01	1.013	0.03	0.05	3.61	0.041	0.07	0.03	98.9
WDDH23-01	least altered	least altered	Dragon North	BIF	Dragon North	0.47	0.04	53.2	53.31	< 0.1	0.02	7.84	0.03	0.302	0.05	0.21	38.34	0.009	0.09	0.02	100.6
WDDH23-02	high	supergene hematite	Dragon North	sandstone	Dragon North	0.36	0.01	84.59	84.7	< 0.1	< 0.01	10.09	0.01	0.678	0.03	0.05	3.26	0.004	0.09	0.08	99.2
WDDH23-03	high	martite - goethite	Dragon North	BIF	Dragon North	0.3	< 0.01	88.71	88.83	< 0.1	< 0.01	7.22	< 0.01	0.483	0.02	0.03	1.63	0.007	0.14	0.08	98.51
WDDH23-04	high	supergne hematite	Dragon North	BIF	Dragon North	0.27	0.01	93.29	93.4	< 0.1	0.01	4.88	0.03	0.576	0.03	0.06	1.42	0.008	0.1	0.14	100.7
WDDH23-06	high	goethite	Dragon North	BIF	Dragon North	0.19	0.01	86.9	87.24	0.3	0.01	8.59	< 0.01	0.828	0.03	0.06	2.29	0.007	0.14	0.03	99.26
WDDH56-01	strong to high	martite - goethite	Anson Main	BIF	Anson Main	0.27	0.08	88.96	89.07	< 0.1	< 0.01	9.69	0.02	0.076	0.01	0.27	1.23	0.004	0.05	< 0.01	100.7
WDDH56-02	high	martite - goethite	Anson Main	BIF	Anson Main	0.22	0.21	87.42	87.86	0.4	< 0.01	9.27	0.07	0.027	0.01	0.26	2.5	0.006	0.03	< 0.01	100.4
WDDH56-05	high	martite - goethite	Anson Main	BIF	Anson Main	0.51	0.22	88.31	88.43	< 0.1	< 0.01	8.73	0.08	0.1	0.01	0.33	1.78	0.006	0.02	< 0.01	100.2
WDDH56-06	high	martite	Anson Main	vein in BIF	Anson Main	0.21	0.03	79.7	80.15	0.4	< 0.01	4.6	0.02	0.052	0.02	0.12	14.01	0.007	0.02	< 0.01	99.22
WDDH56-07	strong to high	martite	Anson Main	BIF	Anson Main	0.34	0.03	62.36	64.36	1.8	0.01	2.07	0.02	0.119	0.03	0.11	31.54	0.026	< 0.01	< 0.01	98.65
WDDH56-08	least altered	least altered	Anson Main	BIF	Anson Main	0.12	0.13	49.72	51.61	1.7	< 0.01	2.58	0.03	0.043	0.02	0.09	45.23	0.003	< 0.01	< 0.01	99.86
WDDH56-14	least altered	least altered	Anson Main	cherty BIF	Anson Main	0.06	0.35	29.35	48.36	17.1	< 0.01	6.32	1.23	0.397	0.03	0.05	44.15	0.003	1.62	0.12	101

Table 1: Whole-rock geochemistry data for major oxides at Wodgina

Sample	As	B	Ba	Be	Bi	Cd	Co	Cr	Cs	Cu	Ga	Ge	Li	Mn	Mo	Nb	Ni	Pb	Rb	Re	Sb	Sc	Se	Sn	Sr	Te	Tl	V	W	Zn	Zr
WDA6-01	14	10	120	0.8	0.04	1.3	44.9	18.2	1.79	59.4	1.9	< 0.5	1.2	> 10000	2.06	0.4	131	3.8	1.2	0.006	0.3	2	1.2	3	64.7	0.2	1.04	9	3.6	376	4
WDA6-02	3.1	9	2	1.1	0.1	< 0.1	14.1	58.6	0.13	45.8	3.1	5.6	4.7	1320	3.69	0.2	61.1	1.4	0.4	0.004	0.6	< 1	0.8	2	1.6	0.3	< 0.05	39	2.9	140	1
WDA6-03	8.9	< 1	20	0.6	0.19	0.2	65.9	13.5	0.65	465	3.2	0.6	1.1	3690	0.62	0.4	165	4.4	2	0.004	0.3	2	2.6	2	14.8	0.3	0.34	21	3.7	294	4
WDA6-04	3.7	3	9	1.1	0.11	< 0.1	1.9	82.1	0.19	35.7	1.2	4.9	3	572	5.58	1.6	13.3	2.9	0.7	0.003	0.4	1	1.1	1	1.8	0.3	< 0.05	4	30.8	25.9	11
WDAM-01	41.8	2	10	2.8	0.06	0.2	57.4	27.2	0.38	48.1	1	0.9	0.9	1570	1.55	0.5	178	5.3	0.5	0.002	0.6	< 1	1.2	3	4.9	0.2	0.27	6	4.1	617	3
WDAM-05	62.8	< 1	6	1.4	0.04	1	56.2	15.5	0.19	23.6	0.4	< 0.5	1.5	1350	0.63	0.4	223	11.9	0.9	0.012	< 0.2	2	0.9	2	4.6	< 0.1	0.12	10	3.1	515	3
WDDN-02	17.6	6	3	3.3	0.05	0.2	5	78.4	0.7	39.6	0.4	5.6	1.4	478	5.03	1.2	34	1	0.9	0.004	0.4	< 1	0.7	12	7	0.1	< 0.05	1	3.4	92.8	5
WDDN-05	151	12	6	7.3	0.03	0.2	8.8	49.8	2.24	27.7	0.7	8	16	361	3.56	0.5	148	1.3	2.8	0.004	< 0.2	< 1	0.6	8	4.6	< 0.1	0.1	4	0.7	93	5
WDDN-08	1230	19	18	4.9	0.11	0.5	27.3	33.9	1.49	67.3	1.5	1.5	0.8	3480	2.14	0.6	85.8	7.1	0.4	0.002	0.4	1	< 0.1	10	5.7	< 0.1	1.06	8	79.2	859	7
WDDN-10	405	14	19	2.9	0.12	0.1	4.1	43.3	8.95	27	2	5.1	10	274	2.37	0.6	38.5	0.8	1.8	0.004	0.3	< 1	< 0.1	15	13.9	< 0.1	0.08	8	26.7	69.1	6
WDDN-12	47	112	50	1.6	1.97	0.3	21.4	271	> 100	140	54.7	2.9	112	663	4.93	3.7	326	58.1	171	0.003	1	34	0.7	27	169	0.9	11.6	180	1	381	95
WDDN-13	60.6	8	3	3.1	0.07	5.3	128	18.4	1.23	46.1	1	1.1	2.8	2470	1.23	0.5	724	3.1	0.7	0.005	0.4	3	2.4	1	6.5	< 0.1	1.36	17	5.5	4100	5
WDDN-16	56.7	10	5	3.6	0.04	0.3	7.3	25.4	5.3	42.7	1.9	4.7	0.6	166	1.07	0.2	202	3.3	1.2	0.002	0.4	1	0.5	< 1	7	0.1	< 0.05	9	1.1	222	4
WDDH18-01	77.6	2	11	0.8	0.43	< 0.1	3	15.8	0.43	99.3	2.1	6.7	< 0.5	366	0.58	0.4	24.2	9.1	0.5	0.002	0.6	3	0.7	3	4.9	0.6	< 0.05	5	1.6	51.6	3
WDDH18-05	48.1	3	348	1.7	0.06	0.4	36.4	77.8	0.24	70.8	0.4	4.1	1.4	8710	1.97	0.5	68.7	1.4	0.3	0.002	< 0.2	2	5.9	1	3.9	0.1	0.77	52	9.9	325	6
WDDH23-01	204	15	116	8.8	0.1	1.7	30.1	23.3	0.18	136	0.6	13.6	0.5	2270	1.4	0.2	44.2	4.8	0.5	0.001	3	3	0.4	16	10.2	< 0.1	0.75	25	31.7	147	3
WDDH23-02	25.4	18	10	3.4	0.04	2.5	30.3	30.4	0.28	225	3.6	3.5	1.1	6240	0.69	0.5	160	3.7	0.5	0.006	< 0.2	2	1.3	9	6.6	< 0.1	0.4	6	> 200	1370	3
WDDH23-03	19.1	19	5	2.7	0.03	1.7	16.3	26.4	0.7	46.7	1.8	3.8	0.6	3900	1.24	0.4	117	1.8	0.2	0.003	< 0.2	2	0.6	11	4.4	< 0.1	0.37	13	3.5	1360	4
WDDH23-04	393	3	4	3.3	< 0.02	3	22.6	21.9	0.8	41.5	0.9	3.8	0.9	4550	1.02	0.2	69.5	0.8	0.8	0.005	< 0.2	2	< 0.1	9	10.6	< 0.1	1.19	10	17.8	957	4
WDDH23-06	8.7	5	2	2.1	0.03	5.7	52.1	16.5	0.46	9.8	6.4	1.6	0.7	6750	0.81	0.2	261	6.3	1	0.002	0.5	4	1.7	3	7.8	< 0.1	0.22	8	4.7	2980	3
WDDH56-01	56.3	3	3	2.2	< 0.02	0.2	6.2	16.2	0.11	55	0.8	8.6	< 0.5	565	1.27	0.4	49.6	6.7	0.2	0.002	0.9	2	0.4	2	1.6	< 0.1	< 0.05	4	2.2	216	5
WDDH56-02	26.2	3	3	2.8	0.06	0.2	4.9	13.9	0.08	78.7	0.9	6.6	< 0.5	165	1.6	0.2	55.9	9.5	0.3	< 0.001	1	1	< 0.1	6	1.2	< 0.1	< 0.05	5	2.9	140	2
WDDH56-05	30.3	5	13	4.9	0.03	0.3	11.7	10.1	0.09	155	1	6.5	0.6	783	0.75	0.3	77	17.3	0.2	0.001	2.6	1	0.4	2	1.5	< 0.1	0.06	3	1.6	279	3
WDDH56-06	16.7	3	11	4.3	0.08	0.2	2.8	56.9	0.32	87.3	11.9	9.7	1.6	363	2.29	0.7	34.5	14.1	0.4	0.003	2.7	2	0.6	4	0.9	0.1	0.05	14	5.6	120	5
WDDH56-07	16.3	4	33	1.6	0.07	0.1	4.3	141	0.38	44.4	0.7	9.1	2.2	926	4.02	0.3	30	11.6	0.6	0.002	2.2	1	< 0.1	8	2	< 0.1	0.18	17	2.2	76.1	2
WDDH56-08	8.3	15	12	1.6	0.04	0.2	2.3	82	0.38	61.8	0.3	7.6	2	285	4.47	0.2	19	3	0.4	0.001	1.2	< 1	< 0.1	< 1	0.8	< 0.1	0.16	3	3.3	107	2
WDDH56-14	3.1	16	4	2.4	0.05	0.1	5.9	38.2	1.27	66.1	0.3	9.2	5.5	3070	2.41	1.4	38.4	1.6	1.2	0.002	0.9	< 1	< 0.1	< 1	0.6	< 0.1	1.18	3	1.2	88.2	18

Table 2: Whole-rock geochemistry data for transitional metals at Wodgina

Sample	La	Ce	Pr	Nd	Sm	Eu	Gd	Tb	Dy	Ho	Er	Tm	Yb	Lu	Y	U	Th
WDA6-01	9.59	14.4	1.62	6.6	1.67	1.09	1.88	0.33	2.48	0.63	2.06	0.327	2.3	0.383	25.8	0.31	0.2
WDA6-02	3.9	6.78	0.73	2.95	0.82	0.535	1.14	0.2	1.35	0.32	1.01	0.157	1.12	0.178	13.5	0.27	< 0.05
WDA6-03	19	29.5	3.33	14.3	3.17	2.01	3.76	0.52	2.99	0.67	2	0.29	1.83	0.309	23.9	0.24	0.38
WDA6-04	3.08	7.27	0.79	3.38	0.99	0.438	1.07	0.22	1.62	0.37	1.14	0.178	1.18	0.191	10.1	0.1	0.19
WDAM-01	3.56	6.74	0.89	3.98	1	0.816	1.47	0.28	1.88	0.42	1.25	0.191	1.24	0.18	11.2	0.51	0.06
WDAM-05	17.2	30.5	3.55	15.3	3.33	2.43	4.23	0.68	4.3	1	3.11	0.453	2.97	0.5	30.3	0.21	0.18
WDDN-02	1.95	2.67	0.39	1.66	0.4	0.215	0.52	0.1	0.65	0.16	0.51	0.076	0.53	0.094	7.3	0.06	0.08
WDDN-05	3.86	6.6	0.79	2.87	0.58	0.382	0.68	0.12	0.73	0.17	0.52	0.082	0.57	0.097	5.5	0.16	0.34
WDDN-08	5.73	11	1.29	5.22	1.29	0.965	1.59	0.29	1.89	0.42	1.31	0.206	1.43	0.229	14.5	0.1	0.06
WDDN-10	1.77	2.67	0.36	1.61	0.34	0.176	0.4	0.07	0.45	0.1	0.3	0.046	0.29	0.041	3	0.26	0.24
WDDN-12	23.3	46.2	5.74	22.5	5.18	2.55	3.51	0.56	3.02	0.56	1.68	0.277	2.12	0.348	15.1	1.38	7.54
WDDN-13	19.7	31.3	4.62	21.5	6.16	3.99	9.65	1.85	12.2	2.83	9.09	1.36	8.81	1.4	111	0.14	0.13
WDDN-16	2.47	3.02	0.64	3.04	0.77	0.535	0.93	0.2	1.33	0.29	0.94	0.16	1.17	0.199	9	0.14	0.09
WDDH18-01	4.32	10.7	1.01	3.86	0.94	0.468	0.91	0.16	1.01	0.22	0.74	0.12	0.86	0.146	6.7	0.18	0.14
WDDH18-05	20	33.2	3.72	16.7	3.84	1.83	4.45	0.78	5.08	1.18	3.79	0.565	3.96	0.632	42.2	0.24	0.21
WDDH23-01	5.37	6.95	1.92	8.22	2.09	1.04	1.86	0.31	1.98	0.45	1.37	0.212	1.38	0.221	12.9	0.88	0.13
WDDH23-02	3.94	8.76	1.45	6.38	2.01	1.41	2.96	0.57	3.69	0.85	2.54	0.378	2.83	0.436	22	0.36	0.16
WDDH23-03	8.06	15.6	2.39	11.3	2.83	1.7	3.27	0.56	3.54	0.72	2.17	0.299	1.97	0.307	22.7	0.08	0.14
WDDH23-04	8.3	17.5	2.52	12.1	3.02	1.5	2.78	0.47	2.57	0.54	1.65	0.246	1.83	0.286	18.4	0.11	0.11
WDDH23-06	29.9	85.6	10.9	50.6	14.4	7.86	13.3	2.26	12.2	2.28	5.89	0.858	5.78	0.848	53.1	0.34	0.14
WDDH56-01	4.65	14.8	1.31	5.36	1.66	1.06	1.82	0.31	2.05	0.47	1.54	0.259	1.91	0.292	13	0.13	0.12
WDDH56-02	2.49	10.7	0.68	2.04	0.8	0.567	1.08	0.18	1.28	0.3	0.92	0.162	1.15	0.191	8.5	0.05	< 0.05
WDDH56-05	5.11	16.1	1.32	4.73	1.37	0.897	1.63	0.3	2.02	0.47	1.38	0.235	1.64	0.26	11.9	0.13	< 0.05
WDDH56-06	3.93	14.7	1.2	5.46	1.37	1.23	1.79	0.37	2.55	0.56	1.75	0.337	2.34	0.338	16.2	0.11	0.13
WDDH56-07	1.95	7.3	0.49	2.49	0.9	0.395	0.66	0.12	0.85	0.19	0.6	0.1	0.73	0.112	5.6	0.12	0.08
WDDH56-08	3.55	9.57	0.97	3.16	1.01	0.588	1	0.19	1.25	0.27	0.83	0.129	0.88	0.137	9.7	0.06	< 0.05
WDDH56-14	4.04	7.12	0.83	2.93	0.86	0.383	1.05	0.19	1.26	0.29	0.89	0.134	0.88	0.13	12.8	0.04	< 0.05

Table 3: Whole-rock geochemistry data for REE+Y, U and Th at Wodgina

wt %. Similar to the overlying goethite-rich ore, the anhedral hematite-rich ore displays significant enrichments in Al_2O_3 and Zn compared to the least-altered BIF (Fig. 8C, N), but does not show evidence for Pb enrichment. Other transitional metal and REE concentrations are similar to those of the goethite ore.

Martite-rich ore

Martite-rich ore mostly occurs within the Anson deposit and to a lesser extent in the Dragon deposit. The martite-rich ore type is characterised by similar amounts of Fe_2O_3 and Al_2O_3 compared to that of goethitic and hematitic ore zones, together with moderate LOI (Fig. 8 A, B, C). Similar to the goethite-rich ore, the martite-rich ore displays a positive Pb anomaly (Fig. 8M). The REE concentrations in the Anson martite-rich ore zone are significantly higher compared to nearby goethitic ore, but do not differ compared to goethitic ore from the Dragon deposit. Importantly, the martite-rich ore geochemistry reflects the contribution of accessory goethite (positive Al_2O_3, Pb anomalies) but also displays singular enrichment in several elements such as Ti and to a lesser extent Na (Fig. 8G, L).

VI. Paragenesis of the main alteration minerals in the Anson and Dragon deposits

The Anson and Dragon deposits exhibit a similar paragenetic mineral sequence that includes up to eight alteration stages (Fig. 11).

Least-altered BIF: Anhedral hematite, anhedral magnetite and chert

These minerals define the least altered BIF both in the Anson and Dragon deposits. Iron oxide-rich bands comprise fine-grained (<5 μm) hematite aggregated with minor anhedral magnetite and chert.

Stage 1: Euhedral magnetite

Large euhedral to subhedral magnetite crystals up to 1,000 μm in width occur as disseminated crystals in iron oxide-rich bands and to a lesser extent in chert-rich bands (Fig. 10A, B).

Stage 2: Martite

Solid-state oxidation of stage 1 magnetite to martite initiates along crystallographic planes (Fig. 10B) and progresses until the complete replacement of magnetite (Fig. 10 C).

Stage 3: Quartz

Martitisation of stage 1 magnetite is followed by the emplacement of quartz veins cutting martite crystals (Fig. 10D). This silicification event is also responsible for the partial replacement of martite crystals by quartz (Figs. 10 E and F).

Stage 4: Mn-oxides

Manganese oxides in the Dragon deposit cut and envelop stage 2 martite grains (Fig. 10G).

Stage 5: Anhedral, acicular and botryoidal goethite

This major alteration event is responsible for the large volumes of goethitic ore in the Anson and Dragon deposits. Goethite forms mainly through (i) direct in situ replacement of existing chert and iron oxides (Fig 10I), (ii) veins that cut earlier mineral phases (Fig. 10H) and (iii) as acicular to botryoidal crystals that fill vugs after prior dissolution and leaching of chert (Fig. 10J, L). In the Dragon deposit, stage 5 goethite fills interstitial spaces around primary quartz grains in sandstone-dominated within BIF (Fig 10K).

Stage 6: Anhedral to botryoidal hematite

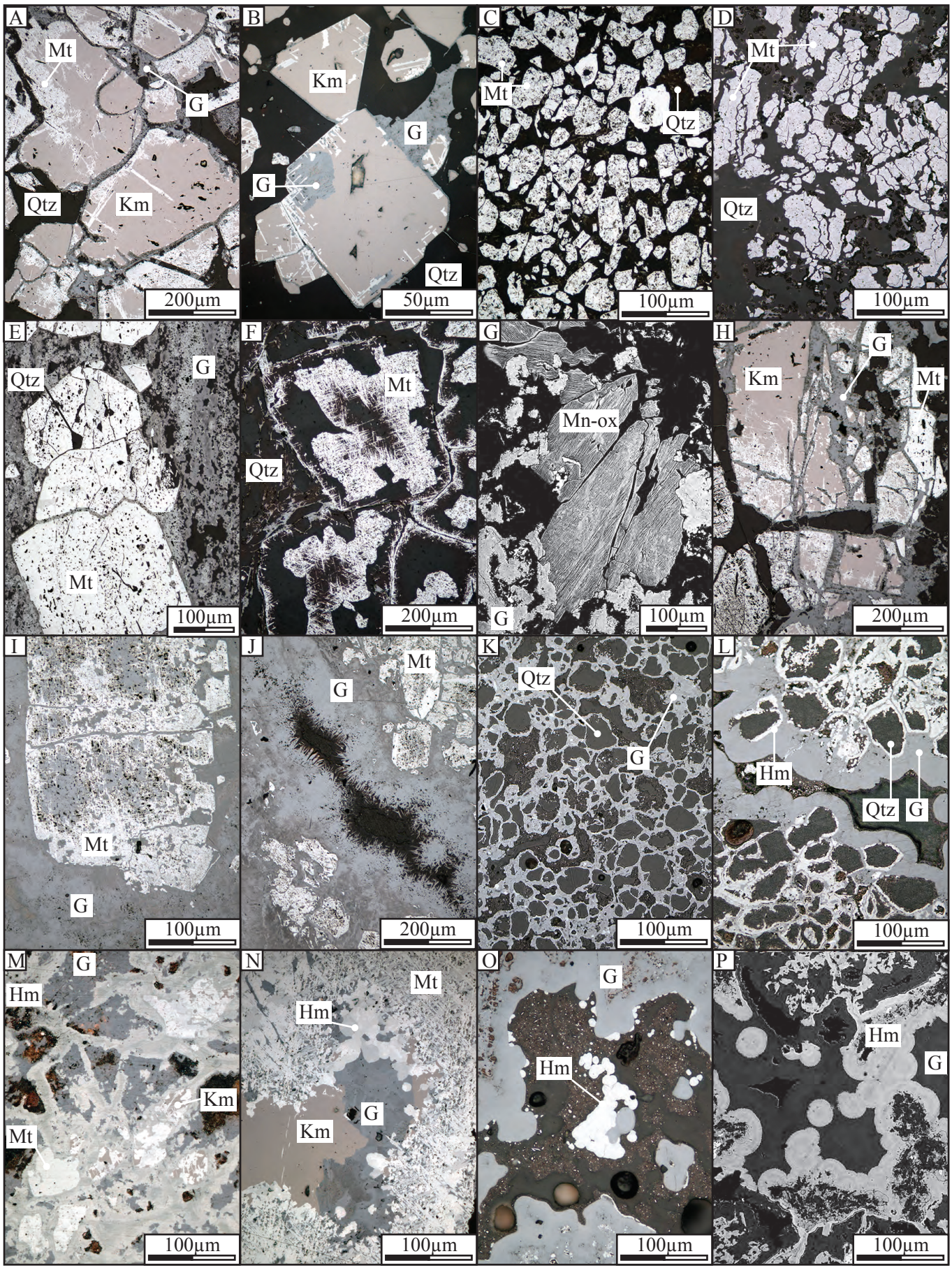

Figure 10: Optic microphotographs of iron oxides and associated minerals at Wodgina. Km = kenomagnetite, Mt = martite, Qtz = quartz, G = goethite, Hm = hematite and Mn-ox = undifferenciated Mn-oxides.

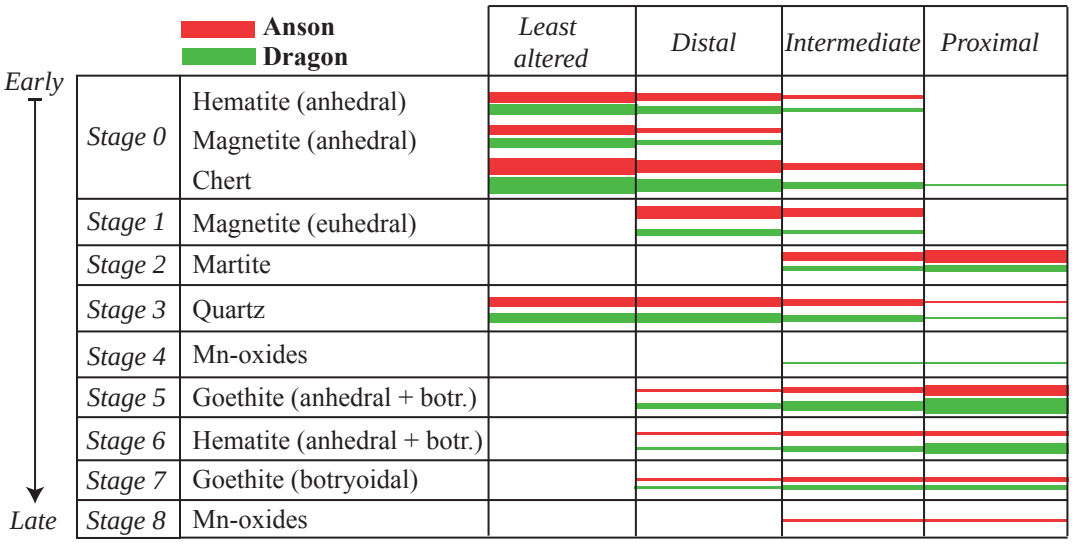

Figure 11: Paragenetic sequence for iron oxides and associated minerals at Wodgina

Stage 6 anhedral to botryoidal hematite occurs in samples from the Dragon deposit (Fig 10L, M, O, P) and to a lesser extent in samples from the Anson deposit (Fig. 10N). Textural observations including (i) the replacement of goethite by hematite along grain boundaries (Fig. 10L) and (ii) the formation of botryoidal hematite overgrowing goethite (Fig 10N, O, P) argue that hematite formed after stage 5 goethite. Nevertheless, other observations, such as the replacement of hematite veins by goethite (Fig 10M), may suggest an opposite interpretation.

Stage 7: Late botryoidal goethite

Stage 7 represents a late event of botryoidal goethite formation mainly observed in the Dragon deposit (Fig 10P). This alteration stage postdates the formation of anhedral to botryoidal hematite and is, therefore, distinguished from stage 5 goethite.

Stage 8: Mn-oxides

A second stage of manganese oxide (psilomelane±pyrolusite) precipitation occurs as veins cutting through martite-goethite mineralisation in the southern section of the Anson deposit. Manganese oxides are associated with the latest stage of alteration recognised in this study and do not appear to be controlled by the main structures.

VII. Mineral trace element geochemistry from LA-ICP-MS analyses

This section documents the chemical composition of (i) stage 1 euhedral magnetite, (ii) stage 2 martite, (iii) stage 5 goethite and (iv) stage 7 goethite. Fine-grained iron oxides from the least altered BIF and stage 6 hematite were not analyzed due to spatial resolution limitations associated with the analytical technique.

Stage 1 magnetite-kenomagnetite

Stage 1 hypogene magnetite displays a Si content ranging from 4,000 to 20,000 ppm. Detected trace elements include Al (200 to 800 ppm), Mg (10 to 20 ppm), Ge (5 to 20 ppm), Ni and Zn (2 to 10 ppm), V and Cr (2 to 4 ppm), Co (0.1 to 0.5 ppm) and W, Pb (0.02 to 0.1 ppm). Most concentrations for REE in stage 1 magnetite are below their respective detection limits (Fig 12).

Stage 2 martite

Compared with Stage 1 magnetite, Stage 2 martite displays an increase in many trace elements including P (30 to 100 ppm), Na (100 to 200 ppm), Mn (20 to 100 ppm), Cr and K (2 to 10 ppm), Cu and As (0.7 to 7 ppm), W (0.2 to 2 ppm), Ba (0.1 to 6 ppm), Pb (0.1 to 2 ppm and U (0.01 to 0.06 ppm). Importantly, V (15 to 80 ppm), Ti (75 to 130 ppm), Ga (4 to 8 ppm) and Sn (1 to 6 ppm) are largely enriched in stage 2 martite compared with all other iron oxide stages (Fig. 13). Si and Al concentrations in stage 2 martite (4,000 to 20,000 and 70 to 400 ppm, respectively) are similar to stage 1 magnetite. PAAS-normalised REE displays a slight increase in the abundance of LREE and flat pattern for HREE, although HREE lie below detection limit for a significant number of analyses.

Stage 5 goethite

Stage 5 goethite displays significantly lower Si (2,000 to 10,000 ppm) and higher Al concentrations (800 to 3,000 ppm) compared to stage 1 magnetite and stage 2 martite. Stage 5 goethite is also characterised by a drastic increase in P (up to 2,000 ppm) and Ca (up to 200 ppm) concentrations. Most transitional metals including Pb, Ni, Co, Zn and As are enriched

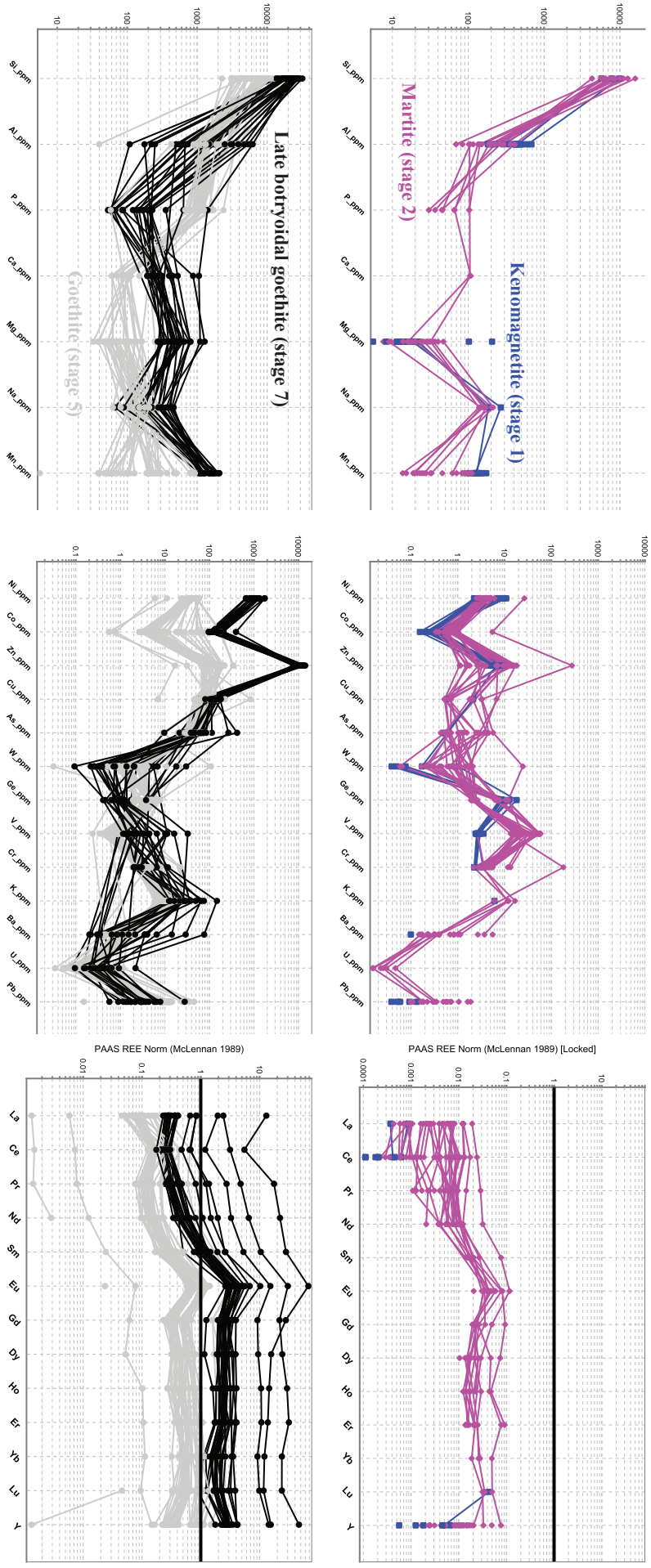

Figure 12: Mineral chemistry data for stage 1 kenomagnetite, stage 2 martite, and stages 5 and 7 goethite at Wodgina.

in stage 5 goethite relative to the stage 1 magnetite and stage 2 martite. In contrast, V, Ti and Ga concentrations (0.2 to 2 ppm) are lower than stage 1 magnetite and stage 2 martite. An increase in individual REE concentrations is observed, together with a positive Ce and Eu anomaly (Figs. 12, 13).

Stage 7 late botryoidal goethite

Compared to stage 5 goethite, stage 7 goethite is characterised by (i) a large range in Al concentrations (100 to 7,000 ppm), (ii) a decrease in P, W and Ge abundance and (iii) an increase in Ca, Mg, Mn, Ni, Co, Zn and V (Fig. 12). Among these, Zn concentrations show the greatest increase (in excess of x100) compared to all other iron oxide stages (Fig. 12, 13). Stage 7 goethite is significantly enriched in all REE compared to stage 5 goethite. Both REE patterns are similar, except the lack of a positive Ce anomaly for stage 7 goethite.

VIII. Constraints on the genetic model for the Wodgina iron ore deposits

The different mineral assemblages documented in the Anson and Dragon deposits reveal a complex mineralisation history resulting from multistage early hypogene alteration and late supergene weathering. Timing and conditions of formation of these mineral assemblages are discussed in the following section based on field and analytical investigations and integration of the geologic evolution of the Pilbara Craton.

Metamorphism and hydrothermal alteration of BIF resulting in $D1_{WD}$ shear zone-hosted, stage 1 hypogene magnetite-rich ore bodies

The formation of euhedral magnetite represents the earliest stage of iron oxide formation recorded at the Anson and Dragon deposits, overprinting primary anhedral hematite and

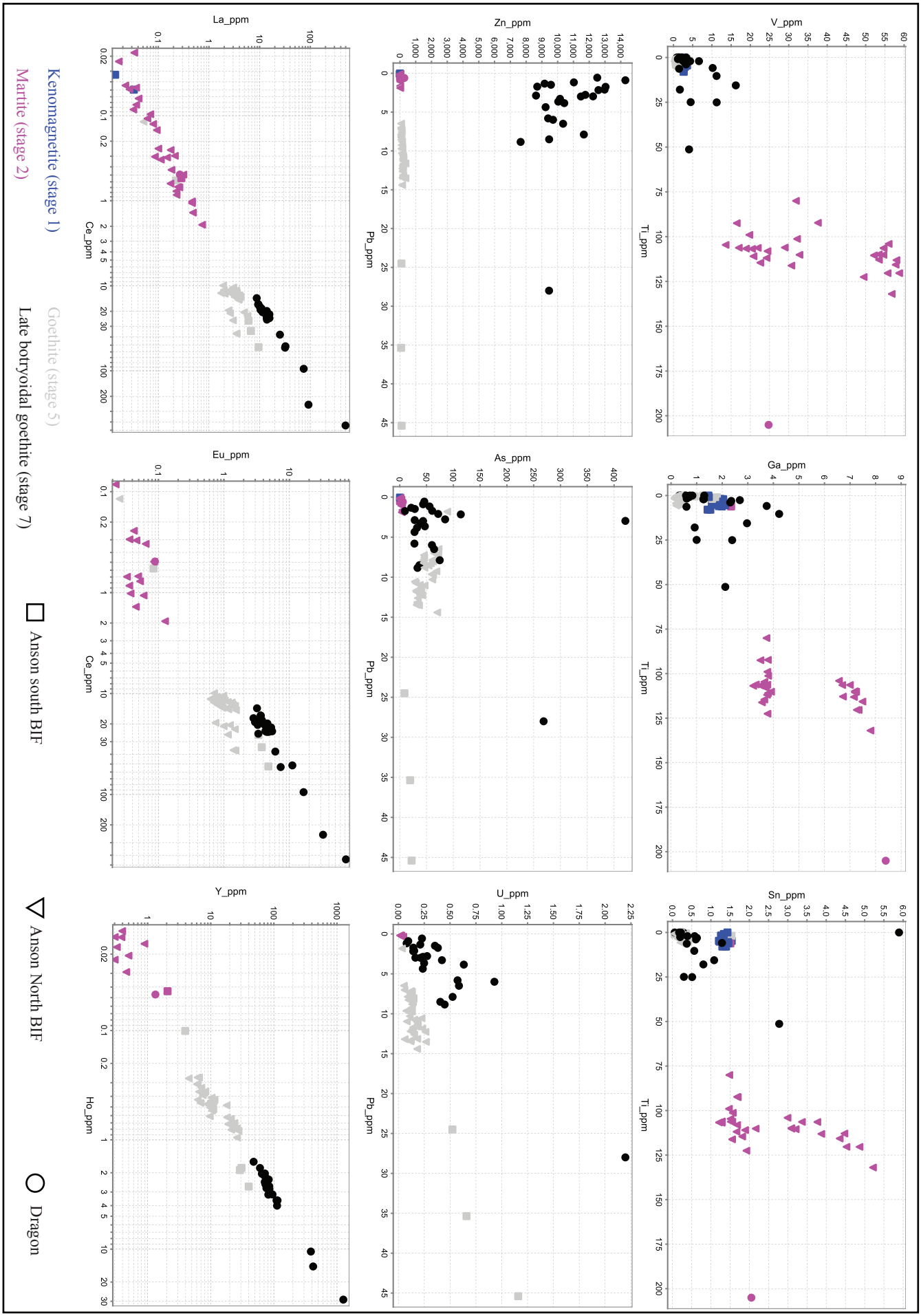

Figure 13: Mineral chemistry data for stage 1 kenomagnetite, stage 2 martite, and stages 5 and 7 goethite at Wodgina.

magnetite within BIF. The localisation of intensely developed stage 1 magnetite alteration in $D1_{WD}$ shear zones in the Anson deposit supports the interpretation that stage 1 magnetite is derived from the circulation of iron-rich fluids within the shear zones and interaction with proximal BIF wall rock. However, the widespread distribution of stage 1 magnetite in BIF away from $D1_{WD}$ shear zones suggests the wide penetration of these fluids into BIF throughout the Wodgina camp, and/or widespread in situ recrystallization of primary iron oxides in undeformed BIF, which takes place during regional metamorphism.

Unweathered Archean BIF typically contains recrystallised, euhedral magnetite and hematite formed during diagenesis and metamorphism (Klein, 2005; Angerer and Hagemann, 2012; Nadoll et al., 2014). Mineral chemistry data for stage 1 magnetite indicates that, with the exception of Al, Fe-substituting cations occur in trace amounts (< 20 ppm). In addition, the ratio Co/Ni does not exceed 0.1. Such characteristics are typical of metamorphic magnetite in BIF (Nadoll et al., 2014) and support a metamorphic origin for stage 1 magnetite. In contrast, hydrothermally altered magnetite in low grade metamorphic hematite–chert BIF from the Carajás Serra Norte deposits, Brazil, is characterized by average Co and Ni concentrations that exceed 500 and 350 ppm, respectively, and Co/Ni ratios greater than 1 (Figueiredo e Silva et al., 2008). The analysed hypogene magnetite from the Serra Norte deposits is interpreted to have been derived from the interaction between the BIF and felsic magma-derived fluids (Figueiredo e Silva et al., 2008).

The evolution of the Pilbara Craton since the deposition of the Cleaverville Formation is marked by several events that could have contributed to the formation of stage 1 euhedral magnetite:

(i) 2950-2940 Ma: The major North Pilbara orogenic event, referred to as the D9 regional deformation event (Hickman and Van Kranendonk, 2008a). D9 orogeny involved greenschist to amphibolite facies metamorphism, as indicated by

metabasalts in the Croydon Group of the Mallina Basin (Van Kranendonk et al., 2002).

(ii) 2930-2900 Ma: The emplacement of late granites of the Sisters Suite and layered mafic-ultramafic intrusions of the Radley Suite, essentially confined to the western half of the Northern Pilbara Craton.

(iii) 2930-2900 Ma: The Mosquito Creek orogeny, restricted to the SE section of the northern Pilbara (regional D12).

(iv) 2900–2803 Ma: Granitic intrusion of the Cutinduna and Split Rock Supersuites and associated with pegmatite-hosted, tin-tantalum mineralisation (Huston et al., 2002).

(v) 2770-2760 Ma: The Fortescue Rifting Event, with likely thermal effects of thick plateau basalt deposition. Many older faults, such as those formed during D9, were reactivated by the regional crustal extension of this event (Thorne and Trendall, 2001).

(vi) 2215-2145 Ma: Regional prehnite-pumpellyite metamorphism with associated temperatures not exceeding 350°C (Smith et al., 1982; Rasmussen et al., 2005, White et al., 2014), followed by widespread metasomatism of the Fortescue basalts (White et al., 2014). Rasmussen et al. (2005) propose that this event was probably driven by the northward-advancing Ophthalmian fold-and-thrust belt that developed during protracted collision with the Pilbara Craton, and argue that the widespread geographic and stratigraphic distribution of ca. 2.2 Ga phosphates suggests that fluid flow was intense and pervasive.

The formation of stage 1 magnetite is most likely related either to the 2950-2940 Ma North Pilbara Orogeny or the 2215-2145 Ma regional metamorphic to metasomatic event, as other

documented events are spatially confined to areas distal to the Wodgina iron camp. Because the circulation of mineralising fluids along fault zones is most efficient when these structures are active, precipitation of euhedral magnetite may have taken place during the North Pilbara Orogeny, along developing D9 fault zones. Alternatively, formation of stage 1 magnetite may be related to the 2215-2145 Ma regional metamorphic to metasomatic event, via the circulation of reduced fluids through reactivated D9 fault zones. In the absence of absolute age constraints for stage 1 alteration event, both the 2950-2940 Ma and 2215-2145 Ma events could be responsible for the formation of stage 1 euhedral magnetite.

Martitisation

The martitisation of stage 1 magnetite to stage 2 martite is characterised by a significant increase in Ti, V, Ga and Sn (Fig. 13). Titanium displays the greatest enrichment (from <1 ppm in stage 1 magnetite to < 200 ppm in stage 2 martite). Martite documented in various iron ore deposits in association with microplaty hematite or goethite (Angerer and Hagemann, 2010; Angerer et al., 2012; Duuring and Hagemann, 2010, 2012) are often interpreted to be the result of oxidising alteration caused by descending ancient meteoric water interacting with BIF. A similar interpretation is well suited for the formation of martite at Corunna Downs and would involve early (Precambrian) supergene fluids. Increase in Ti and V concentrations associated with the martitisation process suggests an interaction between Ti and V-rich fluids and the BIF. Such fluids may have been sourced, or circulated through titanium and vanadium-rich, mafic tholeiitic intrusions, such as the ca. 2980 Ma Maitland River gabbro-anorthosite suite exposed in the Western Pilbara (Huston et al., 2002). However, to date, no significant occurrences of Maitland River intrusive rocks are known to occur proximal (<100 km) to Wodgina.

Silicification

Silicification (stage 3 quartz) of the BIF units took place as quartz veins and as in situ replacement of stage 1 magnetite and stage 2 martite. Silicification processes took place in the Pilbara Craton from the early Archean to the Paleoproterozoic. The absolute timing of silicification at Wodgina is poorly constrained. It is nevertheless assumed that the silicification observed in the Cleaverville BIF at Wodgina is at least 1.8 Ga old, as tectonic and hydrothermal quiescence since the Mesoarchean likely preclude the development of any large silicification event (Huston et al., 2002). This observation provides an important constraint for the timing of stage 2 martitisation in that it excludes the possibility of late (Phanerozoic) supergene martitisation of stage 1 magnetite.

Multistage supergene alteration

Late-stage alteration of the Cleaverville BIF at Wodgina includes (i) an early, local stage of manganese oxide precipitation (stage 4), (ii) intense and pervasive goethitisation of BIF and clastic sedimentary units (stage 5), (iii) formation of anhedral to botryoidal hematite (stage 6), (iv) a later stage of goethitisation that mainly forms colloform to botryoidal textures in open spaces (stage 7) and (v) a final stage of manganese oxide precipitation (stage 8). We hereafter focus our discussion on alteration stages 5 to 7, which represent the dominant supergene mineralisation events involved in the formation of high-grade iron ore at Wodgina. Stage 5 goethite is characterized by significant amounts of phosphorus (ca. 0.1 %), that are higher than in stage 1 magnetite and stage 2 martite, as well as in late goethite (stage 7). It is generally assumed that phosphorus concentration in goethite depends on microtextural characteristics (Dukino et al., 2013 and references therein). The highest phosphorus levels are consistently associated either with goethite composed of ultrafine crystallites (i.e. anhedral) or with late-formed colloform goethite in cracks and pore networks. In contrast, dehydration or recrystallization of goethite typically results in expulsion of the contained phosphorus. The predominance of anhedral goethite over well-crystallised goethite may explain the higher

content in phosphorus observed in stage 5 goethite. Other elements do not show significant increase in concentrations compared to earlier iron oxides (stage 1 magnetite and stage 2 martite), suggesting that the chemisorption of deleterious elements was limited during the formation of stage 5 goethite. This likely indicates a high fluid/rock ratio during stage 5 alteration, which suggests that this early stage of supergene alteration involved high water drainage within the pedogenetic profile. High drainage weathering usually occurs in tropical to subtropical environments where rainfall exceeds 2,000 mm/yr (Retallack et al., 2010). This is at odds with present climatic conditions over the Pilbara Craton (semi-arid to desert conditions with rainfall not exceeding 500 mm/yr; Anand, 2006) but is compatible with Late Cretaceous to mid Eocene tropical conditions (70 to 50 Ma). It is therefore suggested that the stage 5 goethitisation that represents the dominant alteration stage at Wodgina occurred during this period.

Stage 6 anhedral to botryoidal hematite occurs as veins, desiccation cracks and crystal overgrowth after stage 5 goethite. Due to analytical limitations, no reliable mineral chemistry data for stage 6 hematite are available in this study. However, textural observations suggest that stage 6 hematite formed through the dehydration of stage 5 goethite, potentially related to an important change from a well-drained to a poorly drained weathering system. Stage 7 goethite also displays significant chemical changes compared to stage 5 goethite, including a major increase in Zn from less than 100 ppm in stage 5 goethite to over 10,000 ppm in stage 7 goethite. Such anomalously high Zn concentrations in stage 7 goethite most likely reflect high Zn sorption affinity for goethite (Grafe and Sparks, 2005). It is well established that the presence of dissolved sulphate in goethite-precipitating fluids drastically increases the capability of goethite to incorporate zinc into its lattice during crystal growth (Rose and Bianchi-Mosquera, 1993). Dissolution of pedogenic evaporitic minerals is a likely source for high sulphate content in weathering fluids under strongly seasonal, semi-arid climatic

conditions such as observed in the Pilbara region since the mid Eocene. In this context, the formation of stage 6 hematite and stage 7 goethite after stage 5 goethite might reflect environmental changes from tropical to semi-arid conditions over the Pilbara Craton ca. 50 my ago. Alternatively, it cannot be excluded that extremely Zn-enriched fluids were involved in the precipitation of stage 7 goethite. However, Zn-rich rocks that could provide a source of Zn for supergene fluids are not known in the Wodgina area.

IX. Implications for exploration

First-order (critical) controls on the formation of high-grade iron ore deposits in the Wodgina camp include the presence of (i) thick iron-rich primary BIF from the Cleaverville Formation, (ii) structurally fold-thickened BIF such as the tight hinge zones of $F1_{WD}$ (regional D8) and $F2_{WD}$ (regional D9), (iii) areas of high secondary permeability in BIF such as the sheared limbs of folds, (iv) intensely developed supergene alteration and (v) the near-surface exposure of the high-grade iron ore bodies hosted by BIF. Second-order (constituent) controls are those that are locally present in the Wodgina camp, but are not critical for the formation of mineable high-grade ore deposits. These second-order controls include the occurrence of (i) $D1_{WD}$ event, shear-zone-hosted, stage 1 hypogene magnetite-rich ore zones in BIF and (ii) near-surface exposures of tight, synformal fold hinges defined by BIF enclosed by shale-siltstone layers, with the latter acting as an acquitard that concentrates supergene fluids within the BIF synformal fold hinge.

The least-altered BIF from the Cleaverville Formation exposed throughout the Wodgina iron camp is prospective since it contains more than 35 wt.% Fe_2O_3 and thus represents an elevated starting position for subsequent iron enrichment in the rock via interaction with hydrothermal fluids. The primary thickness of major BIF macrobands has an average

thickness of up to 50 m throughout the camp, but increases to up to 100 m thick in areas of structural complexity arising from multiple superimposed fold generations. Proof of the importance of folds in the Wodgina camp is in the concentration of the known iron ore deposits near the hinge of the camp-scale, steeply N-plunging $F2_{WD}$ fold. Within this hinge, individual deposits (such as the Dragon and Constellation) are mainly centred on tight, 50 to 100 m-wavelength, F_3 and F_6 parasitic fold hinges, which increase the primary thickness of the Cleaverville Formation BIF by a factor of about two times. The fold interference patterns resulting from the $F1_{WD}$ and $F2_{WD}$ folding events explain the present distribution, strike and plunge of high-grade iron ore bodies, with ore zones in the Dragon and Constellation deposits consistently plunging in the direction of W-plunging $F2_{WD}$ folds. The predictive exploration implications of fold-interference patterns throughout the camp is that the along-strike continuity of compositionally fertile BIF may be traced towards prospective hinge areas of parasitic $F1_{WD}$ and $F2_{WD}$ folds. The limbs of folds are likely to be traced towards consistently stepping fold hinges with pod-like geometry and predictable plunge direction of fold hinge-controlled high-grade ore bodies. An example of these geometries is displayed in the Avro deposit, where the pod-like geometries of high-grade iron ore bodies lead towards areas of heterogeneous ore grades and difficulties during open pit-style bulk mining. Awareness of these ore body controls is important at a range of exploration and mining scales, from grass-roots exploration through the thoughtful positioning of exploration drill holes through to mining with the realistic modelling of geological features such as iron grade and mineral contaminants. Exposures of BIF present in the southern area of the Wodgina camp (Fig. 2) display similar features to the regional $F2_{WD}$ fold hinge that hosts the known iron ore deposits. It is possible that this southern BIF exposure is the fold repetition of the compositionally fertile BIF featured in the Wodgina iron camp. This area requires further

inspection in light of the first-order importance of the BIF fertility and likelihood of fold hinges.

Mapping of the Wodgina iron ore deposits highlighted the presence of shear zones oriented parallel to the folded limbs of $F1_{WD}$ and $F2_{WD}$ folds. It is likely that these shear zones were formed due to flexural slip during $F2_{WD}$ folding during the $D2_{WD}$ event. These shear zones locally host <30 m-thick zones of stage 1 hypogene magnetite that result in the moderate intensity upgrade of iron in the BIF. Subsequent deformation in the form of $F2_{WD}$ folds resulted in the local thickening of these ore zones, but more importantly, the reactivation of these shear zones by multiple events enhanced and broadened the permeability of these damage zones in BIF. These broad damage zones near fold hinges are the optimum areas for the circulation of later supergene fluids through BIF resulting in the creation of extensive supergene goethite ± hematite-rich ore bodies.

Considering that the shear zone-hosted, magnetite-rich ore zones identified in the Anson pits are narrow (<30 m wide) ore zones of moderate iron grades and relatively high contaminants (e.g. SiO_2), they are unlikely to represent exploration targets for stand-alone high-value ore deposits. Rather, they are important indicators for the presence of early forming deformation zones affecting BIF, which control subsequent supergene alteration. These shear zone-hosted ore bodies have the added potential to control deeper extensions to near surface supergene ore bodies owing to their steep dips and likely presence beneath the weathering front. Targeting stage 1 magnetite alteration using trace element compositions of these minerals is shown not to be possible based on the high iron purity of magnetite with commonly below-detection concentrations of other elements. However, the distinctive chemical signature of its oxidised equivalent (i.e. stage 2 martite) demonstrates significant enrichments in Ti, V, Ga and Sn. Among these, V and Ga might represent the most reliable chemical vectors, as any increase in Ti or Sn could rather represent higher clay content or an interaction with Sn-rich

pegmatite-derived fluids, respectively. These mineral chemistry signatures are potentially translated to bulk rock geochemical signatures provided that the rock comprises mostly stage 2 martite. However, considering the widespread presence of supergene goethite in near-surface exposures of BIF, these pathfinder elements are useful in specific geological conditions and thus have local use as vectors to shear zone-hosted, magnetite (martite)-rich ore zones.

Supergene alteration is the dominant alteration style in all deposits in the Wodgina camp. It is responsible for generating large volumes of high-quality (iron grade and contaminant level) iron ore. Supergene enrichment in the fold-thickened BIF took place as a multi-stage mineralising event involving the interaction between near-surface derived, oxidised fluids and BIF. The earliest recognised stage of supergene alteration (i.e. stage 5 goethite) potentially developed under tropical conditions during the late Cretaceous to mid Eocene and represents the most economically important mineralisation stage at Wodgina in terms of its extensive distribution and high iron contents. Mineral chemical analyses indicate only the presence of phosphorus as a robust pathfinder element for stage 5 goethite, due to the relatively low amount of other contaminant elements. Stage 7 goethite from the Dragon and Anson deposits displays a greater suite of potential indicator elements, with Zn displaying the greatest enrichment relative to other analysed iron oxides (i.e. stage 1 magnetite, stage 2 martite and stage 5 goethite). The demonstrated enrichment of Zn in bulk rock geochemical analysis of high-grade goethite-rich BIF can be attributed to the presence of stage 7 goethite in these rocks.

The likely depth restriction of high-value supergene BIF-hosted ore bodies to shallow areas of the Wodgina camp (within 80 m of the present erosional surface) has implications for exploration in the planning of drill holes and interpretation of geophysical data sets. The use of relatively shallow RC drill holes (30 to 80 m depth) have the potential to test prospective

(supergene-altered) BIF fold hinges that are identified from outcrop and geophysical data. The likelihood of blind hypogene magnetite-rich ore deposits of economic thickness and iron grade is considered to be low based on mapping in the known deposits. Whereas future exploration efforts should be centred on the accurate mapping of BIF occurrence, fold hinges, and intensity and dimensions of damage zones in BIF throughout the Wodgina project area, including the limbs of the $F2_{WD}$ folds in the Wodgina iron camp and the southern BIF exposures in the project area. Upon completion of mapping available outcrop in the project area, the next focus is the predictive exploration of blind supergene ore deposits. This task will involve the identification of the same geological features identified for surface mapping (BIF, folds, deformation zones), but will rely upon interpreting geophysical data beneath areas of transported cover and projecting structural observations to these areas.

This study on the Wodgina iron camp attempted to assess the role of nearby Ta-rich pegmatite intrusions on iron mineralisation. The hypothesis that felsic magmatic-derived fluids interacted with nearby BIF to create extensive hypogene iron ore bodies was tested by mapping the deposits and by chemical analysis of their representative iron ore samples and contained minerals. Mapping of the iron deposits indicated the pegmatite dykes or sills were absent from the iron ore pits and available drill holes. Furthermore, the geochemical analyses for stage 1 magnetite and corresponding bulk rock ore samples did not suggest any direct chemical contribution from felsic magma-derived fluids in their formation. Stage 2 martite displayed enrichment in Sn, but the enrichment is not diagnostic of genesis from magmatic-related fluids, but could have been incorporated from fluids that interacted with Sn-bearing rocks during the process of martitisation in BIF. Analysed supergene goethite (stage 5 and 7) did not display significant enrichment of elements associated with felsic rocks. Thus, pegmatite intrusions had a negligible control on the formation of the known hypogene and

supergene iron ore zones in the Wodgina camp. Any potential influence on BIF countryrocks is likely to be restricted to within 500 m of the exposed pegmatite intrusions.

X. Conclusions

The Anson and Dragon deposits at Wodgina principally consist of goethite-martite rich ore bodies hosted by two to three BIF macrobands of the 3020 Ma Cleaverville Formation in the Wodgina greenstone belt of the Pilbara Craton, Western Australia. Two major deformation events ($D1_{WD}$ and $D2_{WD}$, corresponding to the regional D8 and D9 events, respectively) affect the Cleaverville BIF. $D1_{WD}$ deformation event involves tight, W- to NW-shallowly-plunging $F1_{WD}$ folds associated with several high strain zones. $D2_{WD}$ deformation event is expressed as upright tight folds with steep NNE-plunging and is responsible for the regional syncline of the Wodgina greenstone belt. Unweathered BIF records an early stage of euhedral magnetite precipitation, likely related to regional low-grade metamorphism and circulation of metamorphic-driven reduced fluids at ca 2215-2165 Ma. Although stage 1 alteration is widespread and pervasive, it is largely concentrated along or proximal to high strain $D1_{WD}$ shear zones, which represent focused pathways for alteration fluids. Metamorphic magnetite overprint locally results in an initial upgrade in iron in the BIF from ca 30 to 40-45 wt% Fe and is associated with a similar decrease in SiO_2 through leaching of chert. Subsequent martitisation (stage 2) of stage 1 magnetite is interpreted as an early (Precambrian) process caused by descending ancient meteoric waters interacting with BIF. Stage 2 martitisation is associated with an increase in Ti, Sn, V and Ga concentrations, the two latter elements being potential pathfinders for martite-rich zones. A recent, supergene alteration partly replaces martite-rich BIF, forming the large volumes of goethite that comprise the main portion of high-grade ore zones in both deposits. The recent supergene sequence is dominantly

represented by stage 5 goethite, characterized by limited contamination by deleterious elements. Further development of the supergene system involved the formation of botryoidal to anhedral hematite, and late botryoidal goethite. Together with textural observations, important differences in the trace element composition of goethite, including the strong increase in Zn within stage 7 goethite, are thought to reflect environmental changes in the Pilbara from tropical to semi-arid conditions since the late Cretaceous. The ubiquitous spatial distribution of stage 5 goethite indicates that it represents the dominant mineralisation stage responsible for the formation of volumetrically important ore bodies at Corunna Downs. Nevertheless, it is proposed that stage 7 goethitisation is also of significant importance in the formation of large iron ore bodies at Wodgina. This late mineralisation event may be targeted using Zn as a relevant element pathfinder.

Chapter 3: High-grade, martite-rich Fe mineralisation in Mesoarchean BIF at the Abydos mine, Western Australia

I. Introduction

Exploration for banded iron formation (BIF)-hosted Fe ore in Western Australia has historically targeted Palaeoproterozoic, Superior-type BIFs of the Hamersley Province where a number of world-class, martite – microplaty hematite ± magnetite deposits have been discovered and mined for more than 50 years (e.g. Mount Whaleback, Mount Tom Price, Li et al., 1993; Barley et al., 1999; Hagemann et al., 1999; Morris, 1985; Muller et al., 2005; Powell et al., 1999; Thorne et al., 2004, 2009; Webb et al., 2003). However, due to the advanced maturity of exploration and the increasing difficulty in discovering new deposits in the Hamersley Basin, the past decade has seen the emergence of Archaean granite-greenstone terranes, such as those exposed in the Yilgarn and North Pilbara Cratons, as new fields of exploration for BIF-hosted iron ore. The dominant controls on the formation of iron ore in the Yilgarn Craton have been documented through a number of recent studies, highlighting the importance of hypogene magnetite–(martite–microplaty hematite) mineralisation through

sodic metasomatism (Angerer and Hagemann, 2010; Angerer et al., 2012; Duuring and Hagemann, 2010, 2012a, 2012b). In contrast, BIF-hosted Fe ore deposits in the North Pilbara have received minor scientific attention (Kerr et al., 1994) despite the occurrence of historical mines (e.g. Yarrie mine). Currently, several deposits in the North Pilbara are mined by Atlas Iron Ltd. (e.g. Wodgina, Pardoo, Mt Webber and Abydos mines), with an additional number of recently defined resources (e.g. McPhee Creek, Corunna Downs).

The Abydos iron camp, located in the East Strelley greenstone belt, hosts several high-grade (> 50 wt % Fe) ore bodies that extend for about 700-1,000 m in strike length and 200-300 m width, and from surface to more than 100 m in depth. The Fe camp has a total resource of more than 35 Mt Fe (average grade and cut-off values are 57.3 and 50.0 wt % Fe, respectively; Atlas Iron Ltd. ASX release August 2014) with minor contamination by accessory elements (average SiO_2 = 3.4 wt%, P= 0.08 wt%, Al_2O_3 = 1.6 wt%). The Abydos iron camp, therefore, represents an economically attractive iron ore district and an important case study site for examining geological processes involved in the formation of high-quality iron ore in the Pilbara Craton.

In this Chapter, we present the main outcomes of field and analytical investigations on iron ore-forming processes at Abydos. A multidisciplinary approach was applied, which included geological mapping and core logging, combined with transmitted and reflective microscopy, bulk geochemical and mineral microanalysis. Documented observations and data were integrated to build a genetic model for mineralisation and develop specific tools for exploration at camp scale and elsewhere in the Pilbara.

II. Regional Geology

The Pilbara Craton, exposed over an area of 530 x 230 km in the north-western part of Western Australia (Fig. 1), comprises five terranes: the 3530–3170 Ma East Pilbara Terrane (EPT), representing the ancient nucleus of the craton; the 3180 Ma Kurrana Terrane (KT) and the 3270–3110 Ma West Pilbara Superterrane (WPST), which is a collage of three distinct terranes including the 3270 Ma Karratha Terrane, the 3200 Ma Regal Terrane, and the 3130–3110 Ma Sholl Terrane. These terranes have unique lithostratigraphy, granitic supersuites, structural map patterns, geochemistry and tectonic histories (Van Kranendonk et al., 2002, 2007; Hickman, 2004, 2012). They consist of four principal elements: (i) volcano-sedimentary rocks distributed in a number of early to Mesoarchaean (3530-3050 Ma) greenstone belts, (ii) granitic rocks of similar ages, forming either large, polyphase complexes or single intrusions, (iii) late basins (3050–2930 Ma) of clastic sedimentary rocks, and (iv) post-orogenic granites and ultramafic intrusions (2890–2830 Ma) (Hickman and Van Kranendonk, 2012). All of these rocks are unconformably overlain by volcano-sedimentary rocks of the >2775 Ma Hamersley Basin (Arndt et al., 1991; Trendall et al., 2004), and intruded by dolerite dykes. The regional deformation history of the Pilbara Craton is summarised by Hickman and Van Kranendonk (2008a) and includes up to 12 (D1 to D12) deformation events recorded between 3490 and 2890 Ma. In this scheme, the East Pilbara Terrane and the West Pilbara Superterrane display distinct deformation histories prior to the accretion of these terranes at ca. 3070 Ma. Four early deformation events (D1 to D4, ranging from 3490 to 3240 Ma) are associated with progressive doming of granitic intrusions and creation of synvolcanic structures in the East Pilbara, whereas only one deformation event, dated at ca. 3160 Ma, is recorded in the West Pilbara Superterrane. The East Pilbara Terrane collided with the West Pilbara Superterrane during the Prinsep Orogeny event (D5, ca. 3070 Ma). Subsequently, both terranes share a common deformation history characterised by

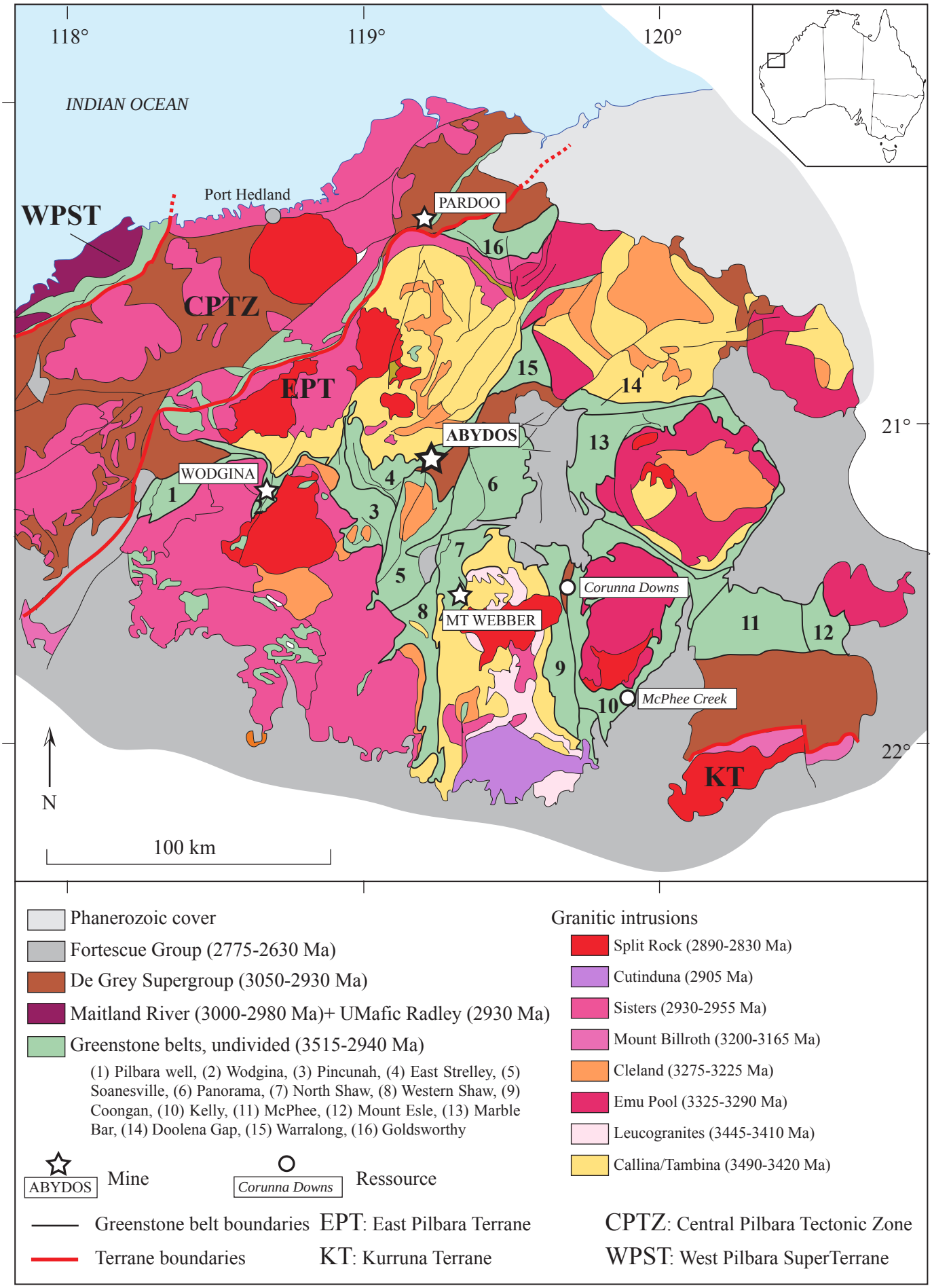

Figure 1: Simplified geology map of the North Pilbara craton including the location of the Abydos iron camp and active iron ore mines across the North Pilbara. *Modified after Hickman, 2012.*

deformation events D6 to D12, taking place from 3020 to 2890 Ga and including a major transpressional event at ca. 2950-2940 Ma (North Pilbara orogeny, D9). Several deformation events of moderate intensity occurred during the deposition of the 2775-2630 Ma Fortescue Group.

Similarly to the Yilgarn Craton, the North Pilbara Fe deposits are mostly hosted by Mesoarchaean BIF units within, or unconformably overlying, greenstone belt volcano-sedimentary sequences. In the North Pilbara, these BIF occurrences are hosted by discrete formations, specifically the 3.23 Ga Pincunah banded-iron member of the Kangaroo Caves Formation, (ii) the 3.19 Paddy Market Formation and (iii) the 3.02 Ga Cleaverville Formation. The Kangaroo Caves and Paddy Market Formations were deposited prior to the accretion of the different terranes during the Prinsep orogeny and are, therefore, restricted to the East Pilbara Terrane (Pincunah BIF: North Shaw and Pincunah greenstone belts; Paddy Market BIF: North Shaw and Soanesville greenstone belts). Deep hydrothermal settings are inferred for the deposition of the Pincunah BIF, whereas the Paddy Market Formation was deposited under mid- to-outer-fan and basin-plain settings as part of the Soanesville sedimentary basin (Hickman, 2012). In contrast, the De Grey Superbasin formed after 3.02 Ga through crustal relaxation and extension after collision between the granite–greenstone terranes and is exposed in most parts of the North Pilbara Craton. It usually includes a basal conglomerate and sandstone overlain by a ~ 1 km-thick unit of BIF, chert, and black shale of the Cleaverville Formation.

Despite intensive field mapping campaigns performed by government geological surveys during the last few decades, the identification of some BIF exposures in the North Pilbara remains problematic due to uncertainties in depositional ages and correlations across the different greenstone belts. Recently, survey mapping programs led by A. Hickman (Van Kranendonk et al., 2006, 2007; Hickman, 2012) resulted in the revision of the stratigraphy

and lithofacies subdivisions within the Pilbara Craton. This revision includes the volcano-sedimentary sequence at Abydos based on recent dating and correlations between greenstone belts; BIF units formerly assigned to the Paddy Market Formation (ca. 3.19 Ga) are reassigned to the 3.02 Ga Cleaverville Formation (Hickman, 2012).

III. Methodology

Mapping and sampling strategy

Field investigations were conducted at the Trigg and the Mettams deposits within the Abydos iron camps (Fig. 2) in July 2014. At that time, the Trigg deposit was being mined as an open pit with a maximum depth of 70 m below the present topographic surface. Production at the nearby Mettams deposit had not commenced and field observations mostly relied on surface exposures. Pit wall (Trigg) and surface (Mettams) lithologic and structural mapping were conducted at 1:2,000 scale (Fig. 4). Field observations were digitised using the ArcGIS program. In addition, three diamond drill holes intersecting the Trigg and Mettams deposits were logged in detail to examine variations in rock types, alteration styles and alteration intensity. Drill holes were chosen based on their spatial distribution (intersecting distal, intermediate and proximal positions relative to high-grade Fe mineralisation) and on their depth of penetration beneath the near-surface weathering profile. The maximum vertical extent of these logged holes is 120 m, whereas the base of intense weathering at Abydos is about 60-80 m, but locally extends to considerably greater depths (i.e. ~over 100 m) along lithological contacts or steeply dipping fault zones. Structural orientations are given as dip angle/strike or plunge/trend orientations, with reference to magnetic north. Location coordinates are given using the Geocentric Datum of Australia 1994 (GDA94), MCA Zone 50, geographic coordinate system. Geochemical data extracted from the Atlas Iron Ltd. drill

hole database were interpolated using the Leapfrog Geo and ArcGIS programs to constrain the distribution of chemical gradation at depth. Company geochemical data were also used to examine the frequency distribution of grade within individual ore bodies. Considering the consistency of individual sample intervals (2 m length) and the regular drill spacing (20 m after infill program) throughout the exploration and mining areas, the frequency distribution of grade within mineralised intervals (Fe > 50 wt.%) provides a good representation of the actual frequency distribution of grade within an ore body. Spatial modelling of the first vertical derivative of the local magnetic field from airborne and downhole magnetic data was conducted by consultant Phil Hawk from Hawk Consultancy company using the software Mag3D (Li and Oldenburg, 1996, 2000) with a cell size of 25 m.

The distinction between the main least-altered rock types (BIF, cherty BIF, chert and terrigeneous units) in field geological maps and cross sections is based on direct observation of these rocks in the field, supported by petrography and geochemistry. Banded iron formation contains more than 35 vol% iron-oxide rich bands (i.e. >25 wt % Fe equivalent in drill holes). Chert comprises less than 15 vol% iron-oxide rich bands (i.e. <10 wt % Fe), whereas cherty BIF displays an intermediate composition between chert and BIF (i.e. 15 to 35 vol% iron-oxide rich bands and 10 to 25 wt% Fe). Mapped terrigeneous sedimentary rocks (e.g. shale, siltstone) display a high Al content (up to 20 wt % Al_2O_3).

Analytical strategy

Sixty-one hand specimens have been collected from surface exposures and diamond drill core from the Trigg and Mettams deposits (Fig. 4). Sampling was conducted from distal to proximal areas relative to the known deposits for the purpose of identifying changes in mineralisation styles and intensity. Twenty-five polished thin sections were prepared from collected samples and examined using reflected/transmitted light and scanning electron

microscopy. Fifteen hand specimens were crushed using a mild steel vibrating disc pulveriser (with potential contamination of Fe up to 0.2 %) at Actlabs, Canada, and pulps were analysed for whole-rock major and trace element geochemistry. Major element oxides were analysed using XRF with Li borate fusion. Trace elements were analysed by ICP-MS with Li borate fusion followed by nitric acid digestion. The loss on ignition (LOI) component was determined by drying sample powders overnight at 110 °C, ignition at 1,100 °C for 25 min and subsequent measurement of the weight loss. The FeO, C-S contents of the powdered samples were determined using titration and infrared methods, respectively. The accuracy of major oxides and trace elements for the international geochemical BIF standard FeR-3 from Temagami, Canada (Bau and Alexander, 2009) lies within typical uncertainty of the XRF (0.05 %) and ICP-MS (5 %) data, respectively. The precision (2σ standard deviation) of the major oxide elements on five laboratory replicates was within 0.10 wt%. In situ trace element chemical analysis was conducted on four thin sections by LA-ICP-MS at Curtin University using the GSD international standard for calibration (Potts et al., 1992). Ablation time and spot sizes were 45 seconds and 75 to 90 microns, respectively. Data processing was conducted using the Sills program (Murray, 2008).

IV. Geology of the Trigg and Mettams deposits, Abydos iron camp

East Strelley greenstone belt geology

The Abydos iron camp is located about 150 km south-east of Port Hedland and lies within the East Strelley greenstone belt of the East Pilbara Terrane. The greenstone belt is wedged between the Carlindi Granitoid Complex and the Strelley Granite (Fig. 1) and comprises an Archaean sequence of (i) mafic-dominated rocks from the Warrawoona group overlain by (ii) sedimentary units of the 3.02 Ga BIF-dominated Cleaverville Formation and the 2.95 Ga

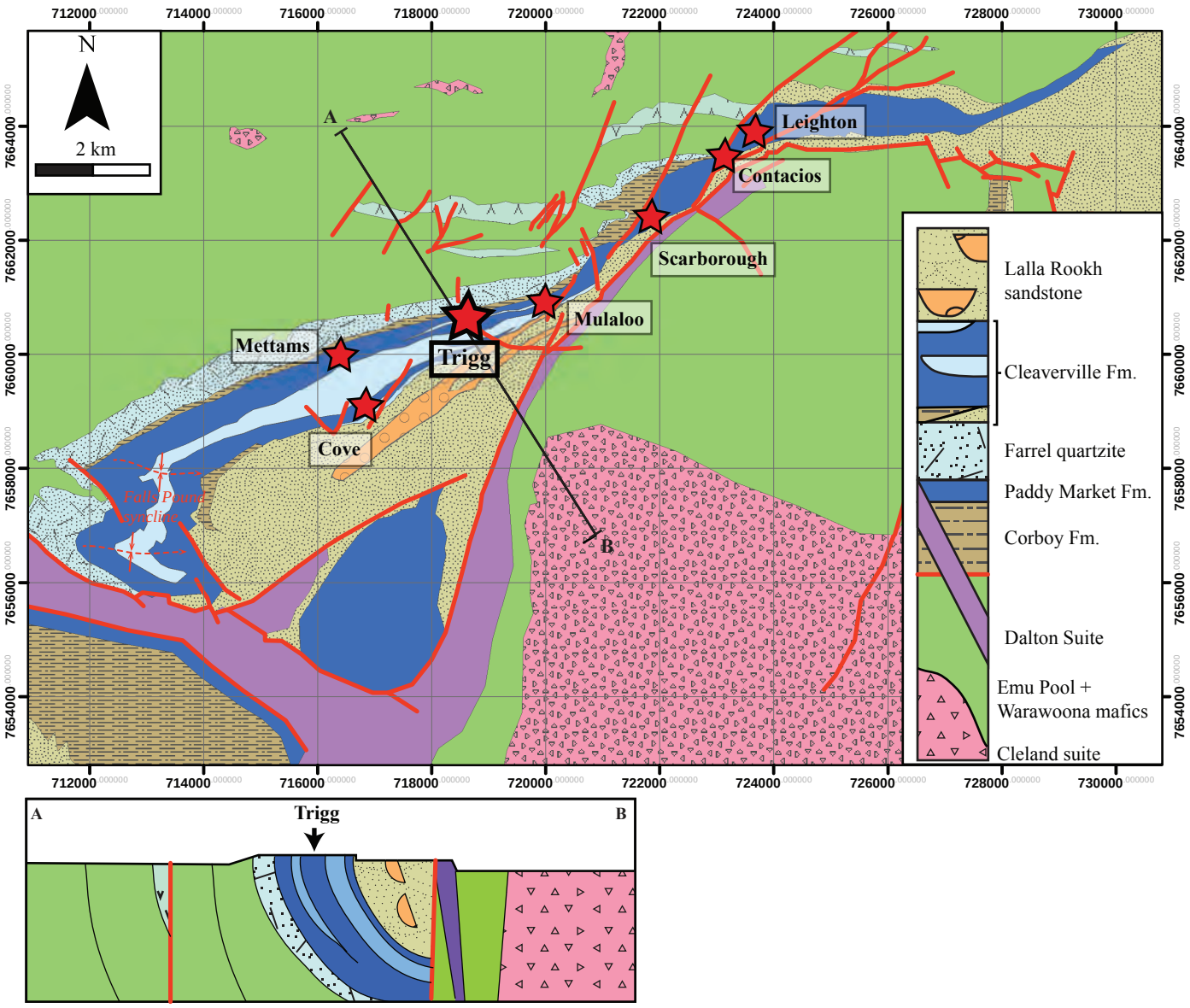

Figure 2: Simplified geology map, cross-section and stratigraphic log of the Abydos iron camp.

Lalla Rookh Sandstone (Fig. 2). The Cleaverville Formation and the Lalla Rookh Sandstone were deposited within fault-bound, extensional basins (Van Kranendonk and Collins, 1998) as part of the De Grey Superbasin. In the western portion of the East Strelley greenstone belt, the Cleaverville Formation consists dominantly of BIF with minor ferruginous shale. This passes along strike to the east into ferruginous shale and mudstone, with local siltstone and sandstone (Van Kranendonk, 2000).

Van Kranendonk (2000) documented the structural history of the East Strelley greenstone belt following a district-scale scheme applied to the North Shaw (NS) area, including (i) $D1_{NS}$ event (>3430 Ma), recorded as isoclinal folds within migmatite veins of early granitic intrusions, (ii) $D2_{NS}$ event (3360 to 3240 Ma), corresponding to the continued doming of granitoid intrusions and associated with the deposition of sub-basins in the East Strelley and Pincunah belts and (iii) $D3_{NS}$, a regional, northwest-southeast oriented transpressional event (ca. 2940 Ma), which pre-dated, or was accompanied by, deposition of the coarse clastic Lalla Rookh Sandstone. $D3_{NS}$ is most strongly developed within the 5–20 km-wide, north-northeasterly trending Lalla Rookh – Western Shaw Structural Corridor (LWSC). The contact between the East Strelley Belt and the LWSC is marked by a major fault zone, referred as to the Lalla Rookh-Western Shaw fault, and several second-order splayed faults that cut across the East Strelley Belt sequence (see Fig. 6 in Van Kranendonk, 2000). Other $D3_{NS}$ structures include easterly to southwesterly trending folds in the De Grey Supergroup. Fold axial traces follow the general outline of the Carlindi Batholith, from east–west in the west, to southwest–northeast in the east. Folds are open, easterly plunging structures in the western section of the belt (i.e. within the Abydos iron camp), including the district-scale Falls Pound synclinal system (Fig, 2). Further east, the folds are more steep and westerly plunging across a splayed $D3_{NS}$, northeasterly striking fault. Post-$D3_{NS}$ deformation events include (iv) $D4_{NS}$ (2.76 to 2.71 Ga), associated with moderate folding and faulting during deposition of the Fortescue

Group. (v) $D5_{NS}$ (<2.71 Ga) is expressed as local gentle folding associated with normal to sinistral displacement along the Antarctic Fault in the North Pole Dome area (Van Kranendonk, 2000). For clarification purposes, we hereafter use the regional deformation nomenclature (D_1 to D_{12}) proposed by Hickman and Van Kranendonk (2008) rather than the local scheme used by Van Kranendonk (2000). Local deformation events $D1_{NS}$, $D2_{NS}$ and $D3_{NS}$ correspond to the regional deformation events D1, D3 and D9, respectively. $D4_{NS}$ and $D5_{NS}$ postdate the regional D12 event.

Lithological and structural relationships in the Cleaverville Formation, Abydos

Least-altered rock types of the Cleaverville Formation exposed in the Abydos camp include BIFs (dominantly jaspilitic), cherty BIF, chert and shale (Fig. 3). The Trigg and Mettams deposits are hosted by a 100 to 200 m-wide jaspilitic BIF macroband situated in the lower portion of the local Cleaverville sequence (Fig. 2). At Trigg, the BIF macroband that hosts iron ore overlies a siltstone-dominated unit and is overlain by alternating, 10- to 80 m-wide shale- and chert-rich macrobands (Fig. 4A). At Mettams, the central portion of the jaspilitic BIF macroband grades eastward along strike into a non-jaspilitic, cherty BIF facies (Fig. 4B).

Bedding in the Abydos camp is mostly steeply dipping and displays a consistent ENE-trending strike (Figs. 4 and 5A). Two generations of folds are identified in the Abydos iron camp. The earliest fold generation is characterised by open to tight folds with subvertical NE- to ENE-trending axial planes and variably NE- to ENE-plunging fold axes (Figs. 5B, D). Folds with irregular geometries and variable fold plunge are located with bedding-parallel, high-strain zones that correspond with the high-grade iron ore body at Trigg. These folds are re-folded by NE- to ENE- trending, recumbent, open folds (Fig 5C, F). Minor brittle, bedding-parallel discrete faults displaying a normal displacement component, displace rare mafic dykes in BIF (Fig. 5G). In addition, subhorizontal faults or joints are filled by

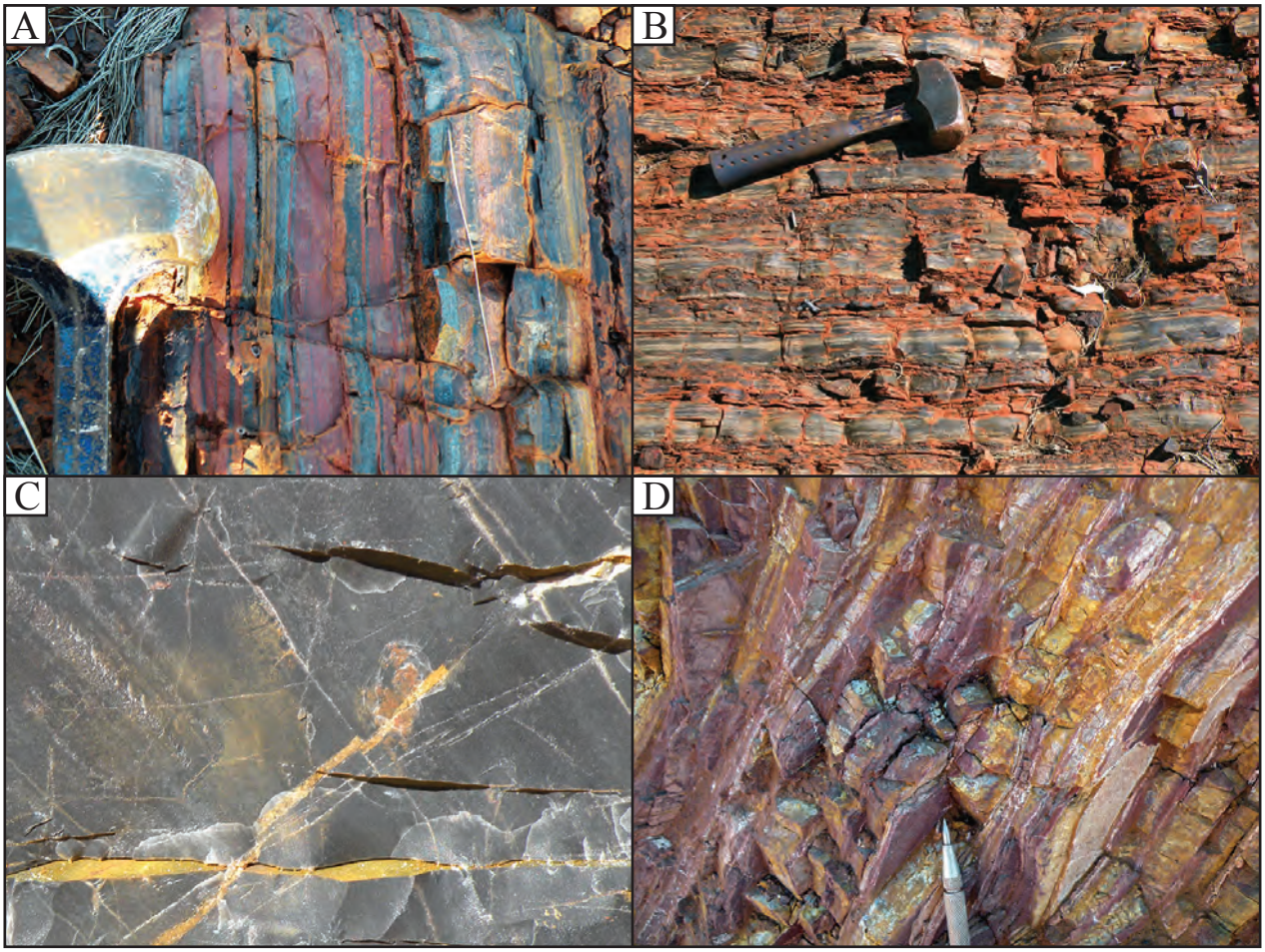

Figure 3: Dominant rock types exposed in the Abydos iron camp. (A) jaspilitic BIF, (B) cherty BIF, (C) carbonaceous chert and (D) siltstone and shale

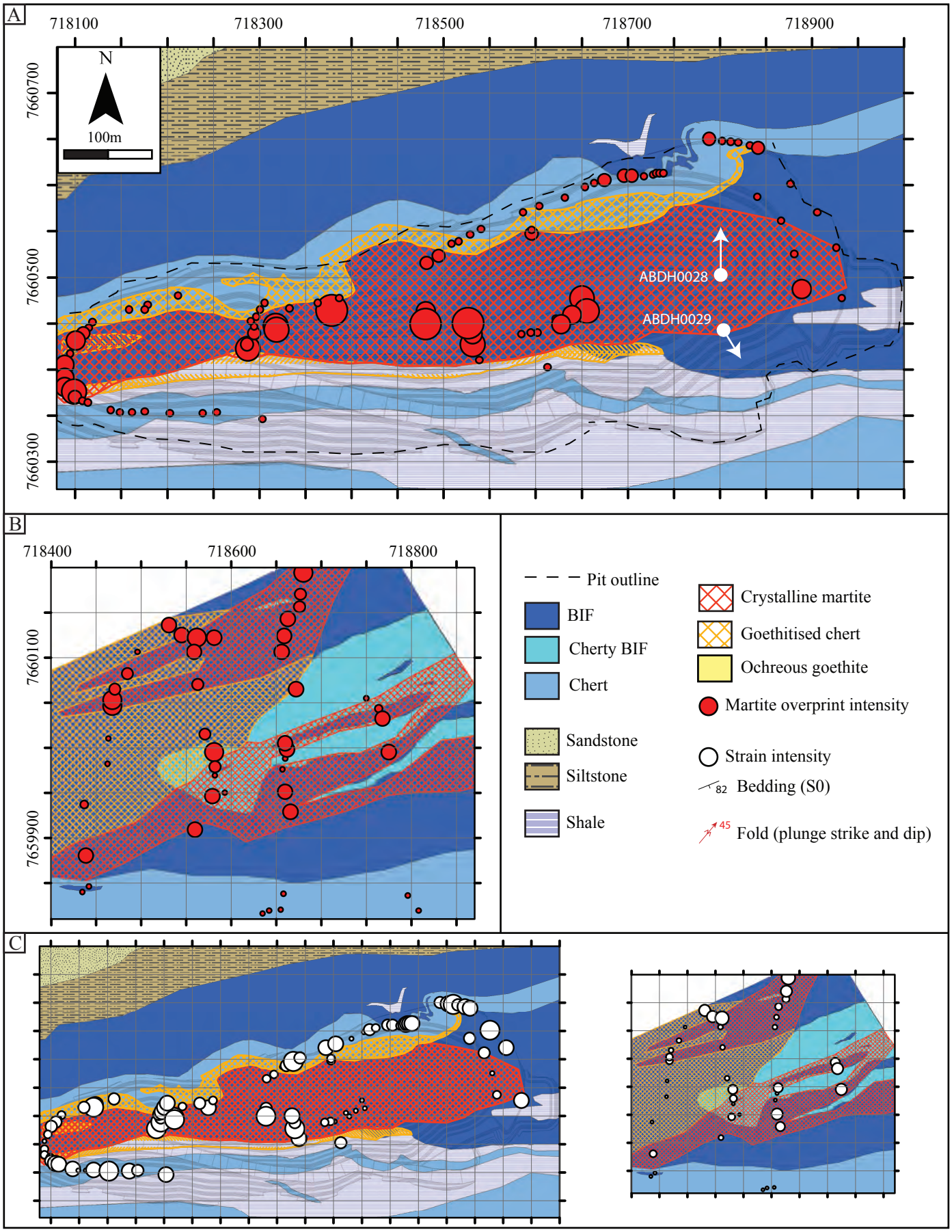

Figure 4: Geology and alteration maps of the Trigg (A) and Mettams (B) deposits. Onset (C) shows the strain intensity in both deposits.

colloform goethite and quartz (Fig. 6J). High-grade iron ore in the Trigg and Mettams deposits coincide with broad (>50 m-wide), bedding-parallel, ductile deformation zones in BIF. The margins of the deformation zones are gradational in that unstrained BIF becomes increasingly sheared towards the centre of each deformation zone, resulting in a decrease in primary band thickness and an increase in strain intensity in BIF. These deformation zones host 5 to 20 vol% disseminated, coarse-grained, crystalline magnetite (Mettams deposit) or martite (Trigg and Mettams deposits). It is possible that the respective bedding-parallel deformation zones in the Trigg and Mettams deposits are connected along strike.

The tilting of the Cleaverville sequence in the Abydos iron camp is interpreted to be the result of the regional D9 transpressional event at ca. 2940 Ma. Folding during the D9 event created the district-scale Falls Pound syncline (Fig. 2) and the early NE- to ENE-plunging folds documented in the Trigg and Mettams deposits are most likely parasitic folds to the district-scale syncline on the basis of their similar fold axial plane and fold axis geometries. Bedding-parallel, broad ductile deformation zones identified in Trigg and Mettams are most likely also related to D9 orogenic event, accommodating the regional NW-SE oriented transpression. Later recumbent folds in the Trigg pit display similar NE-ENE plunging direction to that of the earlier folds and, therefore, may have formed as late D9 structures. Rare mafic dykes that cut BIF are likely related to the emplacement of the Fortescue basaltic province initiated at 2.77 Ga through the development of the Black Range dolerite intrusions and the associated deposition of the Mount Roe Basalt eruptive sequence (Thorne and Trendall, 2001; Hickman, 2012). In this context, the brittle normal faults observed in Trigg (Fig. 5G) are most likely related to normal faulting during the deposition of the Fortescue Group ($D4_{NS}$ or $D5_{NS}$, postdating the regional D12).

Iron mineralisation and ore styles

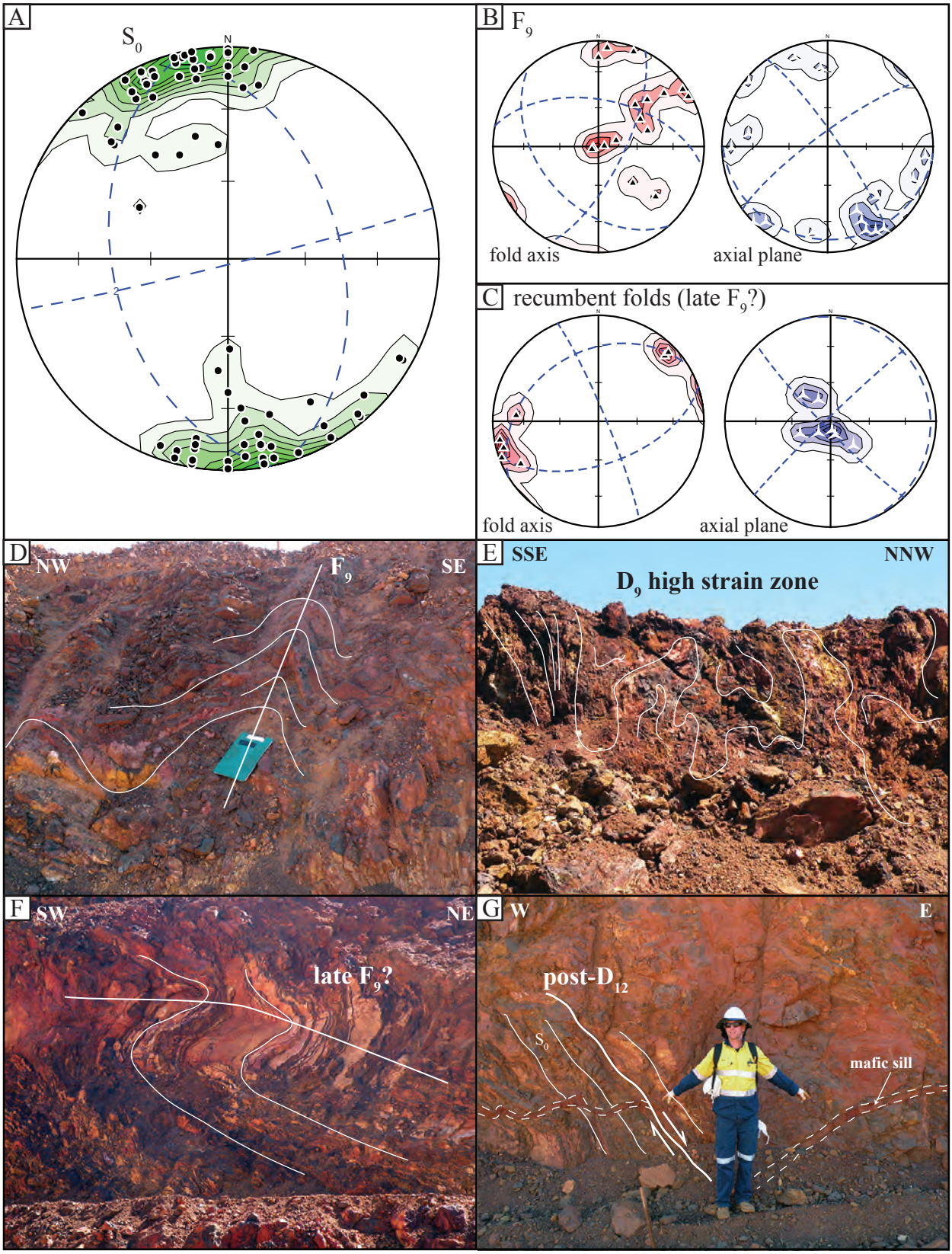

Figure 5: (A) Structural data for bedding, (B,C) structural data for F9 folds (A,B), (D-G) photographs of deformation styles at Abydos.

Most iron ore bodies in the Abydos camp are hosted by a jaspilitic BIF macroband located near the base of the Cleaverville Formation. Surface exposures and drill cores from the Trigg and Mettams deposits record several successive mineralisation events, resulting in a variety of ore styles:

(i) Coarse-grained (up to 0.5 mm), euhedral magnetite (Fe_3O_4)-rich BIF is located within D9 high strain zones oriented subparallel to BIF macrobands (Fig. 4) and within vein networks cutting BIF in proximal areas to D9 structures (Fig. 6A). At the Mettams deposit, euhedral magnetite is widely preserved in unweathered surface exposures. In contrast, euhedral magnetite exposed along pit walls of Trigg deposit have been entirely oxidised to martite. Disseminated euhedral magnetite is present in BIF up to 100 m away from D9 fault zones (Fig. 6B, C). Alteration zonation may be gradational or sharp (Fig. 6D). Coarse magnetite alteration in otherwise fresh BIF results in sub-economic iron concentrations of 45-50 wt. % Fe_2O_3 (see section V, Fig. 9).

(ii) Martite-enriched BIF and martite-rich ore (Fig. 6H, 6I) occur in the Trigg and Mettams deposits. Martite represents the pseudomorphic replacement of magnetite by hematite (Fe_2O_3) and is associated with moderate to strong depletion in silica in BIF. The martite-rich ore zones (i.e. martite-enriched BIF with extensive silica depletion) are best recognised in pit floor and drill core at depths below about 60 m where the goethite overprint is less intense (Figs 6H, 6I, 7A), although relics of martite are also commonly observed in strongly goethitised surface exposures (Fig. 6G). In the following sections, samples defined as martite-rich BIF or martite-rich ore correspond to samples that are dominated by crystalline, euhedral martite (>65 vol%). Martite-rich ore samples have maximum Fe_2O_3 content of ca. 90 wt. % (Fig. 9).

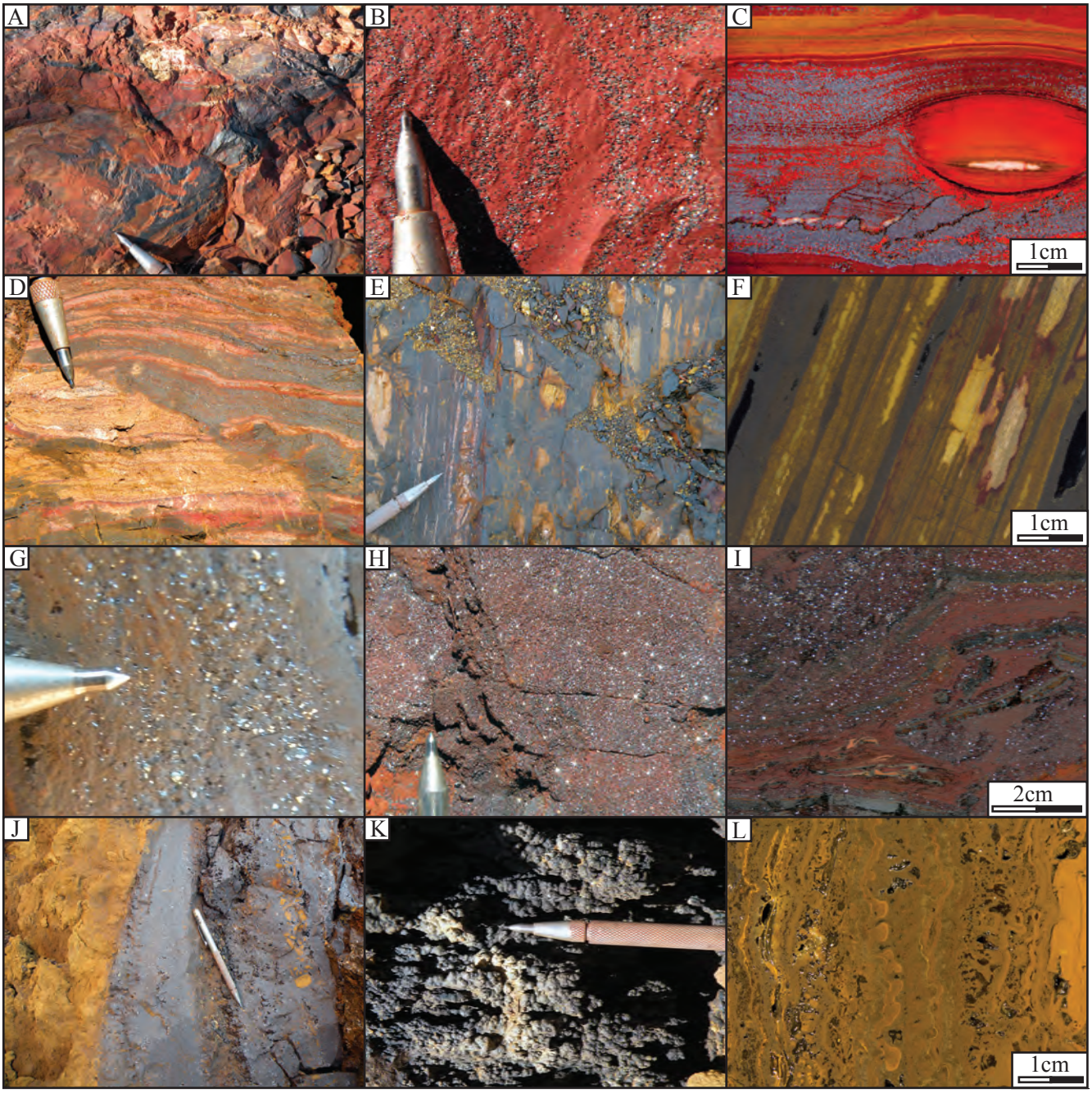

Figure 6: Photographs of alteration styles at Abydos

(iii) Bedded- to massive-textured, anhedral goethite (FeOOH) and goethite-martite ores result from intense supergene goethitisation of least-altered and magnetite- or martite-altered BIF. The distribution of goethite-rich ores is concentrated in fold-thickened BIF located between the present surface and 60 to 80 m depth (Fig. 7A). In areas distal to goethite-rich, high-grade ore zones, anhedral goethite forms preferentially (i) along primary iron oxide-rich bands, (ii) within mm- to cm-thick veins cutting BIF at high angles and (iii) as pervasive replacement of chert in chert-rich bands (Fig. 6E, 6F). Goethite alteration haloes envelop primary iron oxide-rich bands or goethite veins. Vitreous goethite-dominated and mixed martite-goethite ore types have a maximum Fe_2O_3 content of ca. 89 and 93 wt. %, respectively (Fig. 9).

(iv) A second stage of vitreous goethite formation is expressed as large (maximum thickness in excess of 1 m) subhorizontal veins filled with vitreous, massive to botryoidal goethite and colloform silica that cut through bedded to massive goethite ore (Fig. 6J, 6L). Large veins with well-developed botryoidal textures often display a late, 1 to 10 mm-thick coating of botryoidal psilomelane (Fig. 6K).

(v) Ochreous goethite ore forms at the expense of all types of enriched BIF and is usually present from surface to a depth of about 60 m (Fig. 6J, 7).

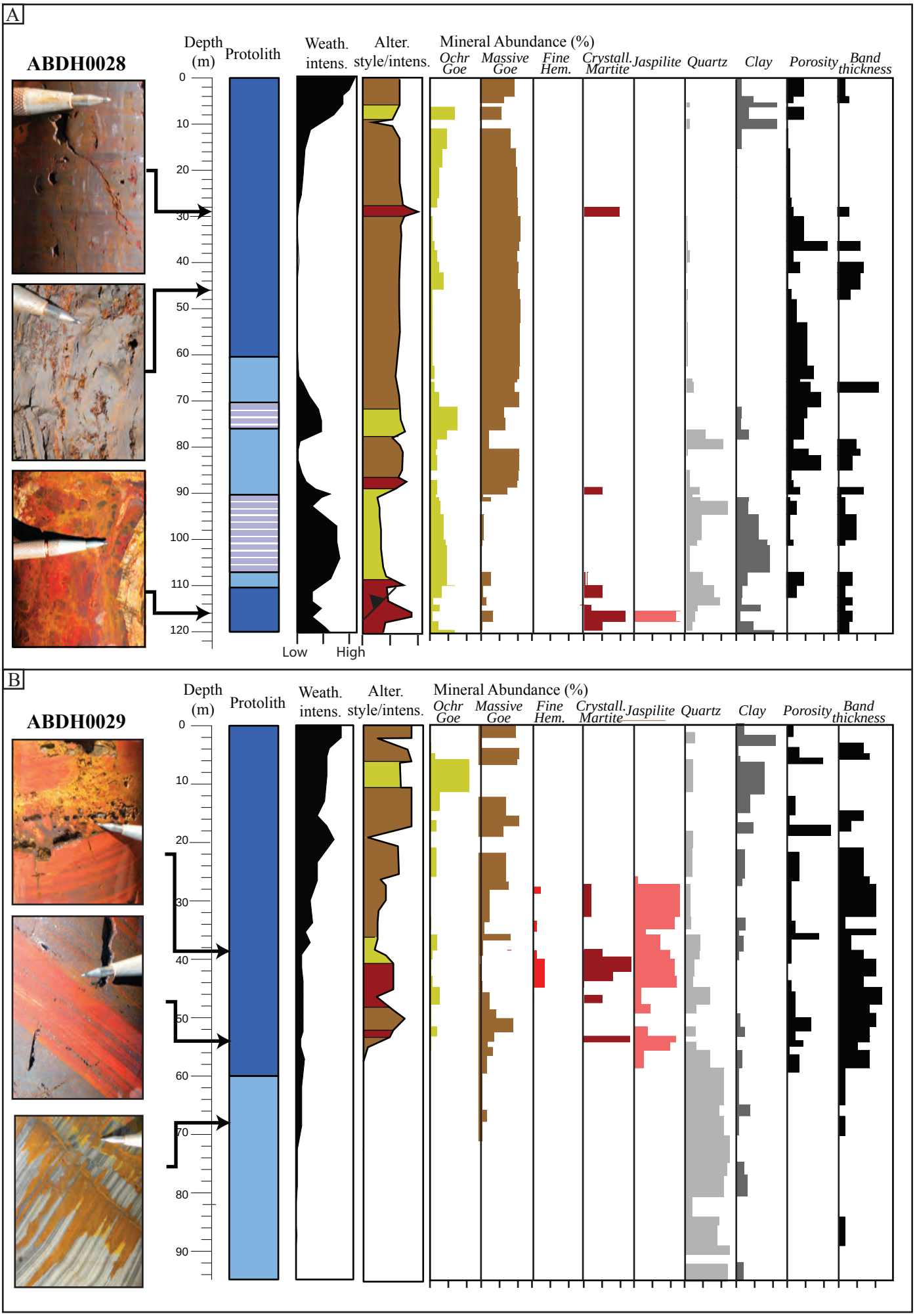

Figure 7: Stratigraphic logs of holes ABDH0028 and ABDH0029 (Trigg deposit).

V. Whole-rock geochemical changes associated with iron mineralisation

Least altered BIF

Two samples of least-altered and unweathered jaspilitic BIF from the Trigg deposit were analysed (Tables 1 to 3). Both samples are characterised by alternating bands of jasper and fine-grained hematite. Least-altered jaspilitic BIF samples yields Fe_2O_3 and SiO_2 contents of 47-48 and 50-51 wt. %, respectively (Fig. 8A). Both samples display low LOI (1 to 2.5 wt. %), Al_2O_3 (0.13 to 0.16 wt. %) and P_2O_5 (0.04 to 0.07 wt. %) contents, respectively (Fig. 8B, 8C, 8I). FeO and K_2O concentrations do not exceed 1.1 and 0.13 wt. %, respectively (Fig. 8D). Other major oxides, including MgO, CaO, Na_2O and TiO_2, display concentrations below 0.05 wt. % (Fig. 8E, 8F, 8H, 9G). Except for Mn (up to 150 ppm), transition metals are below 30 ppm (Ni, Cu, Zn, Cr) and most are below 5 ppm (As, Co, V, Pb) (Fig. 9). REE+Y concentrations normalised to PAAS (McLennan, 1989) and to C1 chondrite (Sun and McDonough, 1991) are shown in Fig. 10. Least-altered BIF samples are enriched in REE+Y compared to the C1 chondrite and display a pattern characterised by negative slope for the LREE, a flat profile for the HREE and a pronounced positive Eu anomaly (Fig. 10A). Normalised to PAAS, the least-altered BIF is depleted in REE+Y and displays a flat to slightly positive slope pattern, with a pronounced Eu positive anomaly (Fig. 10B).

Euhedral magnetite- to martite-enriched BIF

Three samples of magnetite- to martite-enriched BIF were analysed. One sample was collected from a moderately deformed zone exposed in the pit floor of the Trigg deposit, whereas two samples were obtained from outcrop at the Mettams deposit. These BIF samples display >20 vol. % coarse euhedral magnetite, now partly oxidised to martite, but differ from the martite-rich ore samples wherein silica has been removed (see below). Magnetite- to martite-enriched BIF shows an increase in Fe_2O_3 of 10 to 15 wt. % and a corresponding

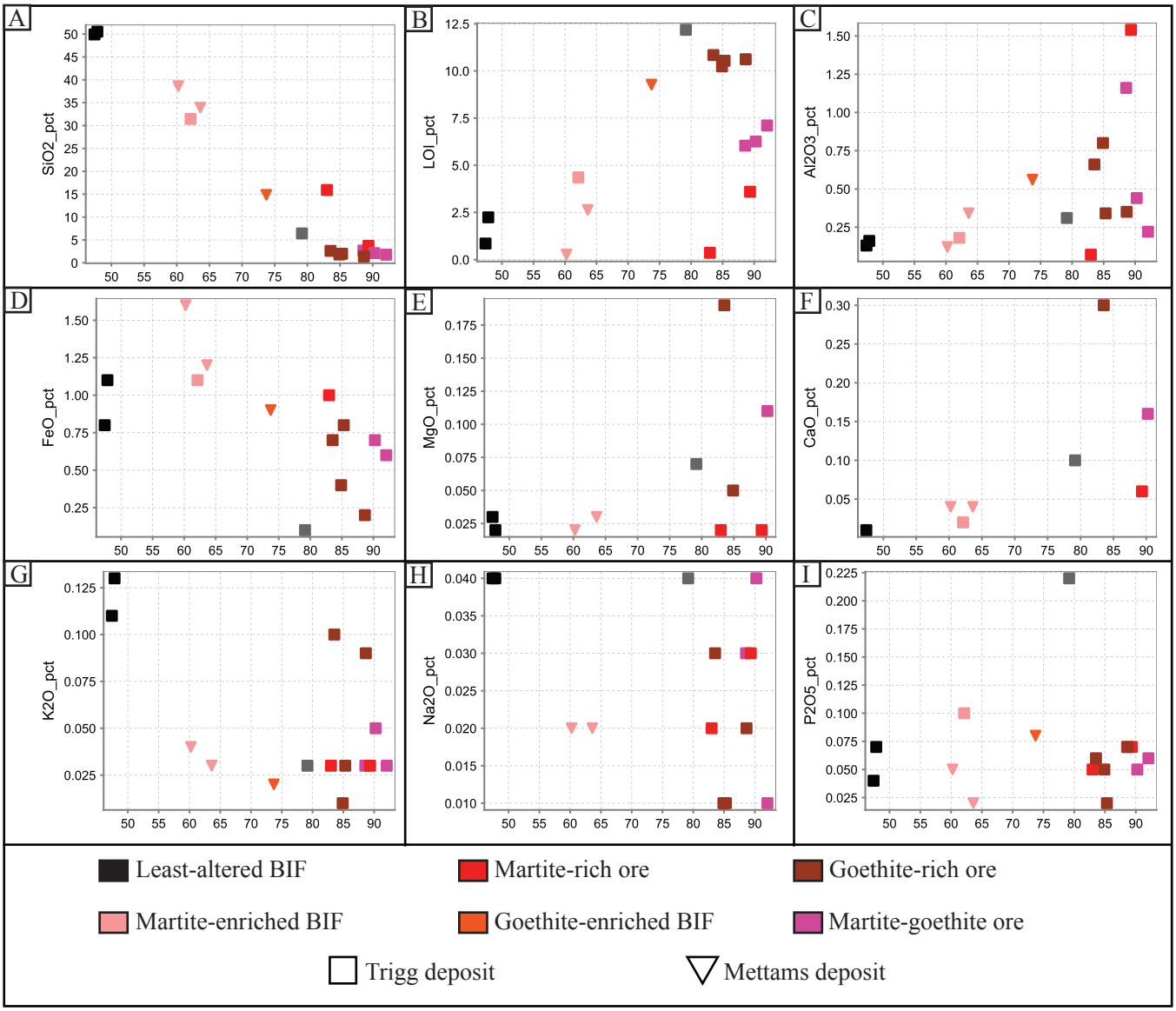

Figure 8: Whole-rock major element geochemistry data for least-altered BIF and iron ore types at Abydos.

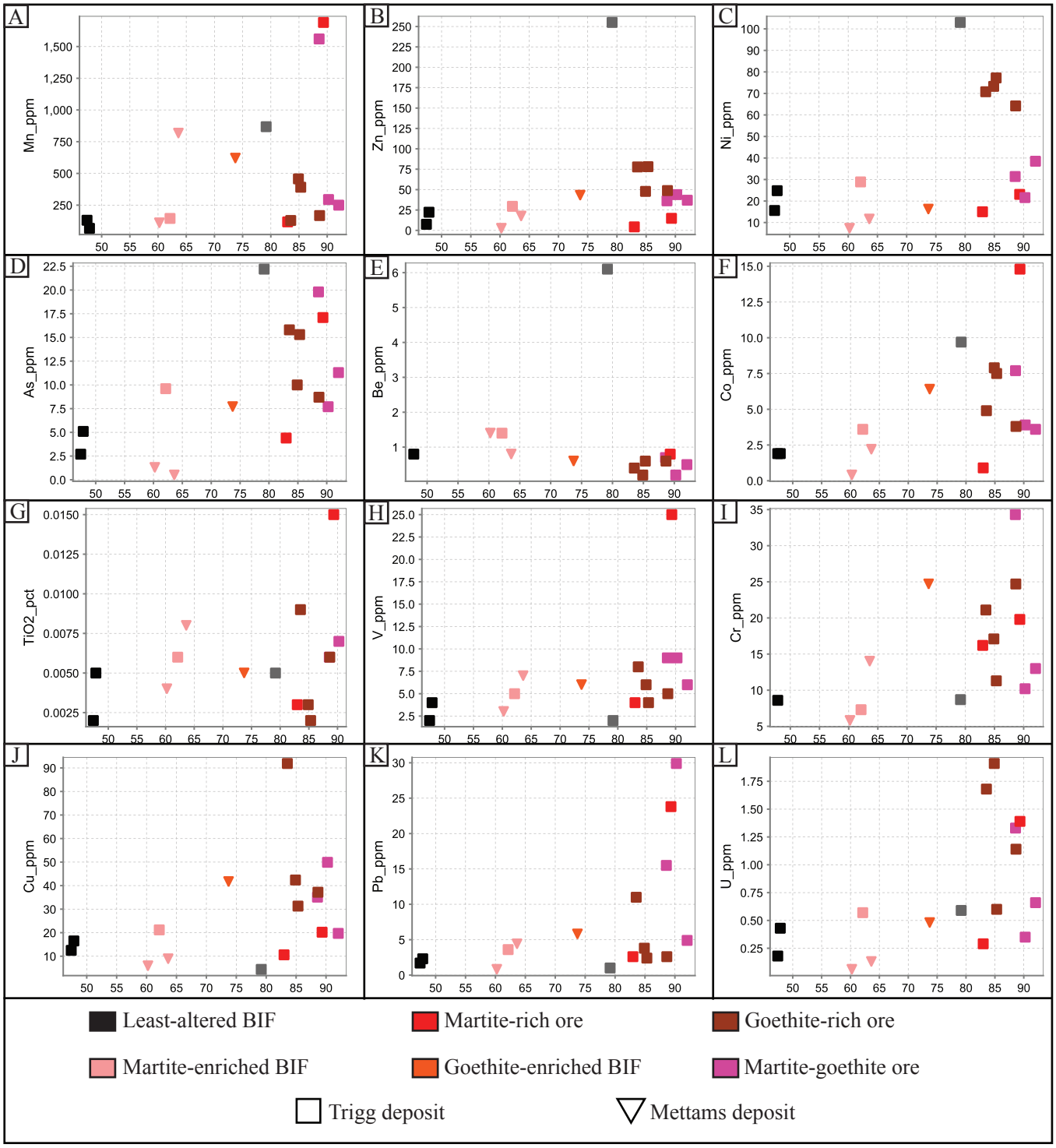

Figure 9: Whole-rock trace element geochemistry data for least-altered BIF and iron ore types at Abydos.

decrease in SiO_2 compared to the least altered BIF (Fig. 8A). No significant increase in the FeO content is observed (Fig. 8D), at odds with the apparent proportion of coarse-grained magnetite (10 to 25%) in hand specimens. This discrepancy likely arises from the fact that a significant portion of magnetite is pseudomorphed by martite in these samples. None of the other major oxides, transitional metals or REE exhibit any statistically significant differences in concentration compared to the parent BIF, with the exception of a minor increase (Fig. 8C, 8F, 9H) in Ca, Ti, V and Al_2O_3 (x1.5 to x3) and a decrease (Fig. 8G) in K_2O (from 0.11-0.13 to 0.03-0.04 wt. %).

Martite-rich ore

Two samples of martite-rich ore collected from the highly deformed central portion of the Trigg deposit at a depth of about 70 m mainly comprise coarse euhedral martite with minor goethite. These samples display extensive depletion in quartz and residual enrichment in martite compared to martite-enriched BIF, as reflected by high Fe_2O_3 (83 to 89 wt. %) and low SiO_2 (3 to 15 wt. %) contents (Fig. 8A). The LOI content in martite-rich ore samples is similar to that of the least altered and magnetite- to martite-enriched BIF (<3.5 wt. %), indicating insignificant contribution of hydrated phases such as goethite. The two samples show high compositional variability for a number of elements, with one sample constantly showing high concentrations in Al_2O_3 (>1.5 wt. %, Fig. 8C), Mn (1,700 ppm, Fig. 9A), As (17 ppm, Fig. 9D), Co (15 ppm, Fig. 9F), TiO_2 (0.015 wt. %, Fig. 9G), V (25 ppm, Fig. 9H), Pb (24 ppm, Fig. 9K), U (1.3 ppm, Fig. 9L) and all REE (Fig. 10). None of the other major oxides, transitional metals or REE exhibit any statistically significant differences in concentration compared to the magnetite- to martite-enriched BIF.

Anhedral goethite-rich and martite-goethite ores

Four samples of goethite ore collected from the Trigg deposit from surface to 50-60 m deep mainly (>95 vol. %) comprise anhedral, bedded to massive goethite. Anhedral goethite ore displays Fe_2O_3, LOI and SiO_2 contents of 83-89, 10-11 and 2-3 wt. %, respectively (Fig. 8A, 8B). Relative to least-altered BIF, the goethite-bearing BIF displays elevated Al_2O_3 (from 0.1-0.2 wt. % in the parent BIF to 0.3-0.8 wt.% in the goethite ore zone, i.e. ~x3 enrichment factor, Fig. 8C), Mn (from 50-150 to 150-500 ppm, ca. x3 enrichment, Fig. 9A), Zn, As, Cu, Ni, Co, Pb, U (ca. x3 enrichment, Fig. 9B, 9C, 9D, 9F, 9J, 9K, 9L) and V, Cr (ca. x2 enrichment, Fig. 9H, 9I). The REE in the anhedral goethite ore samples display a similar pattern to that of the least-altered BIF, together with a systematic enrichment by a factor of 3 to 5 (Fig. 10). In contrast, FeO, K_2O and Na_2O are depleted compared to the parent BIF (Fig. 8D, 8G, 8H). Phosphorus does not exhibit any significant changes compared to the least-altered BIF (Fig. 8I).

Apart from a slightly higher Fe_2O_3 (88 to 93 wt. %) and lower LOI (6 to 7 wt. %) content, mixed martite-goethite ore samples display similar geochemical characteristics to the anhedral goethite ore type, including the documented enrichment in a number of trace elements including As, Cu, Pb, V, Cr (Fig. 8, 9). Interestingly, some elements including Zn, Ni and U are not as enriched as the goethite ore, suggesting that their concentrations are directly related to the proportion of anhedral goethite within a given sample (Fig. 9).

Large, massive to botryoidal goethite-rich veins

One goethite-rich sample collected from a 1 m-thick vein on the southern wall of the Trigg pit at a depth of about 40 m was analysed. The large subhorizontal veins cutting BIF macrobands comprise massive to botryoidal goethite associated with minor colloform silica and often a late coating of psilomelane. The goethite vein sample yields a Fe_2O_3 content of 79

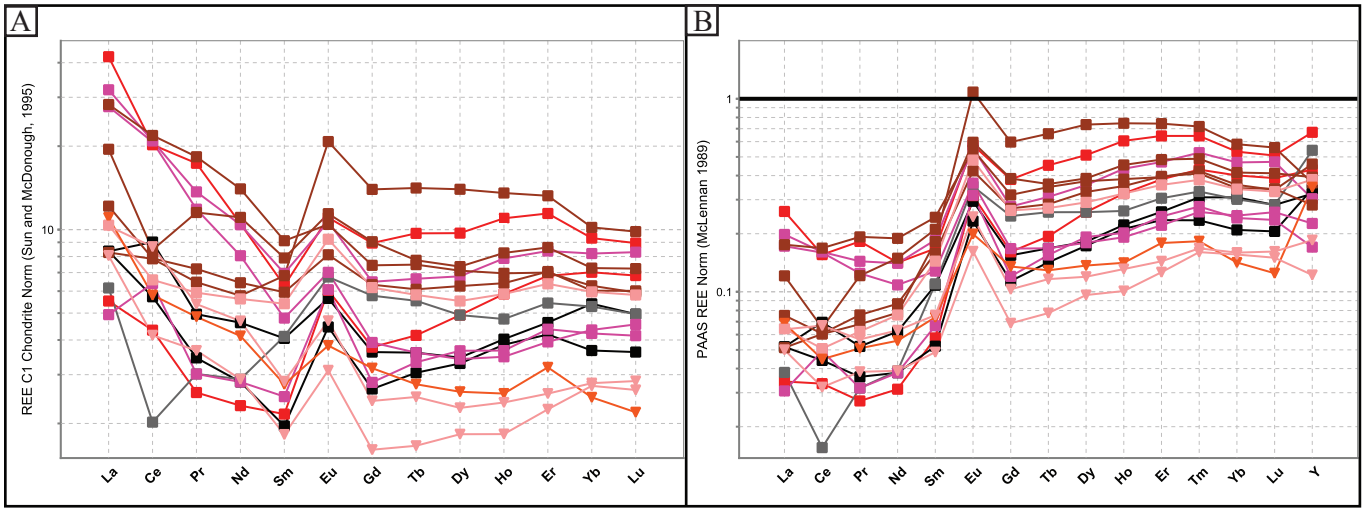

Figure 10: Whole-rock REE chemistry data for least-altered BIF and iron ore types at Abydos. See Figure 8 for colour coding.

Sample	alteration intensity	alteration style	Rock type	Site	Al2O3	CaO	Fe2O3	Fe2O3(T)	FeO	K2O	LOI	MgO	MnO	Na2O	P2O5	SiO2	TiO2	C	S	Total
ABTR06	least altered	least altered	jaspilitic BIF	Trigg	0.24	0.01	30.97	33.08	1.9	0.03	1.08	0.15	0.025	0.04	< 0.01	66.07	0.007	0.12	< 0.01	100.7
ABTR22	least altered	least altered	jaspilitic BIF	Trigg	0.16	< 0.01	46.62	47.84	1.1	0.13	2.24	0.02	0.015	0.04	0.07	50.53	0.005	0.04	< 0.01	100.9
ABTR23	high	martite	jaspilitic BIF	Trigg	0.07	< 0.01	81.87	82.98	1	0.03	0.36	0.02	0.023	0.02	0.05	15.92	0.003	0.04	< 0.01	99.19
ABTR24	least altered	least altered	jaspilitic BIF	Trigg	0.13	0.01	46.51	47.4	0.8	0.11	0.85	0.03	0.024	0.04	0.04	49.92	0.002	0.01	< 0.01	98.55
ABTR28	high	goethite vein	jaspilitic BIF	Trigg	0.31	0.1	79.06	79.17	0.1	0.03	12.18	0.07	0.128	0.04	0.22	6.43	0.005	0.06	< 0.01	98.68
ABTR29	high	martite goethite	jaspilitic BIF	Trigg	1.16	< 0.01	88.46	88.57	< 0.1	0.03	6.04	< 0.01	0.212	0.03	0.07	2.68	0.006	0.07	< 0.01	98.82
ABTR32	high	martite	jaspilitic BIF	Trigg	1.54	0.06	89.23	89.34	< 0.1	0.03	3.6	0.02	0.224	0.03	0.07	3.71	0.015	0.02	< 0.01	98.65
ABTR40	high	martite - goethite	jaspilitic BIF	Trigg	0.44	0.16	89.47	90.24	0.7	0.05	6.26	0.11	0.052	0.04	0.05	2.13	0.007	0.14	< 0.01	99.54
ABDH13- 06	low	pyrite + ankerite	jaspilitic BIF	Trigg	0.2	< 0.01	24.91	59.04	30.7	0.02	29.81	1.49	2.133	0.03	< 0.01	5.95	0.002	9.59	0.28	98.54
ABDH28- 01	high	martite - goethite	jaspilitic BIF	Trigg	0.22	< 0.01	91.37	92.04	0.6	0.03	7.11	< 0.01	0.042	0.01	0.06	1.78	< 0.001	0.02	< 0.01	100.9
ABDH28- 02	high	goethite	jaspilitic BIF	Trigg	0.8	< 0.01	84.45	84.89	0.4	0.01	10.24	0.05	0.057	0.01	0.05	1.8	0.003	0.07	< 0.01	97.74
ABDH28- 03	high	goethite	jaspilitic BIF	Trigg	0.34	< 0.01	84.42	85.31	0.8	0.03	10.54	< 0.01	0.045	0.01	0.02	1.98	0.002	0.03	< 0.01	98.03
ABDH28- 04	high	goethite	jaspilitic BIF	Trigg	0.35	< 0.01	88.42	88.65	0.2	0.09	10.62	< 0.01	0.031	0.02	0.07	1.38	0.006	0.04	< 0.01	100.8
ABDH29- 01	high	goethite	jaspilitic BIF	Trigg	0.66	0.3	82.75	83.53	0.7	0.1	10.84	0.19	0.024	0.03	0.06	2.61	0.009	0.22	< 0.01	98.35
ABDH30- 01	moderate	martite	jaspilitic BIF	Trigg	0.18	0.02	60.9	62.12	1.1	< 0.01	4.36	< 0.01	0.024	< 0.01	0.1	31.45	0.006	0.02	< 0.01	98.27
ABDH45- 01	moderate	goethite	jaspilitic BIF	Mettams	0.56	< 0.01	72.71	73.71	0.9	0.02	9.27	< 0.01	0.071	< 0.01	0.08	14.84	0.005	0.07	< 0.01	98.36
ABME07	moderate	martite	jaspilitic BIF	Mettams	0.12	0.04	58.45	60.23	1.6	0.04	0.26	0.02	0.02	0.02	0.05	38.6	0.004	0.02	< 0.01	99.39
ABME 11	moderate	martite	jaspilitic BIF	Mettams	0.34	0.04	62.28	63.61	1.2	0.03	2.63	0.03	0.126	0.02	0.02	33.92	0.008	0.04	< 0.01	100.8

Table 1: Whole-rock geochemistry data for major oxides at Abydos

Sample	As	Ba	Be	Bi	Co	Cr	Cu	Ga	Ge	Li	Mn	Mo	Nb	Ni	Pb	Rb	Re	Sb	Se	Sr	Ta	V	W	Zn	Zr
ABTR06	1.1	8	< 0.1	0.02	0.9	52.3	5.8	0.4	0.5	1	145	0.22	1	7.2	1.3	1.2	0.005	0.4	1.7	3.3	0.03	9	8.2	9.6	6
ABTR22	5.1	6	0.8	0.03	1.9	8.6	16.5	0.2	0.3	5.6	67	0.86	0.9	24.8	2.3	0.6	0.003	0.5	1.4	1.7	0.02	4	12.7	22.3	4
ABTR23	4.4	8	< 0.1	< 0.02	0.9	16.2	10.6	0.1	0.6	2.7	118	1.68	2	15	2.6	0.4	< 0.001	0.6	0.8	1.2	0.26	4	13.9	4.3	5
ABTR24	2.7	11	< 0.1	0.03	1.9	< 0.5	12.5	< 0.1	0.5	5.3	131	0.13	0.6	15.6	1.7	0.3	< 0.001	0.3	0.6	0.9	< 0.01	2	16.8	7.5	1
ABTR28	22.2	28	6.1	< 0.02	9.7	8.7	4.4	0.1	0.3	< 0.5	868	0.45	0.5	103	1	0.5	< 0.001	0.8	1.4	5	< 0.01	2	15.2	255	6
ABTR29	19.8	65	0.7	0.04	7.7	34.3	35.1	< 0.1	0.4	1.1	1560	0.87	3.1	31.4	15.5	0.3	0.001	4.6	1.3	3.7	0.03	9	12.3	36.3	3
ABTR32	17.1	125	0.8	0.05	14.8	19.8	20.2	0.2	0.5	1.3	1690	1.09	1.7	23.1	23.8	0.5	0.004	5.4	1.8	10.6	0.02	25	17.9	14.8	6
ABTR40	7.7	7	0.2	0.02	3.9	10.2	49.9	0.6	0.6	< 0.5	294	0.43	0.5	21.6	29.9	0.6	0.002	1.3	1.9	6	0.02	9	9.2	43.9	3
ABDH13- 06	2.1	2	< 0.1	< 0.02	2.3	8.7	4.7	0.5	0.2	2.3	> 10000	0.67	1.4	16.4	0.9	0.3	< 0.001	0.4	1.2	1.4	0.09	12	11.1	31.2	1
ABDH28- 01	11.3	4	0.5	< 0.02	3.6	13	19.7	1	0.8	< 0.5	250	0.42	< 0.2	38.5	4.9	< 0.2	0.002	1.2	1.5	1.2	< 0.01	6	8.1	37	< 1
ABDH28- 02	10	10	0.2	< 0.02	7.9	17.1	42.4	0.5	0.3	< 0.5	457	0.38	< 0.2	73.3	3.8	0.5	< 0.001	0.7	0.7	2.7	< 0.01	6	11.6	47.8	2
ABDH28- 03	15.3	6	0.6	< 0.02	7.5	11.3	31.3	0.5	0.7	< 0.5	391	0.26	< 0.2	77.2	2.4	< 0.2	< 0.001	0.7	1.2	1.3	0.02	4	7.8	78.1	1
ABDH28- 04	8.7	3	0.6	< 0.02	3.8	24.7	37.2	0.4	0.2	< 0.5	168	0.38	< 0.2	64.2	2.6	< 0.2	< 0.001	0.4	1.2	1.2	0.04	5	9.9	48.8	3
ABDH29- 01	15.8	10	0.4	0.02	4.9	21.1	91.9	0.2	0.3	< 0.5	129	0.3	0.7	70.8	11	0.5	< 0.001	0.8	1.3	4.2	0.01	8	9.3	77.8	5
ABDH30- 01	9.6	4	1.4	0.02	3.6	7.3	21.2	0.2	0.2	2.4	145	0.86	0.5	28.9	3.6	< 0.2	< 0.001	2.1	0.5	2.4	0.01	5	16.9	29.5	3
ABDH45- 01	7.7	13	0.6	< 0.02	6.4	24.7	41.7	0.6	0.3	0.5	620	2.72	< 0.2	16.2	5.8	< 0.2	< 0.001	2.8	1.6	3	0.01	6	14.8	43.1	2
ABME07	1.3	21	1.4	< 0.02	0.4	5.8	5.9	1.1	0.5	1.2	110	0.12	< 0.2	7.3	0.8	< 0.2	< 0.001	0.6	0.5	4.4	< 0.01	3	12.8	2.5	2
ABME 11	0.5	12	0.8	0.02	2.2	14	8.9	0.5	0.5	2	817	0.21	0.3	11.6	4.4	0.4	< 0.001	0.2	0.6	4.1	0.01	7	12.1	17.5	3

Table 2: Whole-rock geochemistry data for transitional metals at Abydos

Sample	La	Ce	Pr	Nd	Sm	Eu	Gd	Tb	Dy	Ho	Er	Tm	Yb	Lu	Y	U	Th
ABTR06	2.25	2.96	0.35	1.44	0.21	0.121	0.31	0.07	0.51	0.12	0.4	0.058	0.33	0.046	4.3	0.04	0.2
ABTR22	1.98	5.53	0.46	2.11	0.6	0.318	0.72	0.13	0.85	0.22	0.74	0.125	0.87	0.122	8.7	0.43	0.13
ABTR23	1.31	2.66	0.24	1.06	0.32	0.34	0.75	0.15	1.21	0.32	1.09	0.174	1.13	0.168	11.6	0.29	0.29
ABTR24	1.98	3.51	0.32	1.29	0.29	0.251	0.53	0.11	0.81	0.21	0.67	0.095	0.59	0.089	9.2	0.18	0.07
ABTR28	1.46	1.24	0.28	1.32	0.61	0.38	1.15	0.2	1.21	0.26	0.87	0.134	0.85	0.122	14.6	0.59	0.09
ABTR29	6.58	12.7	1.1	3.68	0.71	0.395	0.78	0.13	0.84	0.19	0.63	0.105	0.7	0.112	6.1	1.33	0.26
ABTR32	9.96	12.4	1.61	4.8	0.93	0.622	1.78	0.35	2.39	0.6	1.83	0.26	1.5	0.22	18.1	1.39	0.45
ABTR40	7.57	12.8	1.27	4.76	1.03	0.601	1.29	0.24	1.67	0.43	1.34	0.213	1.32	0.204	8.2	0.35	0.12
ABDH13- 06	1.1	1.75	0.15	0.69	0.15	0.055	0.2	0.04	0.26	0.05	0.14	0.025	0.16	0.018	1.5	0.07	0.12
ABDH28- 01	1.17	3.92	0.28	1.29	0.37	0.342	0.56	0.12	0.9	0.2	0.7	0.112	0.68	0.102	4.6	0.66	0.07
ABDH28- 02	1.96	4.81	0.6	2.64	1.01	1.17	2.78	0.51	3.44	0.74	2.12	0.291	1.64	0.242	9.9	1.91	0.21
ABDH28- 03	4.62	5.18	1.07	5.06	1.17	0.643	1.8	0.28	1.81	0.45	1.38	0.198	1.17	0.178	10.6	0.6	0.1
ABDH28- 04	2.88	4.83	0.67	2.94	0.88	0.457	1.26	0.22	1.54	0.35	1.13	0.166	0.97	0.148	7.6	1.14	0.23
ABDH29- 01	6.7	13.4	1.7	6.41	1.35	0.588	1.48	0.27	1.75	0.38	1.12	0.171	1.01	0.146	12.4	1.68	0.33
ABDH30- 01	2.46	4.04	0.55	2.57	0.8	0.52	1.23	0.21	1.36	0.32	1.02	0.154	0.96	0.143	10.3	0.57	0.12
ABDH45- 01	2.62	3.56	0.45	1.89	0.41	0.215	0.63	0.1	0.64	0.14	0.51	0.074	0.4	0.054	9.4	0.48	0.23
ABME07	1.91	2.55	0.34	1.32	0.27	0.175	0.32	0.06	0.45	0.1	0.36	0.065	0.44	0.065	3.3	0.06	0.08
ABME 11	2.44	5.32	0.5	2.14	0.42	0.264	0.48	0.09	0.56	0.13	0.41	0.068	0.45	0.07	5	0.13	0.14

Table 3: Whole-rock geochemistry data for REE+Y, U and Th at Abydos

wt. % (Fig. 8A). The SiO_2 (6 wt. %) and LOI (12.3 wt. %) contents suggest a contribution from hydrated colloform silica (SiO_2,nH_2O). Anomalously high concentrations, i.e. an enrichment x10 or higher compared to the least-altered BIF, are observed for P_2O_5 (0.22 wt. %, Fig. 8I), Zn (>250 ppm, Fig. 9B), Be (>6 ppm, Fig. 9E), and to a lesser extent (enrichment x5) for Mn (>850 ppm, Fig. 9A), Ni (>100 ppm, Fig. 9C), As (22 ppm, Fig. 9D) and Co (9 ppm, Fig. 9F). In addition, Al_2O_3 and U show a two to threefold increase in concentration compared to the least-altered BIF, similar to that of the anhedral goethite ore type (Fig. 8C, 9L). Other trace elements do not exhibit any significant changes compared to the least-altered BIF. The REE concentration pattern of the large, goethite-rich vein sample is similar to that of the bedded to massive anhedral goethite ore apart from the occurrence of a marked negative Ce anomaly and a less pronounced positive Eu anomaly (Fig. 10).

VI. Deposit-scale geochemical and geophysical signatures of mineralisation

Goethite mineralisation signatures from trace element anomalies

The Trigg and Mettams deposits display kilometre-scale enrichments in As, Cu, Ni and Zn relative to distal occurrences of BIF sampled in between these deposits (Fig. 11). The geochemical enrichments correspond to goethite-rich BIF. The samples analysed by this study show that relative to least-altered BIF (i) Cu is enriched by a factor of three times in the anhedral bedded to massive goethite ore, but not in the massive to botryoidal goethite veins (Fig. 9J), (ii) As and Ni are enriched by a factor of three times in the anhedral goethite ore and by a factor of five times in the large goethite veins (Fig. 9C, 9D) and (iii) Zn is enriched by a factor of three times in the anhedral goethite ore and by a factor of ten times in the large goethite veins (Fig. 9B).

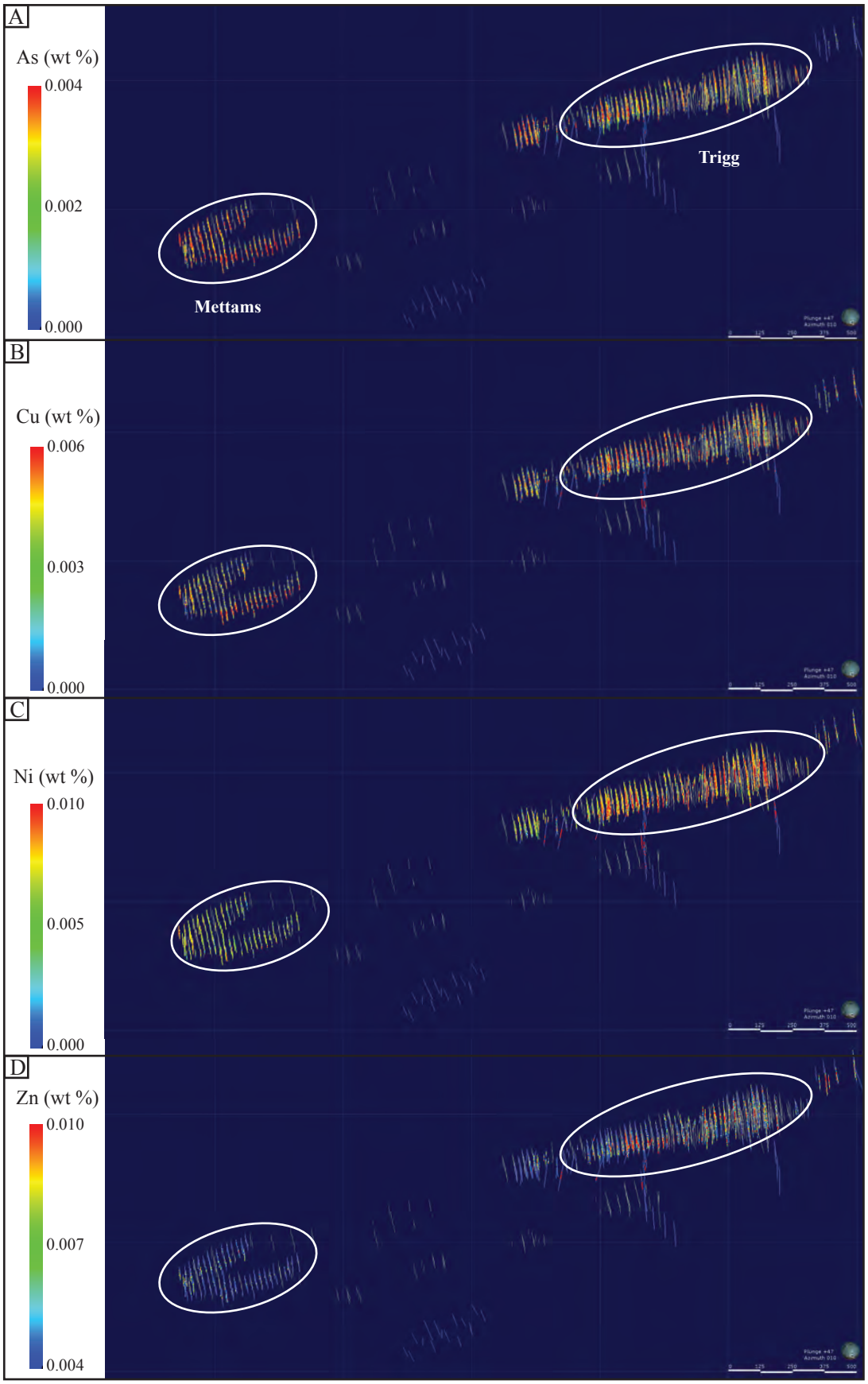

Figure 11: Deposit-scale anomalies of (A) As, (B) Cu, (C) Ni and (D) Zn from company assay data at the Trigg and Mettams deposits.

Within the Trigg pit, the greatest enrichment in Cu (<60 ppm) is located in the western section of the pit (Fig. 11B), corresponding to intensely developed zones of anhedral, bedded to massive goethite in BIF. Nickel and As are enriched up to 100 ppm in the Trigg deposit (Fig. 11A, 11C). Zonation in Ni and As concentrations is less obvious than Cu in the Trigg deposit. This is likely related to the higher proportion of large, massive to botryoidal goethite veins compared with anhedral bedded to massive goethite ores in the central and western section of the pit. Zinc is enriched up to 100 ppm along narrow, discrete subhorizontal zones in the central and eastern sections the Trigg pit. Such enrichments most likely correspond with the presence of subhorizontal goethite veins in this part of the ore body.

Magnetite-enriched BIF signature from magnetic anomalies

A deposit-scale 3D model that shows the first vertical derivative of the magnetic field for the Trigg and Mettams deposit was created using the MAG3D program (Li and Oldenburg, 1996, 2000). Down hole and airborne surveys with 25 m resolution grid were used as input data. MAG3D allows forward modelling and inversion of multi-component magnetic data; modelling of the magnetic field first vertical derivative (1VD) is used because it emphasizes near surface, shorter wavelength features and provides a good spatial representation of deposit-scale zones of magnetic anomalies, especially their upper surface. Results of the 1VD modelling is represented as a block model displaying one ENE-WSW-trending long-section through the Mettams and Trigg deposits, and one N-S-trending cross-section through the eastern section of the Trigg deposit (Fig. 12). Two zones of anomalous magnetic signatures are identified at a depth of 100-200 m below the Trigg and Mettams deposits. These zones follow the ENE-trending strike of the main jaspilitic macroband and display a steep southward plunge. Because these zones are (i) discontinuous along strike and (ii) best expressed in the Trigg and Mettams deposits where evidence for widespread, coarse euhedral magnetite overprint has been documented, it is proposed that these magnetic signatures

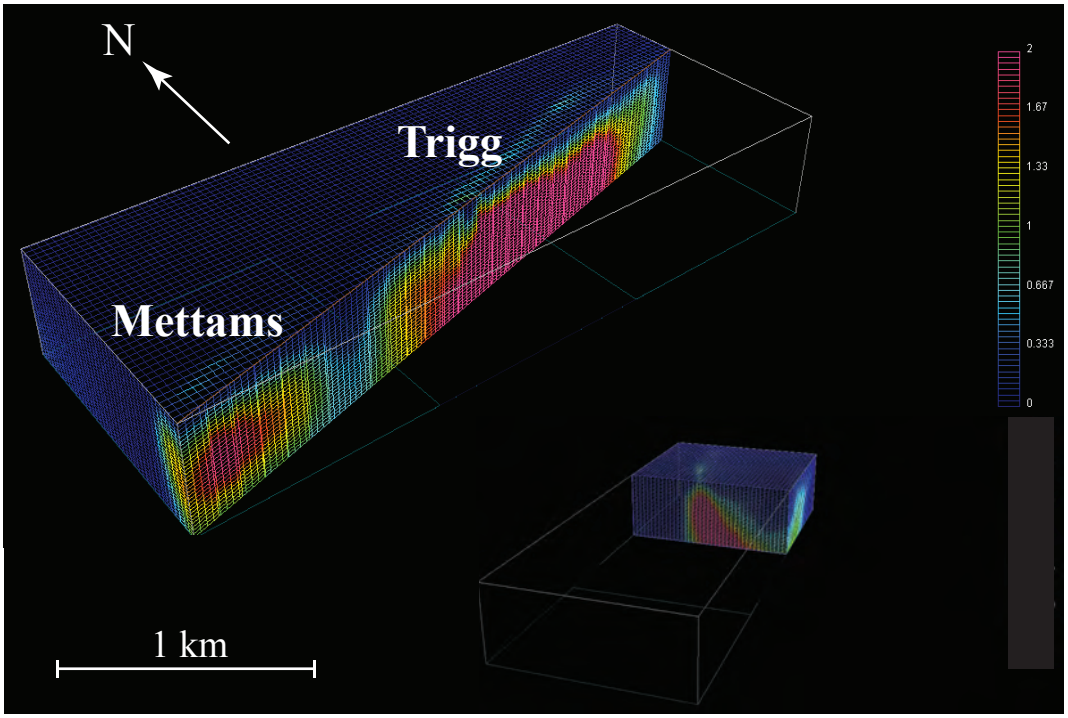

Figure 12: First vertical derivative of the magnetic field at the Trigg and Mettams deposits modelled by P. Hawke (2014) using the MAG3D software (lL and Oldenburg, 2000). Colour scale bar represents arbitrary units

represent discrete zones of extensive, secondary magnetite alteration, rather than simply the magnetic signature of the least-altered BIF macroband. The recognition that fine-grained anhedral hematite constitutes the predominant iron oxide in the least-altered BIF (see section VII) further supports this interpretation. The depth of the upper surface of the anomalous magnetic zones suggests that martitisation extends from surface to a depth of 100-200 m.

VII. Paragenesis of the main alteration mineral phases in the Trigg and Mettams deposits

The Trigg and Mettams deposits exhibit a similar paragenetic mineral sequence that includes up to seven alteration stages (Figs. 13-15).

Least-altered BIF: Anhedral hematite, anhedral magnetite and cryptocrystalline hematite

These minerals define the least altered BIF both in the Trigg and Mettams deposits. Iron oxide-rich bands comprise fine-grained (<5 μm) hematite aggregated with minor jasper or chert (Fig. 14A).

Stage 1: Euhedral magnetite to kenomagnetite

Large euhedral to subhedral magnetite-kenomagnetite crystals up to 500 μm in width occur as disseminated crystals along BIF microbands and as veins that cut BIF (Fig. 14B-14F). Minor quartz veins locally cut euhedral magnetite-rich bands and veins (Fig. 14B, 14F, 14G).

Stage 2: Martite

Solid-state oxidation of stage 1 magnetite to martite initiates along crystallographic planes (Fig. 13E) and progresses until the complete replacement of magnetite (Fig. 14H, 14G, 15A).

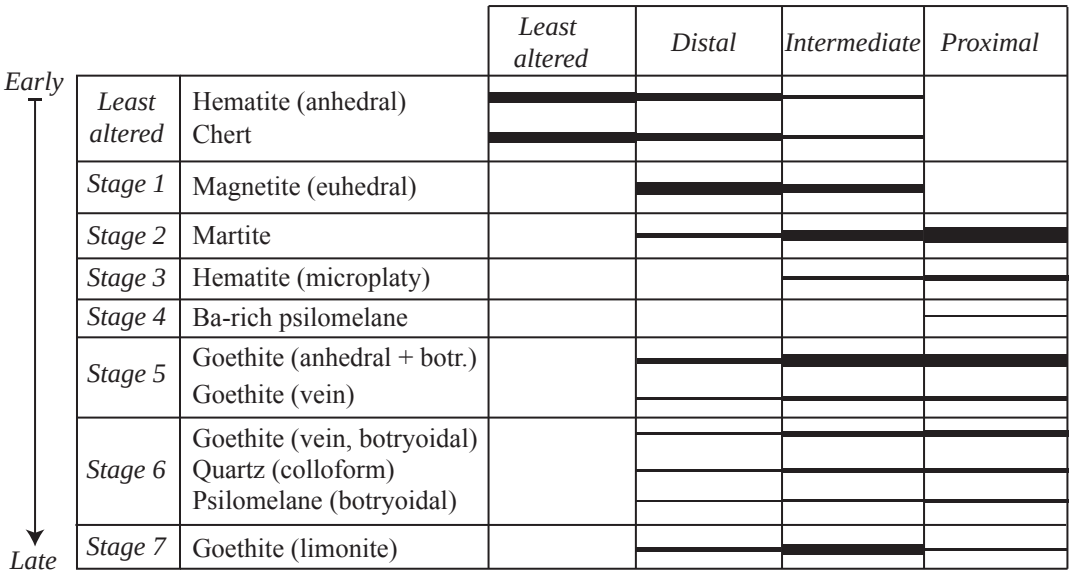

Figure 13: Paragenetic sequence for iron oxides and associated minerals at Abydos.

Stage 3: Microplaty hematite

Hematite microplates up to 5 μm in length locally occur as the dominant iron oxide in unweathered jaspilitic BIF at the Mettams deposit. Microplaty hematite forms as euhedral to subhedral crystals overprinting both stage 1 magnetite (Fig. 13J) and stage 2 martite (Fig. 13K). Locally, larger crystals of microplaty hematite (up to 10 μm in length) occur along veins in equilibrium with quartz (Fig. 13L), suggesting a genetic relationship between veins of microplaty hematite ± quartz and the groundmass of microplaty hematite crystals disseminated within the BIF.

Stage 4: Ba-rich psilomelane

Colloform barium-rich psilomelane locally occurs in the Trigg deposit and is overprinted by stage 5 goethite (Fig. 15B).

Stage 5: Anhedral and botryoidal goethite

This alteration event is responsible for the large volumes of goethitic ore in the Trigg and Mettams deposits. Goethite forms mainly through (i) direct in situ replacement of pre-existing primary hematite, martite and chert (Fig 15D, 15E, 15H), (ii) as botryoidal crystals that fill vugs after prior dissolution and leaching of silica (Fig. 15F) and (iii) as mm- to cm-thick veins that cut chert and martite-rich microbands (Fig. 15G, 15H). Locally, stage 5 goethite veins display an early coating of botryoidal hematite (Fig. 15I).

Stage 6: Massive to botryoidal goethite, colloform chert and psilomelane

In the Trigg deposit, stage 6 massive to botryoidal goethite formed within large (>1 m–thick) veins that cut both unweathered units and bedded to massive goethite ore (Fig. 15J, 15K), in association with minor colloidal silica (Fig. 15L) and late psilomelane.

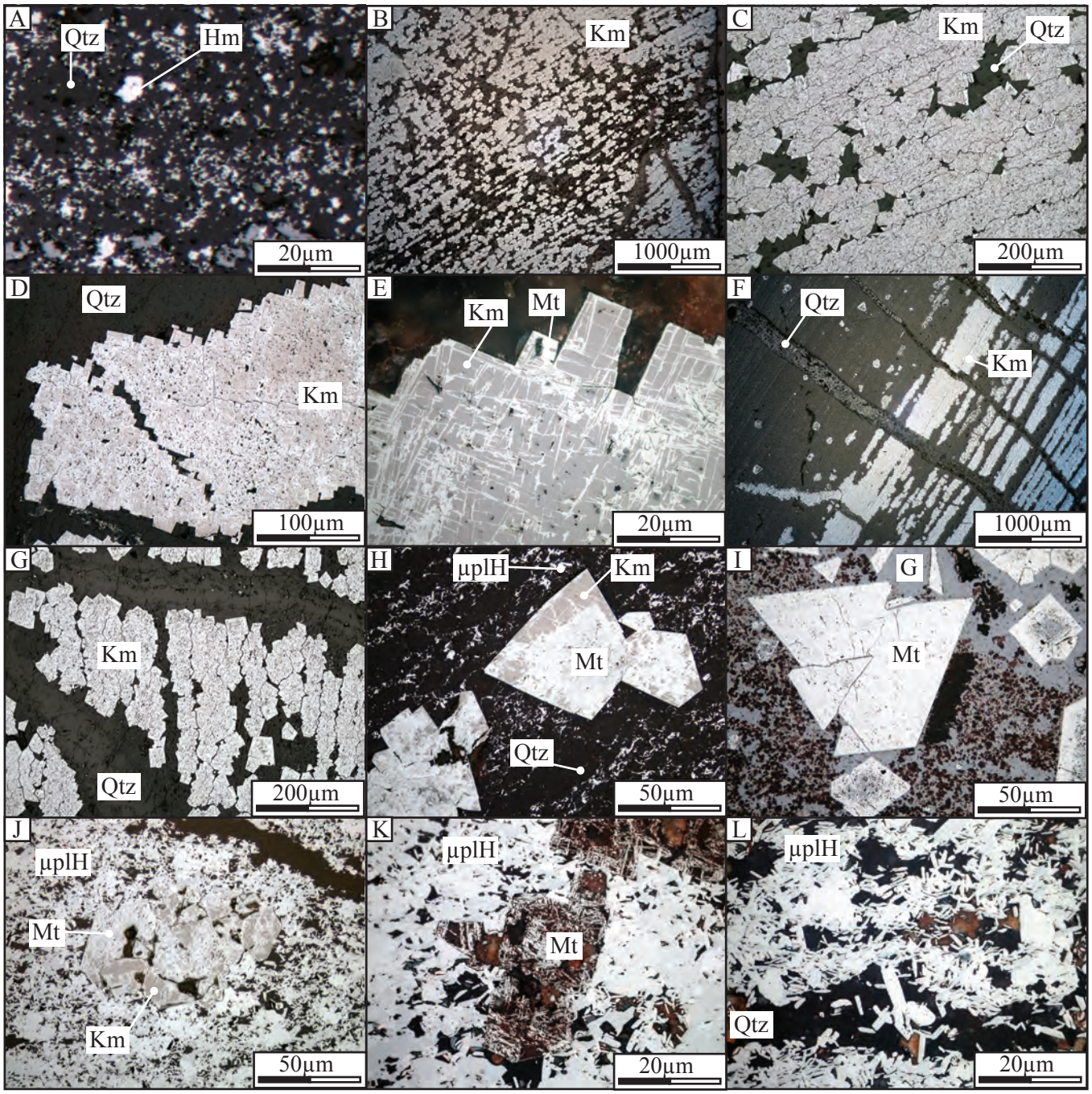

Figure 14: Optic microphotographs of iron oxides and associated minerals at Abydos. Km = kenomagnetite, Mt = martite, Qtz = quartz, G = goethite, Hm = hematite and µplH = microplaty hematite.

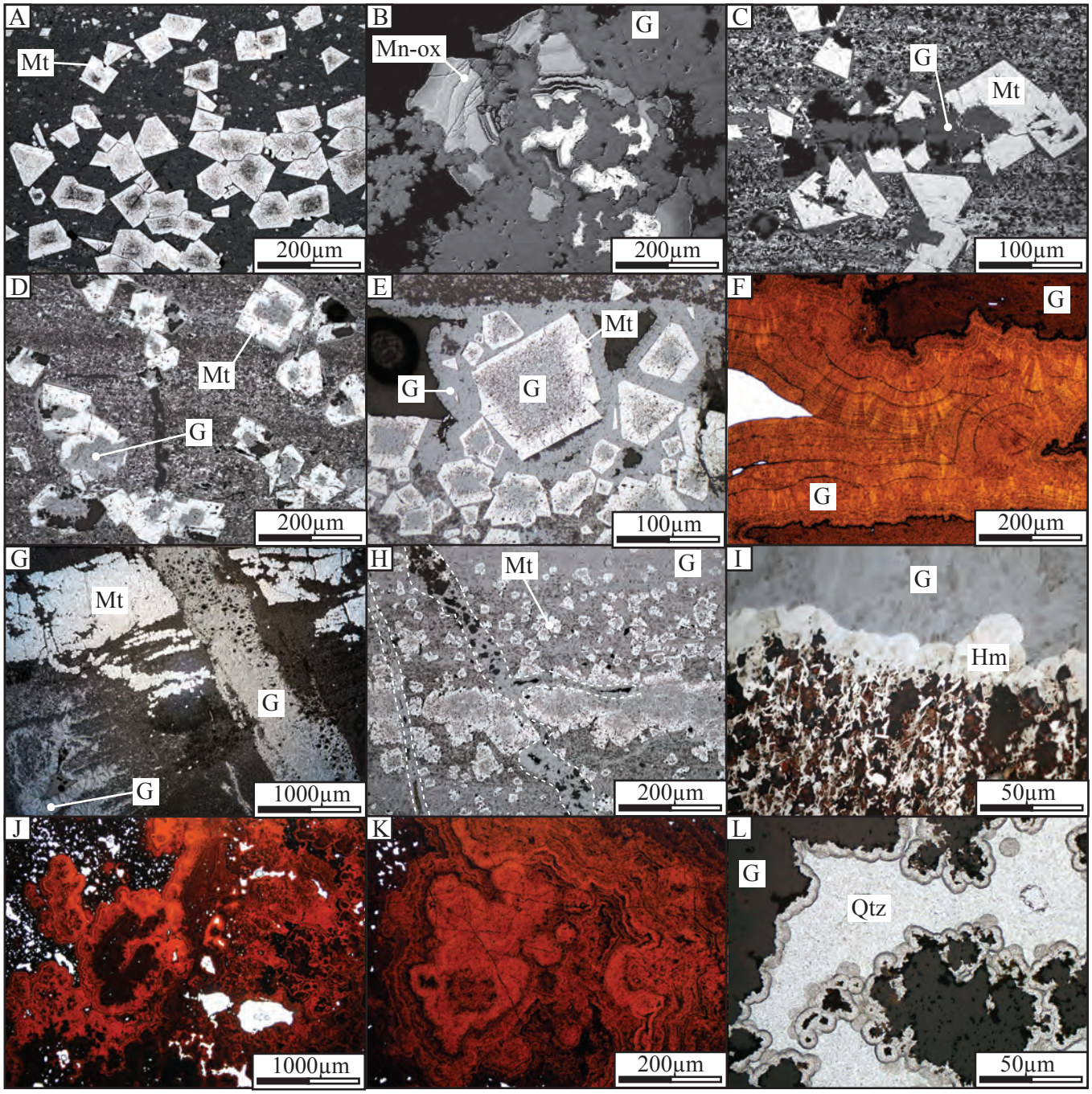

Figure 15: Optic microphotographs of iron oxides and associated minerals at Abydos. Mn-ox = undifferenciated Mn-oxides. See Figure 14 for other mineral abbreviations.

Stage 7: Ochreous goethite

Friable ochreous goethite forms at the expense of stages 5 and 6 goethite (Fig. 6J).

VIII. Mineral trace element geochemistry interpreted from LA-ICP-MS analyses

This section documents the chemical composition of (i) stage 1 euhedral kenomagnetite, (ii) stage 2 martite, (iii) stage 5 goethite and (iv) stage 6 goethite. Fine-grained iron oxides from the least altered BIF and stage 3 microplaty hematite were not analyzed due to spatial resolution limitations associated with the analytical technique.

Stage 1 kenomagnetite (Mettams deposit)

Partial to total martitisation of stage 1 magnetite-kenomagnetite is ubiquitous in the Trigg deposit, and stage 1 euhedral magnetite is best preserved as kenomagnetite in the Mettams deposit. Stage 1 kenomagnetite contains a number of detected trace elements, principally Si (2,000-10,000 ppm), Al (100 to 1,000 ppm), P (20 to 150 ppm), Mg (5 to 100 ppm), Na (5 to 200 ppm), Mn (15 to 200 ppm), Ge (6 to 100 ppm) and Ti (1 to 90 ppm). Importantly, compared to all other iron oxides documented in this section (stage 2 martite, stages 5 and 7 goethite), stage 1 kenomagnetite yields the highest amounts of Ti (up to 90 ppm), Nb (up to 0.09 ppm), and to a lesser extent V (up to 15 ppm), Cr (up to 30 ppm) and Zr (up to 4.5 ppm) (Fig. 18). Ti and Nb show high collinearity and were most likely incorporated together into the lattice during the growth of magnetite crystals. It is proposed that the elevated concentrations in Ti and V, identified from whole-rock geochemistry in the magnetite- to martite-altered samples compared to the least-altered BIF samples, are related to the relatively high amounts of Ti and V within stage 1 kenomagnetite and stage 2 martite (see below), suggesting that these elements may be use as pathfinders for stages 1 and 2 alteration

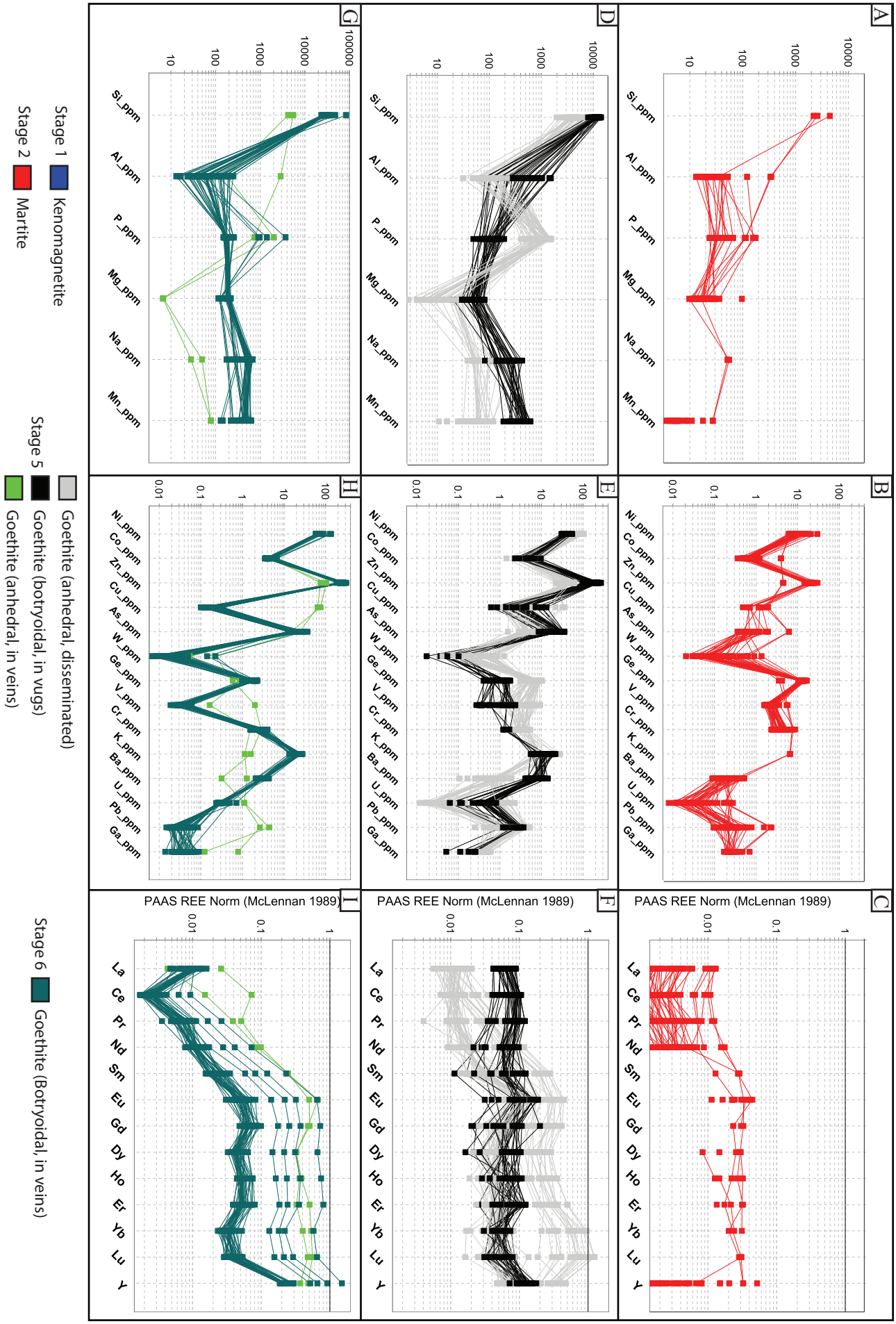

Figure 16: Mineral chemistry data for stages 1, 2, 5 and 6 iron oxides at the Trigg deposit.

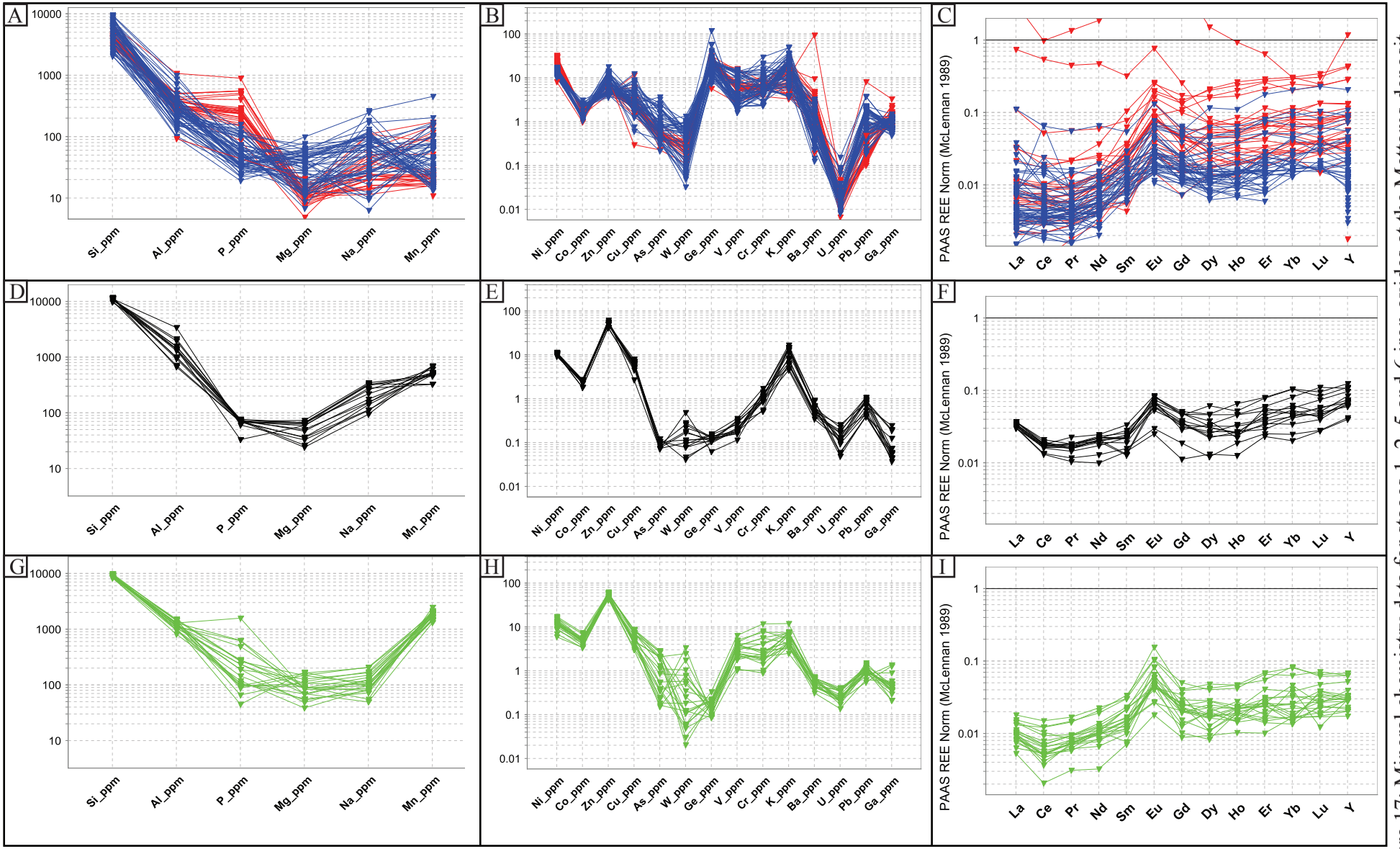

Figure 17: Mineral chemistry data for stages 1, 2, 5 and 6 iron oxides at the Mettams deposit.

events. Normalised to PAAS, stage 1 kenomagnetite displays a flat to slightly positive REE pattern, with minor, positive Ce anomaly and moderate, Eu positive anomaly (Fig. 17).

Stage 2 martite

Trace element chemistry of stage 2 martite from both the Trigg and Mettams deposits was determined. In the Mettams deposit, stage 2 martite displays a clear genetic relationship with nearby kenomagnetite, allowing relevant comparison of the chemistry of both phases. Compared to stage 1 kenomagnetite, stage 2 martite in Mettams is enriched in P (100 to 900 ppm, i.e. ~x5 enrichment), Ni (15 to 35 ppm, x2 enrichment), Zr (1 to 2 ppm, x2 enrichment) and Ga (0.9 to 3.5 ppm, x2 enrichment) (Fig. 17A, 17B, 18). Stage 2 martite also displays REE enrichment (~x3) (Fig. 17C). In contrast, stage 2 martite is depleted in Pb (0.1 to 0.5 ppm, x4 depletion) compared to stage 1 kenomagnetite (Fig. 17, 18). Other trace elements do not exhibit any significant changes compared to stage 1 kenomagnetite.

In the Trigg deposit, stage 1 kenomagnetite is extensively altered to stage 2 martite and was therefore not analysed, precluding a comparison between stage 1 kenomagnetite and stage 2 martite. Stage 2 martite from the Trigg deposit can be compared to stage 2 martite from Mettams. These two populations of martite show important compositional differences with the former (from Trigg) being characterized by lower concentrations of trace elements (typical depletion x2-3), with several elements having much greater (x10 or higher) depletion, including Al (10 to 100 ppm) or Mn (5 to 20 ppm). The most striking compositional difference between stage 2 martite from Trigg and Mettams is observed for Ti, which is strongly depleted (<9 ppm) in Trigg but displays concentrations up to 90 ppm in Mettams. Such discrepancy may arise either from (i) initial compositional difference between stage 1 magnetite from both deposits, or from (ii) removal of Ti during martitisation of stage 1 magnetite in Trigg, whereas Ti remained essentially immobile during martitisation of stage 1 magnetite in Mettams.

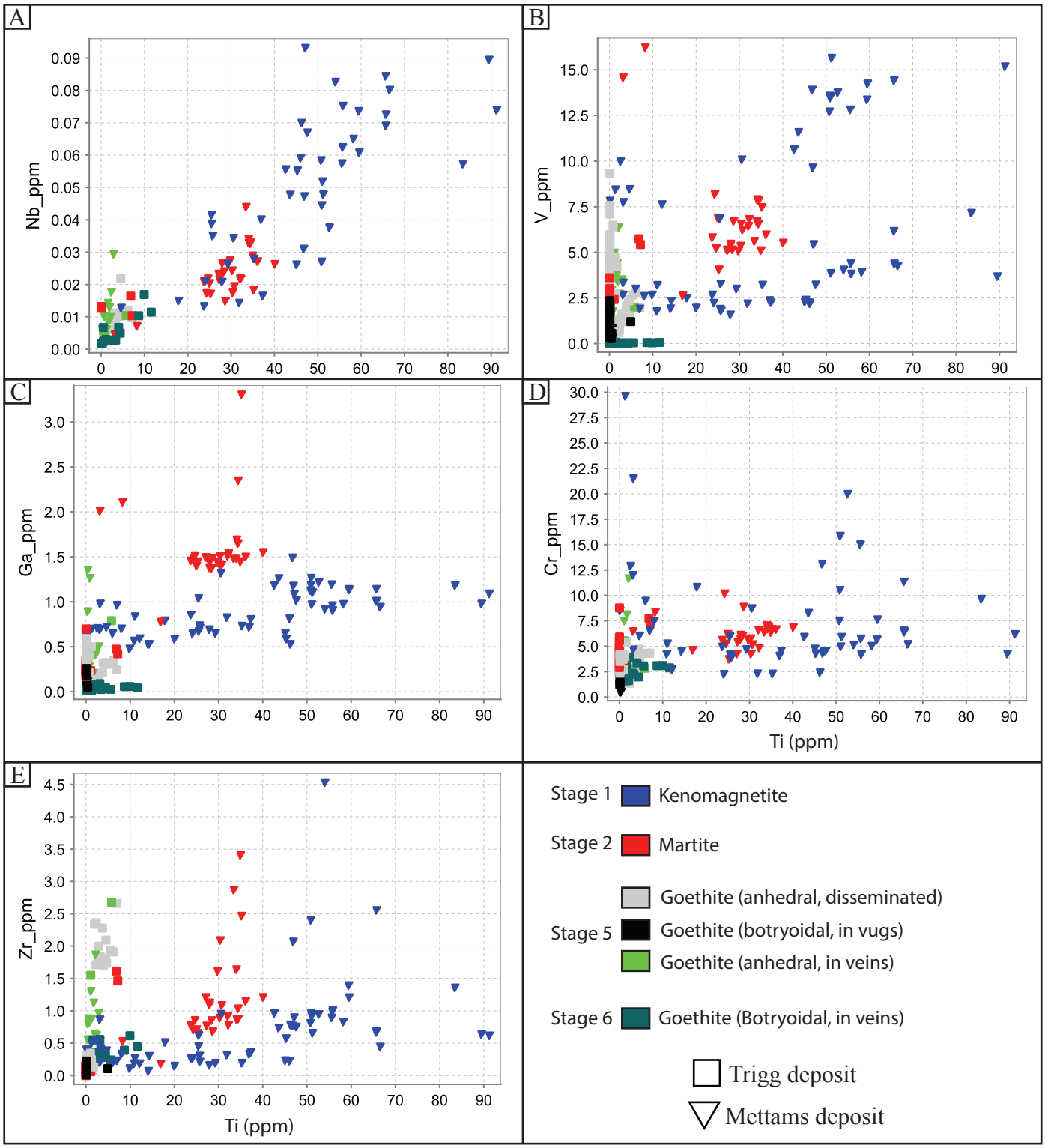

Figure 18: Mineral chemistry data for stages 1, 2, 5 and 6 iron oxides at the Trigg and Mettams deposits.

Stage 5 goethite

Stage 5 goethite displays three main textural types (anhedral goethite disseminated in BIF and other rock types, botryoidal infill of vugs and mm- to cm-thick veins) that show distinct trace element geochemistry. In the Trigg deposit, stage 5 anhedral goethite is characterised by Si (200 to 6,500 ppm), Al (30 to 250 ppm), Mg (3 to 80 ppm), Na (30 to 300 ppm), Mn (10 to 150 ppm), V (0.7 to 10 ppm), Cr (2 to 6 ppm), K (5 to 30 ppm), Ba (0.1 to 2 ppm), U (0.01 to 2 ppm) and Pb (0.2 to 5 ppm) concentrations that are similar to that of stage 1 kenomagnetite and stage 2 martite (Fig. 16). In addition, a number of elements are enriched in stage 5 anhedral goethite compared to stage 1 kenomagnetite and stage 2 martite, including P (200 to 1,500 ppm), Ni (60 to 100 ppm), Co (2 to 10 ppm), Zn (20 to 70 ppm), Cu (1 to 35 ppm), As (2 to 10 ppm), Zr (up to 3 ppm) and HREE (Fig. 16, 18). Conversely, other elements such as Ge (3 to 10 ppm) and Ga (0.1 to 0.6 ppm) are significantly depleted.

In the Trigg deposit, stage 5 botryoidal goethite displays several compositional differences compared to stage 5 anhedral, disseminated goethite, including a threefold increase in Si, Al, Mg, Na, Mn and Ba. Stage 5 botryoidal goethite is also further enriched in Zn (80 to 300 ppm) and As (8 to 35 ppm). At the opposite, stage 5 botryoidal goethite yields lower concentrations of P (40 to 200 ppm), Ni (25 to 60 ppm), Ge (0.3 to 2 ppm), V (0.3 to 2.5 ppm), Cr (1 to 10 ppm) and Ga (0.05 to 0.25 ppm). REE patterns for stage 5 botryoidal goethite are flat with individual elementary concentrations ranging from 0.02 to 0.2 ppm (Fig. 16, 18). Stage 5 botryoidal goethite from the Mettams deposit exhibits most of the compositional characteristics of stage 5 botryoidal goethite from the Trigg deposit, with the exception of much lower As (0.07 to 0.15 ppm, corresponding to a x100 depletion), Ge (0.06 to 0.2, x10 depletion) and Ba (0.3 to 1 ppm, x10 depletion). Other elements including Ni (ca. 10 ppm), Zn (4 to 70 ppm) and V (0.1 to 0.4) show a less pronounced (ca. x4) depletion.

Stage 5 botryoidal goethite in both deposits has similar REE pattern and concentrations, apart from the occurrence of a positive Eu anomaly of moderate intensity in Mettams (Fig. 16. 17).

In the Mettams deposit, stage 5 vein-hosted goethite has similar composition to that of stage 5 botryoidal goethite, apart from (i) higher V (1 to 7 ppm), Cr (1 to 10 ppm), whose concentrations are similar to that of stage 5 botryoidal goethite from Trigg, and (ii) higher Zr (up to 2.5 ppm), whose concentration is similar to that of stage 5 anhedral goethite. In the Mettams deposit, the REE patterns of stage 5 vein-hosted goethite are similar to those of stage 5 botryoidal goethite, although individual element concentrations are two to three times lower and the positive Eu anomaly is more pronounced (Fig. 17, 18). In the Trigg deposit, only two individual analyses of stage 5 vein-hosted goethite have been conducted. These suggest a composition similar to that of stage 5 botryoidal goethite, except for REE which display a pattern similar to that of stage 5 anhedral goethite (Fig. 16).

Bulk samples of bedded to massive goethite ore are dominated by stage 5 anhedral goethite formed by pervasive fluid circulation. Therefore, whole-rock geochemistry of bedded to massive goethite ore samples are mainly controlled by the chemistry of this textural type of stage 5 goethite. The relatively high concentrations in whole-rock samples of a number of elements including Zn, As, Ni, Co and Pb are likely related to the large contribution of stage 5 anhedral goethite to the bedded to massive goethite ore type.

Stage 6 vein-hosted botryoidal goethite (Trigg deposit)

Stage 6 botryoidal goethite formed as thick, late stage veins within the Trigg deposit and displays similar compositions to stage 5 botryoidal goethite, notably higher amounts of Zn (up to 250 ppm), As (up to 40 ppm) and Ba (up to 5 ppm) compared to other textural types of goethite. Significant differences with stage 5 botryoidal goethite include higher Si (20,000 to 90,000 ppm, ca. x3 enrichment), Ti (up to 12 ppm, ca. x10 enrichment) and lower Al (10 to 250 ppm, ca. x8 depletion), Cu (0.1 to 0.2 ppm, ca. x30 depletion), V (0.02 to 0.04 ppm, ca.

x30 depletion), Pb (0.01 to 0.1 ppm, ca. x50 depletion) and Ga (0.01 to 0.1 ppm, ca. x 10 depletion). The REE patterns of stage 6, vein-hosted botryoidal goethite shows a gradational increase from LREE to HREE, together with pronounced negative Ce anomaly and positive Y anomaly (Fig. 16).

Similar to the bedded to massive goethite ore type, high concentrations of a number of elements, including Zn, As, Ni and Ba were identified in whole-rock, massive to botryoidal vein-hosted goethite samples. These can confidently be related to the high concentrations of such elements within stage 6 goethite. As, Ni or Ba may be considered relevant element pathfinders for stages 5 and/or 6 goethite, although additional distinction criteria must be considered to discriminate between these stages. In contrast, Zn represents a reliable and unequivocal pathfinder element for stage 6 goethite. This is supported by the much higher Zn content in the whole-rock sample of late vein-hosted goethite compared to all other analysed samples (Fig. 9B). Similarly, Be displays very high concentrations in late vein-hosted goethite sample (Fig. 9E). Although Be was not analysed during in situ mineral chemistry, it is assumed that stage 6 goethite yields high amounts of Be compared to all other iron oxide phases, and that such elevated concentration is well reflected in whole-rock analyses. Eventually, higher amounts of P occur in the late vein-hosted goethite sample compared to bedded to massive goethite. This is at odds with results from mineral chemistry analyses, which indicate similar amounts of phosphorus in stage 5 anhedral goethite and stage 6 botryoidal goethite.

IX. Constraints on the genetic model for the Abydos iron ore deposits

The different mineral assemblages documented in the Trigg and Mettams deposits reveal a complex mineralisation history resulting from multistage early hypogene alteration and late

supergene weathering. Timing and conditions of formation of these mineral assemblages are discussed in the following section based on field and analytical investigations and integrating the geologic evolution of the Pilbara Craton.

Metamorphic to metasomatic alteration of BIF resulting in D9 fault-hosted, stage 1 hypogene magnetite-enriched BIF

Euhedral magnetite represents the earliest stage of secondary iron oxide formation at the Trigg and Mettams deposits, overprinting primary anhedral hematite and chert bands in BIF. The localisation of intensely developed stage 1 magnetite alteration in D9 high strain fault zones in the Trigg and Mettams deposits supports the interpretation that stage 1 magnetite is derived from the circulation of iron-rich fluids within the fault zones and interaction with proximal BIF wall rock. The presence of stage 1 magnetite in BIF up to 100 m from D9 shear zones suggests the wide penetration of these fluids into BIF wallrock.

Unweathered Archean BIF typically contains recrystallised, euhedral magnetite and hematite formed during diagenetic to metamorphic processes (Klein, 2005; Angerer and Hagemann, 2012; Nadoll et al., 2014). Mineral chemistry data for stage 1 kenomagnetite indicates that, with the exception of Al, Fe-substituting cations occur in trace amounts (< 200 ppm). In addition, the ratio Co/Ni does not exceed 0.1. Such characteristics are typical of metamorphic magnetite in BIF (Nadoll et al., 2014) and are compatible with a metamorphic origin for stage 1 magnetite. In contrast, in the Sierra Norte deposits (Brazil), magnetite is characterized by average Co and Ni concentrations that exceed 500 and 350 ppm, respectively, together with Co/Ni ratios greater than 1, and is interpreted as the result of the interaction between the itabirite and felsic magma-derived fluids (Figueiredo e Silva et al., 2008). The evolution of the Pilbara Craton since the deposition of the Cleaverville Formation is marked by several events that could have contributed to the formation of stage 1 euhedral magnetite:

(i) 2950-2940 Ma: The major North Pilbara orogenic event, referred to as the D9 regional deformation event (Hickman and Van Kranendonk, 2008a). D9 orogeny involved greenschist to amphibolite facies metamorphism, as indicated by metabasalts in the Croydon Group of the Mallina Basin (Van Kranendonk et al., 2002).

(ii) 2930-2900 Ma: The emplacement of late granites of the Sisters Suite and layered mafic-ultramafic intrusions of the Radley Suite, essentially confined to the western half of the Northern Pilbara Craton.

(iii) 2930-2900 Ma: The Mosquito Creek orogeny, restricted to the SE section of the northern Pilbara (regional D12).

(iv) 2900–2803 Ma: Granitic intrusion of the Cutinduna and Split Rock Supersuites and associated with pegmatite-hosted, tin-tantalum mineralisation (Huston et al., 2002).

(v) 2770-2760 Ma: The Fortescue Rifting Event, with likely thermal effects of thick plateau basalt deposition. Many older faults, such as those formed during D9, were reactivated by the regional crustal extension of this event (Thorne and Trendall, 2001).

(vi) 2215-2145 Ma: Regional prehnite-pumpellyite metamorphism with associated temperatures not exceeding 350°C (Smith et al., 1982; Rasmussen et al., 2005, White et al., 2014), followed by widespread metasomatism of the Fortescue basalts (White et al., 2014). Rasmussen et al. (2005) propose that this event was probably driven by the northward-advancing Ophthalmian fold-and-thrust belt that developed during protracted collision with the Pilbara Craton, and argue that the widespread geographic and stratigraphic distribution of ca. 2.2 Ga phosphates suggests that fluid flow was intense and pervasive.

The formation of stage 1 magnetite is most likely related either to the 2950-2940 Ma North Pilbara Orogeny or the 2215-2145 Ma regional metamorphic to metasomatic event, as other documented events are spatially confined to areas distal to the Abydos iron camp. Because the circulation of mineralising fluids along fault zones is most efficient when these structures are active, precipitation of euhedral magnetite may have taken place during the North Pilbara Orogeny, along developing D9 fault zones. Alternatively, formation of stage 1 magnetite may be related to the 2215-2145 Ma regional metamorphic to metasomatic event, via the circulation of reduced fluids through reactivated D9 fault zones. In the absence of absolute age constraints for stage 1 alteration event, both the 2950-2940 Ma and 2215-2145 Ma events could be responsible for the formation of stage 1 euhedral magnetite.

Martitisation and formation of microplaty hematite

The martitisation of stage 1 magnetite to stage 2 martite is characterised by a significant increase in P, Ni, Zr and Ga and a depletion in Pb. Stage 2 martite is then overprinted by stage 3 microplaty hematite, for which no trace element chemistry is available. Martite documented in various iron ore deposits in association with microplaty hematite or goethite (Angerer and Hagemann, 2010; Angerer et al., 2012; Duuring and Hagemann, 2010, 2012) is often interpreted to be the result of oxidising metasomatic processes caused by descending ancient meteoric waters interacting with BIF. A similar interpretation is well suited for the formation of martite at Abydos and would involve early (Proterozoic) supergene fluids, possibly during metasomatism at ca. 2145 Ma. Descending supergene fluids may have also resulted in the formation of stage 3 microplaty hematite, which usually forms at temperatures greater than 100°C (Taylor et al., 2001).

Multistage supergene goethite and hematite alteration

Late-stage alteration of the Cleaverville BIF at Abydos includes (i) an early, local stage of Ba-rich psilomelane precipitation (stage 4), (ii) intense and dominantly pervasive goethitisation of BIF and clastic sedimentary units (stage 5), (iii) formation of secondary, massive to botryoidal goethite hosted by thick subhorizontal veins (stage 6) and (iv) a late stage of ochreous goethite formation (stage 7).

We hereafter focus our discussion on alteration stages 5 and 6, which represent the dominant goethitic mineralisation events involved in the formation of high-grade iron ore at Abydos. Although the relative timing between the formation of the different textural types of stage 5 goethite is unclear, it is assumed that all stages were approximatively coeval, and that stage 5 goethitisation initiated through the progressive replacement of existing chert- and iron oxide-rich bands by anhedral goethite and continued by precipitation of botryoidal goethite in existing vugs and was followed by the formation of mm- to cm-thick mineralized veins. The three textural types of stage 5 goethite can be divided into two groups with distinct chemical signatures: (i) the dominant anhedral goethite formed by pervasive replacement of BIF whereas (ii) the mm- to cm-thick vein-hosted goethite together with botryoidal goethite formed in vugs. The first group is characterized by increased concentrations of several elements including P, As, Zn and Ba compared to stages 1 to 3 iron oxides. The second group shows further enrichment in Al, Zn and Ba but minor enrichment in P and Ni. Stage 6 massive to botryoidal goethite displays a similar composition to that of stage 5 botryoidal goethite including higher concentrations of Zn (up to 250 ppm), As (up to 40 ppm) and Ba (up to 5 ppm) compared to other textural types of goethite. Other workers have established that the presence of dissolved sulphate in goethite-precipitating fluids drastically increases the capability of goethite to incorporate zinc and arsenic into its lattice during crystal growth (Rose and Bianchi-Mosquera, 1993; Swedlund et al., 2009). The noticeable enrichment in Ba

associated with stages 5 and 7 botryoidal goethite may be related to the dissolution of pedogenic evaporitic minerals such as barite by supergene fluids in the upper parts of the weathering profile. In such a case, the release of sulphate into descending supergene fluids may be responsible for the elevated Zn and As in crystallising goethite. Although Zn, As and Ba display higher concentrations in stages 5 and 7 botryoidal goethite compared to earlier kenomagnetite and martite, the intensity of Zn, As and Ba enrichment is moderate compared with the Wodgina iron camp. At Wodgina, two main stages of goethite formation include (i) earlier goethite mineralisation dominantly through pervasive fluid circulation and (ii) formation of late, botryoidal hematite. The earlier goethite yields Zn, As and Ba concentrations similar to those of stages 5 and 6 goethite documented in Abydos. However, later botryoidal goethite at Wodgina displays much higher Zn, As and Ba concentrations (up to 10,000, 400 and 70 ppm, respectively) when compared to all types of goethite in Abydos. Such drastic increase in the concentrations of Zn, As and Ba in goethite has been interpreted to be the result of major changes in weathering conditions at ca. 50 Ma, from warm and humid tropical environment favouring the development of deep weathering profiles to strongly seasonal, semi-arid environment favouring cyclical precipitation and dissolution of evaporitic minerals. It remains unclear whether such an interpretation is equally suitable to stages 5 and 6 goethitisation events in Abydos.

X. Implications for exploration

First-order (critical) controls on the formation of high-grade iron ore deposits in the Abydos camp include the presence of (i) thick iron-rich primary BIF from the Cleaverville Formation, (ii) D9 event, fault zone-hosted, stage 1 hypogene magnetite-rich ore zones in BIF, (iii) intensely developed pervasive supergene alteration and (iv) the near-surface exposure of the

high-grade iron ore bodies hosted by BIF. Second-order (constituent) controls are those that are locally present in the Abydos camp, but are not critical for the formation of mineable high-grade ore deposits. These second-order controls include the occurrence of (i) formation of microplaty hematite after martitisation and (ii) emplacement of late-stage, thick subhorizontal goethite veins (stage 7).

The least-altered BIF from the Cleaverville Formation exposed throughout the Abydos iron camp is prospective since it contains more than 35 wt. % Fe_2O_3 and thus represents an elevated starting position for subsequent iron enrichment in the rock via interaction with hydrothermal fluids. The primary thickness of major BIF macrobands has an average thickness of up to 100 m throughout the camp, but increases up to 2,500 m thickness in areas of structural complexity arising from F9 folds and thickening of BIF units.

Mapping of the Abydos iron ore deposits highlighted the presence of fault zones oriented parallel to bedding. It is likely that the titling of BIF macrobands and activation of these fault zones occurred during regional transpression at ca. 2950-2940 Ma (regional D9 event). These shear zones locally host <50 m-thick zones of stage 1 hypogene magnetite that result in the moderate intensity upgrade of iron in the BIF. Reactivation of these shear zones by multiple events likely enhanced and broadened the permeability of these damage zones in BIF. These broad damage zones are the optimum areas for the circulation of later supergene fluids through BIF resulting in the creation of extensive supergene goethite ± hematite-rich ore bodies.

Considering that the shear zone-hosted, magnetite-rich ore zones identified in the Trigg and Mettams deposits are narrow (<50 m wide) ore zones of moderate iron grades (60-65 wt. % Fe_2O_3), they are unlikely to represent exploration targets for stand-alone high-value ore deposits. Nevertheless, they represent zones where early upgrade of the least-altered BIF

favours the development of large ore bodies after subsequent supergene alteration, especially as the presence of early forming deformation zones affecting BIF also controls, to some extent, the later supergene alteration. These shear zone-hosted ore bodies have the added potential to control deeper extensions to near surface supergene ore bodies owing to their steep dips and likely presence beneath the weathering front. Targeting stage 1 magnetite alteration using trace element compositions of these minerals is challenging but remains possible based on its relatively high contents in Ti and V identified from whole-rock and mineral chemistry analyses. Considering the widespread presence of supergene goethite in near-surface exposures of BIF, these pathfinder elements are useful in specific geological conditions and thus have local use as vectors to shear zone-hosted, magnetite (martite)-rich ore zones. Predictive exploration for stage 1 magnetite in Abydos can also confidently rely on airborne and ground based magnetic surveys, as both the Trigg and Mettams deposits display well expressed highly magnetic zones. In addition, the position of the upper surface of anomalous magnetic zones in 3D forward inversion models may provide first-order information on the depth of demagnetised zones, i.e. zones of intensive martitisation and/or goethitisation, although such anomalism may be more subdued in areas of thick transported cover.

Supergene goethitisation is the dominant alteration style in all deposits in the Abydos camp. It is responsible for generating large volumes of high-quality (iron grade and contaminant level) iron ore. Supergene enrichment in the fold-thickened BIF took place as a multi-stage mineralising event involving the interaction between near-surface derived, oxidised fluids and BIF. The earliest recognised stage of supergene goethitisation (i.e. stage 5 goethite) represents the most economically important mineralisation stage at Abydos in terms of its extensive distribution. Mineral chemical analyses indicate that Ni and As positive anomalies, detectable from whole-rock mineral chemical analysis, may be used as pathfinders for stages

5 and 6 goethite-rich iron ore. In addition, stage 6 goethite can unequivocally be recognised using Zn and Be as element pathfinders. The unequivocal targeting of stage 5 goethite remains challenging as most of the potential elementary pathfinders display positive anomalies both in stages 5 and 6 goethite. Nevertheless, a combination of several pathfinder elementary signatures (e.g. positive Ni and/or As enrichment combined with the absence of Be enrichment and/or absence of extreme Zn enrichment, i.e. > 100 ppm) can be confidently used to specifically target stage 5 goethite.

Future exploration efforts should be centred on the accurate mapping of magnetite- to martite-altered jaspilitic BIF occurrence and location of thick structural damage zones in BIF throughout the Abydos project area. Upon completion of mapping available outcrop in the project area, the next focus is the predictive exploration of blind supergene ore deposits. This task will involve the identification of the same geological features identified for surface mapping (BIF, folds, deformation zones), but will rely upon interpreting geophysical data beneath areas of transported cover and projecting structural observations to these areas. It should be noted that this study focussed on just two deposits within the Abydos camp with the aim of interpreting geological controls on iron ore formation in BIF. Areas of structural interest in the wider camp, such as the presence of potentially fold-thickened BIF located along strike to the SW of the Mettams deposit was not tested but represent an obvious area for testing structural controls on iron mineralisation.

XI. Conclusions

The Trigg and Mettams deposits at Abydos principally consist of goethite-martite rich ore bodies hosted by a 100 to 250 m-wide jaspilitic BIF macroband of the 3.02 Ga Cleaverville Formation in the East Strelley greenstone belt of the Pilbara Craton, Western Australia. One

major deformation event at ca. 2950-2940 Ma (North Pilbara Orogeny, regional deformation event D9) affects the Cleaverville BIF through tilting of the BIF units and emplacement of bedding-parallel, broad fault zones. Unweathered BIF records an early stage of euhedral magnetite precipitation concentrated along D9 fault zones, likely related either to the North Pilbara Orogeny, or to regional low-grade metamorphism to metasomatism from 2215 to 2145 Ma. Although stage 1 alteration is widespread and pervasive, it is largely concentrated along, or proximal to, high strain D3 shear zones, which represent focused pathways for alteration fluids. Formation of D9 fault zone-hosted, metamorphic to metasomatic magnetite locally results in an initial upgrade in iron in the BIF from ca 30 to 40-45 wt% Fe. Subsequent martitisation (stage 2) of stage 1 magnetite and formation of microplaty hematite (stage 3) is interpreted as an early (Proterozoic) process caused by heated, descending ancient meteoric waters interacting with BIF. Stage 1 magnetite and stage 2 martite are associated with relatively high amounts of Ti and V which represent potential pathfinders for alteration stages 1 and 2. Recent (Cretaceous to Cenozoic) supergene alteration partly replaces martite-rich BIF, forming the large volumes of goethite that comprise the main portion of high-grade ore zones in both deposits. The recent supergene sequence is dominantly represented by stage 5 goethite, mainly occurring as disseminated anhedral goethite via pervasive fluid related to weathering. Further development of the supergene system involved the formation of vein-hosted, massive botryoidal goethite. The ubiquitous spatial distribution of stage 5 goethite indicates that it represents the dominant mineralisation stage responsible for the formation of volumetrically important ore bodies at Corunna Downs. Nevertheless, stage 6 goethitisation is also of significant importance in the formation of the larger iron ore body at Trigg. Stage 5 goethite may be confidently targeted using a combination of elements including Ni, As, Zn and Be. Stage 6 event may be targeted using Zn or Be as standalone element pathfinders.

Chapter 4: High-grade Fe mineralisation in Mesoarchean BIF at the Pardoo mine, Western Australia

I. Introduction

Exploration strategies for detecting high-grade (>55 wt. %) iron ore in the Pilbara Craton have historically relied upon the identification of exposed supergene hematite-goethite-rich orebodies. However, exploration in the Pilbara (Western Australia) is now reaching a mature state in that discovery success is slowing using the current exploration model. The opportunity now exists to develop a more predictive exploration strategy using innovative techniques for the Pilbara Craton; a strategy that targets (i) near-surface supergene hematite-goethite ore, (ii) deeper extensions of hypogene magnetite-rich ore and (iii) the detection of "blind" orebodies beneath surface transported cover and unmineralized BIF. The key to this predictive approach to exploration lies in (i) establishing the geological criteria that control the location of high-grade iron orebodies within an iron camp and (ii) extrapolating these findings to other iron camps and the remainder of the Pilbara Craton. For this reason, the

Ridley Magnetite project area, located about 60 km east of Port Hedland, is an important locality for understanding the combined effects of supergene and hypogene processes on the formation of high-grade iron ore. In this context, it is the aim of this study to identify the main controls on high-grade (>50 wt. % Fe or 70 wt. % Fe_2O_3) iron ore in the Bobby and ALX deposits within the Pardoo iron camp, North Pilbara Craton, Western Australia.

In this Chapter, we first summarize the main outcomes of previous investigations conducted by Kollert (2014) at the Alice Extension (ALX) deposit and the neighbouring Rosita prospect and Hemme (2014) at the Bobby and adjacent Glenda deposits (see Appendices 1 and 2). Both studies focus on the main controls on iron mineralisation at Pardoo, including the documentation of local geology, deformation sequence and whole-rock geochemistry. Secondly, based on new observations conducted on additional samples, we propose an update of the paragenetic sequence documented by Kollert (2014) at the ALX deposit and Rosita prospect, including the recognition of two stages of supergene goethite-hematite mineralisation postdating the first two stages of hypogene magnetite and hematite alteration. We present new mineral chemistry data for iron oxides derived from ALX and Rosita ore zones. The conditions and timing of iron mineralisation at Pardoo are discussed before pathfinder elements are proposed for high-grade iron ore.

II. Previous work

Regional and deposit geology

The Pardoo project is located about 75 km east of Port Hedland (Fig. 1) and lies within the Ord Range Greenstone Belt of the Central Pilbara Tectonic Zone (Fig. 2). The southern extent of the Ord Range is defined by the Pardoo fault, which is an extension of the Tabba Tabba shear zone (Fig. 2). Iron mineralisation in the Ord Range is mainly hosted by banded iron formation assigned to the Cleaverville Formation (formerly Nimingarra Iron Formation, ca. 3016 Ma) of the Gorge Creek Group. At Pardoo, the Cleaverville Formation is characterised by a succession of five major BIF members referred to as the Upper BIF, the Ord-Ridley BIF, the Bobby BIF, the Olivia BIF and the lower BIF. These form prominent ridges defining a camp-scale S-shaped fold (a southern anticline and a northern syncline). Investigated areas at Pardoo were conducted on the northern limb of the camp-scale syncline and include the Bobby and Glenda pits (Bobby BIF member) as well as the ALX pits and prospects (Ord Ridley BIF member).

In the Bobby and Glenda pits areas, the Bobby BIF member is only about 100 m-thick, E-W trending and subvertical to steeply S-dipping. The Bobby pit is centred on the southern margin of the Bobby BIF whereas the Glenda pit is positioned on its northern margin. The least altered BIF in ALX is an alternating sequence of fine-grained iron oxide (dominantly hematite), quartz and jasper bands, whereas the least altered BIF in Bobby and Glenda pits show an alternating sequence of micro- to mesobands of quartz and goethite. At Bobby, clastic sedimentary rocks occur to the north and south of the main BIF macroband; the northern contact between BIF and clastic rocks (exposed in the northern wall of the Glenda pit) is sharp, whereas the southern contact exposed in the Bobby pit forms a 50 m-thick transitional zone of alternating rock types. Several examples of 0.2 to 3 m-thick, intensely

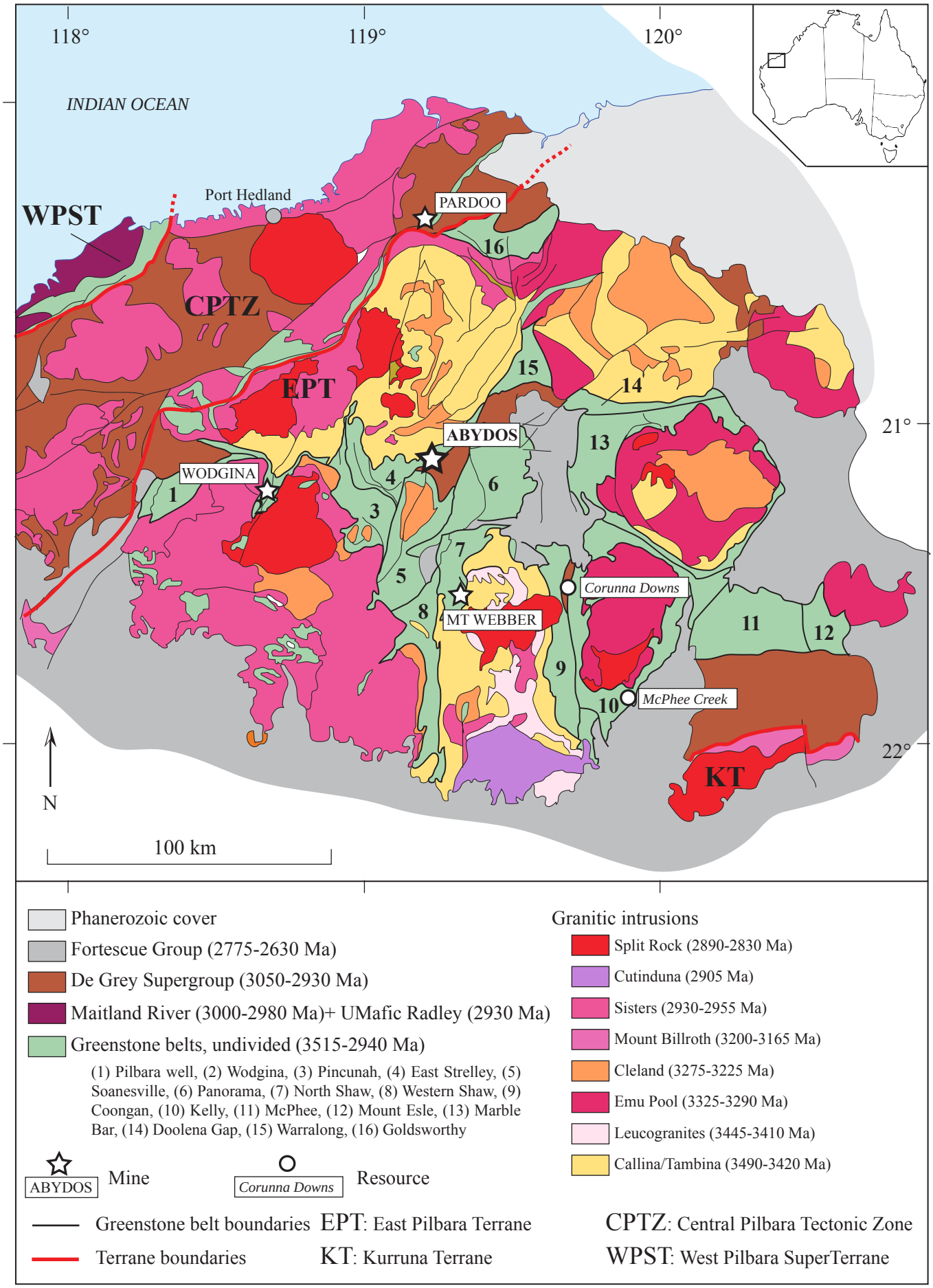

Figure 1: Simplified geology map of the North Pilbara craton including the location of the Pardoo iron camp and active iron ore mines across the North Pilbara. *Modified after Hickman, 2012.*

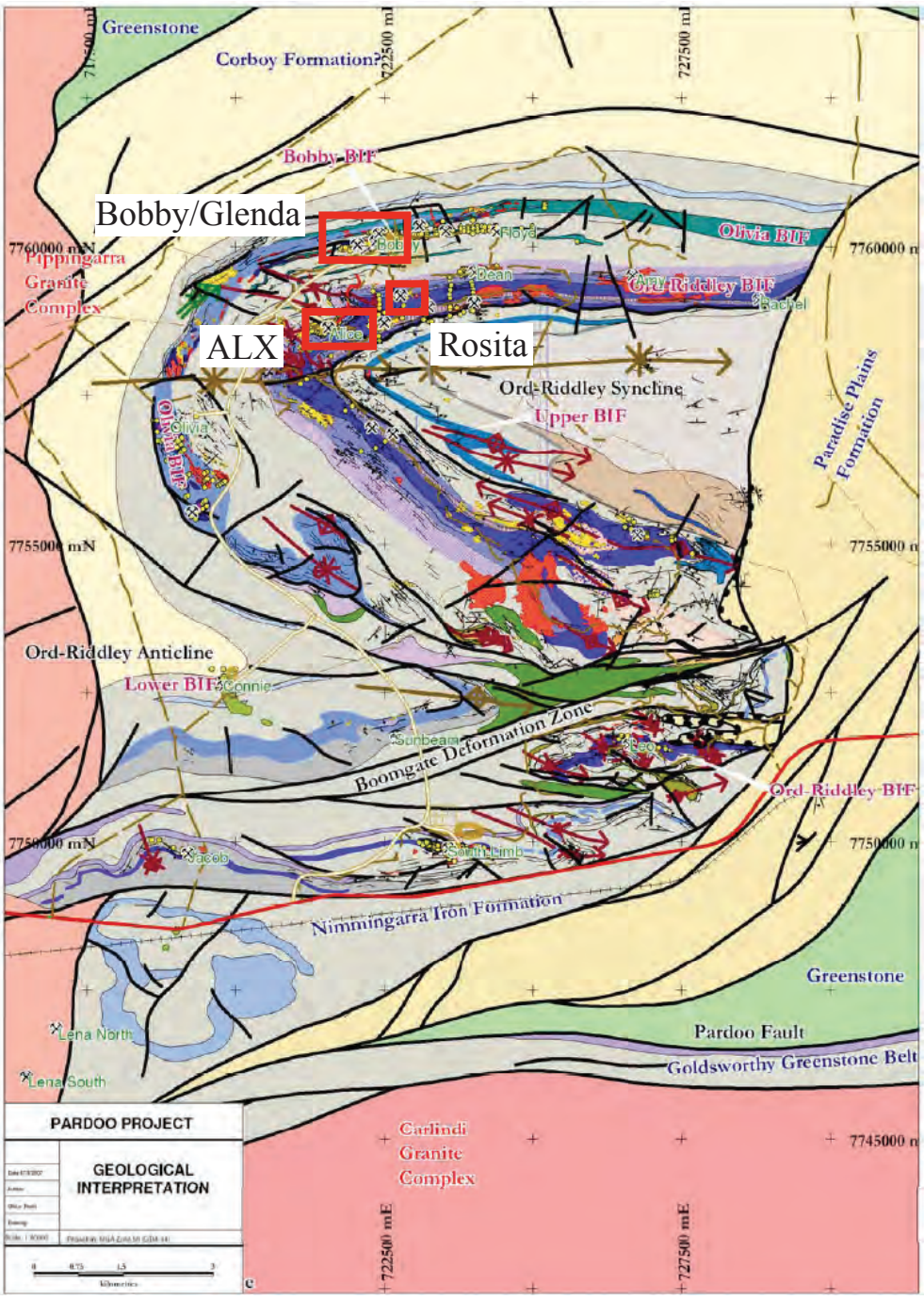

Figure 2: Simplified geology map of the Pardoo iron camp. *Modified from Atlas Iron Ltd*

weathered, steeply dipping mafic dykes cut the clastic sedimentary rocks and BIF in the Bobby and Glenda pits.

In the ALX pit and neighbouring Rosita prospect, the Ord-Ridley BIF member is about 500 m-thick, ENE-SSW trending and steeply S-dipping. The least altered BIF consist of an alternating sequence of fine-grained iron oxide (dominantly hematite), quartz and jasper bands. Both the ALX pit and the Rosita prospect lie along the northern edge of the Ord-Ridley BIF. Clastic sediments to the north of ALX and Rosita are poorly exposed. Several examples of 0.2 to 3 m-thick, intensely weathered, steeply dipping mafic dykes cut the clastic sedimentary rocks and BIF in the Bobby and ALX deposits.

Structural controls on mineralisation at the ALX deposit and Rosita prospect

The deformation and mineralisation histories at the ALX deposit (and the neighbouring Rosita prospect) and the Bobby + Glenda deposits, documented by Kollert (2014) and Hemme (2014), include a series of events that can be defined within a local scale scheme (AL for ALX and Rosita, BB for Bobby and Glenda, and PD for the global Pardoo camp). In addition, numbering of deformation (D_i) and folding (F_j) events as proposed by Kollert (2014) and Hemme (2014) have been homogenised to match the deformation scheme (i.e. D_i deformation event produces F_i folds).

- $D1_{PD}$ event, characterised by brittle-ductile shear zones that host medium- to coarse-grained euhedral magnetite and local platy hematite (specularite) together with wider jaspilitic alteration halos, represents the earliest significant deformation event recorded in the ALX deposit and Rosita prospect. A 10 to 20 m-thick, hypogene and supergene altered shear zone occurs in the centre of the ALX pit. This main shear zone is associated with intense ochreous goethite-hematite supergene alteration overprinting earlier hypogene magnetite and hematite. The shear zone results in a broad, 50-70 m thick,

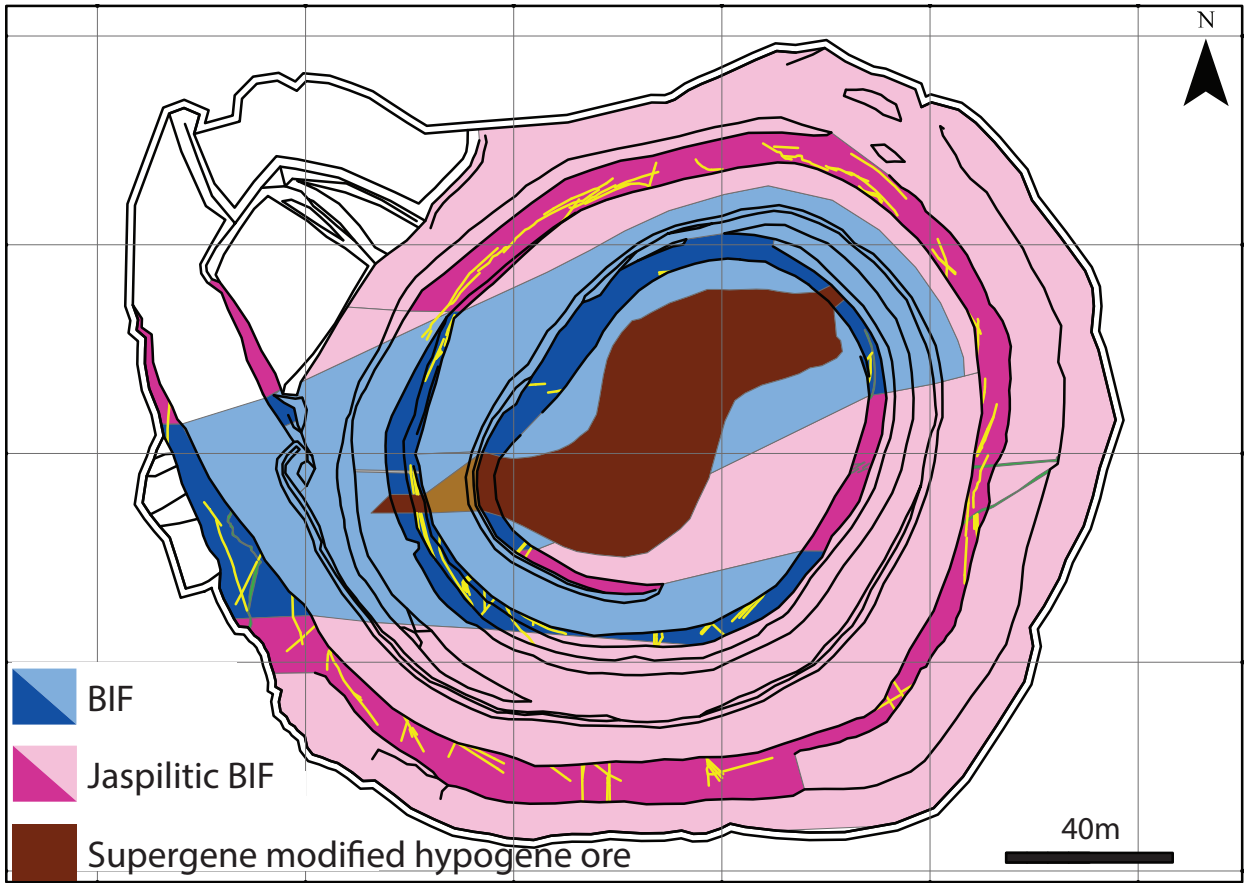

Figure 3: Simplified geology map of the ALX deposit. *Kollert, 2014*

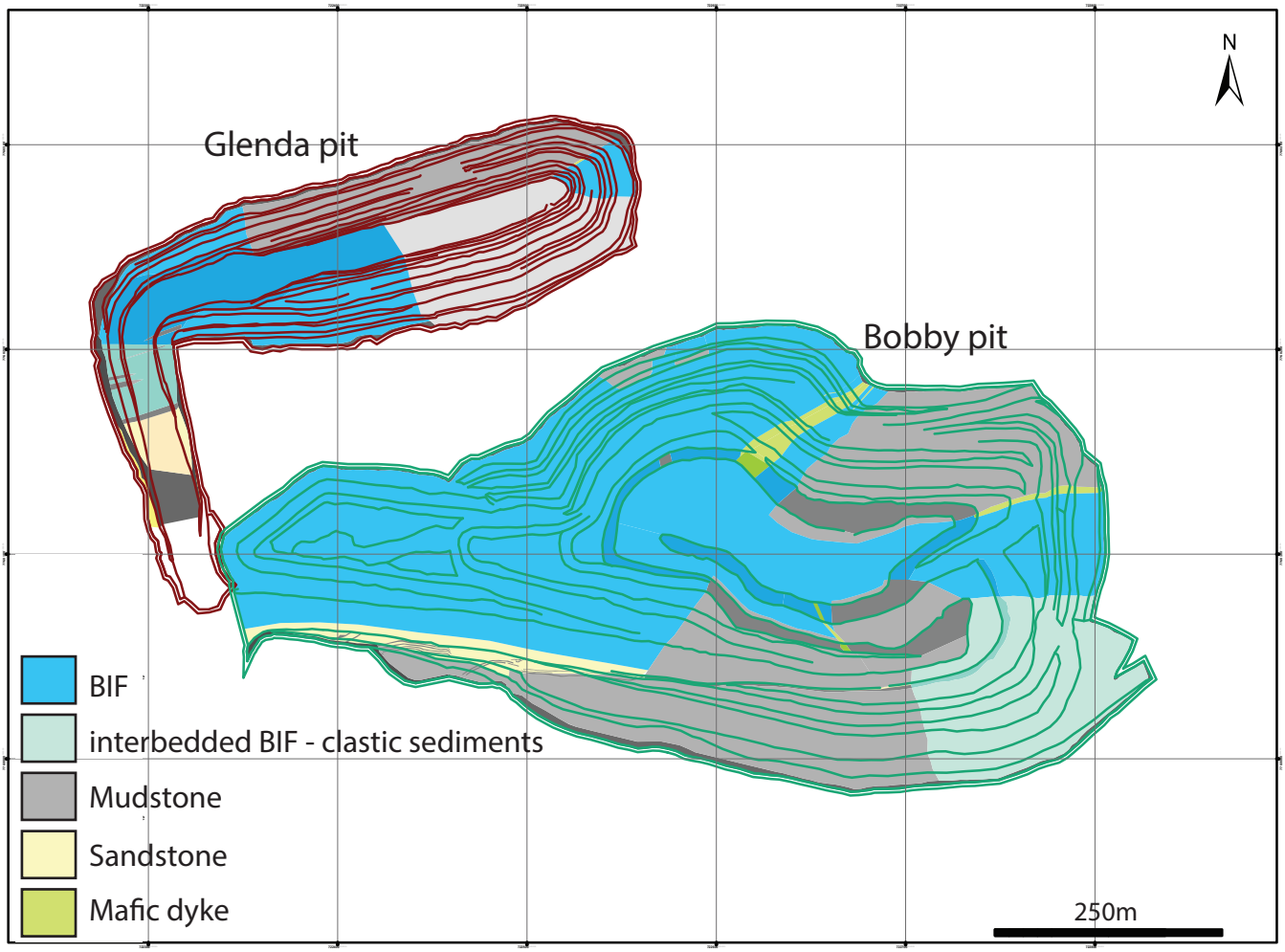

Figure 4: Simplified geology map of the Bobby and Glenda deposits. *Hemme, 2014*

supergene-modified hypogene ore body that displays a S-shaped geometry resulting from later $F2_{PD}$ folding. Comparable but narrower (1 to 3 m-thick) mineralised shear zones are present in the Rosita prospect.

- $D2_{PD}$ event formed tight, early S-shaped folds that plunge 60 to 80º to the SE in the ALX pit and Rosita prospect. This deformation stage resulted in the important thickening of the BIF and $D1_{PD}$ hypogene mineralised shear zones.

- Bedding, $D1_{PD}$ mineralised shear zones, and $F2_{PD}$ folds are subsequently folded by open, $F3_{PD}$ folds that strike SSE and have axial planes that dip about 80° towards 230°-270°. The $F3_{PD}$ folds plunge 60-80° towards the SE and have subvertical N-S trending axial planes.

- The schistose fabric in late brittle-ductile shear zones in the ALX pit is crenulated to define centimetre-scale open, recumbent $F4_{AL}$ folds with axial planes that dip 20° towards NE.

- Mafic dykes ($D5_{AL}$) locally occur in the ALX pit. These dykes are unaffected by $D1_{AL}$ to $D4_{AL}$ events but are displaced by $D6_{AL}$ to $D8_{AL}$ brittle faults.

- Primary bands and $D1_{AL}$ to $D4_{AL}$ structures are cut by $D6_{AL}$ to $D8_{AL}$ brittle fault zones. At least three generations of brittle faults are recognised based on their orientations. The first generation of fault zones is mostly oriented NW with a dip of 40° to 50°. The second generation is oriented NE with a low dip of about 10°. A third generation plots about NW to SW with a steep dip of about 85°. The cross-cutting relationship of these three fault generations is unknown.

Structural controls on mineralisation at the Bobby and neighbouring Glenda deposits

- The earliest structures observed in the Bobby and Glenda pits are ESE-plunging folds that fold bedding contacts and bands within BIF, displaying a S-asymmetric shape in plan view and mostly N-limb-down asymmetric in sectional view. These folds are equivalent to the $F2_{AL}$ folds observed at the ALX deposit.

- The first generation of fault zones ($D3_{BB}$) are mostly oriented parallel to bedding (~60°/160°). The faults are subsequently filled by 0.01 to 10 m-thick, massive vitreous goethite veins.

- $F2_{BB}$ folds and $D3_{BB}$ faults are folded by upright, open $F4_{BB}$ folds that trend N-S.

- Mafic dikes ($D5_{BB}$) cut bedding but are not affected by the early $F2_{BB}$ and $F4_{BB}$ folding events.

- The second generation of faults ($D6_{BB}$) trend approximately NW and dip steeply towards 240-250°. The faults displace bedding contacts in sandstone with a normal W-side-down displacement of at least 20 m. A subparallel fault located in the southern wall of the Bobby pit also records normal fault movement. The deformed mudstone layers on the western side of the fault zone display drag folding associated with the displacement. Minor vitreous goethite alteration is associated with the fault zone.

- A third generation of faults ($D7_{BB}$) trends NNE and dips about 60 ° towards 100-120°. The third-generation faults cut bedding contacts with centimetre-scale displacements. These faults are locally filled with quartz, kaolinite, or vitreous goethite veins.

- A 20 m-thick, E-W trending, steeply S-dipping fault or shear zone ($D8_{BB}$) cuts the BIF in the centre of the Bobby pit. Within this deformation zone, BIF is intensely altered to ochreous goethite and martite. A strong schistosity is defined by the alignment of iron

oxide mineral and flattened primary BIF bands. This shear zone coincides with the thickest high-grade goethite-hematite orebody in the Bobby deposit. The goethite-hematite altered shear zone results in the local fragmentation of earlier vitreous goethite veins. Ochreous goethite is the dominant iron oxide within the shear zone. BIF is very soft and friable due to the replacement of primary quartz bands by ochreous goethite. The Glenda pit coincides with the sheared northern contact of the BIF. In this locality, the shear zone is narrow (<1 m wide) and characterized by intense supergene hematite alteration. Displacement lineations are preserved along the planes of the hematite-altered shear zone.

The local deformation sequences documented in the ALX, Bobby and Glenda deposits and in the Rosita prospect show important similarities. Early shear zones ($D1_{AL}$) only occur in the ALX deposit and neighbouring Rosita prospect. In contrast $D2_{AL+BB}$ folds are well-expressed at the camp-scale in all investigated areas. Upright $F3_{AL}$ and $F4_{BB}$ folds are likely related to the same generation event. Mafic dikes ($D5_{AL+BB}$) and later fault zones ($D6\text{-}8_{AL+BB}$) are also observed in both deposit areas. Several of these deposit- to camp-scale deformation events may be interpreted within the framework of the regional deformation scheme proposed by Hickman and Van Kranendonk (2008a). In this context, the tilting of the BIF and the ubiquitous $D2_{AL+BB}$ folding can be confidently assigned to the regional D9, 2950-2940 Ma North Pilbara Orogeny as it represents the only deformation event of major intensity that affected the BIF between its deposition at 3020 Ma and the deposition of the overlying, undeformed <2775 Ma Fortescue Group (Thorne and Trendall, 2001). Because the timing of early shear zone development in the BIF macrobands at ALX ($D1_{AL}$) is bracketed between the tilting of bedding and the $D2_{AL+BB}$ folding, it likely occurred as an early D9 event. The emplacement of mafic dikes is most likely related to the emplacement of the Fortescue basaltic province (post-D12 in the regional scheme) initiated at 2775 Ga through the

development of the Black Range dolerite intrusions and the associated deposition of the Mount Roe Basalt eruptive sequence (Thorne and Trendall, 2001; Hickman, 2012). In this context, the multiple generations of late brittle, essentially normal faults are likely related to normal faulting during or shortly after the deposition of the Fortescue Group.

Whole-rock geochemistry

The Fe_2O_3 content of least-altered BIF in Bobby and Glenda pits is 63.79-63.83 wt. % whereas the least altered samples of ALX show an abundance of 22-27 wt. %. This difference is primarily due to the absence of fresh BIF samples in Bobby, where the least-altered BIF samples display significant supergene enrichment. The high C content (3.1-5.0 wt. %) and the high LOI values (9.5-16 wt. %) of least-altered BIF in ALX highlight the abundance of iron-rich ankerite. In the Bobby deposit, the high LOI of 7.42-8.1 wt. % results from the partial goethitisation of the least-altered BIF. In all deposits, supergene goethitic ore displays significant enrichment (>100%) of several elements, most notably As, Zn, Cu and Ba. In addition, the ALX deposit displays weakly weathered, hypogene altered BIF that is strongly enriched in W (212 %) and moderately enriched in Be (93 %), Lu (75 %), and Yb (59 %) (Kollert, 2014). All these elements may potentially be used as pathfinders towards zones of hypogene and/or supergene alteration in BIF.

III. Revised paragenetic sequence for the ALX deposit and Rosita prospect

The ALX deposit and the Rosita prospect exhibit a similar paragenetic mineral sequence that includes up to six alteration stages (Fig. 5-7).

Least altered: Anhedral hematite, anhedral magnetite and jasper

This mineral association defines the least altered BIF in the ALX deposit and the Rosita prospect. Iron oxide-rich bands comprise fine-grained (<5 μm) hematite aggregated with

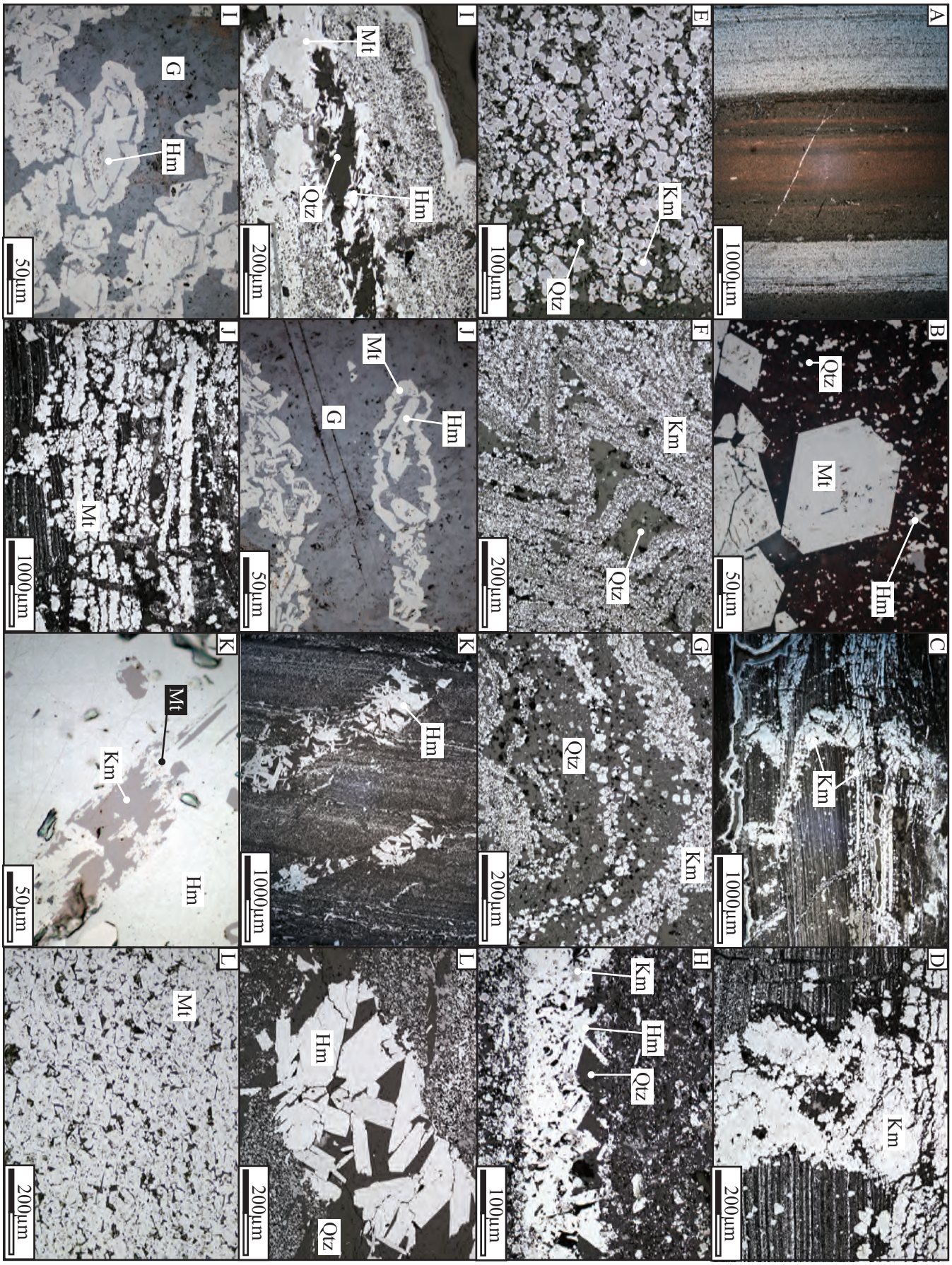

Figure 5: Optic microphotographs of iron oxides and associated minerals at ALX and Rosita. Km = kenomagnetite, Mt = martite, Qtz = quartz, G = goethite and Hm = hematite.

minor magnetite, jaspilite or chert (Fig. 5A, 5B). Iron-oxide poor bands are dominantly composed of quartz locally associated with ankerite.

Stage 1: Euhedral magnetite to kenomagnetite

Large euhedral to subhedral magnetite-kenomagnetite crystals up to 200 µm in width occur as disseminated crystals along BIF iron-rich microbands and as veins cutting BIF (Fig. 5C-5E). Bands of disseminated stage 1 magnetite are folded by $F2_{AL}$ folds (corresponding to the regional D9 deformation event), demonstrating the early timing of stage 1 magnetite formation.

Stage 2: Platy hematite (specularite)

Stage 2 platy hematite occurs band-parallel and cross-cutting veins in association with quartz (Fig. 5H-5L). Platy hematite also replaces or overgrows stage 1 magnetite-kenomagnetite (Fig. 5H-5J) or pre-existing ankerite (Fig. 5I).

Stage 3: Martite

Solid-state oxidation of stage 1 magnetite to martite initiates along crystallographic planes and progresses until the complete replacement of magnetite (Fig. 5J). The relative timing between stage 2 platy hematite and stage 3 martite remains poorly constrained and these two stages may have been coeval, although local textural relationships may be interpreted as evidence for the earlier timing of stage 2 platy hematite (Fig. 5K). Alternatively, it is possible that martitisation occurred during early alteration in association with platy hematite and during later alteration in association with goethite. Martitisation of the magnetite-enriched BIF is locally associated with important leaching of silica, resulting in a significant residual enrichment in iron (Fig. 5L).

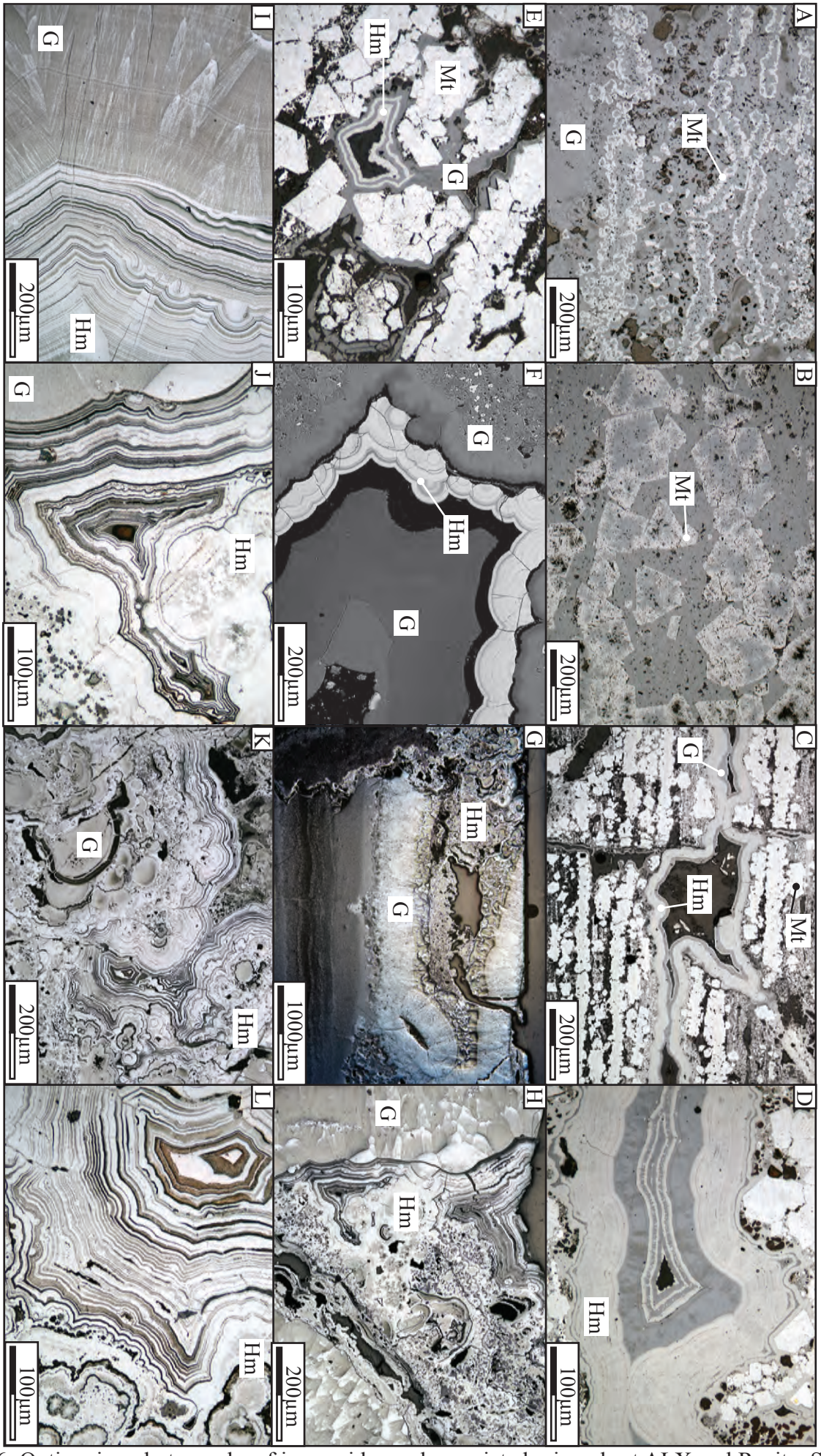

Figure 6: Optic microphotographs of iron oxides and associated minerals at ALX and Rosita. See Figure 5 for mineral abbreviations.

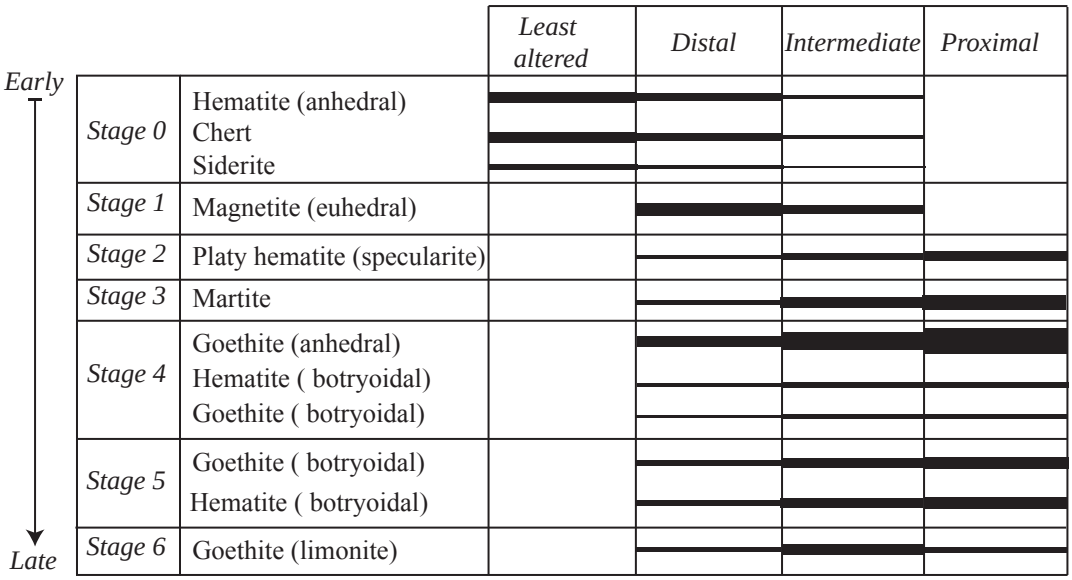

Figure 7: Paragenetic sequence for iron oxides and associated minerals at Pardoo

Stage 4: Anhedral goethite, botryoidal hematite and goethite

Stage 4 goethitisation corresponds to the most significant event of goethitic mineralisation at ALX and Rosita. Anhedral goethite replaces primary chert and iron-bearing minerals as well as other hypogene iron oxides (Fig. 6A, 6B). It is locally accompanied and/or followed by the formation of botryoidal hematite and goethite in open spaces and along mm- to cm-thick veins. Botryoidal hematite commonly formed before botryoidal goethite (Fig. 6C, 6D), although more complex textures are locally expressed with multiple alternations of hematite and goethite defining colloform layers (Fig. 6E).

Stage 5: Secondary botryoidal goethite and hematite

A second stage of alternating botryoidal goethite and hematite is widely expressed at ALX and Rosita. It is characterised by the formation of botryoidal goethite overgrown by botryoidal hematite displaying complex zoning textures most likely inherited from variations in the concentration of elements such as Al or Si substituting for Fe (6F-6L). Locally, stage 5 botryoidal hematite is overgrown by botryoidal goethite (Fig. 6F).

Stage 6: Ochreous goethite

Friable ochreous goethite forms at the expense of stages 4 and 5 goethite.

IV. Mineral chemistry

This section documents the chemical composition of (i) stage 1 euhedral kenomagnetite, (ii) stage 2 platy hematite, (iii) stage 3 martite, (iv) stage 4 goethite and hematite and (v) stage 5 goethite and hematite from the ALX deposit and Rosita prospect. Fine-grained iron oxides from the least altered BIF were not analyzed due to spatial resolution limitations associated with the analytical technique.

Stage 1 kenomagnetite

Stage 1 kenomagnetite contains a number of detected trace elements (Fig. 8A-C, 9A), principally base cations such as Si (3,000-30,000 ppm), Mg (400-20,000 ppm), Ca (60-2,000 ppm), Mn (30-10,000 ppm), Na (60-250 ppm), K (10-200 ppm) and Al (20-150 ppm). Other trace elements occurring in significant amounts include P (10-50 ppm), Cr (3-0 ppm), Ti (2-20 ppm), Ge (5-10 ppm), Zn (3 to 10 ppm), As (0.5-7 ppm), Co (3-6 ppm), Ni (1.5-3.5 ppm) and Ba (0.5-4 ppm). Stage 1 kenomagnetite also contains minor (1 ppm or lower) V, Zr, Ga, W, Cu, Sn, Mo, Rb, Sr and Pb. La, Ce and Y are the only REE detected in stage 1 kenomagnetite (Fig. 9B). Interestingly, stage 1 kenomagnetite displays the highest Mg content of all iron oxides analysed in the present study, suggesting that this element may be used as pathfinder for stage 1 alteration. However, due to the presence in significant amounts of Mg-bearing carbonates in least-altered BIF, positive Mg anomalies in whole-rock analysis cannot be unequivocally related to the presence of high-Mg magnetite overprint as it could also result from the presence of early carbonates.

Stage 2 platy hematite

Stage 2 platy hematite, often occurring as replacement or overgrowth after stage 1 magnetite-kenomagnetite, is consistently depleted in base cations and other trace elements compared to stage 1 kenomagnetite (Fig. 8A-C, 9A, 9B). Strong depletion is observed for Mg (10-500 ppm, i.e. x40 depletion), Al (0.5-10 ppm, i.e. x20 depletion), Ca (<10 ppm, i.e. x20 depletion), Ni, Co, Cu (x20 depletion) and Ga, Ge, Zn, K, Ba, Rb (x10 depletion). A threefold decrease is also observed for Si, P, Mn, Cr. Na, Zr, Sn, Mo. Detectable REE+Y (La, Ce, Y) do not exhibit any significant changes in concentration from stage 1 kenomagnetite to stage 2 platy hematite. In contrast, Ti (30-100 ppm), V (1.8-3 ppm) and W (0.07-1 ppm) are enriched in stage 2 platy hematite compared to stage 1 kenomagnetite by a factor ~x4.

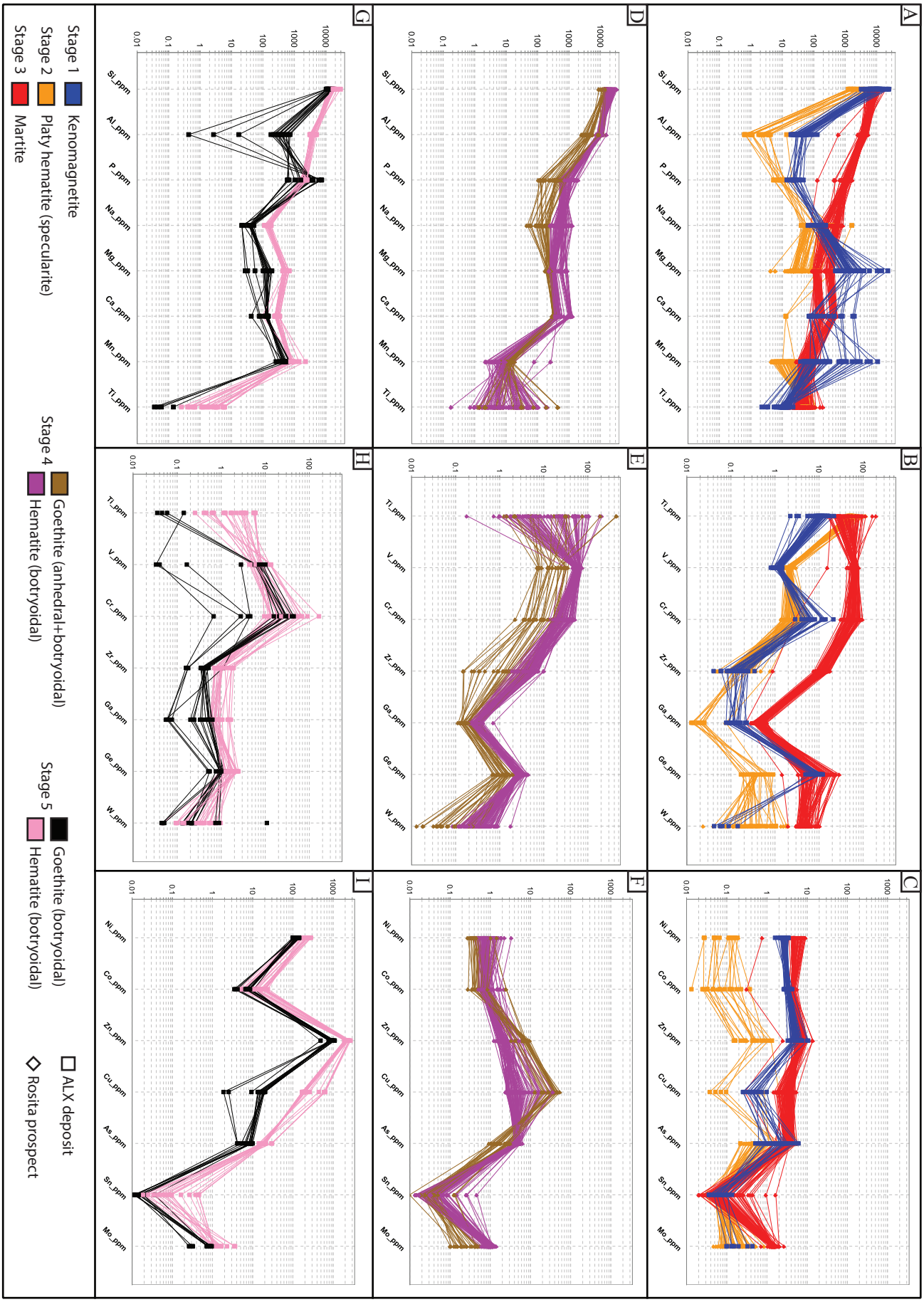

Figure 8: Mineral chemistry data for stages 1 to 5 iron oxides from ALX and Rosita.

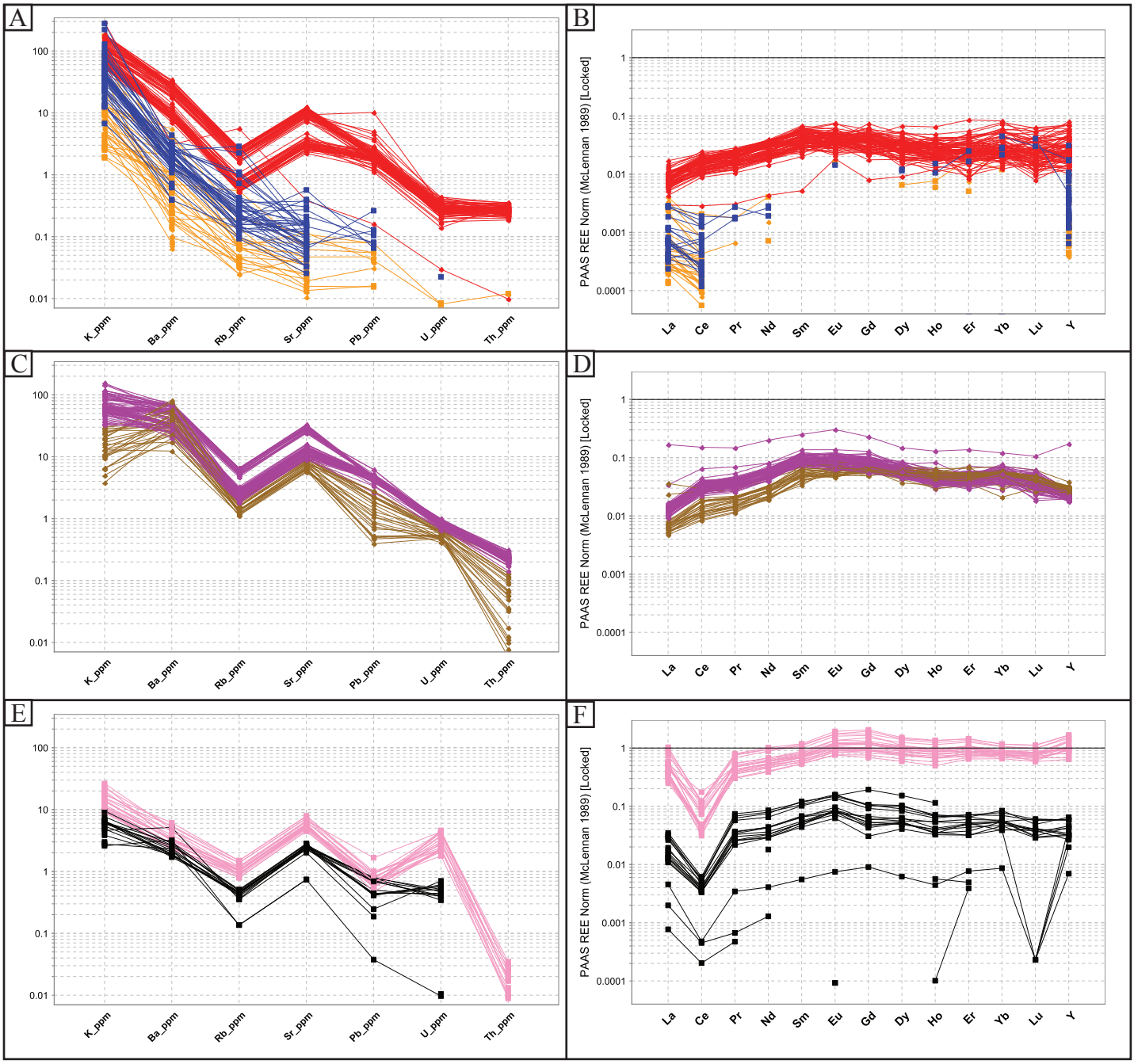

Figure 9: Mineral chemistry data for stages 1 to 5 iron oxides from ALX and Rosita. See Figure 8 for colour coding.

Stage 3 martite

Stage 3 martite displays significant compositional changes compared to stage 1 kenomagnetite and stage 2 platy hematite (Fig. 8A-C, 9A). Compared to stage 1 kenomagnetite, these changes include a large increase in Al (250-400 ppm, i.e. x60 enrichment), P (400-1,500 ppm, x40 enrichment), V (40-90 ppm, x50 enrichment), Cr (30-100 ppm, x10 enrichment), W (3 to 10 ppm, x50 enrichment), Zr (8 to 20 ppm, x100 enrichment), Sr (2-10 ppm, x50 enrichment), Pb (1-5 ppm, x50 enrichment) together with U and Th that are higher than 0.1 ppm. Other significant enrichments are observed for Ti, Cu, Ba, Rb and Mo (ca. x10) and for Na and Ga (ca. x5). All REE+Y are enriched in stage 3 martite, and display a slightly positive slope pattern for LREE and a flat pattern for HREE (Fig. 9B). As most of these elements are depleted in stage 2 platy hematite compared to stage 1 kenomagnetite, the enrichment observed in stage 3 martite is even more pronounced when compared to stage 2 platy hematite. Si, Ca, Ge, Co, Zn, As and Sn do not exhibit any significant changes compared to stage 1 kenomagnetite. In contrast, only Mg shows a pronounced depletion in stage 3 martite, compared to stage 1 kenomagnetite (100-400 ppm, x10 depletion). Importantly, among all the iron oxides documented in the present study, stage 3 martite shows the highest concentrations in W and Zr, which may be used as pathfinder elements for stage 3 alteration. The positive anomaly in W documented by Kollert (2014) from whole-rock geochemical analysis of hypogene ore likely relates to the observed high W content within stage 3 martite. Ge, which yields high concentrations in stage 1 kenomagnetite and its oxidised equivalent, stage 3 martite, may also be used as a pathfinder for stage 3 alteration.

Stage 4 goethite and hematite

Alteration stage 4 is characterised by the formation of (i) anhedral goethite pervasively replacing primary hematite, stage 1 kenomagnetite, stage 2 platy hematite and stage 3 martite) and chert, and (ii) formation of botryoidal hematite and goethite in vugs and along veins. Stage 4 goethite and hematite show quite similar composition to stage 3 martite (Fig. 8D-F, 9C); compositional characteristics of stage 4 iron oxides are therefore compared in this section to stage 3 martite rather than to stage 1 kenomagnetite. In addition, stage 4 anhedral and botryoidal goethite display undistinguishable composition, supporting a common origin from a single mineralisation event, and are thereafter merged and referred to as stage 4 goethite. Apart from P and Na, which display similar concentrations compared to stage 3 martite, a number of elements are enriched in stage 4 goethite by a factor x5, including Al, Mg, Ca, Ba and Cu. In contrast, stage 4 goethite is depleted by a factor x10 or higher in K, Mn, V, Cr, Zr, Ga, Ge, W, Ni, Co and Mo. Other elements, including REE+Y, do not exhibit significant differences compared to stage 3 martite (Fig. 9D).

Stage 4 botryoidal hematite displays systematic element enrichments by a factor x2-3 compared to stage 4 goethite, with the exception of (i) Ti, Sn, Ba and HREE+Y that yield similar concentrations in both minerals and (ii) Mn, Zn, Cu that, in contrast, are slightly depleted (x2-3) in the botryoidal hematite (Fig. 8D-F, 9C, 9D).

Stage 5 botryoidal goethite and hematite

Stage 5 alteration resulted in the overgrowth of botryoidal goethite by botryoidal hematite. Locally, botryoidal hematite is overgrown by late goethite. Compared to stage 4 goethite, stage 5 botryoidal goethite displays increased amounts of P (700-8,000 ppm, x4 enrichment), Mn (200-500 ppm, x20 enrichment), Ni (100-200 ppm, x400 enrichment), Co (3-10 ppm, x10 enrichment), Zn (500-1000 ppm, x100 enrichment) and As (5-10 ppm, x 2 enrichment) (Fig 8G-I). In contrast, it yields lower amounts of Al (100-1,000 ppm, x5 enrichment), Na (20-50

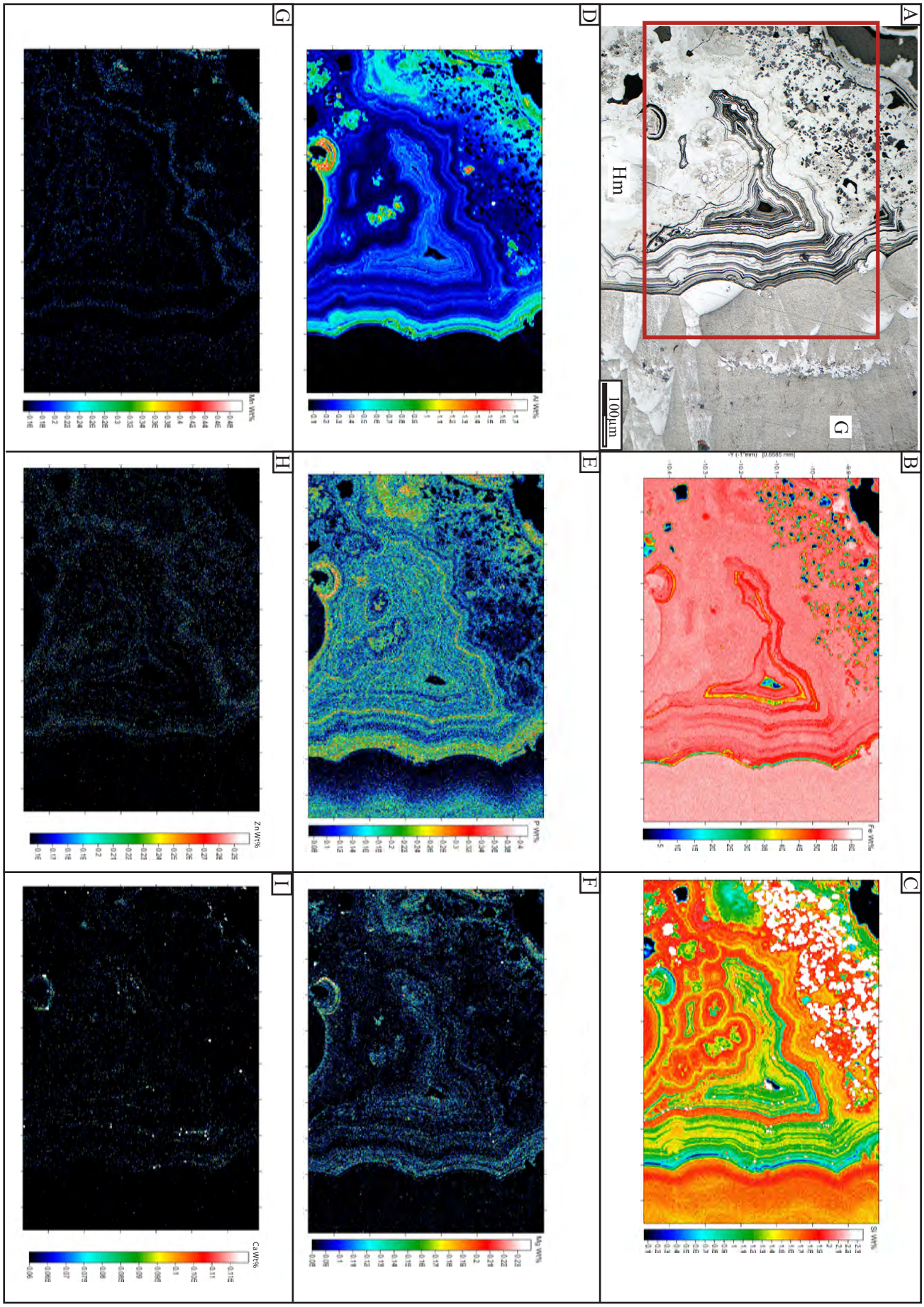

Figure 10: (A) BSE imaging and (B-I) wavelength-dispersive energy elementary mapping of stage 5 botryoidal goethite and hematite. (B) Fe, (C) Si, (D), Al, (E) P, (F) Mg, (G) Mn, (H) Zn and (I) Ca. All concentrations are expressed in wt. %.

ppm, x4 depletion), Mg (30-200 ppm, x2 depletion), Ca (50-150 ppm, x2 depletion), Ti (0.03-0.1 ppm, x100 depletion), K (3-10 ppm, x4 depletion), Ba (1.5-5 ppm, x15 depletion), Rb (0.2-0.5 ppm, x3 depletion) and Sr (1-3 ppm, x3 depletion) (Fig. 8G-I, 9E). Other elements including Si, Zr, Ga, Ge, W, As, Cu, Sn Mo and REE+Y, with the exception of Ce which displays a pronounced negative anomaly, do not exhibit significant differences between stages 4 and 5 goethite. Stage 5 botryoidal hematite is enriched in most elements by a factor of x2-3 compared to stage 5 goethite. Element mapping of stage 5 botryoidal goethite and hematite highlights the increase in concentration of several deleterious elements from goethite to hematite. Enrichments are observed for Cu (x20) and REE+Y (x10) (Fig. 8I, 9F, 10). Stage 5 botryoidal hematite therefore displays the highest contents of Zn, Cu, As and Co compared to all other iron oxides documented in this section. In contrast, P concentration does not exhibit any significant difference compared to stage 5 goethite.

V. Constraints on the genetic model for the Pardoo iron ore deposits

The different mineral assemblages documented in the Pardoo iron camp reveal a complex mineralisaton history resulting from early hypogene alteration and late supergene weathering. Timing and conditions of formation of these mineral assemblages are discussed in the following section based on field and analytical investigations and integrating the geologic evolution of the Pilbara craton.

Metamorphic to metasomatic alteration of BIF resulting in D9 fault-hosted, stage 1 hypogene magnetite-enriched BIF

Euhedral magnetite represents the earliest stage of secondary iron oxide formation at the ALX deposit and Rosita prospect, overprinting primary anhedral hematite and chert bands in BIF. The localisation of intensely developed stage 1 magnetite alteration in D9 shear zones at

ALX and Rosita supports the interpretation that stage 1 magnetite is derived from the circulation of iron-rich fluids within the fault zones and interaction with proximal BIF wall rock. The presence of stage 1 magnetite in BIF up to 100-200 m from D9 shear zones suggests the wide penetration of these fluids into BIF wallrock.

Unweathered Archean BIF typically contains recrystallised, euhedral magnetite and hematite formed during diagenetic to metamorphic alteration (Klein, 2005; Angerer and Hagemann, 2012; Nadoll et al., 2014). Mineral chemistry data for stage 1 kenomagnetite indicates that several Fe-substituting cations occur in significant amounts, including Mg (500-20,000 ppm), Mn (20-10,000 ppm) and Ca (60-2,000 ppm). This contrasts with stage 1 kenomagnetite identified in other iron camps of the North Pilbara (i.e. Corunna Downs, Wodgina, Abydos) where the concentration in those elements does not exceed 100 ppm (see respective Chapters). In addition, Co and Ni occur in trace concentration (<5 ppm) but display a Co/Ni ratio about 1 or higher, and therefore differs from the <0.1 ratio observed in stage 1 kenomagnetite from other camps. Such differences may result from a different alteration fluid composition and/or geodynamic environment involved in the formation of stage 1 magnetite. In other iron camps, the absence of significant cations substituting for Fe in stage 1 magnetite is interpreted, following Nadoll et al. (2014), as strong evidence for a metamorphic to metasomatic origin. In addition, the low Co and Ni concentrations, together with the low Co/Ni ratio, are considered as further support against any felsic magmatic-sourced hydrothermal influence for stage 1 kenomagnetite at Corunna Downs, Wodgina and Abydos. In this context, the significant amounts of Mn and Ca in stage 1 kenomagnetite at ALX and Rosita may reflect a contribution from mafic rocks to the alteration fluid. However, Mn is also present is stage 1 magnetite, although this element is usually not a major constituent of mafic rocks. Alternatively, the singular composition of stage 1 magnetite at Pardoo results from a primary compositional difference in the parent BIF, i.e. the presence of primary to

diagenetic Fe-Mg-Ca-Mn-bearing carbonates. Dissolution of early carbonates associated with stage 1 alteration likely resulted in the remobilisation of Mg, Ca and Mn into magnetite. In this model, stage 1 magnetite at Pardoo formed under similar conditions to those found in the other regional iron camps, i.e. metamorphic to metasomatic alteration, but yields a different trace element composition due to primary compositional differences in the parent BIF. The evolution of the Pilbara Craton since the deposition of the Cleaverville Formation is marked by several events that could have participated to the formation of stage 1 euhedral magnetite:

(i) 2950-2940 Ma: The major North Pilbara orogenic event, referred to as the D9 regional deformation event (Hickman and Van Kranendonk, 2008). D9 orogeny involved greenschist to amphibolite facies metamorphism, as indicated by metabasalts in the Croydon Group of the Mallina Basin (Van Kranendonk et al., 2002).

(ii) 2930-2900 Ma: The emplacement of late granites of the Sisters Suite and layered mafic-ultramafic intrusions of the Radley Suite, mostly confined to the western half of the Northern Pilbara Craton.

(iii) 2930-2900 Ma: The Mosquito Creek orogeny, restricted to the SE section of the northern Pilbara (regional D12).

(iv) 2900–2803 Ma: Granitic intrusion of the Cutinduna and Split Rock Supersuites and associated with pegmatite-hosted, tin-tantalum mineralisation (Huston et al., 2002).

(v) 2770-2760 Ma: The Fortescue Rifting Event, with likely thermal effects of thick plateau basalt deposition. Many older faults, such as D9, were reactivated by the regional crustal extension of this event (Thorne and Trendall, 2001).

(vi) 2215-2145 Ma: Regional prehnite-pumpellyite metamorphic with associated temperatures not exceeding 350°C (Smith et al., 1982; Rasmussen et al., 2005,

White et al., 2014), followed by widespread metasomatism of the Fortescue basalts (White et al., 2014). Rasmussen et al. (2005) propose that this event was driven by the northward-advancing Ophthalmian fold-and-thrust belt that developed during protracted collision with the Pilbara Craton, and argue that the widespread geographic and stratigraphic distribution of ca. 2.2 Ga phosphates suggests that fluid flow was intense and pervasive.

Importantly, textural observations unambiguously indicate that D9 folding postdates the formation of stage 1 magnetite at ALX and Rosita. Therefore, formation of stage 1 magnetite predates, or is coeval to the 2950-2940 Ma North Pilbara Orogeny. Based on the observation that (i) the North Pilbara Orogeny is the most important deformation event recorded in the North Pilbara Craton after deposition and (ii) stage 1 magnetite alteration of the Cleaverville BIF is recognised at a regional scale, it is proposed that the formation of stage 1 euhedral magnetite at Pardoo is related to the North Pilbara Orogeny during or prior to the development of D9 folds in the BIF macrobands. This interpretation is supported by the spatial association between D9 shear zones and stage 1 magnetite overprint, which suggests that reducing, metamorphic or metasomatic fluids circulated along these structures, forming spatially restricted zones (> 20 % vol.) of euhedral magnetite. The presence of stage 1 magnetite in distal areas to shear zones (up to 100-200 m) indicates the extensive circulation of structurally-controlled fluids in BIF units.

Formation of platy hematite and martite

Large (up to 300 μm) stage 2 platy hematite, formed after stage 1 magnetite, occurs band-parallel and in cross-cutting veins in equilibrium with quartz. Such textural features support a scenario involving hot (>150°C) oxidising fluids for the formation of stage 2 platy hematite (Taylor et al., 2001). The trace element chemistry of stage 2 platy hematite indicates a

systematic depletion in most base metal cations and other trace elements compared to stage 1 magnetite, suggesting that fluids involved in the formation of stage 2 platy hematite presented a higher fluid/rock ratio. The low Mg and Ca concentrations in stage 2 platy hematite may be explained by the low sorption capability of Mg^{2+} and Ca^{2+} into hematite (Scott and Pain, 2009). Alternatively, low Mg and Ca in stage 2 platy hematite may result from lower Mg and Ca concentrations in stage 2 fluids compared to stage 1 fluids. Such depletion may be explained by the lack of carbonate contribution to stage 2 fluids, as primary carbonates experienced comprehensive dissolution prior to stage 2 alteration (i.e. during stage 1 alteration).

Alteration stage 3 resulted in the martitisation of stage 1 magnetite. Martite documented in various iron ore deposits in association with microplaty hematite or goethite (Angerer and Hagemann, 2010; Angerer et al., 2012; Duuring and Hagemann, 2010, 2012a, 2012b) is often interpreted to be the result of oxidising alteration caused by heated, descending ancient and or/recent meteoric waters interacting with BIF. The relative timing between stage 2 platy hematite and stage 3 martite remains unclear. Textural observations suggest that stage 3 martitisation may be coeval to, and/or postdates stage 2 platy hematite. Because the formation of stage 2 platy hematite involved oxidising hot fluids, it is most likely that such fluids participated, to some extent, to the martitisation of stage 1 magnetite. In such conditions, the formation of stage 2 platy hematite and stage 3 martite may involve early (Proterozoic) heated supergene or hypogene fluids, possibly during metasomatism at ca. 2145 Ma. In addition, it is most likely that martitisation of stage 1 magnetite also took place during late goethitic alteration, although no definitive textural nor chemical evidence for a two-stage martitisation process has been recognized.

Multistage supergene goethite and hematite alteration

Late-stage alteration of the Cleaverville BIF at Pardoo includes (i) intense and dominantly pervasive goethitisation of BIF and clastic sedimentary units, associated with minor vein- and vug-hosted botryoidal hematite and goethite (stage 4), (ii) formation of secondary, botryoidal goethite and hematite with complex growth textures (stage 5) and (iii) a late stage of ochreous goethite formation (stage 6). These three goethite-dominated mineralising stages are all interpreted to result from recent (<70 Ma) supergene weathering of the Pilbara Craton under a tropical to semi-arid climate (Anand, 2010).

We hereafter focus our discussion on alteration stages 4 and 5, which represent the dominant supergene mineralisation events involved in the formation of high-grade iron ore at Pardoo. Although the relative timing between the formation of the different textural types of stage 4 goethite is unclear, it is assumed that all stages were approximatively coeval, and that stage 4 goethitisation initiated through the progressive replacement of existing chert- and iron oxide-rich bands by anhedral goethite and continued by precipitation of botryoidal goethite and hematite in existing vugs and veins. Stage 4 goethite and hematite display elevated concentrations in most trace elements compared to stage 3 martite, with botryoidal hematite systematically yielding twice to thrice higher amounts in trace elements compared to stage 4 goethite. Stage 5 botryoidal goethite and hematite are characterized by further increases in trace element amounts; compared to stage 4 iron oxides, stage 5 goethite and hematite are enriched in P, Ni, Zn and As. Similar to stage 4 goethite and hematite, stage 5 botryoidal hematite is systematically enriched by a factor of x2-3 compared to stage 5 botryoidal goethite, with the exception of Cu (greater enrichment, ~x20). Stage 5 iron oxides, and more particularly botryoidal hematite, therefore displays the highest contents of Cu, Ni, Zn, As and P compared to all other iron oxides documented in this section. This contrasts with other iron camps in the North Pilbara (e.g. Abydos) where early anhedral goethite (i.e. equivalent of

alteration stage 4 at Pardoo) is characterized by elevated P and Ni and where late botryoidal goethite (equivalent of Pardoo stage 5) displays abundances for Zn and As.

The precipitation of goethite and hematite is largely controlled by the pH of the mineralizing fluid, as goethite formation is optimal at both low (pH = 4) and high (pH = 12) pH whereas hematite formation is optimal at neutral (pH=7-8) (Schwertmann and Murad, 1983). Therefore, the alternation of botryoidal goethite and hematite precipitation likely results from fluctuations in the pH of supergene alteration fluids, potentially under the influence of seasonally controlled climate. The behaviour of trace elements during supergene weathering is mainly controlled by the water content, the availability of complexing and oxidizing agents, the redox potential and hydrogen ion activity (Eh-pH); all of these parameters are externally driven by climate, biological activity, parent rock composition, topography and time (Scott and Pain, 2009). An enhancement of oxidizing conditions in a given weathering system increases the oxidation state of several trace elements, resulting in the decrease (As, Mn or Cu) or increase (V, Cr, W) of their respective solubility (Scott and Pain, 2009). Other workers have established that the presence of dissolved sulphate in supergene precipitating fluids drastically increases the capability of goethite and hematite to incorporate zinc, and possibly arsenic, into its lattice during crystal growth (Rose and Bianchi-Mosquera, 1993; Swedlund et al. 2009). The large increase in As, Zn, Mn and Cu observed from stage 4 to stage 5 goethite and hematite suggests a marked change in weathering environment towards more oxidising conditions, possibly coupled with an increase in the amounts of dissolved sulphate. The natural downward progression, through time, of the weathering profile is a likely cause for the enhancement of oxidising conditions, favouring the sorption of As, Mn and Cu in stage 5 iron oxides compared to those of stage 4. Also, the onset of semi-arid conditions over the Pilbara since 50 Ma (Anand, 2005) resulted in the development of seasonally controlled weathering. In such conditions, repeated precipitation and dissolution of

sulphate evaporites may have introduced significant dissolved sulphate into descending supergene fluids, which could have produced late-forming (stage 5) goethite and hematite with higher Zn and As contents. Importantly, elevated amounts of Zn (>10 ppm), Cu (>50 ppm), As (>5 ppm), Ni (> 10 ppm) and P (> 1,000 ppm) identified from whole-rock geochemistry in goethite-rich and mixed goethite-martite ore samples likely reflect the contribution of stage 5 goethite – hematite.

VI. Implications for exploration

First-order (critical) controls on the formation of high-grade iron ore deposits in the Pardoo camp include the presence of (i) thick iron-rich primary BIF from the Cleaverville Formation, particularly the Ord Ridley and the Bobby BIF members, (ii) intensely developed pervasive supergene alteration and (iii) the near-surface exposure of the high-grade iron ore bodies hosted by BIF. Second-order (constituent) controls are the (i) D9 event, fault zone-hosted, stage 1 hypogene magnetite-rich ore zones in BIF, (ii) formation of platy hematite in bands and cross-cutting veins, (iii) fold-thickening of the shear zone-hosted magnetite-rich hypogene ore zones and (iv) reactivation of structures that increases fluid permeability and repeated upgrade of iron in the BIF.

The least-altered BIF from the Ord Ridley BIF member exposed in the ALX deposit and the Rosita prospect is moderately prospective since it contains less than 30 wt. % Fe_2O_3 but has an average thickness exceeding 500 m. The thinner (~ 100 m-thick) Bobby BIF member has an apparent higher Fe content (>50 wt. % Fe_2O_3), largely due to significant supergene overprint. It remains therefore unclear whether the Bobby BIF member had an initial Fe content higher than that of the Ord Ridley BIF member. It is suggested that a higher initial Fe

content in the Bobby BIF member could have counterbalanced the absence of early hypogene upgrade of the BIF as observed in the ALX deposit.

Mapping of the Pardoo iron ore deposits highlighted the presence of fault zones oriented parallel to bedding. It is likely that the titling of BIF macrobands and activation of these fault zones occurred during regional transpression at ca. 2950-2940 Ma (regional D9 event). These shear zones locally host <50 m-thick zones of stage 1 hypogene magnetite that result in the moderate intensity upgrade of iron in the BIF. Reactivation of these shear zones by multiple events likely enhanced and broadened the permeability of these damage zones in BIF. These broad damage zones are the optimum areas for the circulation of later supergene fluids through BIF resulting in the creation of extensive supergene goethite ± hematite-rich ore bodies.

Considering that the shear zone-hosted, magnetite-rich ore zones identified in the Ord Ridley BIF member are narrow (<20 m wide), they are unlikely to represent exploration targets for stand-alone high-value ore deposits. This is supported by the observation that, at Rosita, the weakness of the supergene overprint after early hypogene enrichment prevented the formation of an economic deposit. These shear zone-hosted ore bodies have the added potential to control deeper extensions to near-surface supergene ore bodies owing to their steep dips and likely presence beneath the weathering front. Targeting stage 1 magnetite alteration using trace element compositions of these minerals is challenging as most elements that display elevated concentrations in stage 1 magnetite (Mg, Ca, Mn) are likely sourced from nearby unaltered carbonate-rich BIF bands. Nevertheless, trace elements such as W or Be may constitute robust pathfinders for the oxidised relative of stage 1 magnetite, i.e. stage 3 martite, but would require the use of high detection limit techniques such as ICP-MS.

Supergene goethitisation is the dominant alteration style in all deposits in the Pardoo camp. It is responsible for generating large volumes of high-quality (iron grade and contaminant level) iron ore. Supergene enrichment in the fold-thickened BIF took place as a multi-stage mineralising event involving the interaction between near-surface derived, oxidised fluids and BIF. The earliest recognised stage of supergene goethitisation (i.e. stage 4 goethite) represents the most economically important mineralisation stage at Pardoo in terms of its extensive distribution. Mineral chemical analyses indicate that P, Ni, As, Zn and Cu positive anomalies, detectable from whole-rock chemical analysis, are largely related to later, stage 5 goethitisation event, which may therefore be targeted using these pathfinder elements.

As the BIF units are well exposed in the Ord range, there is limited potential for the discovery of iron enrichment at surface, other than that already identified. Future exploration efforts should therefore be centred on evaluating the potential of undercover BIF extensions. In the northeast section of the Pardoo area, the Bobby BIF member lies underneath recent alluvial cover, and has the potential to host unexposed mineralised BIF such as that which is present at the Bobby deposit. This task will involve the identification of the same geological features identified for surface mapping (BIF, folds, deformation zones), but will rely upon interpreting geophysical data beneath areas of transported cover and projecting structural observations to these areas. In addition, further efforts should be devoted to accurate mapping of magnetite- to martite- altered jaspilitic BIF occurrences together with the location and dimensions of thick damage zones in BIF throughout the Pardoo area, especially along strike of the ALX deposit towards the southwest and the hinge of the district scale, D9-related Ord Ridley syncline.

VII. Conclusions

The ALX deposit at Pardoo principally consists of supergene-modified hypogene goethite-martite rich ore body hosted near the base of the Ord Ridley BIF member of the 3.02 Ga Cleaverville Formation. In contrast, the nearby Bobby deposit, hosted by the Bobby BIF member, only consists of supergene goethite ore. One major deformation event at ca. 2950-2940 Ma (North Pilbara Orogeny, regional deformation event D9) affects the Cleaverville BIF in both deposits, through tilting of the BIF units. In the Ord Ridley BIF member, this event is also associated with the emplacement of bedding-parallel, broad fault zones that record an early stage of euhedral magnetite precipitation. Stage 1 magnetite is largely concentrated along or proximal to high strain D9 shear zones, which represent focused pathways for alteration fluids, locally resulting in an initial upgrade in iron in the BIF from ca 30 to 40-45 wt% Fe. Subsequent formation of platy hematite (stage 2) and martite (stage 3) after stage 1 magnetite is interpreted as an early (Proterozoic) process caused by heated, descending ancient meteoric waters interacting with BIF, although the occurrence of secondary martitisation during recent supergene alteration is suggested. Stage 3 martite may be targeted using W and/or Be as elementary pathfinders, although such approach would require high detection limit techniques (e.g. ICP-MS). The recent supergene sequence is dominantly represented by stage 4 goethite, essentially occurring as disseminated anhedral goethite formed through pervasive fluid alteration. Further development of the supergene hydrothermal fluid system involved the formation of vein-hosted, massive botryoidal goethite (stage 5). The ubiquitous spatial distribution of stage 4 goethite indicates that it represents the dominant mineralisation stage responsible for the formation of volumetrically important ore bodies at Pardoo. Stage 5 goethite may be targeted using several pathfinder elements including Ni, As, Zn, Cu and P.

Chapter 5: Regional and local controls on BIF-hosted iron ore in the North Pilbara Craton: implications for exploration targeting

Introduction

This Chapter provides a synthesis of observations and interpretations derived from the individual camp-scale studies presented in Chapters 1 to 4. The aim of this Chapter is to make a concise comparison of these iron camps in order to assess their key geological commonalities and differences and interpret how these variables influence the relative prospectivity of different regions of the Pilbara craton. This Chapter first presents a comparison of the main iron camps in the Pilbara in terms of their (i) geological framework, (ii) deformation histories, (iii) controls on iron ore formation, (iv) multi-stage hypogene and supergene fluid alteration events affecting BIF and (v) the geochemical signatures of their respective high-grade iron orebodies. Based on these comparisons, a genetic model is proposed for the genesis of iron orebodies in the Pilbara craton and the results are synthesised into a Mineral Systems model with implications for iron ore exploration.

I. Key characteristics of BIF-hosted iron ore in the East Pilbara Terrane

Facies variations and differences in iron content of the Cleaverville BIF throughout the East Pilbara Terrane

The recent reassessment conducted by the Geological Survey of Western Australia (GSWA) on the lithostratigraphy of the Pilbara craton has important implications for the recognition of Mesoarchean BIF units throughout the craton. Of particular relevance to iron ore exploration is the distinction between the (i) 3230 Ma Pincunah Banded Iron Member of the Kangaroo Caves Formation, (ii) 3190 Ma Paddy Market Formation and (iii) the 3020 Ma Cleaverville Formation (Hickman, 2012; Hickman and Van Kranendonk, 2012, Van Kranendonk et al., 2007).

Following the GSWA revision of geochronological constraints and stratigraphic correlations in the East Pilbara Terrane, the Gorge Creek Group was reassigned from the >~3.2 Ga Pilbara Supergroup to the <3.07 Ga De Grey Supergroup, thereby including the 3020 Ma Cleaverville Formation in the new classification. Previously, the Cleaverville Formation was only recognised in the West Pilbara Superterrane, but now extends to the East Pilbara Terrane. In addition, the former Soanesville Subgroup that includes the 3190 Ma Paddy Market Formation (previously included in the Gorge Creek Group) was reassigned to the Soanesville Group (it is now considered to be younger than the Pilbara Supergroup but older than the De Grey Supergroup). Prior to the stratigraphic revision by GSWA, all BIF units in the East Pilbara Terrane that are younger than the 3200 Ma Corboy Formation stratigraphic marker were assigned to the 3190 Ma Paddy Market Formation. However, a number of these BIF exposures in the East Pilbara Terrane are now reassigned to the Cleaverville Formation.

Importantly, BIF macrobands that host iron ore in the Abydos, Wodgina and Corunna Downs iron camps are now classified as Cleaverville Formation. At Pardoo, BIF macrobands that

were formerly assigned to the Nimingarra Iron Formation (local terminology for BIF macrobands in the Ord Ridley and Goldsworthy greenstone belts) are now considered to be Cleaverville Formation. Consequently, all BIF macrobands that host iron ore examined by this study are likely to be expressions of the 3020 Ma Cleaverville Formation, which formed during the deposition of the 3050-3016 Ma Gorge Creek basin.

The Gorge Creek basin formed as a consequence of the widespread erosion of the 3070 Ma Prinsep Orogeny and probably developed in response to post-orogenic crustal relaxation and subsidence (Hickman and Van Kranendonk, 2012). Deposition took place in shallow water and included evaporite and fluviatile deposits (Sugitani et al. 1998, 2003). In the East Pilbara Terrane, the Gorge Creek Group comprises three formations: (i) a basal unit of metamorphosed sandstone and conglomerate called the Farrel Quartzite; (ii) a central unit of chert, BIF, carbonaceous shale, and local siltstone and sandstone, named the Cleaverville Formation; and (iii) an upper unit of conglomerate, sandstone and shale, named the Cundaline Formation. The thickness of the group (up to 2,000 m) testifies to significant basin subsidence, but lateral facies changes in the East Pilbara Terrane suggest that the basin was broken by islands. Local erosion of the Cleaverville Formation during deposition of the Cundaline Formation suggests localised uplift of some areas (Hickman and Van Kranendonk, 2012).

Mapping and geochemical data for least-altered BIF samples collected during this study demonstrate significant facies variations across the four investigated camps in the East Pilbara Terrane (Fig. 1). For example at Wodgina, clastic sedimentary rocks such as siltstone and sandstone are abundantly present throughout the Cleaverville Formation, suggesting a shallower depositional environment relative to the other studied iron camps. In a similar manner, Cleaverville Formation BIF macrobands exposed in the northern parts of the Pardoo iron camp are intercalated with a high proportion of siltstone units. Furthermore, BIF

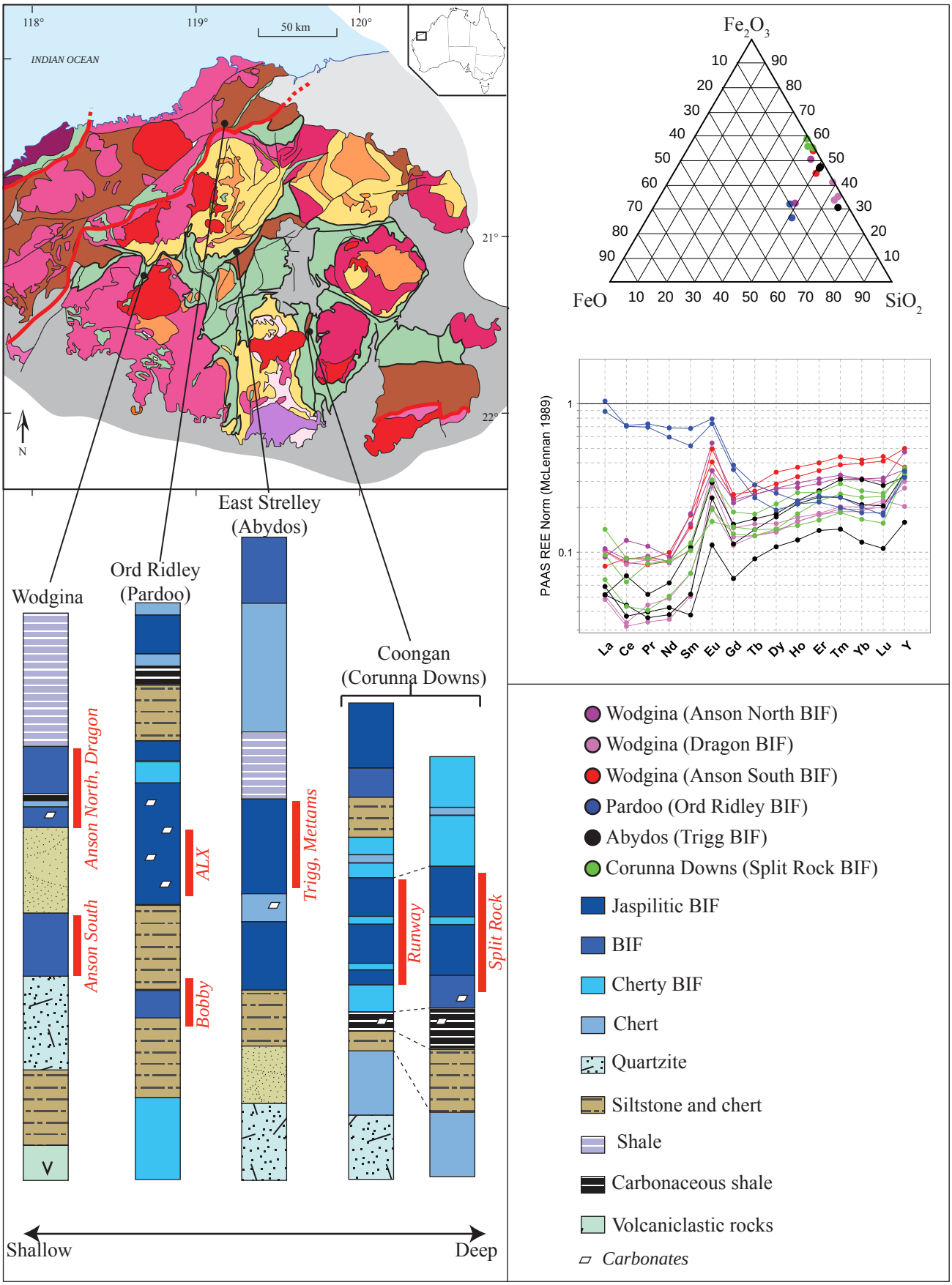

Figure 1: Lithostratigraphic sequence of the Cleaverville Formation at Wodgina, Pardoo, Abydos and Corunna Downs (left). Ternary plot of FeO-Fe_2O_3-SiO_2 and PAAS-normalised REE+Y pattern for least-altered BIF (right).

sampled from the Ord Ridley Member in the Pardoo camp contain primary ankerite (identified in thin section and supported by elevated LOI geochemical contents). The presence of primary ankerite indicates deposition of the BIF at intermediate water depths, compatible with the qualitative model proposed for Mesoarchean BIF deposition in South Africa (Smith et al., 2013).

At Abydos, the Cleaverville Formation conformably overlies the Farrel quartzite. The Cleaverville Formation includes a basal sandstone unit that grades upwards into siltstone and then BIF, chert and minor carbonaceous shale units. These facies transitions suggest that deposition of the Cleaverville Formation began in a shallow water environment, but evolved to intermediate and deep water settings. For comparison at Corunna Downs, apart from a siltstone unit near the base of the sequence, the Cleaverville Formation is mainly represented by BIF, chert and carbonaceous shale, arguing for a deeper depositional environment. Although not visited during this study, the McPhee Creek iron camp (Kelly greenstone belt, south-east Pilbara) reportedly contains Cleaverville Formation that is dominated by BIF and chert units (Bagas, 2005; Goldsworthy et al., 2011), suggesting a relatively deep water depositional environment. Taken together, these camp-scale observations support a depositional model for the Cleaverville Formation in the East Pilbara Terrane wherein the Gorge Creek basin progressively deepens both spatially, from west to east, and temporally, with a deepening of the basin through time.

An important observation is that the proportion of BIF macrobands relative to Fe-poor units (e.g. chert, siltstone and sandstone) is higher in the Abydos and Corunna Downs compared with the less endowed Wodgina and Pardoo camps. In addition to these recognised differences in the primary thickness of Cleaverville Formation BIF macrobands, there are measureable differences in the iron content of the BIF protoliths. All petrologically examined examples of least-altered BIF from the different camps comprise alternating primary iron

oxide- and silica-rich bands. The iron oxide-rich bands contain anhedral hematite with minor anhedral magnetite, whereas the silica-rich bands display mainly microcrystalline quartz. Primary ankerite is locally present in the least altered Ord Ridley Member BIF in the ALX deposit at Pardoo, and is present in the upper BIF unit at the Anson deposit (Wodgina).

The variations in the proportion of iron oxides, iron-bearing carbonates and chert in least-altered BIF sampled from the different iron camps translates to differences in the measured abundance of the total Fe content for primary BIF. These chemical differences in the primary BIF are important in that they influence the potential for a BIF macroband to subsequently host high-grade (>50 wt. % Fe, or >70 wt. % Fe_2O_3(T) , i.e. all Fe considered as Fe_2O_3) iron ore. In most cases (apart from carbonate-rich BIF occurrences), all the Fe present in the least-altered BIF samples occurs as Fe_2O_3, therefore resulting in very similar values of Fe_2O_3 and Fe_2O_3(T). The jaspilitic BIF macroband that hosts iron ore at the Split Rock and Runway deposits (Corunna Downs) yields the highest Fe_2O_3(T) (55-60 wt. %) and lowest SiO_2 (40-45 wt. %) content (Fig. 1). In contrast, at Abydos, the jaspilitic BIF protolith displays a lower total Fe content, with Fe_2O_3(T) and SiO_2 contents of 35-50 and 50-65 wt. %, respectively. At Wodgina, the analysed BIF units display heterogeneous values for the total Fe content; the sample with the highest Fe content is the carbonate-free upper BIF unit from the Anson North pit (ca. 55 wt. % Fe_2O_3(T)). In contrast, least-altered BIF from the Dragon pit, which is interpreted to be a lateral equivalent of the Anson North BIF, displays a lower Fe content (35-40 wt. % Fe_2O_3(T)). Such geochemical variations may be explained by lateral facies variations in the Cleaverville Formation BIF at Wodgina. At Pardoo, the Ord Ridley BIF that hosts the ALX deposit yields a notably low Fe_2O_3 content (21-27 wt. %), which is partly counterbalanced by the contribution of primary ankerite as FeO (17-18 wt. %), resulting in a total FeO content of 20-32 wt. % or 29-46 wt% Fe_2O_3(T).

Rare Earth Element (REE) patterns (normalised against Post Archean Australian Shale, PAAS) for least altered Cleaverville Formation BIF analysed from the studied iron camps demonstrate that they are mostly similar (Fig. 1). Two analyses that are clearly different are associated with carbonate-rich BIF sampled from the ALX deposit. Apart from these two samples, the PAAS-normalised REE+Y patterns display an increase in abundances from LREE to HREE (but flat patterns for La, Ce, Pr and Nd), and strong positive Eu anomalies (Fig. 1). The two carbonate-rich BIF samples from Pardoo display higher La, Ce, Pd and Nd values, a negative slope for LREE to HREE and a less pronounced positive Eu anomaly. Positive Y anomalies exist for least-altered BIF from Pardoo, Corunna Downs and Abydos.

Redox-sensitive REEs, Eu and Ce, can be used to infer information about the redox state of ancient seawater and differences in the oxygenation of the contemporary atmosphere through time (Frei et al., 2008). The effects of post-depositional processes, such as diagenesis and metamorphism, on the REE distribution in iron formations have been discussed by Bau (1993) and are demonstrated to be minor in most cases. Greenstone belts in the Pilbara Craton experienced prehnite-pumpellyite-(epidote) facies peak metamorphism from 2215 to 2165 Ma (Smith et al., 1982). Accordingly, we consider that the distributions of Y and REEs observed in the Cleaverville BIF units reflect those in the primary marine precipitates. None of the BIF sequences studied here exhibits Ce anomalies (either negative or positive), but they all indicate positive anomalies for Eu and Y (with the exception of Y for Wodgina). The absence of Ce anomalies suggests that the decoupling of redox-sensitive Ce from its redox-insensitive REE neighbours (i.e. the oxidative removal of Ce), did not occur in the depositional environment that formed the Cleaverville Formation BIF or in the Gorge Creek basin seawater. The positive Eu anomalism for all samples is a clear indication that high-temperature hydrothermal solutions similar to modern black-smoker-type fluids were an important contributor to the REE+Y inventory of Mesoarchean seawater in the Gorge Creek

basin. The positive slope for all measured REE+Y patterns (except Pardoo) is similar to that of the Late Archean Nemo Iron Formation in the Black Hills, South Dakota (Frei et al., 2008), as well as least altered BIF sampled from various iron camps in the Yilgarn craton (e.g. Windarling camp: Angerer et al. 2012; Madoonga camp: Duuring et al. 2012; Jack Hills camp: Maskell, 2010). In these cited studies, the REE trends for the respective Meso- to Late-Archean BIF occurrences are interpreted to have formed from anoxic seawater with strong hydrothermal influence. The dissimilar, negative REE+Y patterns for the Ord Ridley BIF Member from Pardoo is likely to be related to the presence of REE-bearing phosphate minerals associated with primary ankerite in these rocks.

Deformation events affecting the Cleaverville Formation

All camps investigated by this study display a comparable multistage deformation history that is mainly characterised by a major craton-wide deformation event related to the 2950-2940 Ma North Pilbara Orogeny (i.e. the D9 regional event of Hickman and Van Kranendonk, 2008a) (Tables 1, 2).

The earliest structures recorded by the Cleaverville Formation in the Gorge Creek Basin are extensional growth faults (equivalent to the D6 event of Hickman and Van Kranendonk, 2008). These growth faults are prevalent in the Coongan 1:100,000 geology map (Van Kranendonk, 2010), but were not recognised in any of the camps investigated by this present study. The only significant deformation event that likely predates the North Pilbara Orogeny (D9) is that which results in tight upright, shallowly plunging folds at Wodgina (refer to the detailed description of these $D1_{WD}$ folds in Chapter 2). These $D1_{WD}$ folds are refolded by the regional D9 event, which is responsible for the NNE-trending camp-scale syncline at Wodgina. The $D1_{WD}$ folds are most likely the product of the ca. 2970 Ma folding event that

	Deformation event	Age	Characteristics	Intensity	Zone of influence	Proximal to
Regional deformation event (Hickman and Van Kranendonk, 2008)	D6	ca. 3020 Ma	Extensionnal growth faults in the Gorge Creek Group	Moderate	Regional?	All camps?
	D7	3015-3010 Ma	Tight to isoclinal upright folding	High	West Pilbara	Wodgina, Pardoo?
	D8	ca. 2970 Ma	Folding event in the Mallina basin	Moderate	West-central Pilbara	Wodgina, Pardoo?
	D9	**2950-2940 Ma**	**North Pilbara Orogeny (greenschist to amphibolite facies)**	**High**	**Regional**	**All camps?**
	D10	ca. 2930 Ma	Localised deformation along the Maitland shear zone	Low	West Pilbara	-
	D11	ca. 2920 Ma	Late dextral movement along the Sholl shear zone	Low	West-central Pilbara	-
	D12	2905-2890 Ma	Mosquito Creek Orogeny	High	South-east Pilbara	Corunna Downs, McPhee Creek?
Additionnal events	D10'	2930-2900 Ma	Post-orogenic Sisters Suite granites + layered Umafic Radley Suite intrusions	High	West-central Pilbara	Wodgina, Pardoo
	D11'	ca. 2890 Ma	Faulting and folding	Moderate	Central Pilbara	Wodgina
	D12'	2900-2830 Ma	Cutindunna and Split Rock granitoids	High	Central to SE Pilbara	Wodgina > Corunna Downs > Mc Phee
	D13	2775-2765 Ma	Black Range dolerite intusions, Fortescue rifting event	Moderate?	Regional?	All Camps?
	D14	**2215-2165 Ma**	**Prehnite-pumpelleyite-epidote facies metamorphism, metasomatism**	**High**	**Regional**	**All Camps**

Table 1: Regional deformation scheme (post-Cleaverville Fm.) in the Pilbara craton, including zones of influence and proximity to iron camps.

Regional scheme	Corunna Downs	Pardoo	Abydos	Wodgina
D8	-	Pre-$D1_{AL}$?	-	$D1_{WD}$
D9	$D1_{CD}$ (+$D2_{CD}$?)	$D1_{PD}$, $D2_{PD}$	$D1_{AB}$, $D2_{AB}$?	$D2_{WD}$
D11'		$D3_{BB}$?, $D4_{AL}$?	-	$D3_{WD}$
D12'	-	-	-	$D4_{WD}$
D13	$D3_{CD}$	$D5_{PD}$, $D6\text{-}8_{AL+BB}$	$D3_{AB}$, $D4_{AB}$	-

Table 2: Correspondence between regional deformation scheme (see Table 1) and district-scale deformation schemes (see Chapters 2 to 4).

	Regional scheme	**Local schemes**			
		Corunna Downs	**Wodgina**	**Abydos**	**Pardoo**
Hypogene magnetite	**Stage 1**	Stage 1	Stage 1	Stage 1	Stage 1
Platy hematite	**Stage 2**	Stage 2	N.A.	N.A.	Stage 2
Martite	**Stage 3**	Stage 3	Stage 2	Stage 2	Stage 3
Psilomelane	**Stage 4**	N.A.	Stage 4	Stage 4	N.A.
Goethite (+hematite)	**Stage 5**	Stage 4	Stage 5	Stage 5	Stage 4
Microplaty hematite	**Stage 6**	Stage 5	N.A.	N.A.	N.A.
Goethite (+hematite)	**Stage 7**	Stage 6	Stages 6+7	Stage 6	Stage 5
Ochreous goethite + Mn ox.	**Stage 8**	Stage 7	Stage 8	Stage 7	Stage 6

Table 3: Correspondence between regional and district-scale mineralisation schemes.

affected the Mallina basin, which corresponds to the regional D8 deformation event (Hickman and Van Kranendonk, 2008a).

The North Pilbara Orogeny (D9, 2950-2940 Ma) is responsible for tight folding of the Cleaverville Formation in the Corunna Downs, Wodgina, Pardoo and Abydos camps. The folds commonly display steeply plunging fold axes. Intense folding during the regional D9 event resulted in significant increases in the primary thickness of the BIF macrobands, and involved shearing along fold limbs that resulted in broad (> 20 m-wide) damage zones in BIF that are oriented subparallel to major lithological contacts. Importantly, these deformation zones locally host up to 20 vol. % stage 1 hypogene magnetite (now largely oxidised to martite), which provides an early Fe enrichment in BIF. Within each studied camp, the location of the thickest iron orebodies is commonly associated with the areas of greatest structural complexity associated with the regional D9 event. For example, the Split Rock deposit in the Corunna Downs camp coincides with the intersection between a 100 m-wide, subvertical-plunging D9 fold hinge defined by the Cleaverville Formation BIF and sheared fold limbs. The plunge direction of the fold hinge combined with the steep intersection lineation defined by the intersecting sheared limbs produce a steep-plunging damage zone in BIF that is later exploited by supergene fluids.

Deformation events that post-date the D9 event include a folding and faulting event that affected the Central Pilbara at ca. 2890 Ma (referred to as D11' in Table 1). This event is expressed at Wodgina as brittle faults that displace BIF macrobands ($D3_{WD}$), and is possibly related to the late, post D9 open folds observed at Pardoo ($D3_{BB}$, $D4_{AL}$). At Wodgina, emplacement of the Split Rock and Cuntidunna granitoid suites at ca. 2850 Ma (D12') resulted in the local emplacement of pegmatite into the Cleaverville Formation, within about 500 m of the Dragon and Constellation iron deposits. The Split Rock and Sisters granitoids suites were emplaced mainly in the Central and West Pilbara Terranes, but also formed as

isolated late intrusions within older batholiths in the East Pilbara Terrane. Interestingly, granitic rocks from the Split Rock suite intruded the Shaw batholith within 5 km of iron orebodies in the Corunna Downs camp. This study demonstrates that no genetic association exists between fluids derived from the felsic intrusions and BIF-hosted iron ores (based on the absence of granitophile elements in altered BIF and their iron oxide ore minerals).

Following the stabilisation of the Pilbara craton by ca. 2830 Ma, the development of extensional growth faults at >2765 Ma (regional D13, Table 1) coincided with the deposition of the basalt-dominated 2775-2630 Ma Fortescue Group and cogenetic dolerite intrusions. The D13 is recorded in most of the investigated camps in the form of steeply dipping, normal brittle faults and the emplacement of mafic dikes. It is likely that the D13 event also reactivated D9 faults (Hickman and Van Kranendonk, 2008a). Subsequent (post-2765 Ma) deformation events are locally expressed in individual camps as brittle faults and fractures; they are likely to be unrelated to craton-wide deformation events.

Iron ore types in the East Pilbara Terrane

Outcrop, pit exposures and drill core examined from the studied iron camps in the East Pilbara Terrane record remarkably similar iron ore styles that are the product of early hypogene alteration followed by supergene alteration overprint. From oldest to youngest, the iron ore types include:

(i) Coarse-grained (up to 0.5 mm), euhedral hypogene magnetite-rich BIF located within discrete, 1 to 10 m-wide, D9 shear zones oriented subparallel to BIF macrobands. The most obvious examples are magnetite-rich shear zones at the Rosita prospect and ALX deposit in the Pardoo camp, and exposures of steeply-dipping magnetite-rich shear zones in fresh BIF exposed in the Anson pits at Wodgina. Proximal BIF wallrock zones to these shear zones display networks of

magnetite-rich veinlets that cut primary bands at high angles. Disseminated euhedral magnetite that replaces primary iron oxide- and silica-rich bands is commonly present in BIF up to 100 m away from D9 fault zones. Coarse magnetite alteration in otherwise fresh BIF results in sub-economic iron concentrations of 65-70 wt. % Fe_2O_3(T), i.e. 45-50 wt.% Fe.

(ii) Martite-rich BIF occurs after magnetite-rich BIF; it is present in most iron camps at depths below the near-surface goethite weathering front, commonly about 60 m below the present surface. Corunna Downs and Abydos display the thickest intervals of martite-rich BIF compared to other camps. Relative to least-altered BIF, martite-rich BIF is enriched in Al and Mn (Fig. 2) (apart from Pardoo where the primary carbonate-rich BIF is rich in Mn), as well as P_2O_5, K_2O, TiO_2 and U (Fig. 2, 3). In contrast, CaO, MgO and FeO are depleted in the martite-rich BIF compared to the least-altered BIF. Martite-rich BIF is most likely a supergene alteration product in most camps, but may also be the result of alteration of BIF by an oxidised hypogene fluid prior to supergene alteration.

(iii) Bedded- to massive-textured, anhedral goethite and goethite-martite ores result from intense supergene goethitisation of least-altered, magnetite- or martite-altered BIF. The vertical limit of goethite-rich ores is a critical parameter controlling the volume of mineralisation in the studied camps. At Wodgina, goethite high-grade ore extends from surface to about 80 m deep. At Abydos, these ore zones extend up to 130 m below surface, whereas at Corunna Downs goethite high-grade ore zones reach 200 m below surface. Vitreous goethite-dominated and mixed martite-goethite ores have a maximum Fe_2O_3 content of about 89 and 93 wt. %, respectively. Compared to martite-rich BIF, goethite-rich

Figure 2: Whole-rock geochemistry of major oxides for least-altered BIF together with martite, martite-goethite, goethite and ochreous goethite ores types. Significant chemical changes from least-altered BIF to ore are indicated.

Figure 3: Whole-rock geochemistry of trace elements for least-altered BIF together with martite, martite-goethite, goethite and ochreous goethite ores types. Significant chemical changes from least-altered BIF to ore are indicated.

and mixed martite-goethite ores display enrichment in Zn, As, Cu, Ni and U (Fig. 3).

(iv) A second stage of vitreous goethite ore is expressed as late veins of massive to botryoidal goethite, with colloform silica locally present. Although vitreous goethite is expressed in all iron camps, it is best developed in the Trigg deposit (Abydos camp) where metre-thick veins of massive to botryoidal goethite cut bedded to massive goethite ore zones. Compared to bedded to massive goethite ores, the vitreous goethite ore is commonly enriched in Zn and As.

(v) Ochreous goethite ore locally replaces all other types of iron-enriched BIF at depths of up to 60 m beneath the present surface. Ochreous goethite often overprints manganese oxides such as psilomelane. Compared with earlier types of goethitic ores, ochreous goethite is enriched in Al and U (Fig. 3).

Paragenetic sequence for altered Cleaverville Formation BIF in the East Pilbara Terrane

BIF-hosted iron ore examined from the East Pilbara Terrane includes up to eight alteration stages (Fig. 4 and Table 4). The regional paragenetic sequence includes:

(i) Stage 1 euhedral magnetite formed within or proximal to D9 fault zones in all camps. Magnetite grain size varies from a few tens of microns for disseminated crystals in iron oxide bands, to up to 500-1,000 μm for magnetite crystals located within D9 shear zones or veins (Fig. 4A).

(ii) Stage 2 platy hematite (Fig. 4B) locally replaces primary iron oxide bands and stage 1 magnetite alteration zones at Pardoo (ALX deposit and Rosita prospect, Ord Ridley BIF Member) and at Corunna Downs (Split Rock deposit). Stage 2 platy hematite most likely formed due to the interaction between BIF and oxidised

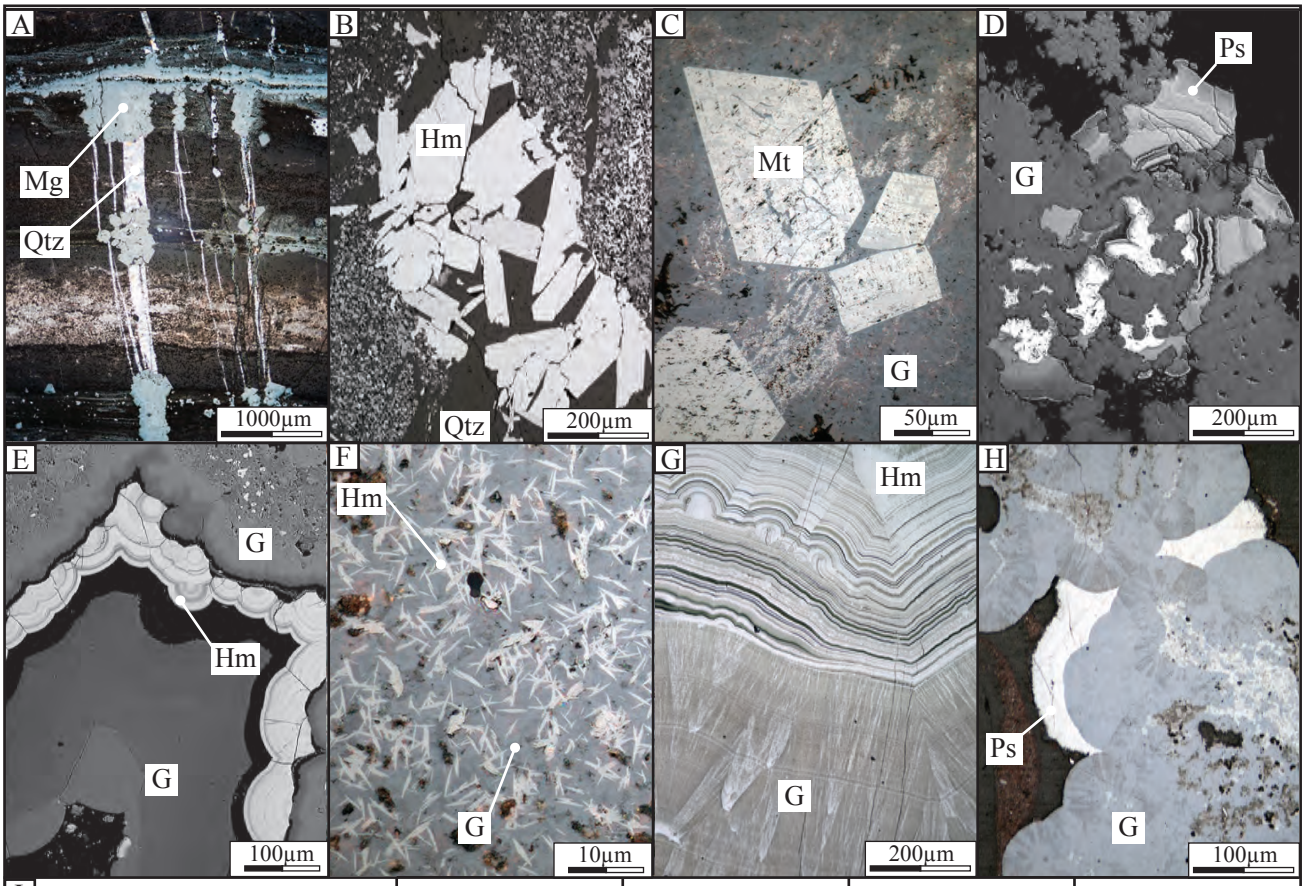

I

	Pardoo	Wodgina	Abydos	Corunna Downs
Stage 1 Magnetite (euhedral), Quartz				
Stage 2 Hematite (platy), Quartz				
Stage 3 Martite				
Stage 4 Ba-rich psilomelane				
Stage 5 Hematite (botryoidal), Goethite (anhedral), Goethite (botryoidal)				
Stage 6 Hematite (microplaty)				
Stage 7 Goethite (vein, botryoidal), Quartz (colloform), Hematite (botryoidal)				
Stage 8 Psilomelane (botryoidal), Goethite (limonite)				

<1 vol. %
1 to 5 vol. %
5 to 20 vol. %
20 to 50 vol. %
>50 vol. %

Figure 4: Optic microphotographs (A-C, F-H), backscatter electron images (D, E) and synthetic paragenetic sequence (I) for iron oxides and associated minerals at Corunna Downs, Pardoo, Abydos and Wodgina. (A) stage 1 magnetite and quartz vein, (B) stage 2 platy hematite and quartz, (C) stage 3 martite and stage 5 goethite, (D) stage 4 psilomelane and stage 5 goethite, (E) stage 5 goethite and hematite, (F) stage 5 goethite and stage 6 microplaty hematite, (G) stage 7 goethite and hematite and (H) stage 7 goethite ans stage 8 psilomelane. Mg = magnetite, Qtz = quartz, Mt = martite, G = goethite, Hm = hematite, Ps = psilomelane

hot (>100°C) fluids, possibly derived from the heating of descending Paleoproterozoic meteoric waters with increasing depth.

(iii) Stage 3 martite (Fig. 4C) is present in all camps due to the solid state replacement of stage 1 magnetite and perhaps diagenetic magnetite by oxidised fluids. Textural relationships between stage 2 platy hematite and stage 3 martite at Pardoo and Corunna Downs suggest that these iron oxides may be cogenetic in some camps. That is, martitisation of stage 1 magnetite and precipitation of platy hematite may have formed from oxidised ancient (Paleoproterozoic) fluids, rather simply being a product of BIF interaction with recent (Cretaceous to Cenozoic) oxidised meteoric fluids. Laser ablation ICP-MS analysis of stage 1 magnetite and stage 3 martite indicate similar enrichments in Ti, V Ga and Ge compared to later-formed goethite. Stage 3 martite is often enriched in P and Zn compared to stage 1 magnetite (Fig. 5).

(iv) Stage 4 psilomelane (Fig. 4D) locally occurs at Wodgina and Abydos after martite but prior to stage 5 goethite. It is often associated with high concentrations (> 10 wt. %) of Ba.

(v) Stage 5 massive to bedded anhedral goethite (Fig. 4D, 4E) is present in all camps and volumetrically represents the dominant style of high-grade iron ore. Stage 5 goethite is enriched in Ni, Cu, Zn, As, P and U compared to stage 3 martite. Local examples of botryoidal goethite and hematite have similar trace element abundances (Fig. 5, 6).

(vi) Stage 6 microplaty hematite locally occurs on surface exposures of the Split Rock deposit at Corunna Downs. Textural observations suggest that it formed after stage 5 anhedral hematite, but before stage 7 botryoidal goethite (Fig. 4F). Stage 6 microplaty hematite at Split Rock may have formed due to dehydration of stage 5

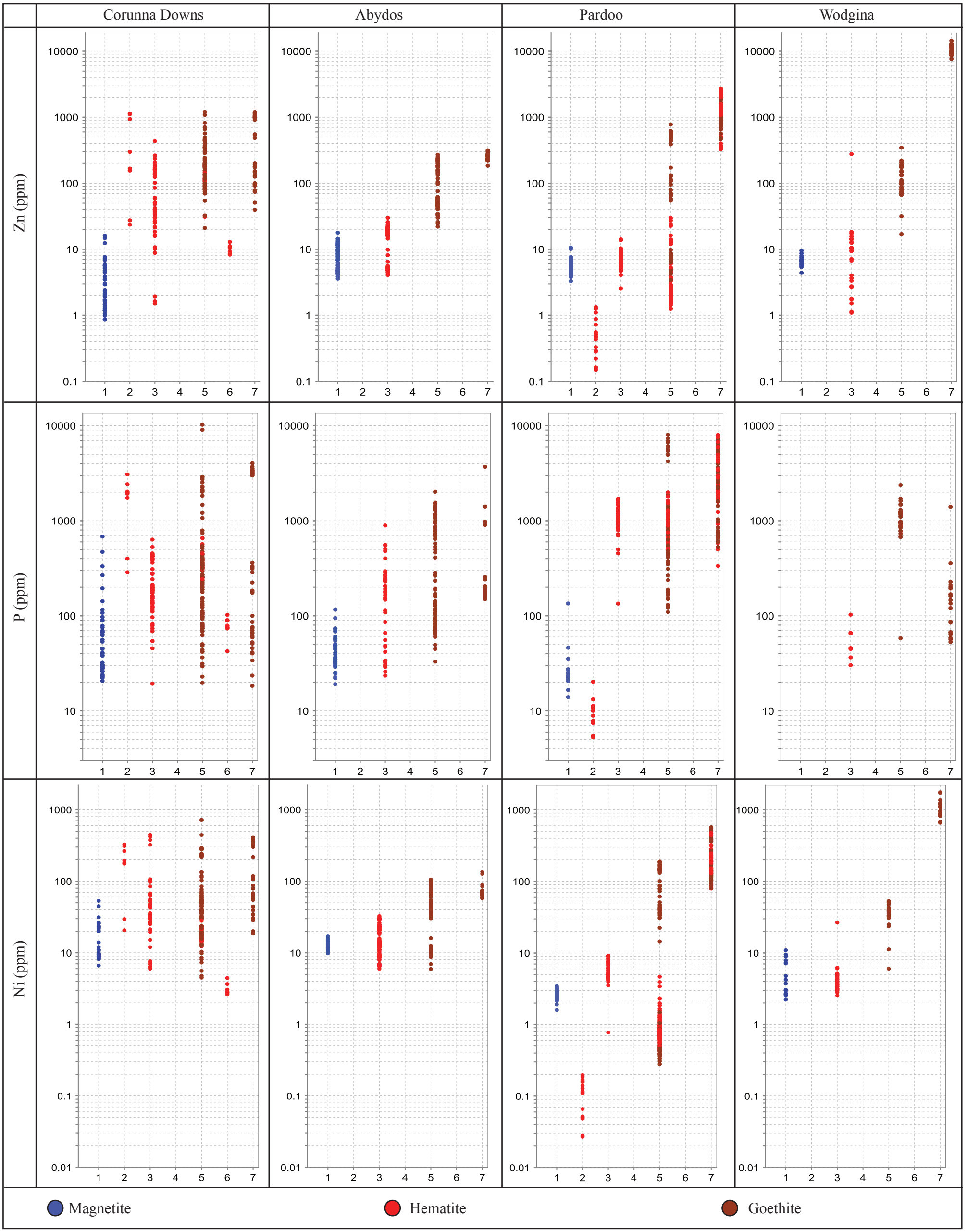

Figure 5: Plots of Zn, P and Ni abundances from stage 1 to stage 7 iron oxides at Corunna Downs, Abydos, Pardoo and Wodgina. 1 = stage 1 kenomagnetite, 2 = stage 2 platy hematite, 3 = stage 3 martite, 4 = stage 4 psilomelane (not analysed), 5 = stage 5 goethite and hematite, 6 = stage 6 microplaty hematite, 7 = stage 7 goethite and hematite.

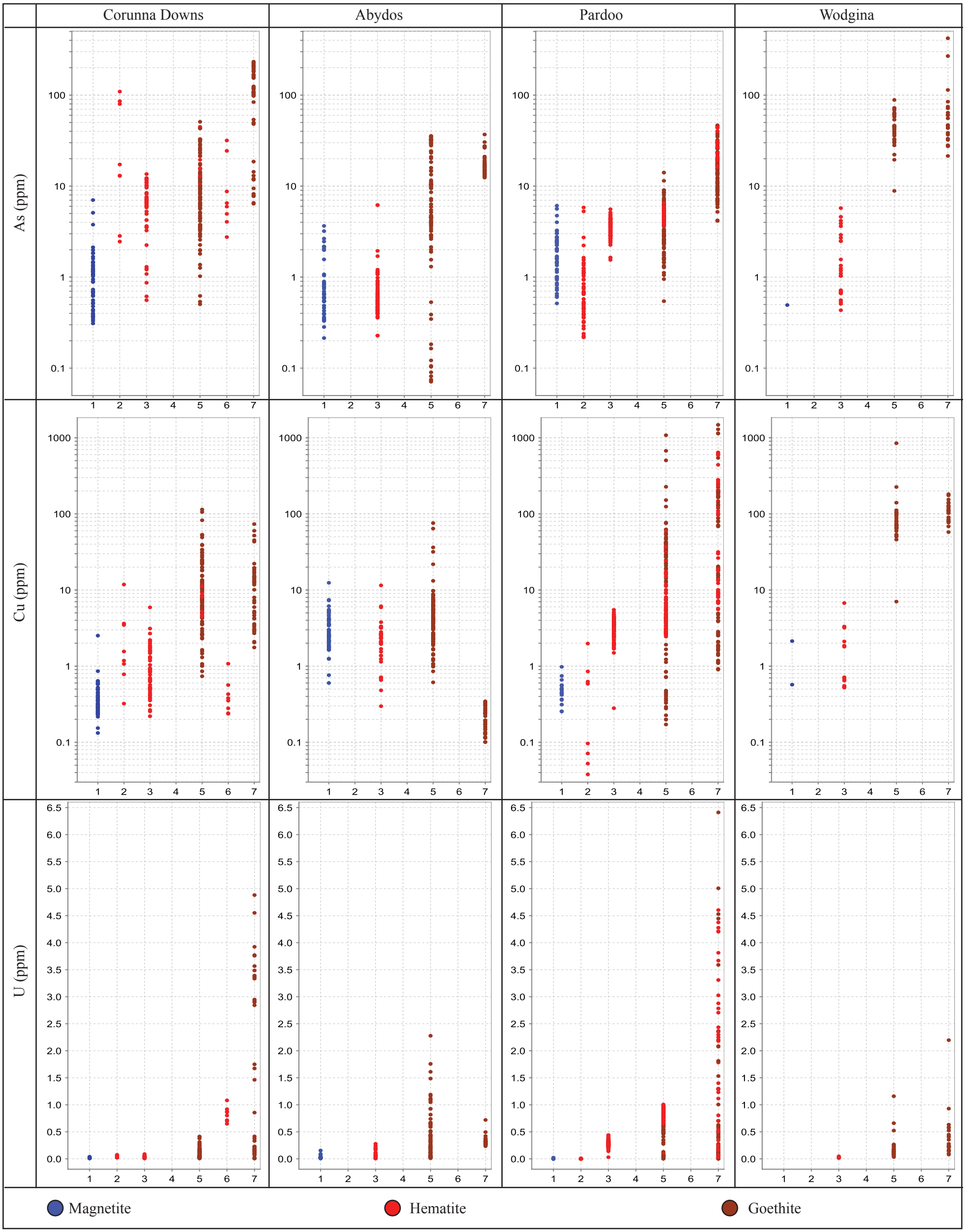

Figure 6: Plots of As, Cu and U abundances from stage 1 to stage 7 iron oxides at Corunna Downs, Abydos, Pardoo and Wodgina. X axis values: 1 = stage 1 kenomagnetite, 2 = stage 2 platy hematite, 3 = stage 3 martite, 4 = stage 4 psilomelane (not analysed), 5 = stage 5 goethite and hematite, 6 = stage 6 microplaty hematite, 7 = stage 7 goethite and hematite.

goethite after exposure to wildfires and/or prolonged solar radiation. Stage 6 microplaty hematite is depleted in P, Zn, Ni and Cu but enriched in U relative to stage 5 goethite (Fig. 5, 6).

(vii) Stage 7 vein- and vug-hosted, massive to botryoidal goethite (Fig. 4G) displays accessory colloform quartz and psilomelane (Fig. 4H). Stage 7 goethite is enriched in Zn, Ni and As, but depleted in P compared with stage 5 goethite (Fig. 5, 6).

(viii) Stage 8 ochreous goethite is present in all camps, and is locally associated with accessory psilomelane.

Deposit-scale geochemical and geophysical signatures of iron ores

The Split Rock and Runway deposits in the Corunna Downs camp, as well as the Trigg and Mettams deposits at Abydos, display kilometre-scale enrichments in Ni (up to 0.01 wt. %, i.e. 100 ppm) and Zn (up to 200 ppm) relative to distal BIF (Fig. 7). These geochemical patterns expressed in company assay data correspond to the presence of goethite-rich BIF in each iron camp. Specifically, the enrichments correspond to stage 5 and/or stage 7 goethite. Furthermore, Cu and As enrichments are identified in the Trigg and Mettams deposits only (see Chapter 3). Based on the distinction of stages 5 and 7 goethite using LA-ICP-MS mineral chemistry data, it is possible to distinguish stage 5 from stage 7 goethite in company assay data. For example at Abydos, a positive Ni and/or As enrichment combined with depletion in Be and/or low Zn values (i.e. < 100 ppm) can be used to target stage 5 goethite. Interestingly, at Corunna Downs, deposit-scale enrichments in Zn and Ni are only observed at the Split Rock and Runway deposits, whereas the Shark Gully and Glenn Herring deposits do not exhibit these enrichments. A reason for this disparity in element enrichments between deposits in the Corunna Downs camp is likely related to relative differences in the local

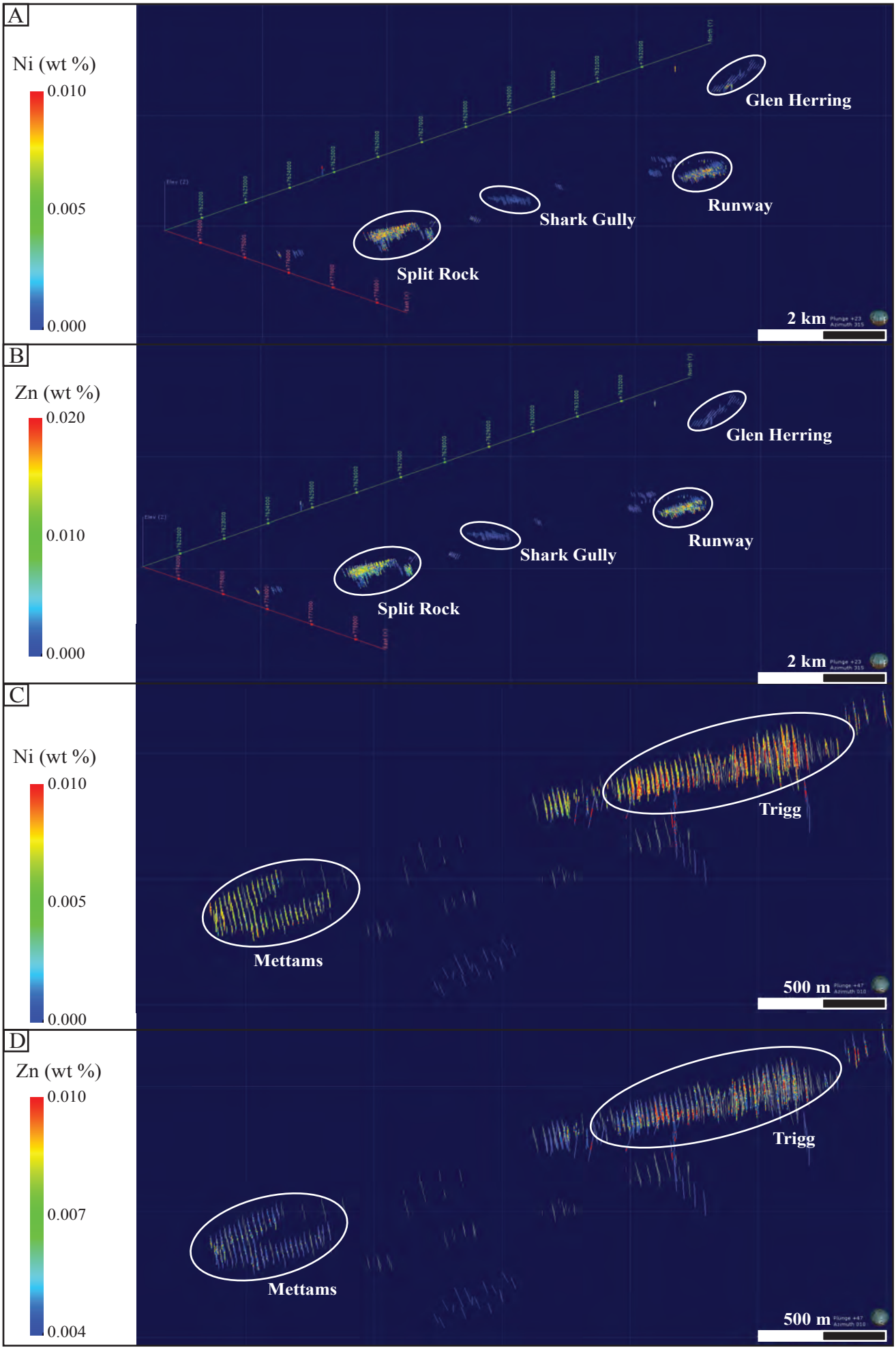

Figure 7: Geochemical anomalies associated with ore bodies identified from company assay data. A) Ni anomalies at Corunna Downs, B) Zn anomalies at Corunna Downs, C) Ni anomalies at Abydos, D) Zn anomalies at Abydos.

geology within the camp. Carbonaceous shale that lies adjacent to the BIF macroband at Split Rock and Runway deposits most likely contributed to the high Ni and Zn concentrations (up to 750 ppm and 2,800 ppm, respectively) in stages 5 and/or 7 goethite in these orebodies.

The presence of stage 1 hypogene magnetite alteration in BIF is best detected by magnetic surveying within a district, using least-altered and unmineralised BIF as a basis for comparison. At Corunna Downs and Abydos, areas of stage 1 magnetite in the Cleaverville Formation BIF can be differentiated from unmineralised BIF based on elevated anomalies in the total magnetic intensity data. However, intense martitisation and goethitisation of stage 1 magnetite may inhibit the magnetic anomalies caused by stage 1 magnetite alteration, depending both on the extent of the magnetic anomalies and the depth of the oxidised zone. At Abydos, subvertical BIF units likely extend to depths of 500 m below surface. An associated strong magnetic anomaly suggests extensive stage 1 magnetite alteration beneath the Trigg and Mettams deposits. Because martitisation and goethitisation of the BIF do not extend over 130 m below surface, it does not balance the strong magnetic signature resulting from stage 1 magnetite alteration. Therefore, the Trigg and Mettams deposits correspond to zones of strong positive magnetic anomalies. In contrast, BIF at Split Rock (Corunna Downs) is unlikely to extend more than 200-300 m below surface, i.e. a depth similar to that of the goethitisation front. In such conditions, the decrease in the total magnetic intensity due to BIF oxidative alteration overcomes the positive magnetic anomaly associated with magnetite alteration. Therefore, the Split Rock deposit displays a neutral to negative magnetic signature relative to least-altered BIF.

II. Genetic model for Cleaverville BIF-hosted iron ore in the East Pilbara Terrane and the Mallina Basin

Six major stages of deformation and/or mineralisation are recognised (Fig. 8):

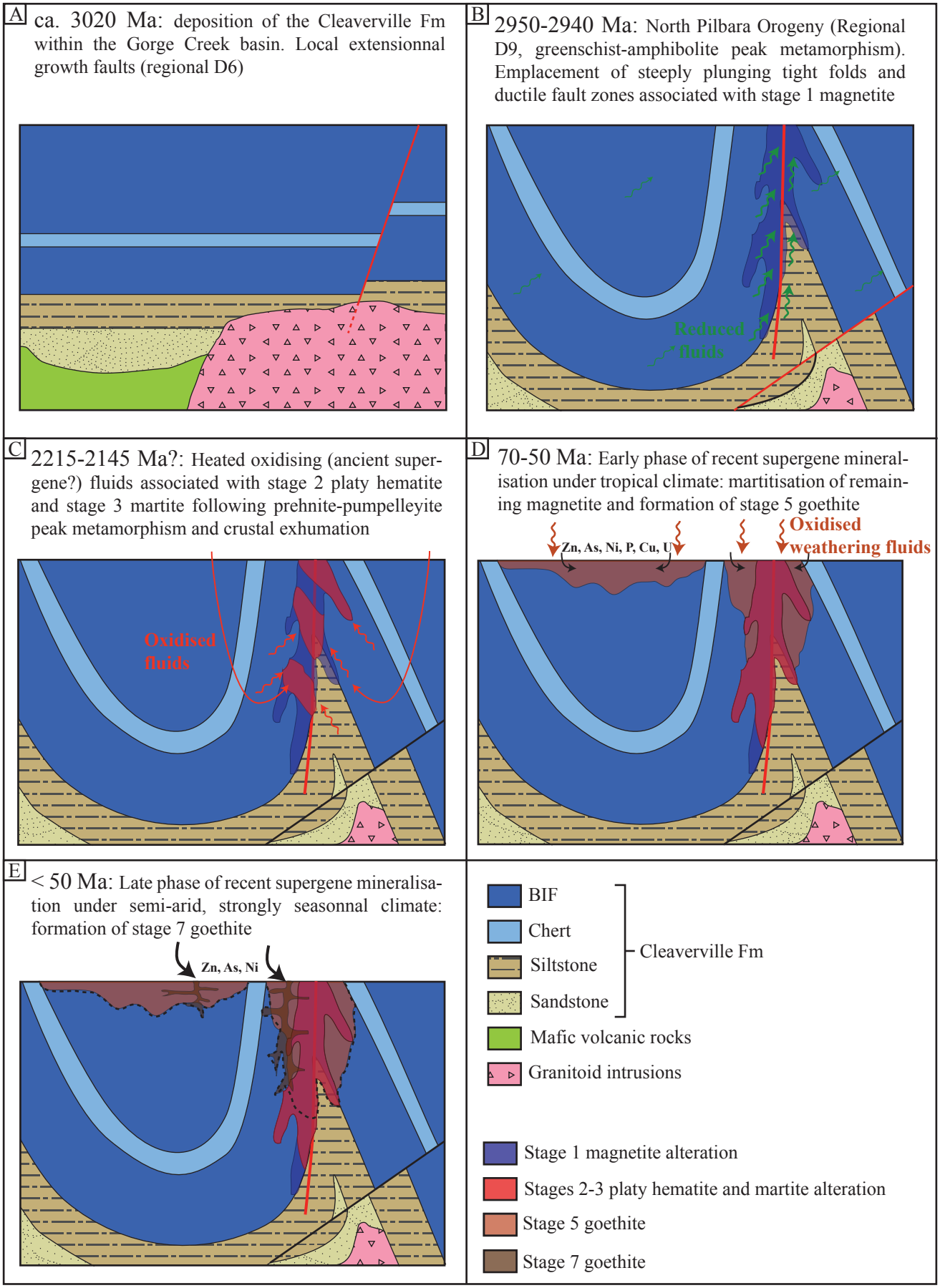

Figure 8: Schematic genetic model for the formation of Cleaverville BIF-hosted martite-goethite Fe ore bodies in the North Pilbara craton.

(i) ca. 3020 Ma: Deposition of the Cleaverville Formation as part of the Gorge Creek basin and development of growth faults (Fig. 8A). The Cleaverville Formation is thickest in the central parts of the Pilbara craton and deposited in shallow-water environments, therefore suggesting that sedimentation and subsidence rates were balanced. In contrast, the Cleaverville Formation in the East Pilbara Terrane displays a higher proportion of BIF versus chert and terrigenous sedimentary rocks, which suggests progressive deepening of the basin in eastern parts of the basin.

(ii) ca. 2950-2940 Ma: The craton-wide D9 deformation event related to the North Pilbara Orogeny resulted in tight folding and significant thickening of the Cleaverville Formation in all camps (Fig. 8B). D9 resulted in the development of steeply dipping ductile to brittle-ductile deformation zones along fold limbs. The circulation of reduced hypogene fluids through these shear zones resulted in stage 1 hypogene magnetite enrichment in BIF. The migration of hypogene fluids up to 100 m from shear zones precipitated disseminated hypogene magnetite in distal BIF wallrock.

(iii) Platy hematite and martite (stages 2 and 3) are interpreted to have formed due to circulation of hot oxidised fluids (Fig. 8C) through the reactivation of existing structures. Although the timing of this event remains poorly constrained, it is likely that oxidised fluids were heated due to geothermal gradients with depth during the Paleoproterozoic, possibly during or after crustal exhumation related to the 2215-2165 Ma metamorphic event in the Pilbara.

(iv) Exposure of the Cleaverville Formation BIF to tropical weathering (hot and humid conditions) from 70 to 50 Ma resulted in the complete martitisation of near-surface magnetite in BIF, followed by the formation of large volumes of stage 5

goethite (Fig. 8D). Goethite developed over unaltered and/or undeformed BIF forms a thin lateritic hard cap (typically <30 m in width). In contrast, areas of structurally-controlled high permeability in BIF are localities of deep (< 200 m) goethitisation of BIF. Stage 5 goethite is usually associated with enrichments in Zn, P, Ni, As, Cu and U compared to stage 1 magnetite, stage 2 platy hematite and stage 3 martite.

(v) Changes from tropical to semi-arid conditions with a strong seasonal control across the Pilbara region at ca. 50 Ma resulted in less intense weathering and leaching of silica in BIF. This late stage of supergene alteration resulted in the formation of secondary massive to botryoidal goethite within veins and vugs in BIF (Fig, 8E).

III. A Mineral System model for BIF-hosted iron ore in the Pilbara craton and implications for iron ore exploration

A mineral system model for BIF-hosted iron ore considers all key geological processes that control the formation and preservation of iron deposits. A four-step process has been proposed for linking the conceptual mineral system with data available to support exploration targeting. These steps include translation from (1) critical processes of the mineral system, to (2) constituent processes of the mineral system, to (3) targeting elements reflected in geology, and (4) targeting criteria used to detect the targeting elements directly or by proxy (cf. McCuaig et al., 2010). In this section, we apply this conceptual approach to Mesoarchean BIF-hosted iron ore in the North Pilbara craton (Fig. 9). Potential geochemical pathfinders for the individual iron camps are summarised in Table 5.

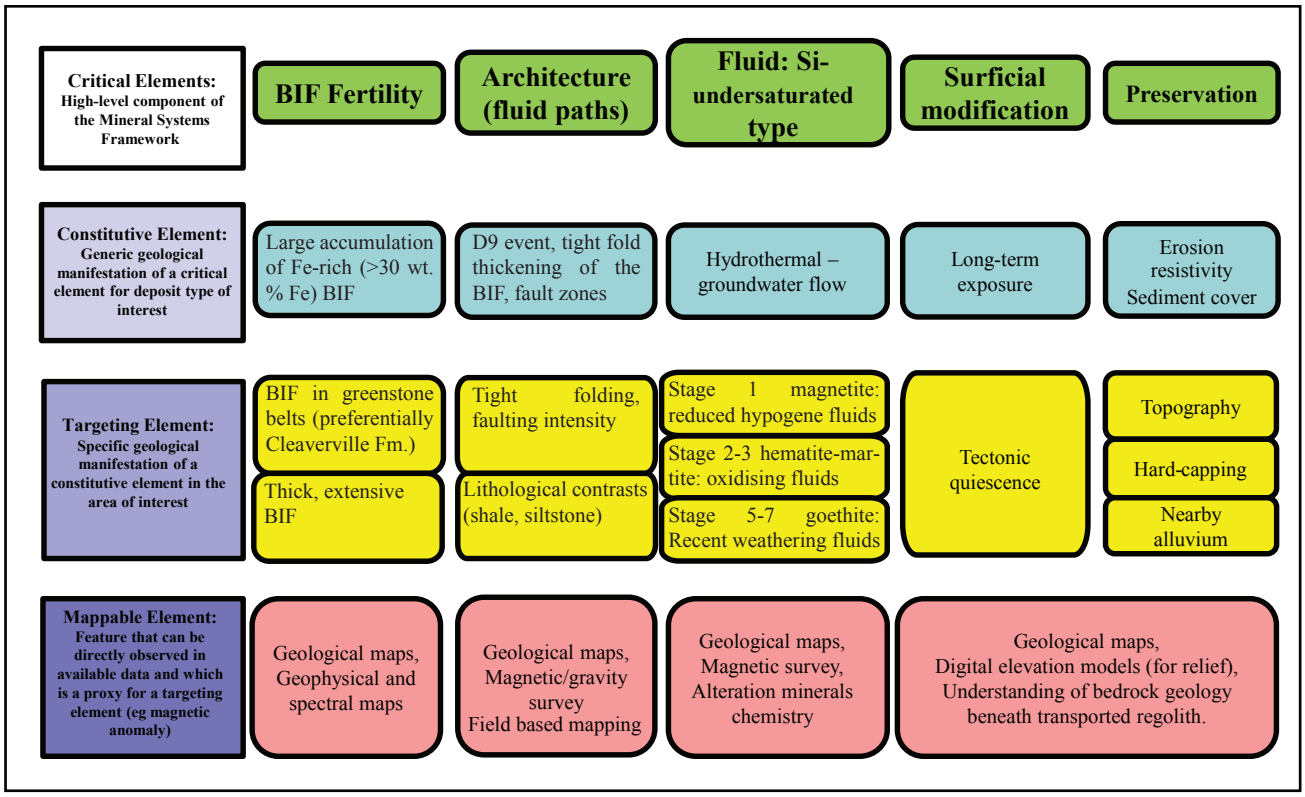

Figure 9: Mineral system flow chart for BIF-hosted iron ore in the North Pilbara craton.

BIF fertility

The main critical element for the formation of BIF-hosted iron ore is the occurrence of BIF macrobands that have a strong potential (fertility) for subsequent upgrade and mineralisation. The fertility of a given BIF macroband is primarily controlled by the extent, thickness and iron content of the primary BIF. Within the North Pilbara, BIF macrobands from the Cleaverville Formation display much greater thicknesses and are more laterally continuous compared to earlier BIF macrobands of the 3190 Ma Paddy Market Formation and the Pincunah Iron Member of the 3230 Ma Kangaroo Caves Formation. The Cleaverville Formation therefore represents the most prospective target for BIF-hosted iron ore in the North Pilbara Craton. Significant facies and primary grade variations are documented for the Cleaverville Formation throughout the central and east Pilbara. The proportion of BIF macrobands compared with Fe-poor sedimentary rocks increases from west to east across the East Pilbara Terrane. Furthermore, the total Fe content of the parent BIF is commonly higher (up to 60 wt. % Fe_2O_3) in BIF located in the eastern parts of the terrane (e.g. Corunna Downs). The recognition of these fertile BIF macrobands at a terrane scale largely relies on the availability of accurate outcrop geology maps, combined with geophysical surveys in areas of cover. Key parameters are BIF macroband thickness, lateral continuity, the proportion of BIF macrobands versus country rocks, and the primary grade of representative mesobands in BIF. At the district- to deposit-scale, ground-based mapping is preferred to test regional targets.

An important outcome of this study is a GIS-based prospectivity database for the Pilbara Craton (see the digital appendices). This GIS database includes geological outcrop and interpretation maps sourced from GSWA. BIF macrobands are categorised based on their host formation, age and dominant lithofacies. A qualitative ranking system has been used to identify the prospectivity of these macrobands (Table 4). An example of rankings within an

area within the craton-wide prospectivity map is shown for the Wodgina – Abydos – Mt Webber area in Figure 10. In this example, the western extension of the Wodgina greenstone belt is highlighted as an important potential acquisition target based on the likelihood that it hosts BIF macrobands that are comparable in primary chemistry to that documented in the Wodgina iron ore deposits. Important structural elements that control hypogene and supergene orebodies, such as multiple tight folds and stage 1 magnetite altered shear zones, may be present in this area.

Structural architecture: governing rock permeability and degree of fluid interaction with BIF

A critical element for the formation of BIF-hosted iron ore in the North Pilbara is the structural thickening of primary BIF macrobands via folding or shear zone duplication, together with the generation of broad damage zones related to shear zones or fault zones, which favour the circulation of fluids and alteration of BIF macrobands. The presence of shear zone-hosted stage 1 magnetite in all studied camps suggests the importance of early-formed structures in that they increase the total iron content of the primary BIF macrobands, but they also localise stress during subsequent deformation events and are common sites for reactivation. An early shear zone or fault zone that is repeatedly reactivated results in cyclical changes in local stress conditions in BIF, during which hypogene or supergene fluids are channelled through damage zones and cause step-wise, progressive removal of silica from BIF. Consequently, early-formed structures are favourable targets within a district due to their potential to be reactivated and to be the loci for fluid alteration of BIF. These structures can be recognised during mapping based on the observation of 1 to 10 m-thick zones of increasing strain, coincident with decreasing mesoband and microband thicknesses. The presence of stage 1 magnetite in these high-strain zones indicates the presence of a reduced

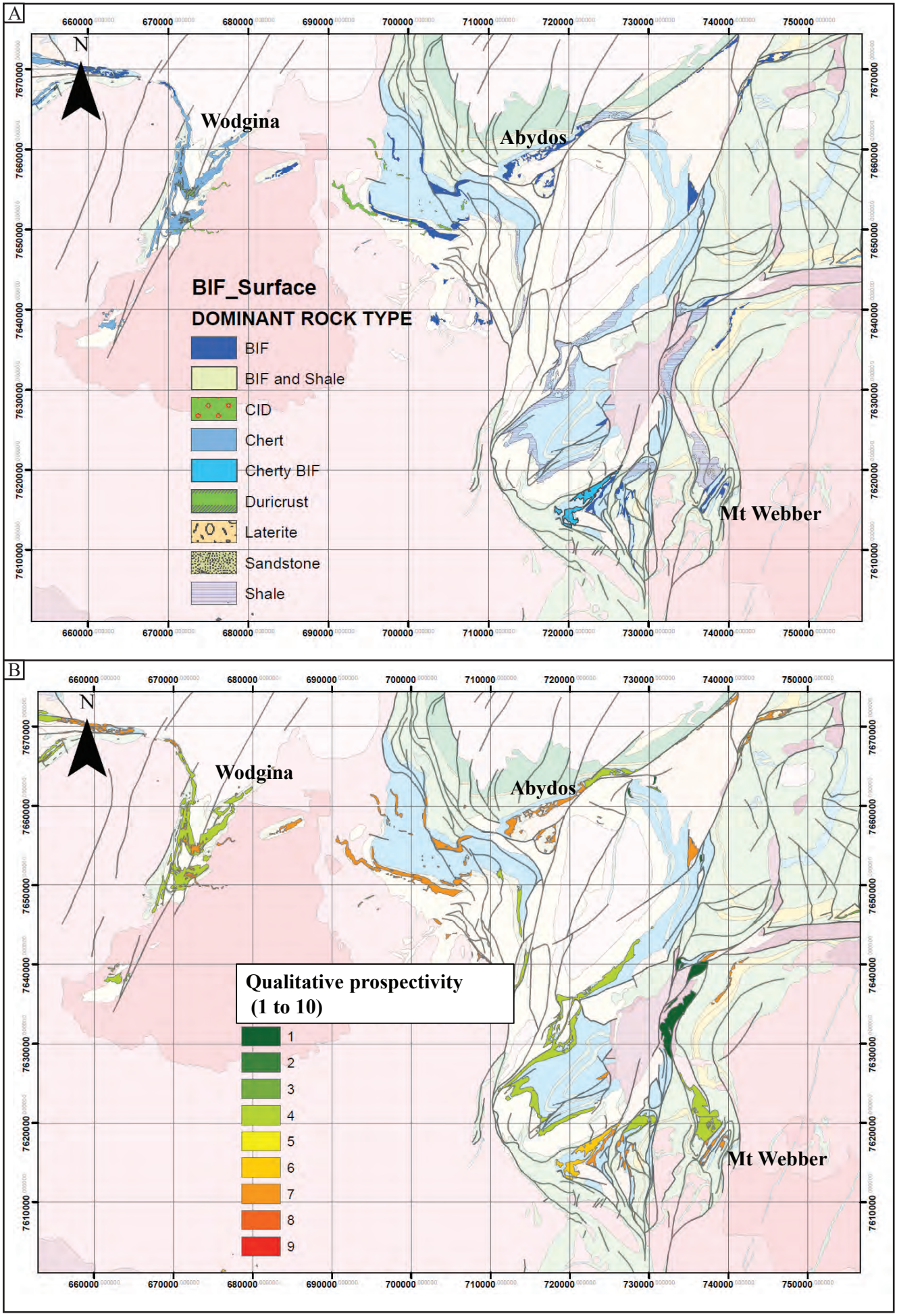

Figure 10: Distribution of dominant rock types and qualitative fertility of BIF-rich formation exposures in the Wodgina - Abydos - Mt Webber area, based on the compilation of digital 1:100,000 geology maps (GSWA).

CODE	FORMATION NAME	AGE MIN	AGE MAX	QUALITATIVE PROSPECTIVITY (10)	DOMINANT ROCK TYPE	DESCRIPTION
Qsf	Quaternary	0	2	2	Eolian	Eolian sand with lag deposits; ironstone-pebble, rock-fragment, or quartz-pebble veneer; in sheets and between dune
Qp	Quaternary	0	2	2	Eolian	Lag and eolian deposits_ironstone pebble, rock fragment, or quartz pebble veneer with eolian sand; between dunes; overlies
Czl	Cainozoic	2	65	7	Laterite	Laterite deposits, massive and pisolitic laterite, and ferruginous duricrust
Czap	Cainozoic	2	65	9	CID	Pisolitic, ferruginous channel deposits_ limonite, goethite, and hematite deposits; dissected old drainage line
Czaz	Cainozoic	2	65	7	CID	Silicified and ferruginized channel deposits; cemented quartzite and banded-iron formation clasts in conglomerat
Czcf	Cainozoic	2	65	7	CID	Consolidated ferruginous colluvium, recemented fragmented laterite, ironstone pebbles, clay, silt, and sand; canga deposits,
Czrf	Cainozoic	2	65	6	Duricrust	Residual ferruginous duricrust; includes massive, pisolitic, and nodular laterite
_R3r-f	Cainozoic	2	65	7	Duricrust	Ferruginous duricrust; includes massive, pisolitic, and nodular ferricrete; dissected by present-day drainag
_R3-f	Cainozoic	2	65	7	Duricrust	Ferruginous duricrust and ferruginous colluvium; locally includes ferruginous alluvium; consolidated to partly consolidated; re
A-STmt-xmu-mc	Millindinna intrusion	2925	2925	5	BIF	Interleaved talc–serpentine–chlorite schist and banded iron-formation, chert, and quartz–sericite schist; local cordierite hornf
ADch	Constantine sandstone	2970	2990	4	Shale	Shale, commonly ferruginized and/or silicified, lesser interbeds of poorly sorted arkose; minor banded iron-formation; metam
ADchi	Constantine sandstone	2970	2990	6	BIF and Shale	Ferruginized shale and banded iron-formation; metamorphosed
ADhe	Constantine sandstone	2970	2990	4	Shale	Metamorphosed ferruginous shale; locally abundant chert and mafic schist, and minor quartzÉmica schist and metamorphose
A-GC-s	Unassigned	2980	3016	5	Sandstone	Sandstone, siltstone, conglomerate, shale, chert, and banded iron-formation; metamorphosed
AGCe-ca	Cleaverville Formation	3016	3022	7	BIF	banded iron-formation, ferruginous chert, sandstone, siltstone, and shale; minor grey-white chert and felsic volcaniclastic roc
A-GCe-ca	Cleaverville Formation	3016	3022	7	BIF	banded iron-formation, ferruginous chert, sandstone, siltstone, and shale; minor grey-white chert and felsic volcaniclastic roc
AGCe-ci	Cleaverville Formation	3016	3022	7	BIF	Banded iron-formation and ferruginous chert; local banded quartz–magnetite–grunerite rock; metamorphosed
A-GCe-ci	Cleaverville Formation	3016	3022	7	BIF	Banded iron-formation and ferruginous chert; local banded quartz–magnetite–grunerite rock; metamorphosed
A-GCe-sh	Cleaverville Formation	3016	3022	4	Shale	Black shale, with minor chert and banded iron-formation; local siltstone; metamorphosed
A-GCe-shi	Cleaverville Formation	3016	3022	4	Shale	Ferruginous shale; metamorphosed
A-GCe-shz	Cleaverville Formation	3016	3022	1	Chert	Grey- and white-layered chert derived from shale; minor silicified sandstone
AGCe-xmc-md	Cleaverville Formation	3016	3022	4	Chert	Metachert and metamorphosed siliciclastic rocks
A-GCe-xmc-md	Cleaverville Formation	3016	3022	4	Chert	Metachert and metamorphosed siliciclastic rocks
AGl	Cleaverville Formation	3016	3022	6	Cherty BIF	chert and banded iron-formation; minor felsic volcaniclastic rock; metamorphosed
AGlc	Cleaverville Formation	3016	3022	4	Chert	Chert; white and grey; locally banded; minor iron-formation; metamorphosed
AGli	Cleaverville Formation	3016	3022	8	BIF	Banded iron-formation; metamorphosed
AGn	Nimingarra iron Formation	3016	3022	8	BIF	banded iron-formation, jaspilite, banded and ferruginous chert, and black carbonaceous shale; metamorphosed
AGncc	Nimingarra iron Formation	3016	3022	1	Chert	Chert; laminated white and grey chert, weakly banded to massive white chert, and dark-grey chert after carbonaceous shale;
AGncss	Nimingarra iron Formation	3016	3022	2	Chert	Laminated white and grey chert, white chert, dark-grey chert, and fine-grained siltstone and sandstone; local ferruginous che
AGnccw	Nimingarra iron Formation	3016	3022	2	Chert	Massive to weakly banded white chert with local banded white and grey chert; local ferruginous chert and jaspilite; metamor
AGnccx	Nimingarra iron Formation	3016	3022	1	Chert	Massive to weakly banded white chert containing beds of chert conglomerate and sedimentary chert breccia; metamorphose
AGnci	Nimingarra iron Formation	3016	3022	8	BIF	Banded iron-formation, jaspilite, banded and ferruginous chert, and black carbonaceous shale; metamorphosed
AGncic	Nimingarra iron Formation	3016	3022	5	Chert	Ferruginous chert, jaspilite, and ironstone; lesser banded iron-formation, and black carbonaceous shale; metamorphosed
AGncix	Nimingarra iron Formation	3016	3022	5	Chert	Tectonically brecciated ferruginous chert, jaspilite, ironstone, banded iron-formation, and shale; metamorphosed
AGnssc	Nimingarra iron Formation	3016	3022	2	Sandstone	Poorly sorted, poorly graded, fine-grained sandstone and siltstone beds with locally abundant chert beds; locally ferruginous;
A-GCe-cij	Unassigned - Gorge Creek Group	2980	3070	8	BIF	Banded iron-formation and jaspilite
A-xmc-mtq-P	Prinsep Orogeny	3060	3070	3	Chert	Layered white and grey metachert, and quartzite; local minor jaspilite and iron-formation
A-SOy-ci	Pyramid Hill Formation	3070	3190	7	BIF	Banded iron-formation; minor chert and shale; metamorphosed
A-SOy-sh	Pyramid Hill Formation	3070	3190	3	Shale	Red-weathered, ferruginized, black shale; metamorphosed
A-SOy-shz	Pyramid Hill Formation	3070	3190	1	Shale	Silicified shale; grey, white, and black layered chert; metamorphosed
A-SOp-ci	Paddy Market Formation	3190	3190	6	Cherty BIF	Thinly bedded black, white, red, and grey, cherty banded iron-formation; minor ferruginous shale; weakly metamorphosed
A-SOp-cci	Paddy Market Formation	3190	3190	6	Cherty BIF	Cherty banded iron-formation and chert; thinly bedded and partly jaspilitic; minor ferruginous shale; metamorphosed
A-SOp-fdw	Paddy Market Formation	3190	3190	1	Dacite	Massive to spherulitic dacite; metamorphosed
A-SOp-mi	Paddy Market Formation	3190	3190	7	BIF	Meta-iron formation
A-SOp-shz	Paddy Market Formation	3190	3190	1	Shale	Silicified shale; grey- and white-layered secondary chert; metamorphosed
A-SOa-sh	Cardinal Formation	3200	3228	4	Shale	red-weathered, ferruginized black shale, with minor siltstone; local banded iron-formation, chert, sandstone, and conglomera
A-SSk-sh	Kunagunarrina Formation	3240	3240	4	Shale	Shale; local wacke, sandstone, siltstone, or banded iron-formation; metamorphosed
A-SScp-ci	Pincunah Banded Iron Member (Kangaroo Caves Formation)	3235	3252	7	BIF	iron-formation; jaspilitic; minor layered chert and shale; metamorphosed
ASOc-i	Corboy Formation	3200	3270	7	BIF and Shale	Banded iron-formation and shale; weakly metamorphosed
AG(ci)	Unassigned	2980	3400	7	Cherty BIF	Thinly bedded black, white, and red banded iron-formation interbedded with ferruginous chert and minor ferruginous shale;
AG(cis)	Unassigned	2980	3400	6	Cherty BIF	Sheared cherty banded iron-formation; white chert and limonitic layers; weakly metamorphosed
A-WAp-ci	Panorama Formation	3427	3449	7	BIF	Banded iron-formation; local ferruginous shale; metamorphosed
A-WAp-cij	Panorama Formation	3427	3449	7	BIF	Jaspilite banded iron-formation; metamorphosed
A-WAdm-ccb	Duffer Formation - Marble Bar Chert Member	3463	3463	2	Chert	red, white, and grey layered chert; metamorphosed
A-WAdm-ccj	Duffer Formation - Marble Bar Chert Member	3463	3463	3	Chert	Jaspilitic chert; metamorphosed
A-WAd-xci-bb	Duffer Formation	3463	3474	6	BIF and Basalt	Interlayered iron formation and basalt; metamorphosed
AWdsh	Duffer Formation	3463	3474	6	BIF and Shale	Dark red- to black-weathering shale and banded iron-formation; thinly bedded; weakly metamorphosed
A-WAd-shi	Duffer Formation	3463	3474	4	Shale	Shale with interbeds of red and white layered chert, grey tuffaceous sandstone, and iron formation; metamorphosed
A-WAh-ci	McPhee Formation	3477	3481	7	BIF	Banded iron-formation; metamorphosed
Ac	Unassigned Pilbara Supergroup	3310	3490	4	Chert	Banded grey and white chert, locally abundant ferruginous chert, and minor banded iron-formation and fine-grained clastic ro
Acf	Unassigned Pilbara Supergroup	3310	3490	6	Chert	Ferruginous chert, banded iron-formation, and metamorphosed intercalated fine-grained clastic sedimentary rock
Aci	Unassigned Pilbara Supergroup	3310	3490	8	BIF	Banded iron formation; minor ferruginous cher

Table 4: Metadata table built for compilation of digital geology maps and prospectivity analysis study.

Abydos	Pardoo	Wodgina	Corunna Downs

Alteration stage	Alteration intensity	Mineral chemistry	Whole-rock chemistry	Company assay data	Magnetic surveys
Stage 1 *Magnetite*	4/10 4/10 2/10 5/10	↗ Ti, V None None None	↗ Ti, V ↗ W, Be None None	None None None None	Highly magnetic broad zones > 1km
Stage 2 *Platy hematite*	0/10 1/10 0/10 1/10	N.A. ↗ Sn? N.A. ↗ P	N.A. None N.A. None	N.A. None N.A. None	N.A.
Stage 3 *Martite*	4/10 4/10 2/10 5/10	↗ Ti, V, Ga, P ↗ P, V, Cr, W ↗ V, Ti, Ga, Sn, W ↗ W	None None ↗ Ti ↗ W, Sb	None None None None	Demagnetised zones < 1km-scale if magnetite oxidation extends through the entire BIF thickness
Stage 5 *Goethite Hematite*	5/10 5/10 7/10 7/10	↗ P, Ni, Cu, Zn, As ↗ P, Ca, Cu, Ba ↗ P, Ni, Ca, Zn, As ↗ Zn, Ba	↗ P, Ni, Cu, Zn, As ↗ P, Zn, Cu, Ba ↗ P, Zn ↗ P, Ni, Cu, Zn	↗ Ni, Cu, Zn, As None None ↗ Ni, Zn	
Stage 6 *Microplaty hematite*	0/10 0/10 0/10 1/10	N.A. N.A. N.A. None	N.A. N.A. N.A. None	N.A. N.A. N.A. None	
Stage 7 *Goethite Hematite*	3/10 3/10 2/10 2/10	↗ Si, Zn, As ↗ P, Ni, Zn, As, Co ↗ Ca, Mg, Ni, Zn ↗ As, U	↗ Si, Zn, Be, P ↗ P, Zn, Cu, Ba ↗ P, Zn ↗ P, Ni, Cu, Zn	↗ Ni, Zn, As None None ↗ Ni, Zn	

Systematic enrichments: P, Zn (stages 5 and 7)

Common enrichments: Ni, As, Ba, Cu, U (stages 5 and 7)

Camp-dependant enrichments: Ti, V, W, Sb, Ga (stages 1 to 3)

Table 5: Summary of geochemical and geophysical anomalies identified from mineral chemistry, whole-rock chemistry, company assay data and magnetic surveys for the main alteration stages at Abydos, Pardoo, Wodgina and Corunna Downs.

hypogene fluid and constrains the relative timing and depth of deformation. Documented early shear zones in the studied iron camps are oriented subparallel to bedding, indicating their likely formation via flexural slip during folding and subsequent shearing after folding. Transposition of these shear zones and bedding contacts aligns these structures. Hence, shear zone-hosted magnetite-rich ore zones are likely to be oriented subparallel to bedding contacts in BIF macrobands and are difficult targets to discriminate using remotely acquired geophysical surveys or aerial imaging surveys. These targets are more readily and accurately identified in outcrop during reconnaissance mapping and prospecting. The confluence of reactivated early-formed shear zones and fold hinge zones are the best target for the generation of high-volume, high-quality, goethite-hematite orebodies (e.g. the Split Rock deposit, Corunna Downs iron camp). In these areas, the plunge of fold axes and intersection lineations derived from merging shear zones can be used to predict the plunge of high-grade ore zones. These early observations recorded during mapping provide an assessment about the likelihood that surface expressions of high-grade goethite-hematite ore continue to greater depths.

Si-under saturated fluids

A third critical element for the formation of BIF-hosted iron deposits is the availability of abundant Si-under saturated fluids. Fluid inclusion studies on hypogene iron oxides and related gangue minerals were not possible in this study due to the lack of suitable gangue material and the small size of the iron oxides. For example, stage 1 magnetite that is present in each studied iron camp is locally intergrown with fine-grained (<25 μm) quartz (e.g. magnetite-quartz veins at Corunna Downs) that was too fine for observing trapped fluid inclusions. Instead, mineral assemblages are used to constrain the composition, temperature, pressure and redox conditions for hypogene fluids (cf. Barnes, 1979). In this case, stage 1

magnetite likely precipitated from a relatively reduced, hot, deeply circulating, silica-bearing fluid. Interestingly, this hypogene fluid alteration event also resulted in the localised addition of hypogene quartz to BIF, thus moderating the potential benefit of adding hydrothermal iron oxides to the primary BIF. Consequently, stand-alone examples of shear zone-hosted magnetite-rich ore zones are likely to have a significant silica content. These magnetite-enriched occurrences require subsequent supergene alteration to remove the silica to form a high-grade iron ore. During mapping, the identification of magnetite-enriched locations should be traced along strike into zones of supergene goethite-hematite alteration, or areas of cover, for the purpose of targeting likely deep extensions of near-surface higher-grade iron ore.

In comparison with hypogene fluids, the composition of later supergene fluids is likely to be influenced by the weathering environment in which these fluids were sourced and the interaction between these surface-derived oxidised, low-temperature fluids and rocks encountered along the fluid pathway. Under tropical conditions (i.e. stage 5 alteration at 70 to 50 Ma), weathering involved acidic, Si-under saturated meteoric fluids (Anand, 2010). These fluids have a strong potential to dissolve silica, thus favouring the concentration of iron in BIF macrobands and the formation of goethite ore. However, under semi-arid conditions (i.e. stage 7; <50 Ma) meteoric fluids have a neutral pH and are therefore less efficient for the dissolution of silicate minerals. For example at Abydos, volumetrically important stage 5 goethite contains less Si in its lattice compared with stage 7 goethite. The latter goethite stage is also commonly associated with colloform quartz.

Surficial modification and preservation

A fourth critical element for the formation of BIF-hosted iron deposits in the Pilbara is the length of time that these primary and hypogene magnetite-rich BIF macrobands were exposed

at surface and subjected to the interaction with near-surface derived supergene fluids, as well as the necessary preservation of these supergene- or supergene-modified ore bodies. As mentioned previously, supergene alteration under tropical conditions from ca. 70 to 50 Ma was a dominant process in the formation of iron orebodies in the North Pilbara. However, it is unclear whether the entire North Pilbara was uniformly exposed and subjected to weathering since the late Cretaceous. In the absence of regionally extensive high rates of erosion, deep weathering profiles are not only formed, but are preserved. Preservation is greatest in the arid interior, beyond the marginal zones of valley incision, or on land surfaces with mainly subdued relief. In the studied iron camps, BIF macrobands are more resistant to erosion compared with surrounding ultramafic, mafic or granitoid rocks. However, within a single laterally continuous BIF macroband, the supergene and supergene-modified hypogene iron ore bodies are generally coincident with topographic depressions within the exposed strike-parallel ridges (e.g. the Split Rock deposit at Corunna Downs). The development of lateritic hard caps on top of iron deposits in most camps protects underlying ore bodies from complete erosion. The location of hard cap over fold hinges and intersecting steeply dipping shear zones (detected from structural mapping and interpretation of geophysical data) is a target area for exploration on the basis of the likely preservation of deeper (hidden) ore zones.

In some areas of the Pilbara, the presence of eolian or fluviatile sediments on top of BIF-hosted iron orebodies may provide favourable conditions for the preservation of the iron ore bodies. For instance, the recent (<15 Ma) eolian sand deposits that cover the eastern margin of the Pilbara Craton locally overly BIF units from the Cleaverville Formation (e.g. in the Isabella 1:100,000 geology map). In this area, sand cover may protect iron orebodies from erosion but hinders their surface detection via mapping. We recommend the evaluation of areas where the Cleaverville BIF is overlain by recent (<15 Ma) eolian or alluvial cover for the presence of supergene or supergene-modified hypogene iron ore.

Guidelines for exploration methodology

A possible exploration strategy for Cleaverville BIF-hosted iron ore includes:

(i) Compilation of remotely acquired data sets to map out anomalously thickened areas of BIF macrobands.

(ii) Establishing the geophysical and geochemical properties of unmineralised, unaltered BIF macrobands in the area (i.e. defining a base-level for comparison), before identifying any anomalous areas in terms of magnetism or density (magnetite-rich vs. hematite vs. goethite enrichment).

(iii) Establishing the broad, district-scale deformation history and identifying the earliest structures. These structures may potentially be reactivated during subsequent deformation events and interpreted far-field stress conditions.

(iv) Ranking of these targets based on the before-mentioned regionally-based targeting methods. Perform field-based mapping of ranked targets by creating detailed structural, alteration and lithological maps of the target areas.

(v) Identify areas that display the key structural architecture (i.e. fold hinges, reactivated early shear zones, intersecting shear zones, intersection lineaments as guides to the plunge of iron orebodies).

(vi) Locate areas of hypogene alteration in BIF by identifying likely hypogene alteration minerals (e.g. disseminated, euhedral magnetite grains that overprint silica-rich primary bands). Follow these hypogene-altered zones in BIF macrobands towards areas of supergene enrichment and/or cover by transported sediment.

(vii) Use a weighting system and exploration matrix to rank these targets before selecting areas for follow-up drill testing.

This process is iterative and requires observational data to be fed back into the evolving Mineral Systems model.

The before-mentioned district-scale targeting method is an efficient and cost-effective process for generating targets for testing by more time-consuming and costly drilling. There is an obvious benefit in identifying the potential endowment of a new district as early as possible within an exploration campaign. This type of assessment has been applied to some of the major gold and nickel camps (McCuaig et al., 2000). In these camps, the recognition of the largest resources is used as a predictor for the existence of the number and size of smaller resources, based on the common Power Law distribution of resources within a district. Notable absences within the Power Law distribution curve are interpreted as an indicator or potentially undiscovered orebodies in the district. Work conducted by P. Hawke on iron ore resource sizes for the Pilbara Craton shows a typical decreasing Power Law distribution for iron ore resource size (Fig. 11A). Based on these trends, the Pilbara Craton represents a mature region for iron ore exploration. However, it should be noted that this approach strongly depends on the assumption that all BIF units are equally fertile, and that it does not account for differences in the metallurgical properties and presence of contaminants in iron ore (i.e. iron ore quality).

A second measure of a new district or deposit's potential endowment may be assessed during early stages of drilling by measuring the distribution of iron grades (Fig. 11). In this study, we have plotted the distribution of iron grades for the major iron ore deposits and prospects in the Abydos (Fig. 11C) and Pardoo camps (Fig. 11D). The high-quality iron deposits are those with a greater proportion of high-grade iron ore intersected by drilling (e.g. the Trigg deposit in the Abydos camp and the Alice deposit in the Pardoo camps). Provided that the drill density is sufficient, these types of plots are useful for comparing the quality of iron deposits.

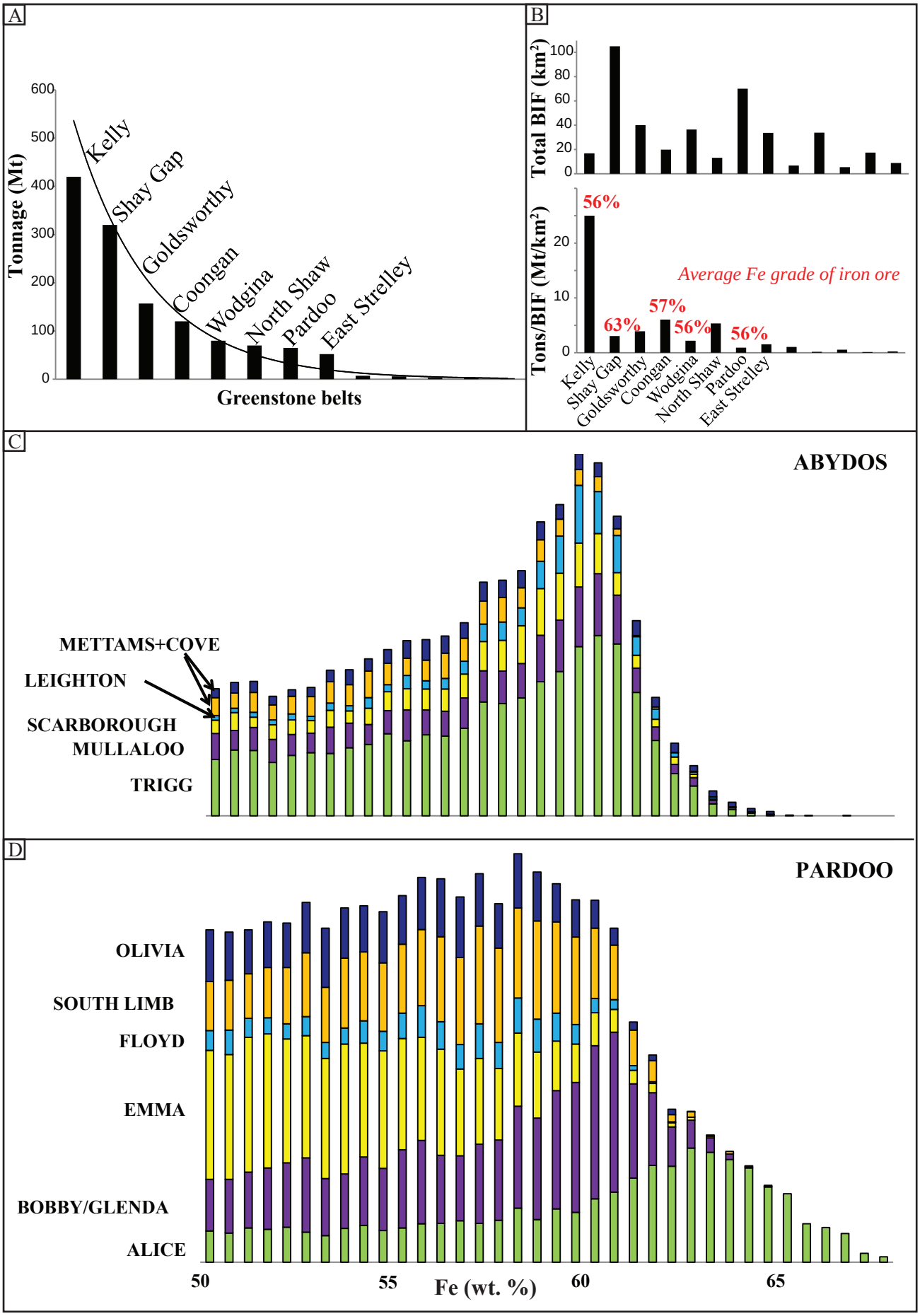

Figure 11: (A) Estimated iron ore tonnages for individual greenstone belts and best fit with decreasing power law, (B) total surface (in km2) of exposed BIF and degree of mineralisation expressed as the tonnage/exposed BIF surface ratio. (C) and (D) frequency distribution of Fe grade in ore bodies (>50 wt. % Fe at Abydos and Pardoo, respectively). Diagrams shown in onsets A and B are based on data compilation by P. Hawke (2014). Diagrams shown in onsets C and D were established using company assay data.

This frequency distribution for iron grades from drilling is useful for the early assessment of an exploration target.

IV. Conclusions

This study documents the (i) geological framework, (ii) deformation histories, (iii) controls on iron ore formation, (iv) multi-stage hypogene and supergene fluid alteration events affecting BIF and the (v) geochemical signatures of their respective high-grade iron orebodies. A Mineral Systems model for the genesis of BIF-hosted iron orebodies is presented for the Pilbara Craton with implications for iron ore exploration.

Following the recent revision of the lithostratigraphy of the Pilbara craton by the GSWA, the BIF macrobands that host iron ore in the Abydos, Pardoo, Wodgina and Corunna Downs iron camps are classified as 3020 Ma Cleaverville Formation. In comparison, BIF macrobands of the 3230 Ma Pincunah Bander Iron Member of the Kangaroo Caves Formation and the 3190 Ma Paddy Market Formation do not host comparable iron ore deposits in terms of resource size. A comparison of mapped and sampled BIF macrobands from the studied iron camps demonstrates important facies variations from west to east across the East Pilbara Terrane. Specifically, primary BIF macrobands are generally more iron-rich, thicker and have a higher proportion of BIF versus Fe-poor sedimentary rocks (such as chert and siltstone) in the eastern parts of the East Pilbara Terrane. These craton-scale observations support a depositional model for the Cleaverville Formation in the East Pilbara Terrane wherein the Gorge Creek basin progressively deepens both spatially, from west to east, and temporally, with a deepening of the basin through time. REE + Y trends for examples of least-altered BIF sampled from each camp indicate that the representative BIF macrobands from the Cleaverville Formation formed from anoxic seawater with strong hydrothermal influence,

equivalent to noted trends for Meso- to Late-Archean BIF occurrences reported in the Yilgarn Craton and South Africa.

Cleaverville Formation BIF in all the studied iron camps record a similar deformation history that is compatible with that documented by previous workers for the Pilbara Craton. Although early folds and shear zones are present in the Wodgina camp, the dominant deformation event recorded by each camp is equivalent to the regional D9 event for the Pilbara Craton. This event is expressed in the camps by the prevalence of fold hinges and shear zones located along fold limbs. Subsequent deformation events resulted in the tightening of these fold hinges, the transposition of structural elements and bedding planes, and the transition to transpressional deformation and associated strike-slip shearing along steeply dipping contacts within the folded greenstone belts.

Iron ore types are remarkably similar in all iron camps in the East Pilbara Terrane. Iron ore types include, in order of formation: (i) hypogene magnetite-rich ore hosted by early shear zones, (ii) martite-rich BIF with local microplaty hematite, which are the product of early hypogene and/or late supergene alteration events, (iii) goethite and goethite-martite ores that result from intense supergene goethitisation of least-altered, magnetite- or martite-altered BIF, (iv) a second stage of vitreous goethite ore expressed as late veins of massive to botryoidal goethite, with colloform silica and (v) ochreous goethite ore.

The analysis of representative bulk rock samples of these iron ore types (combined with in situ LA-ICP-MS analysis of iron oxide minerals) demonstrates useful pathfinder element indices associated with the increase in total iron content and the decrease in silica for altered BIF. In all studied camps, it is noted that high-grade goethite-rich supergene orebodies have enrichments in P and Zn that correspond to matching enrichments in stage 5 and 7 goethite. In most camps, stage 5 and 7 goethite-rich orebodies are indicated by enrichments in Ni, As, Ba, Cu or U. Whereas localised enrichments in Ti, V, W, Sb or Ga are restricted to specific

camps. The widely present pathfinder elements (P and Zn) are most useful in terms of their craton-wide application. The more localised element enrichments indicate that camp- to deposit-scale geological controls are influencing these enrichment patterns. For example, the presence of thick shale units likely controls the presence of local Ni and Zn enrichment in areas of the Corunna Downs camp.

The Mineral Systems model for the genesis of BIF-hosted iron orebodies in the Pilbara craton identifies four critical elements: (i) BIF fertility, (ii) structural architecture governing rock permeability and degree of fluid interaction with BIF, (iii) Si-under saturated fluids and (iv) surficial modification and preservation.

The main critical element for the formation of BIF-hosted iron ore is the occurrence of BIF macrobands that have a strong potential (fertility) for subsequent upgrade and mineralisation. The fertility of a given BIF macroband is primarily controlled by the extent, thickness and iron content of the primary BIF. Within the North Pilbara, BIF macrobands from the Cleaverville Formation display much greater thicknesses and are more laterally continuous compared to earlier BIF macrobands of the 3190 Ma Paddy Market Formation and the Pincunah Iron Member of the 3230 Ma Kangaroo Caves Formation. The Cleaverville Formation therefore represents the most prospective target for BIF-hosted iron ore in the North Pilbara Craton. The recognition of these fertile BIF macrobands at a terrane scale largely relies on the availability of accurate outcrop geology maps, combined with geophysical surveys in areas of cover. An important outcome of this study is a GIS-based prospectivity database for the Pilbara Craton (see the digital appendices). This GIS database includes geological outcrop and interpretation maps sourced from GSWA. BIF macrobands are categorised based on their host formation, age and dominant lithofacies. A qualitative ranking system has been used to identify the prospectivity of these macrobands. The western extension of the Wodgina greenstone belt is highlighted as an important potential acquisition

target based on the likelihood that it hosts BIF macrobands that are comparable in primary chemistry to that documented in the Wodgina iron ore deposits. Important structural elements that control hypogene and supergene orebodies, such as multiple tight folds and stage 1 magnetite altered shear zones, may be present in this area.

A critical element for the formation of BIF-hosted iron ore in the North Pilbara is the structural thickening of primary BIF macrobands via folding or shear zone duplication, together with the generation of broad damage zones related to shear zones or fault zones, which favour the circulation of fluids and alteration of BIF macrobands. The presence of shear zone-hosted stage 1 magnetite in all studied camps suggests the importance of early-formed structures in that they increase the total iron content of the primary BIF macrobands, but they also localise stress during subsequent deformation events and are common sites for reactivation. Consequently, early-formed structures are favourable targets within a district due to their potential to be reactivated and to be the loci for fluid alteration of BIF. These structures can be recognised during mapping based on the observation of 1 to 10 m-thick zones of increasing strain, coincident with decreasing mesoband and microband thicknesses. The confluence of reactivated early-formed shear zones and fold hinge zones are the best target for the generation of high-volume, high-quality, goethite-hematite orebodies (e.g. the Split Rock deposit, Corunna Downs iron camp). In these areas, the plunge of fold axes and intersection lineations derived from merging shear zones can be used to predict the plunge of high-grade ore zones.

A third critical element for the formation of BIF-hosted iron deposits is the availability of abundant Si-under saturated fluids. Stage 1 magnetite likely precipitated from a relatively reduced, hot, deeply circulating, silica-bearing fluid. This hypogene fluid alteration event also resulted in the localised addition of hypogene quartz to BIF, thus moderating the potential benefit of adding hydrothermal iron oxides to the primary BIF. Consequently, stand-alone

examples of shear zone-hosted magnetite-rich ore zones are likely to have a significant silica content. These magnetite-enriched occurrences require subsequent supergene alteration to remove the silica to form a high-grade iron ore. In comparison with hypogene fluids, the composition of later supergene fluids is likely to be influenced by the weathering environment in which these fluids were sourced and the interaction between these surface-derived oxidised, low-temperature fluids and rocks encountered along the fluid pathway. Under tropical conditions (i.e. stage 5 alteration at 70 to 50 Ma), weathering involved acidic, Si-under saturated meteoric fluids. These fluids have a strong potential to dissolve silica, thus favouring the concentration of iron in BIF macrobands and the formation of goethite ore. However, under semi-arid conditions (i.e. stage 7; <50 Ma) meteoric fluids have a neutral pH and are therefore less efficient for the dissolution of silicate minerals.

A fourth critical element for the formation of BIF-hosted iron deposits in the Pilbara is the length of time that these primary and hypogene magnetite-rich BIF macrobands were exposed at surface and subjected to the interaction with near-surface derived supergene fluids, as well as the necessary preservation of these supergene- or supergene-modified ore bodies. Preservation is greatest in the arid interior, beyond the marginal zones of valley incision, or on land surfaces with mainly subdued relief. The development of lateritic hard caps on top of iron deposits in most camps protects underlying ore bodies from complete erosion. The location of hard cap over fold hinges and intersecting steeply dipping shear zones (detected from structural mapping and interpretation of geophysical data) is a target area for exploration on the basis of the likely preservation of deeper (hidden) ore zones. In some areas of the Pilbara, the presence of eolian or fluviatile sediments on top of BIF-hosted iron orebodies may provide favourable conditions for the preservation of the iron ore bodies. The Cleaverville Formation documented in the Isabella 1:100,000 geology map is here identified

as an exploration target based on the potential to discover iron orebodies within BIF macrobands that are hidden beneath a veneer of eolian cover.

Step-wise guidelines for exploration strategy include (i) the compilation of remotely acquired data sets to map out anomalously thickened areas of BIF macrobands, (ii) establishing the geophysical and geochemical properties of unmineralised, unaltered BIF macrobands in the area so as to define a base-level for comparison, (iii) establish the district-scale deformation history and identifying the earliest structures and(iv) ranking regional-scale targets and test by field-based mapping. An early assessment of the likely endowment of a new exploration district or deposit-scale target can be made by applying a Power Law distribution curve to known resource sizes in a given district. Gaps within this decreasing frequency curve highlight potential undiscovered orebodies. A second measure of a new district or deposit's potential endowment may be assessed during early stages of drilling by measuring the distribution of iron grades. The high-quality iron deposits are those with a greater proportion of high-grade iron ore intersected by drilling (e.g. the Trigg deposit in the Abydos camp and the Alice deposit in the Pardoo camps). Provided that the drill density is sufficient, these types of plots are useful for comparing the quality of iron deposits. This frequency distribution for iron grades from drilling is useful for the early assessment of an exploration target.

References

Angerer, T., Hagemann, S.G., 2010. The BIF-hosted high-grade iron ore deposits in the Archean Koolyanobbing greenstone belt, Western Australia: Structural control on synorogenic- and weathering-related magnetite-, hematite-, and goethite-rich iron ore. Economic Geology 105, 917-945.

Angerer, T., Hagemann, S.G., Danyushevsky, L., 2012. High-grade iron ore at Windarling, Yilgarn Craton: a product of syn-orogenic deformation, hypogene hydrothermal alteration and supergene modification in an Archean BIF-basalt lithostratigraphy. Miner Deposita 48, 697-728.

Archer, D., 2009. Geology of the Wodgina region. Unpublished report for Atlas Iron Ltd.

Arndt, N.T., Nelson, D.R., Compston, W., Trendall, A.F., Thorne, A.M., 1991. The age of the Fortescue Group, Hamersley basin, Western Australia, from ion microprobe zircon U-Pb dating. Aust. J. Earth Sci. 38, 261-281.

Bagas, L., Van Kranendonk, M.J., Pawley, M., 2004. Geology of the Split Rock 1:100 000 sheet. Western Australia Geological Survey, 1:100 000 Geological Series Explanatory Notes, 43p.

Barley, M.E., Pickard, A.L., Hagemann, S.G., Folkert, S.L., 1999. Hydrothermal origin for the 2 billion year old Mount Tom Price giant iron ore deposit, Hamersley Province, Western Australia. Miner Deposita 34, 784-789.

Bau, M., 1993. Effects of syn-depositional and postdepositional processes on the rare-earth element distribution in Precambrian iron-formations. Eur. J. Mineral. 5, 257-267.

Bau, M., Alexander, B.W., 2009. Distribution of high field strength elements (Y, Zr, REE, Hf, Ta, Th, U) in adjacent magnetite and chert bands and in reference standards FeR-3 and FeR-4 from the Temagami iron-formation, Canada, and the redox level of the Neoarchean ocean. Precambrian Research 174, 337-346.

Blewett, R.S., 2002. Archaean tectonic processes: a case for horizontal shortening in the North Pilbara Granite–Greenstone Terrane, Western Australia. Precambrian Research 113, 87-120.

Blewett, R.S., Champion, D.C., 2005. Geology of the Wodgina 1:100 000 sheet. Western Australia Geological Survey, 1:100 000 Geological Series Explanatory Notes, 33p.

Dermatas, D., Braida, W., Christodoulatos, N.S., Strigul, N., Panikov, N., Los, M., Larson, S., 2004. Solubility, Sorption, and Soil Respiration Effects of Tungsten and Tungsten Alloys. Environmental Forensics 5, 5-13.

Duuring, P., Hagemann, S.G., 2012a. Genesis of superimposed hypogene and supergene Fe orebodies in BIF at the Madoonga deposit, Yilgarn Craton, Western Australia. Miner Deposita 48, 371-395.

Duuring, P., Hagemann, S.G., 2012b. Leaching of silica bands and concentration of magnetite in Archean BIF by hypogene fluids: Beebyn Fe ore deposit, Yilgarn Craton, Western Australia. Miner Deposita 48, 341-370.

Figueiredo e Silva, R.C., Lobato, L.M., Rosiere, C.A., Hagemann, S.G., Ziucchetti, M., Baars, F.J., Morais, R., Andrade, I., 2008. Hydrothermal origin for the jaspilite-hosted, giant Serra Norte iron ore deposits in the Carajás mineral province, Para State, Brazil. Reviews in Economic Geology 15, 255-290.

Frei, R., Dahl, P.S., Duke, E.F., 2008. Trace element and isotopic characterization of Neoarchean and Paleoproterozoic iron formations in the Black Hills (South Dakota, USA): Assessment of chemical change during 2.9–1.9 Ga deposition bracketing the 2.4–2.2 Ga first rise of atmospheric oxygen. Precambrian Research 162, 441-474.

Gimenez, J., Martinez, M., de Pablo, J., Rovira, M., Duro, L., 2007. Arsenic sorption onto natural hematite, magnetite, and goethite. Journal of Hazardous Materials 141, 575-580.

Goss, C.J., 1987. The kinetics and reaction mechanism of the goethite to hematite transformation. Mineralogical Magazine 51, 437-451.

Grafe, M., Sparks, D.L., 2005. Kinetics of zinc and arsenate co-sorption at the goethite–water interface. Geochimica Et Cosmochimica Acta 69, 4573-4595.

Heim, J.A., Vasconcelos, P.M., Shuster, D.L., Farley, K.A., Broadbent, G., 2006. Dating paleochannel iron ore by (U-Th)/He analysis of supergene goethite, Hamersley province, Australia. Geological Society of America 34, 173-176.

Hemme, C., 2014. Main Alteration Controls on High-Grade Supergene Goethite-Hematite Iron Ore in the Bobby and Glenda Pits (Pardoo Mine), Pilbara, Western Australia. Master Thesis Applied Geosciences, The University of Western Australia & Aachen University.

Hickman, A.H., 2004. Two contrasting granite−greenstone terranes in the Pilbara Craton, Australia: evidence for vertical and horizontal tectonic regimes prior to 2900 Ma. Precambrian Research 131, 153-172.

Hickman, A.H., 2012. Review of the Pilbara Craton and Fortescue Basin, Western Australia: Crustal evolution providing environments for early life. Island Arc 21, 1-31.

Hickman, A.H., Van Kranendonk, M.J., 2008a. Archean crustal evolution and mineralization of the northern Pilbara craton — a field guide. Geological Survey of Western Australia, Record 2008/13, 79p.

Hickman, A.H., Van Kranendonk, M.J., 2008b. Marble Bar, WA Sheet 2855. Geological Survey of Western Australia, 1:100,000 Geological Series.

Hickman, A.H., Van Kranendonk, M.J., 2012. Early Earth evolution: evidence from the 3.5–1.8 Ga geological history of the Pilbara region of Western Australia. Episodes 35, 283-297.

Huston, D.L., Sun, S.S., R., B., Hickman, A.H., Van Kranendonk, M.J., Philipps, D., Baker, D., Brauhart, C., 2002. The Timing of Mineralization in the Archean North Pilbara Terrain, Western Australia. Economic Geology 97, 733-755.

Kerr, T.L., O'Sullivan, A.P., Podmore, D.C., Turner, R., Waters, P., 1994. Geophysics and iron ore exploration: examples from the Jimblebar and Shay Gap-Yarrie regions, Western Australia. In "Geophysical Signatures of Western Australian Mineral Deposits", Geology and Geophysics Department (Key centre) & UWA Extension, The University of Western Australia, Publication No. 26, 1994, pages 355-367.

Klein, C., 2005. Some Precambrian banded iron-formations (BIFs) from around the world: Their age, geologic setting, mineralogy, metamorphism, geochemistry, and origin. American Mineralogist 90, 1473-1499.

Kollert, N., 2014. Importance of Early Hypogene and Late Supergene Alteration of Archean Banded Iron Formation at the Alice Extension Pit and Joan and Rosita Prospects (Pardoo Mine), Pilbara, Western Australia. Master Thesis Applied Geosciences, The University of Western Australia & Aachen University.

Li, Y., Oldenburg, D.W., 1996. 3-D Inversion of Magnetic Data. Geophysics 61, 394-408.

Li, Y., Oldenburg, D.W., 2000. Joint Inversion of Surface and Three-Component Borehole Magnetic Data. Geophysics 65.

Li, Z.X., Powell, C.M., Bowman, R., 1993. Timing and genesis of Hamersley iron-ore deposits. Exploration Physics 24, 631-636.

Maskell, A., 2010. Multi-stage structural controls and hypogene alteration of high-grade Fe-mineralisation at Matthew Ridge prospect, Jack Hills greenstone belt, Yilgarn craton, Faculty of Natural and Agricultural Sciences. The University of Western Australia, Perth, Australia, p. 50.

Maskell, A., Duuring, P., Hagemann, S.G., 2013. Hydrothermal alteration events controlling magnetite-rich iron ore at the Matthew Ridge prospect, Jack Hills greenstone belt, Yilgarn Craton. Aust. J. Earth Sci.

McCuaig, T.C., Beresford, S., Hronsky, J., 2010. Translating the mineral systems approach into an effective exploration targeting system. Ore Geology Reviews 38, 128-138.

Morris, R.C., 1985. Genesis of iron ore in banded iron-formation by supergene and supergene-metamorphic processes; a conceptual model, in: Wolf, K.H. (Ed.), Handbook of Strata-bound and Stratiform Ore Deposits. Elsevier Science Publications, Amsterdam, pp. 73-235.

Morris, R.C., 2012. Microplaty hematite—its varied nature and genesis. Aust. J. Earth Sci. 59, 411-434.

Muller, S.G., Krapez, B., Barley, M.E., Fletcher, I.R., 2005. Giant iron-ore deposits of the Hamersley province related to the breakup of Paleoproterozoic Australia: New insights from in situ SHRIMP dating of baddeleyite from mafic intrusions. Geological Society of America 33, 577-580.

Nadoll, P., Angerer, T., Mauk, J.L., D., F., J., W., 2014. The chemistry of hydrothermal magnetite: a review. Ore Geology Reviews 16, 1-32.

Neumayr, P., Ridley, J.R., McNaughton, N.J., Kinny, P.D., Barley, M.E., Groves, D.I., 1998. Timing of gold mineralization in the Mt York district, Pilgangoora greenstone belt, and implications for the tectonic and metamorphic evolution of an area linking the western and eastern Pilbara Craton. Precambrian Research 88, 249-265.

Powell, C.M., Oliver, N.H.S., Li, Z.X., Martin, D.M., Ronaszeki, J., 1999. Synorogenic hydrothermal origin for giant Hamersley iron oxide ore bodies. Geology 27, 175-178.

Rasmussen, B., Fletcher, I.R., Sheppard, S., 2005. Isotopic dating of the migration of a low-grade metamorphic front during orogenesis. Geology 38, 773-776.

Rose, A.W., Bianchi-Mosquera, G.C., 1993. Adsorption of Cu, Pb, Zn, Co, Ni, and Ag on goethite and hematite: A control on metal mobilization from red beds into stratiform copper deposits. Economic Geology 88, 1226-1236.

Sabins, F.F., 1987. Remote Sensing: Principles and Interpretation. 2nd Ed.

Shuster, D.L., Vasconcelos, P.M., Heim, J.A., Farley, K.A., 2005. Weathering geochronology by (U-Th)/He dating of goethite. Geochimica Et Cosmochimica Acta 69, 659-673.

Smith, A.J.B., Beukes, N.J., Gutzmer, J., 2013. The composition and depositional environments of mesoarchean iron formations of the West Rand Group of the Witwatersrand Supergroup, South Africa. Economic Geology 108, 111-134.

Smith, R.E., Perdrix, J.L., Parks, T.C., 1982. Burial metamorphism in the Hamersley Basin, Western Australia. J. Petrol. 23, 75-102.

Sugitani, K., Mimura, K., Kazuhiro, S., Nagamine, K., Sugisaki, R., 2003. Stratigraphy and sedimentary petrology of an Archean

volcanic-sedimentary succession at Mt. Goldsworthy in the Pilbara Block, Western Australia: implications of evaporite (nahcolite) and barite deposition. Precambrian Research 120, 55-79.

Sugitani, K., Yamamoto, K., Adachi, M., Kawabe, I., Sugisaki, R., 1998. Archean cherts derived from chemical, biogenic and clastic sedimentation in a shallow restricted basin: examples from the Gorge Creek Group in the Pilbara Block. Sedimentology 45, 1045-1062.

Sweetapple, M.T., Collins, P.L.F., 2002. Genetic Framework for the Classification and Distribution of Archean Rare Metal Pegmatites in the North Pilbara Craton, Western Australia. Economic Geology 97.

Thompson, A., Amistadi, M.K., Chadwick, O.A., Chorover, J., 2013. Fractionation of yttrium and holmium during basaltic soil weathering. Geochimica Et Cosmochimica Acta 119, 18-30.

Thorne, H.M., Trendall, A.F., 2001. Geology of the Fortescue Group, Pilbara craton, Western Australia. Geological survey of Western Australia 144.

Thorne, W., Hagemann, S., Vennemann, T., Oliver, N., 2009. Oxygen Isotope Compositions of Iron Oxides from High-Grade BIF-Hosted Iron Ore Deposits of the Central Hamersley Province Western Australia: Constraints on the Evolution of Hydrothermal Fluids. Economic Geology 104, 1019-1035.

Thorne, W.S., Hagemann, S.G., Barley, M., 2004. Petrographic and geochemical evidence for hydrothermal evolution of the North Deposit, Mt Tom Price, Western Australia. Miner Deposita 39, 766-783.

Trendall, A.F., Compston, W., Nelson, D.R., De Laeter, J.R., Bennett, V.C., 2004. SHRIMP zircon ages constraining the depositional chronology of the Hamersley Group, Western Australia. Aust. J. Earth Sci. 51, 621-644.

Trolard, F., Tardy, Y., 1989. A model of Fe-kaolinite, Al-goethite, Al-hematite equilibria in laterites. Clay Minerals 24, 1-21.

Van Kranendonk, M.J., 2000. Geology of the North Shaw 1:100 000 sheet. Western Australia Geological Survey, 1:100 000 Geological Series Explanatory Notes, 86p.

Van Kranendonk, M.J., 2010. Geology of the Coongan 1:100 000 sheet. Geological Survey of Western Australia, 1:100 000 Geological Series Explanatory Notes, 67p.

Van Kranendonk, M.J., Hickman, A.H., Smithies, R.H., Nelson, D.R., 2002. Geology and tectonic evolution of the Archean North Pilbara Terrain, Pilbara Craton, Western Australia. Economic Geology 97, 695-732.

Van Kranendonk, M.J., Smithies, R.H., Hickman, A.H., Champion, D.C., 2007. Review: secular tectonic evolution of Archean continental crust: interplay between horizontal and vertical processes in the formation of the Pilbara Craton, Australia. Terra Nova 19, 1-38.

Webb, A.D., Dickens, G.R., Oliver, N.H.S., 2003. From banded iron-formation to iron ore: geochemical and mineralogical constraints from across the Hamersley Province, Western Australia. Chemical Geology 197, 215-251.

Wells, M.A., Gilkes, R.J., Anand, R.R., 1989. The formation of corundum and aluminous hematite by the thermal dehydroxylation of aluminous goethite. Clay Minerals 24, 513-530.

White, A.J.R., Smith, R.E., Nadoll, P., Legras, M., 2014. Regional-scale Metasomatism in the Fortescue Group Volcanics, Hamersley Basin, Western Australia: Implications for Hydrothermal Ore Systems. J. Petrol. 55, 977-1009.

Appendices for the M426 Final report

For the purpose of brevity, only selected data sets for the M426 project are included here. A more comprehensive set of appendices has been submitted in digital form with the M426 Final Report.

The digital appendices include:

1. A functional GIS database (geological maps generated during the M426 study)
2. Digitised records of logged drill holes
3. Field photographs
4. Hand specimen photographs
5. Thin section photographs
6. Whole rock geochemical data
7. Isotope data
8. Mineral chemistry data

   Important hand specimens, thin sections, geochemical pulps and excess mineral separation separates have been catalogued and stored in the UWA museum in Crawley or a the Shentone Park storage facility, Perth

Main Alteration Controls on High-Grade Supergene Goethite-Hematite Iron Ore in the Bobby and Glenda Pits (Pardoo Mine), Pilbara, Western Australia

Master Thesis Applied Geosciences
by

Christina Hemme
August 2013

The Bobby and Glenda high-grade (>55 wt% Fe) iron ore deposits are located in the Pardoo iron camp in the Pilbara Craton, Western Australia. Both deposits comprise supergene hematite-goethite iron orebodies hosted by Banded Iron Formation (BIF) of the 3.02 Ga Cleaverville Formation. The orebodies in Bobby and Glenda pits contain a maximum of 60 wt% Fe (the average grade is about 50 wt%), with Si, Ba and Al being the main contaminant elements.

Both deposits are structurally-controlled and are located within an 80 m-wide, brittle-ductile shear zone in the centre of the E-W trending, subvertical Bobby BIF member. These deposits record eight stages of progressive deformation (D1-D8) coupled with several stages of hypogene and supergene alteration of the BIF. Early hypogene alteration in BIF is only locally and weakly preserved in the Bobby deposit in the form of minor disseminated euhedral magnetite grains replacing primary quartz bands and which are now oxidized to hematite (i.e. martite). In contrast, supergene alteration is intense and pervasive in the Bobby BIF.

Supergene alteration post-dates hypogene alteration and is most likely the product of widespread supergene fluid circulation through areas of high permeability in the Bobby BIF, during several discrete stages of reactivation of the main E-W trending, subvertical shear zone. The earliest preserved evidence for supergene mineralization are 0.1 to 2 m-thick, E-W striking, steeply-dipping, vitreous goethite veins that cut the Bobby BIF and proximal siltstone country rocks. The veins are most common and widest in the Glenda pit where they form either discrete veins or vein networks with metre-wide goethite alteration of BIF wallrock. To a lesser extent the goethite veins are present within the south wall of the Bobby pit, and they are exposed as a series of parallel veins in outcrop up to 500 m to the west and along strike of the Bobby pit. These massive and vug-rich vitreous goethite veins represent narrow high-grade iron ore zones in BIF and clastic sedimentary rocks. Although they contain high-grade iron ore (<57 wt% Fe), they commonly host fragments of more siliceous

BIF wallrocks, which lowers their potential value as a likely stand-alone, bulk commodity exploration target in the Pardoo iron camp.

The early goethite vein-style mineralization is subordinate to later E-W trending, shear zone-hosted, ochreous goethite-hematite ore zones that are oriented subparallel to BIF margins. From Mesozoic to recent times, repeated active deformation of the Bobby BIF and the contemporaneous circulation of near-surface derived, oxidized meteoric waters resulted in intense supergene alteration within the 80 m-wide shear zone. The presence of several generations of cross-cutting goethite-hematite-rich veins and associated superimposed supergene wallrock alteration zones within the shear zone provides evidence for the progressive deformation and supergene enrichment of iron oxides in BIF. The fluid circulation and alteration most likely took place during the active deformation of the shear zone, but also between the active deformation events, as a result of the downward passive flow of supergene fluids through the structurally-controlled permeable zones. These supergene fluids progressively removed silica from the altered BIF via silica dissolution and by the direct replacement of quartz by goethite. Mass balance calculations using Al_2O_3 and TiO_2 as least-mobile elements demonstrate that intensively supergene-altered BIF are depleted in SiO_2 by up to 98 % of the original silica contents. Relative to least-altered BIF, the high-grade iron ore zones are consistently enriched in Ba (259 %), P, Mn, As, Cu, Sr and Loss on Ignition components, and display local enrichments in V, Be and Y. Together, these elemental trends represent likely pathfinder elements that are useful for targeting supergene high-grade iron ore bodies in the Bobby BIF.

The Bobby and Glenda deposits demonstrate the importance of structurally-controlled, multistage supergene fluid flow and supergene alteration of BIF in the formation of large volumes of high-grade goethite-hematite iron ore in the Pardoo iron camp. The rare occurrence of hypogene magnetite in the Bobby BIF suggests that either hypogene alteration was not very significant in the formation of the Bobby iron orebody, or that it was poorly preserved due to intense overprinting by supergene enrichment due to intense weathering and downflow of recent meteoric water. Regardless of the importance of early hypogene alteration, this study shows the importance of wide deformation zones, reactivated structures and supergene alteration events in the formation of near-surface iron ore in the Pardoo iron camp.

Importance of Early Hypogene and Late Supergene Alteration of Archean Banded Iron Formation at the Alice Extension Pit and Joan and Rosita Prospects (Pardoo Mine), Pilbara, Western Australia

Master Thesis Applied Geosciences
By

Nils Kollert
August 2013

The Alice Extension pit and the Joan and Rosita prospects are located in the Pardoo iron ore camp about 60 km east of Port Hedland in the Pilbara Craton, Western Australia. The Alice Extension pit is a shear zone-controlled, supergene-modified hypogene iron ore deposit hosted by the Ord Ridley Banded Iron Formation (BIF) member of the 3.02 Ga Cleaverville Formation. BIF-hosted iron ore in the Alice Extension pit has a maximum iron content of 68 wt%, with an average Fe content of 47 wt%. The nearby Joan and Rosita prospects display comparable examples of shear zone-hosted hypogene magnetite and specularite ore zones that are overprinted by supergene goethite-hematite alteration. However, the breadth and intensity of iron enrichment is lower in these latter prospects.

Eight deformation events (D1-D8) are recorded by BIF in the deposit. The first event involved tight folding (Pre-F1) with a plunge of about 248°/64°. The D2 event resulted in early, bedding-parallel, brittle-ductile shear zones that host hypogene magnetite and specularite alteration. These proto-ore zones are indicated by a dramatic decrease in SiO_2, LOI, MgO and CaO, associated with the leaching of primary quartz and siderite, and an increase in W, Fe_2O_3 as well as HREE. The D3 and D4 deformation events resulted in folds (F1 and F2) that control the S-shaped geometry (in plan) and plunge of the high-grade iron ore shoots in the Alice Extension deposit. Mafic dikes, most likely genetically affiliated with the overlying 2.97 to 2.95 Ga Paradise Plains Formation, intruded BIF in the Alice Extension deposit during the D5 deformation event. Intense supergene alteration was associated with E-W trending, subvertical, brittle-ductile shear zones that formed during D6. Supergene fluids, most likely involving near-surface oxidized meteoric waters, circulated vertically and horizontally within the E-W-trending shear zones and resulted in the oxidation of hypogene magnetite to martite and the replacement of primary silica, siderite and iron oxide bands by supergene goethite ± hematite. Changes in the geochemistry of the primary BIF and hypogene iron ores involved further enrichment in $Fe_2O_{3\ (total)}$ and the contemporaneous depletion of SiO_2, MgO, CaO and LOI. The supergene alteration event was important in

removing quartz from the hypogene magnetite- and specularite-rich proto-ores in BIF. The D7 and D8 events resulted in gentle recumbent folding (F3 folds) that modified the geometry of the steeply dipping beds, earlier F1 and F2 folds and the schistose fabric in supergene-altered shear zones.

The main geochemical vectors to supergene-modified, hypogene high-grade ore are the major depletions in SiO_2, MgO, CaO and LREE, and coincident enrichments in Fe_2O_3, P_2O_5, Ni, Be and HREE. In addition, the hypogene iron ore zones are notably enriched in W and Co compared with least-altered BIF (and supergene iron ore zones). The main controls on high-grade iron ore in the Alice Extension deposit and the Joan and Rosita prospects are the fold-thickening of BIF, the reactivation of shear zones, and the superposition of early hypogene ore zones by intense supergene alteration.

Sample	alteration intensity	alteration style	Rock type	Project	Site	collected	Easting	Northing	Depth (m)	photo	Whole Rock	Thin section	Mineral chem	Isotopes
ABTR06	least altered	least altered	jaspilitic BIF	Abydos	Trigg	Pit	718089	7660391	0	x	x			
ABTR07	strong	martite - goethite	jaspilitic BIF	Abydos	Trigg	Pit	718089	7660381	0	x		x	x	
ABTR22	least altered	least altered	jaspilitic BIF	Abydos	Trigg	Pit	718640	7660459	0	x	x			x
ABTR23	high	martite	jaspilitic BIF	Abydos	Trigg	Pit	718640	7660459	0	x	x			x
ABTR24	least altered	least altered	jaspilitic BIF	Abydos	Trigg	Pit	718640	7660459	0	x	x			x
ABTR28	high	goethite vein	jaspilitic BIF	Abydos	Trigg	Pit	718539	7660410	0	x	x	x	x	
ABTR29	high	martite goethite	jaspilitic BIF	Abydos	Trigg	Pit	718532	7660427	0	x	x			x
ABTR32	high	martite	jaspilitic BIF	Abydos	Trigg	Pit	718481	7660449	0	x	x			x
ABTR40	high	martite - goethite	jaspilitic BIF	Abydos	Trigg	Pit	718319	7660443	0		x			
ABTR42	moderate	goethite	cherty BIF	Abydos	Trigg	Pit	718364	7660472	0	x		x	x	
ABDH13- 06	low	pyrite + ankerite	cherty BIF	Abydos	Trigg	hole ABDH0013	718762.21	7660441	139.4	x	x	x		
ABDH13- 07	low	pyrite + ankerite	cherty BIF	Abydos	Trigg	hole ABDH0013	718762.21	7660441	146.7	x		x		
ABDH28- 01	high	martite - goethite	jaspilitic BIF	Abydos	Trigg	hole ABDH0028	718799.86	7660497	28.9	x	x			x
ABDH28- 02	high	goethite	jaspilitic BIF	Abydos	Trigg	hole ABDH0028	718799.86	7660497	31.9	x	x			x
ABDH28- 03	high	goethite	jaspilitic BIF	Abydos	Trigg	hole ABDH0028	718799.86	7660497	46.8		x			
ABDH28- 04	high	goethite	jaspilitic BIF	Abydos	Trigg	hole ABDH0028	718799.86	7660497	50.2	x	x			x
ABDH29- 01	high	goethite	jaspilitic BIF	Abydos	Trigg	hole ABDH0029	718798.98	7660448	40	x	x			
ABDH30- 01	moderate	martite	jaspilitic BIF	Abydos	Trigg	hole ABDH0030	718760.32	7660503	53.3	x	x	x	x	x
ABDH45- 01	moderate	goethite	jaspilitic BIF	Abydos	Mettams	hole ABDH0045	716439.92	7660016	30.4		x			
ABME07	moderate	martite	jaspilitic BIF	Abydos	Mettams	Surface	716660	7659951	0	x	x	x		
ABME10	moderate	magnetite	jaspilitic cherty BIF	Abydos	Mettams	Surface	716680	7660194	0	x		x	x	x
ABME 11	moderate	martite	jaspilitic BIF	Abydos	Mettams	Surface	716581	7660122	0	x	x	x	x	x
ABME 22	moderate	magnetite + goethite	jaspilitic BIF	Abydos	Mettams	Surface	?	?	0	x	x	x	x	x
CD0-M03	moderate	martite	jaspilitic BIF	Corunna Downs	Split Rock	Surface	?	?	0			x		
CD1-M03	moderate	magnetite	jaspilitic BIF	Corunna Downs	Split Rock	Surface	776405	7622556	0			x	x	x
CD1-M05	moderate	magnetite martite	jaspilitic BIF	Corunna Downs	Split Rock	Surface	776405	7622556	0		x			
CD1-M07	high	microplaty hem + goethite	jaspilitic BIF	Corunna Downs	Split Rock	Surface	776225	7622714	0			x	x	
CD6-M03	strong	martite - goethite	jaspilitic BIF	Corunna Downs	Split Rock	Surface	776159	7622853	0	x		x	x	
CD6-M08	least altered	least altered	jaspilitic BIF	Corunna Downs	Split Rock	Surface	776190	7622793	0	x	x	x		x
CD7-M06	moderate to strong	magnetite	jaspilitic BIF	Corunna Downs	Runway	Surface	777569	7628433	0	x		x	x	
CDDH1-09	moderate	goethite	BIF	Corunna Downs	Split Rock	Hole CDDH0001	776205.86	7623109	150.8	x	x			
CDDH1-11	high	ochreous goethite	jaspilitic BIF	Corunna Downs	Split Rock	Hole CDDH0001	776205.86	7623109	92.1		x			
CDDH1-16	high	martite - goethite	jaspilitic BIF	Corunna Downs	Split Rock	Hole CDDH0001	776205.86	7623109	36	x	x			x
CDDH1-17	high	goethite	jaspilitic BIF	Corunna Downs	Split Rock	Hole CDDH0001	776205.86	7623109	17.4		x			
CDDH1-18	high	martite - goethite	jaspilitic BIF	Corunna Downs	Split Rock	Hole CDDH0001	776205.86	7623109	8.3	x	x			x
CDDH2-03	least altered	least altered	jaspilitic BIF	Corunna Downs	Split Rock	Hole CDDH0002	776232.63	7623284	87.5	x	x			
CDDH2-04	moderate	martite - goethite	jaspilitic BIF	Corunna Downs	Split Rock	Hole CDDH0002	776232.63	7623284	70.6	x		x	x	
CDDH2-07	high	goethite	jaspilitic BIF	Corunna Downs	Split Rock	Hole CDDH0002	776232.63	7623284	56.2	x	x			x
CDDH2-08	high	martite	jaspilitic BIF	Corunna Downs	Split Rock	Hole CDDH0002	776232.63	7623284	52.6	x	x			
CDDH2-09	high	martite	jaspilitic BIF	Corunna Downs	Split Rock	Hole CDDH0002	776232.63	7623284	50.5	x	x			
CDDH2-10	high	martite	jaspilitic BIF	Corunna Downs	Split Rock	Hole CDDH0002	776232.63	7623284	35.6	x	x			
CDDH2-14	high	martite	jaspilitic BIF	Corunna Downs	Split Rock	Hole CDDH0002	776232.63	7623284	8.4	x	x	x	x	
CDDH3-01	high	martite - goethite	jaspilitic BIF	Corunna Downs	Split Rock	Hole CDDH0003	776211.94	7623359	24.4		x	x	x	
CDDH3-02	high	goethite	jaspilitic BIF	Corunna Downs	Split Rock	Hole CDDH0003	776211.94	7623359	25.4	x	x			
CDDH3-04	least altered	least altered	jaspilitic BIF	Corunna Downs	Split Rock	Hole CDDH0003	776211.94	7623359	48.2	x	x	x	x	x
CDDH3-08	moderate	martite - goethite	jaspilitic BIF	Corunna Downs	Split Rock	Hole CDDH0003	776211.94	7623359	116.6	x		x		
CDDH3-09	high	ochreous goethite	jaspilitic BIF	Corunna Downs	Split Rock	Hole CDDH0003	776211.94	7623359	125		x			x
CDDH4-19	high	martite - goethite	jaspilitic BIF	Corunna Downs	Split Rock	Hole CDDH0004	776245.52	7623444	19.4		x	x	x	
CDDH5- 2	high	martite - goethite	jaspilitic BIF	Corunna Downs	Split Rock	Hole CDDH0005	776128.74	7623069	60	x	x			x
CDDH9- 2	high	ochreous goethite	jaspilitic BIF	Corunna Downs	Runway	Hole CDDH0009	776128.74	7623069	27.5		x			x

CDDH9- 8	high	goethite	jaspilitic BIF	Corunna Downs	Runway	Hole CDDH0009	776128.74	7623069	65.9	x	x			x
CDDH9-09	high	goethite	jaspilitic BIF	Corunna Downs	Runway	Hole CDDH0009	776128.74	7623069	73.9			x	x	
CDDH9- 10	high	goethite	jaspilitic BIF	Corunna Downs	Runway	Hole CDDH0009	777759.14	7628636	79.6	x	x			x
CDDH9- 12	high	goethite	jaspilitic BIF	Corunna Downs	Runway	Hole CDDH0009	777759.14	7628636	83.3	x	x			x
CDDH9- 14	high	martite - goethite	jaspilitic BIF	Corunna Downs	Runway	Hole CDDH0009	777759.14	7628636	88.5		x			
CDDH9- 15	high	martite	jaspilitic BIF	Corunna Downs	Runway	Hole CDDH0009	777759.14	7628636	89.5		x			x
CDDH9- 16	high	martite	jaspilitic BIF	Corunna Downs	Runway	Hole CDDH0009	777759.14	7628636	94.2		x			
CDDH9- 17	high	martite	jaspilitic BIF	Corunna Downs	Runway	Hole CDDH0009	777759.14	7628636	101.5		x			
CDDH9- 18	high	martite	jaspilitic BIF	Corunna Downs	Runway	Hole CDDH0009	777759.14	7628636	104.8		x			
CDDH9- 19	high	martite	jaspilitic BIF	Corunna Downs	Runway	Hole CDDH0009	777759.14	7628636	122.5		x			x
CDDH10-20	moderate	pyrite + ankerite	cherty BIF	Corunna Downs	Runway	Hole CDDH0010	777827.28	7628554	123.8	x		x		
WDA6-01	high	martite + supergene hematite	BIF	Wodgina	Anson stage 6	Pit	672183	7654028	0	x	x	x		x
WDA6-02	least altered	least altered	BIF	Wodgina	Anson stage 6	Pit	672134	7654065	0		x			x
WDA6-03	high	martite + supergene hematite	BIF	Wodgina	Anson stage 6	Pit	672141	7654059	0		x			x
WDA6-04	weak	martite	BIF	Wodgina	Anson stage 6	Pit	672087	7654011	0	x	x	x	x	x
WDAM-01	moderate to strong	martite	BIF	Wodgina	Anson Main	Pit	672107	7654371	0		x	x	x	x
WDAM-05	high	supergene hematite	BIF	Wodgina	Anson Main	Pit	672107	7654371	0	x	x			
WDDN-02	least altered	least altered	BIF	Wodgina	Dragon North	Pit	673371	7654493	0	x	x			x
WDDN-05	weak	martite - goethite	sandstone	Wodgina	Dragon North	Pit	673371	7654493	0		x			
WDDN-08	high	goethite	BIF	Wodgina	Dragon North	Pit	673383	7654434	0		x			x
WDDN-10	least altered	least altered	shale	Wodgina	Dragon North	Pit	673389	7654417	0		x			
WDDN-12	least altered	least altered	black shale	Wodgina	Dragon North	Pit	673312	7654328	0		x			
WDDN-13	high	supergene hematite	BIF	Wodgina	Dragon North	Pit	673208	7654384	0	x	x	x	x	x
WDDN-16	weak	martite - goethite	sandstone	Wodgina	Dragon North	Pit	673288	7654424	0	x	x			
WDDH18-01	moderate to strong	martite - goethite	BIF	Wodgina	Anson stage 6	Hole WDDH0018	672160.618	7653999	12.5	x	x			x
WDDH18-05	high	magnetite - martite	BIF	Wodgina	Anson stage 6	Hole WDDH0023	672160.618	7653999	65	x	x			
WDDH23-01	least altered	least altered	BIF	Wodgina	Dragon North	Hole WDDH0023	673204.623	7654401	22	x	x			
WDDH23-02	high	supergene hematite	sandstone	Wodgina	Dragon North	Hole WDDH0023	673204.623	7654401	34	x	x	x		
WDDH23-03	high	martite - goethite	BIF	Wodgina	Dragon North	Hole WDDH0023	673204.623	7654401	40		x			
WDDH23-04	high	supergne hematite	BIF	Wodgina	Dragon North	Hole WDDH0023	673204.623	7654401	48	x	x			x
WDDH23-06	high	goethite	BIF	Wodgina	Dragon North	Hole WDDH0023	673204.623	7654401	58.4		x	x		
WDDH23-07	high	goethite - hematite	BIF	Wodgina	Dragon North	Hole WDDH0023	673204.623	7654401	69.1	x		x		
WDDH56-01	strong to high	martite - goethite	BIF	Wodgina	Anson Main	Hole WDDH0056	672131.126	7654360	8.3	x	x	x	x	x
WDDH56-02	high	martite - goethite	BIF	Wodgina	Anson Main	Hole WDDH0056	672131.126	7654360	21.8	x	x	x		
WDDH56-05	high	martite - goethite	BIF	Wodgina	Anson Main	Hole WDDH0056	672131.126	7654360	28.5	x	x			x
WDDH56-06	high	martite	vein in BIF	Wodgina	Anson Main	Hole WDDH0056	672131.126	7654360	37.7		x	x		
WDDH56-07	strong to high	martite	BIF	Wodgina	Anson Main	Hole WDDH0056	672131.126	7654360	37.7		x	x		x
WDDH56-08	least altered	least altered	BIF	Wodgina	Anson Main	Hole WDDH0056	672131.126	7654360	40		x			
WDDH56-14	least altered	least altered	cherty BIF	Wodgina	Anson Main	Hole WDDH0056	672131.126	7654360	76	x	x			x
APNK 1	least altered	least altered	BIF	Pardoo	ALX	Pit			0	x	x	x		x
APNK 67	moderate	magnetite	BIF	Pardoo	ALX	Pit			0		x			
APNK 3	least altered	least altered	jaspilitic BIF	Pardoo	ALX	Pit			0	x	x			x
APNK 61	moderate	magnetite	BIF	Pardoo	ALX	Pit			0		x			
APNK 2	least altered	least altered	jaspilitic BIF	Pardoo	ALX	Pit			0	x	x			
APNK24	low	martite + platy hematite	jaspilitic BIF	Pardoo	ALX	Pit			0	x		x	x	
APNK 49	least altered	least altered	cherty BIF	Pardoo	ALX	Pit			0	x	x			
APNK 66	moderate	goethite	BIF	Pardoo	ALX	Pit			0		x			
APNK 56	high	kaolinite	mafic dike	Pardoo	ALX	Pit			0		x			
APNK 29	high	martite - goethite	jaspilitic BIF	Pardoo	ALX	Pit			0	x	x			x
APNK33	high	goethite	jaspilitic BIF	Pardoo	ALX	Pit			0			x	x	
APNK 39	high	goethite	jaspilitic BIF	Pardoo	ALX	Pit			0	x	x	x		
APNK76	moderate	martite	jaspilitic BIF	Pardoo	ALX	Pit			0	x		x		

ALX_PDDH 045/04	high	martite - goethite	jaspilitic BIF	Pardoo	ALX	Hole PDDH0045	721860.5	7758743			x			x
PDDH46-14	moderate	magnetite	jaspilitic BIF	Pardoo	ALX	Hole PDDH0046	721810.147	7758660		x		x	x	
APNK 106	high	martite + platy hematite	jaspilitic BIF	Pardoo	ALX	Pit			0		x			
APNK 111	high	martite + platy hematite	jaspilitic BIF	Pardoo	ALX	Pit			0		x			x
APNK 112	high	martite + platy hematite	jaspilitic BIF	Pardoo	ALX	Pit			0		x			x
RPNK3	strong	martite + platy hematite	jaspilitic BIF	Pardoo	Rosita	Surface			0	x		x	x	
RPNK15	moderate	martite	jaspilitic BIF	Pardoo	Rosita	Surface			0			x		x
RPNK17	moderate	martite - goethite	jaspilitic BIF	Pardoo	Rosita	Surface			0	x		x		x
RPNK21	strong	martite + supergene hematite	jaspilitic BIF	Pardoo	Rosita	Surface			0	x		x	x	
B_PDDH 006/03	moderate	kaolinite	mafic dike	Pardoo	Bobby	Hole PDDH0006	722599.074	7760090			x			
Bob_Pit 059	moderate	kaolinite	mafic dike	Pardoo	Bobby	Pit			0		x			
Bob_Pit 078	moderate	kaolinite	mudstone	Pardoo	Bobby	Pit			0	x	x			
Bob_Pit 057	moderate	kaolinite	mudstone	Pardoo	Bobby	Pit			0		x			
Bob_Pit 085	high	goethite	sandstone	Pardoo	Bobby	Pit			0		x			
Glenda_Pit 005	least altered	least altered	sandstone	Pardoo	Glenda	Pit			0		x			
Glenda_Pit 012	moderate	goethite	cherty BIF	Pardoo	Glenda	Pit			0		x			
G_PDDH 019/002	high	goethite	BIF	Pardoo	Glenda	Hole PDDH0019	722427.02	7760230			x			
Glenda_Pit 013	high	goethite	BIF	Pardoo	Glenda	Pit			0		x			
Bob_Pit 022	high	goethite	BIF	Pardoo	Bobby	Pit			0		x			x
Bob_Pit 034	moderate	goethite	cherty BIF	Pardoo	Bobby	Pit			0		x			
Bob_Pit 020	high	goethite	BIF	Pardoo	Bobby	Pit			0	x	x	x		
Bob_Pit 023	moderate	goethite	BIF	Pardoo	Bobby	Pit			0	x		x	x	
Bob_Pit 031	strong	goethite	BIF	Pardoo	Bobby	Pit			0	x		x	x	
B_PDDH 006/7	high	goethite	BIF	Pardoo	Bobby	Hole PDDH0006	722599.074	7760090				x	x	
B_PDDH 006/16	high	goethite	BIF	Pardoo	Bobby	Hole PDDH0006	722599.074	7760090				x		
B_PDDH 006/12	moderate	goethite	BIF	Pardoo	Bobby	Hole PDDH0006	722599.074	7760090		x	x			x
B_PDDH 006/11	moderate	goethite	BIF	Pardoo	Bobby	Hole PDDH0006	722599.074	7760090		x	x			
B_PDDH 018/009	moderate	goethite	BIF	Pardoo	Bobby	Hole PDDH0018	722719.05	7760132		x	x			

This Report is the product of a joint research initiative coordinated by the Minerals Research Institute of Western Australia (MRIWA) involving Atlas Iron Ltd, the Centre for Exploration Targeting (CET) at The University of Western Australia, RWTH Aachen University, and the Geological Survey of Western Australia (MRIWA Project M426).

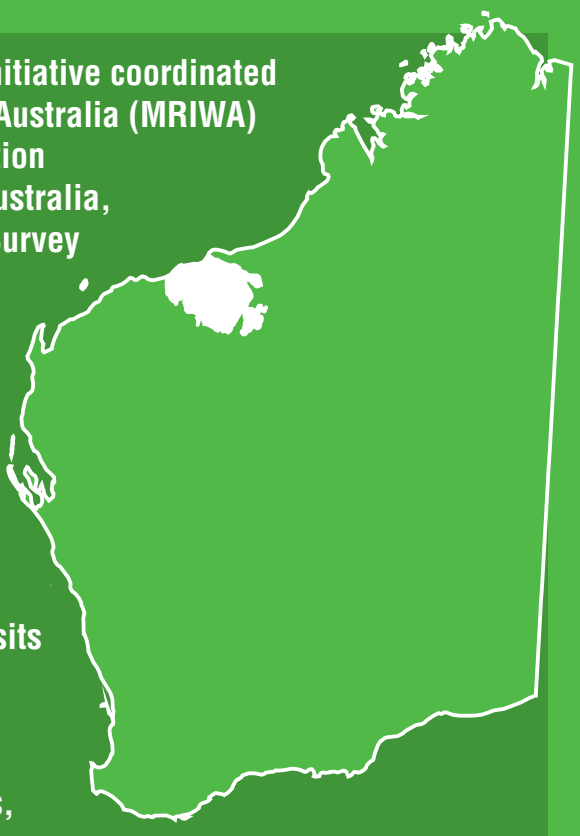

The Pilbara Craton includes greenstone sequences that comprise mainly volcanic and clastic sedimentary rocks, with minor intervals of Mesoarchean banded iron-formation (BIF) that are thickest and most laterally extensive in the eastern parts of the craton. This contribution presents an overview of the main BIF-hosted iron ore deposits in the Pilbara Craton (that is, excluding the Hamersley Basin), with an emphasis on relationships between the BIF host, structures, iron ore types, alteration mineral assemblages, and indicator geochemistry for high-grade iron ore zones.

Further details of geological products and maps produced by the Geological Survey of Western Australia are available from:

Information Centre
Department of Mines and Petroleum
100 Plain Street
EAST PERTH WA 6004
Phone: (08) 9222 3459 Fax: (08) 9222 3444

www.dmp.wa.gov.au/GSWApublications

DUURING et al.

MRIWA REPORT PROJECT M426: EXPLORATION TARGETING FOR BIF-HOSTED FE DEPOSITS IN THE PILBARA CRATON, WESTERN AUSTRALIA

REPORT 163